Degradation mechanisms of oxide ceramics under molten regolith electrolysis conditions

Thesis by

Kevin Yu

In Partial Fulfillment of the Requirements for

the degree of

Doctor of Philosophy in Materials Science

CALIFORNIA INSTITUTE OF TECHNOLOGY

Pasadena, California

2026

Defended September 26, 2025

© 2025

Kevin Yu
ORCID: 0000-0003-3130-4309

ACKNOWLEDGEMENTS

First, I would like to thank my advisor, Professor Katherine T. Faber. Leaving my previous job to pursue a Ph.D. was not easy, but I couldn't have asked for a better advisor. Thank you for letting me explore the research topics that I am passionate about. I know that the contents of this thesis are a departure from existing work in your group, but your continued support and encouragement have allowed us to perform amazing science and occasionally, some engineering as well. It has been such a pleasure working with you and learning from you!

Next, I would like to thank Professor Brent Fultz, Professor Guruswami (Ravi) Ravichandran, and Professor Kimberly See for serving on my thesis committee and helpful discussions through my research. I'd also like to thank Professor Joe Falson and Professor Julia Kornfield for serving on my candidacy committee. Finally, I'd like to thank Professor Hosea Nelson and Professor George Rossman for providing guidance and resources when I hit a roadblock in my research. The interactions I have had with the faculty at Caltech have taught me how to become a better scientist and researcher.

Next, I would like to thank all my collaborators, including Dr. Jamesa Stokes and Dr. Bryan Harder at NASA Glenn, Dr. Lorlyn Reidy and Dr. Jesus Dominguez at NASA Marshall, Dr. William West at JPL, and Dr. Kunal Jha and Professor Hosea Nelson at Caltech. To Jamesa and Bryan, thank you for making every visit fun and for bringing the can-do attitude to every meeting, whether it was in person or virtual. To Lorlyn and Jesus, thank you for sitting through my long MRE reactor design reviews and for providing guidance that enabled us to build the laboratory-scale MRE cell. To Will, thank you for helping me make this hollow anode idea a reality and for supporting me every step along this journey. To Hosea and Kunal, thank you for your time and resources spent on solving a crystal structure that stumped everyone else I spoke with.

Beyond my collaborators, I'd like to thank all the other people who have helped me along the way, whether it was providing resources or having helpful discussions, including Dr. Bekah Webster, Dr. Ben Kowalski, Dr. Kang Lee, Dr. Nate Jacobsen, Dr. Gustavo Costa, Dr. Ben Hulbert, Dr. Richard Rogers, Dr. Laura Wilson, Dr. Donald Dornbusch, Dr. Will

Huddleston, Leland Hoffman, and John Setlock at NASA Glenn; Dr. Thierry Caillat, Dr. Ike Chi, Dr. Nick Heinz, Dr. Fivos Drymiotis, Dr. John-Paul Jones, George Nakatsukasa, Keith Billings, Kevin Smith, Billy Li, Greg Gerig, Flora Yang, and Paul Santillana at JPL; Dr. Laurent Sibille and Dr. Kevin Grossman at NASA Kennedy; and Professor Jean-Philippe Harvey at École Polytechnique de Montréal. I'd also like to thank the Caltech scientists and staff for their assistance, including Dr. Chi Ma from the GPS Analytical Facility, Dr. Sonjong Hwang from CCE solid state NMR facility, Nate Hart from the CCE glass shop, and Paul Stovall and Trent Wilson from the MCE machine shop.

I also want to thank all the members of the Faber group, past and present, for keeping me sane and productive during my time at Caltech, including Dr. Benjamin Herren, Dr. Celia Chari, Dr. Vince Wu, Dr. Laura Quinn, Sara Gorske, Seneca Velling, Zac Chase, Wes Patel, and Maia Hannahs. A big shout-out to Sara, who helped me get through the initial coursework after not having taken classes for 5 years prior to starting at Caltech.

I would also like to thank my friends at Caltech, Dr. Thomas Tran, Dr. Emily Hwang, Lily Shiau, and Sahil Patel, who have helped with both technical discussions and good distractions at Red Door. I'd also like to thank Dr. Cullen Quine and Dr. Will Palfey for their research help and emotional support when I've needed it.

I want to acknowledge the wonderful events and support I have gotten from the Keck Institute for Space Studies. It has been amazing talking with both the staff and affiliates about our shared interest in space science and exploration. The events have been so unique and allowed me to broaden my knowledge in other fields relating to space. To Professor Bethany Ehlmann, Harriet Brettle, Professor Tom Prince, Michele Judd, Janet Seid, and Antonio Soriano, thank you for everything.

I'd also like to thank all the people who motivated me and encouraged me to go and get my Ph.D., including Dr. Kathy Lee, Brian Phan, Dr. Ike Chi, Dr. Dean Cheikh, Sutinee Sujittosakul, Michell Aranda, Obed Villalpando, Dr. Araseli Cortez, Megan Cooper, Dr. Chen-Kuo Huang, Dr. Fivos Drymiotis, Dr. Nick Heinz, Dr. Caitlin Crawford, Dr. Giacomo Cerretti, Samad Firdosy, Kevin Smith, Billy Li, Dr. Thierry Caillat, Stan Pinkowski, Dr.

David Woerner, Dr. Terry Hendricks, Dr. Steven Jones, Professor Matthew Barry, Dr. Fran Hurwitz, Dr. Stevie Steiner, and Dr. Mihail Petkov. I like to joke that it took a global pandemic for me to finally decide to get my Ph.D., but really, it was the encouragement I received from you all that finally got me to commit to Caltech.

I would like to thank all of Caltech's administration staff that I have interacted with in my time here, including Christy Jenstad, Jennifer Blankenship, Katie Pichotta, Mabby Howard, and Pam Albertson. It's been a long 5 years, but you have all made it go as seamlessly as possible on the administrative side. To Christy, thank you for everything, from just hanging out, to helping me track my grant budget, to listening to my rants, to coordinating construction projects around my experiments. You have truly handled everything not related to lab work and allowed me to focus my energy on getting the research done.

I would like to gratefully acknowledge the NASA Space Technology Graduate Research Opportunities and the Foster and Coco Stanback Space Innovation Fund for funding and supporting my thesis research.

To my non-Caltech friends, thank you for keeping me grounded and reminding me there is a life outside of the lab. It has been so wonderful seeing everyone on their own path, whether that's having a kid, getting married, finding a better job, opening a coffee shop, etc. To my friends who've stuck with Gang Green, we won the Super Bowl right before the Apollo 11 landed on the Moon. I pray that this is a sign that we'll have another Super Bowl before Artemis 3 lands on the Moon.

Lastly, thank you to my family. To my parents, Hongchao and Huaping, thank you for supporting and encouraging me throughout graduate school. To my brother, Brian, thank you for always being there and hanging out in the limited time I have at home. To my freeloading cat, Betsy, thanks for existing and being soft. To my wife, Ivana, thank you for always believing in me and forever being my inspiration. Your love and companionship have gotten me through this degree. I never would have gotten through this without you.

- Kevin

ABSTRACT

Molten regolith electrolysis (MRE) is a promising in situ resource utilization process that produces both metals and O_2 through the direct electrolysis of molten lunar regolith (dirt), in support of a permanent human presence on the Moon. However, MRE requires an operational temperature of 1600°C, involves contact with corrosive molten regolith, and causes an oxidizing atmosphere during electrolysis. These conditions prevent the usage of many refractory materials due to rapid degradation. Moreover, there are additional challenges associated with MRE, such as bubble detachment and O_2 collection at the anode.

In this thesis, a hollow anode design, composed of an oxygen-conducting yttria-stabilized zirconia (YSZ) shell and a platinum current collector, is presented to address the challenges of MRE. Research is performed to evaluate the performance of YSZ electrolytes and containment materials in the extreme MRE environment and identify the mechanisms governing their degradation. From these experiments, a laboratory-scale MRE cell is designed and fabricated to support hollow anode testing. Electrolysis experiments with lunar regolith simulants successfully demonstrate sustained oxygen production for up to 12 hours. Extended testing with a degradation mitigation strategy further increases O_2 production efficiencies and enables cumulative operation of 40 hours, establishing design life estimates for YSZ hollow anodes and guidelines for integration into industrial-scale MRE systems.

A previously unreported Sc_2O_3-rich phase, silicon aluminum scandate (SAS), is discovered while performing materials compatibility testing. The crystal structure of SAS is solved using microcrystal electron diffraction, and its material properties are characterized. These results indicate that SAS is an entropy-stabilized oxide with potential applications as a thermally insulating, refractory oxide material.

Ultimately, the work presented demonstrates the feasibility of YSZ hollow anodes for MRE and expands the understanding of ceramic behavior in molten oxide environments. The successful production of O_2 with a hollow anode provides a foundation for scaling MRE toward industrial operation on the lunar surface, while the discovery of SAS highlights the potential for uncovering new oxide materials in extreme environments.

PUBLISHED CONTENT AND CONTRIBUTIONS

K. Yu, J. Stokes, B. Harder, L. Reidy, K.T. Faber (2024). “Thermochemical interactions between yttria-stabilized zirconia and molten lunar regolith simulants”. In: *Journal of the American Ceramic Society* 107(11), pp. 7119-7130. DOI: 10.1111/jace.19821

K.Y. led the experimental work and writing of the manuscript.

K. Yu, W. West, J. Stokes, B. Harder, L. Reidy, J. Dominguez, K.T. Faber (2025). “Improving molten regolith electrolysis with zirconia-based hollow anode technology”. In: *Acta Astronautica* 235, pp. 723-735. DOI: 10.1016/j.actaastro.2025.06.028

K.Y. led the experimental work and writing of the manuscript.

K. Yu, J. Stokes, K.K. Jha, B. Harder, H.M. Nelson, K.T. Faber (n.d.). “Discovery and characterization of a silicon aluminum scandate (SAS) material”. In: *Under review.*

K.Y. led the experimental work and writing of the manuscript.

K. Yu, W. West, K.T. Faber (n.d.). “Zirconia-based hollow anodes for improved molten regolith electrolysis”. US patent application number: 19/046,915.

K.Y. is the first named inventor. Utility patent application has been submitted to USPTO.

K. Yu, K.T. Faber, J. Stokes, B. Harder (n.d.). “Silicon Aluminum Scandate (SAS) Refractory Ceramics”. US patent application number: 19/338,267.

K.Y. is the first named inventor. Utility patent application has been submitted to USPTO.

TABLE OF CONTENTS

Acknowledgements iii
Abstract vi
Published Content and Contributions vii
Table of Contents viii
List of Illustrations xii
List of Tables xix
Chapter 1: Introduction 1
1.1 Background 1
1.1.1 Motivation for in situ O_2 production on the lunar surface 1
1.1.2 O_2 production through in situ resource utilization 2
1.1.3 Molten regolith electrolysis 3
1.2 MRE challenges 6
1.2.1 Materials degradation 6
1.2.2 O_2 collection in MRE reactors 8
1.3 Hollow anode design 9
1.4 Thesis outline 10
References 13
Chapter 2: Evaluation of unary oxides with molten regolith simulants 19
2.1 Introduction 19
2.2 Experimental procedures and materials 22
2.2.1 Lunar regolith simulants 22
2.2.2 Powder experiments 22
2.3 Results 23
2.3.1 ZrO_2 23
2.3.2 HfO_2 27
2.3.3 Y_2O_3 31
2.3.4 Sc_2O_3 36
2.3.5 EDS vs. EPMA 40
2.4 Discussion 40
2.4.1 ZrO_2 and HfO_2 particle morphology 40
2.4.2 Lack of zircon and hafnon 41
2.4.3 Dissolution during MRE 42
2.5 Conclusion 46
References 48
Chapter 3: Degradation of yttria-stabilized zirconia by molten regolith simulants 53
3.1 Introduction 53
3.2 Experimental procedures and materials 55
3.2.1 Lunar regolith simulants 55
3.2.2 Powder experiments 55
3.2.3 Crucible experiments 56
3.2.4 FactSage thermochemistry model 57

3.3 Results 57
3.3.1 Powder experiments 57
3.3.2 Crucible experiments 62
3.3.2.1 Bulk regolith behavior 62
3.3.2.2 YSZ/regolith interfacial behavior 66
3.4 Conclusion 72
References 74
Chapter 4: Electrolysis of lunar highlands regolith using zirconia-based hollow anodes 77
4.1 Introduction 77
4.2 Materials and methodology 79
4.2.1 Lunar regolith simulants 79
4.2.2 Molten regolith electrolysis experiments 80
4.2.2.1 Electrolysis cell fabrication 81
4.2.2.2 Electrolysis conditions 81
4.2.3 Characterization 81
4.2.3.1 Optical microscopy 82
4.2.3.2 Electron microscopy 82
4.2.3.3 Raman spectroscopy 83
4.2.3.4 FactSage analysis 83
4.3 Results 84
4.3.1 Electrolysis data 84
4.3.2 Cathodic products 88
4.3.3 Solidified regolith analysis 92
4.3.4 FactSage thermochemical results 93
4.3.5 YSZ interactions 95
4.3.5.1 Thermochemically-induced interactions 95
4.3.5.2 Potential-induced interactions 98
4.4 Implications for hollow anode design 101
4.4.1 YSZ regeneration 102
4.4.2 Design life 102
4.4.3 Thermal cycling behavior 103
4.4.4 Anode mass payback ratio 103
4.4.5 Lunar maria electrolysis 104
4.5 Conclusions 105
References 107
Chapter 5: Testing yttria-stabilized zirconia electronic conductivity suppression methods 111
5.1 Introduction 111
5.2 Rationale for regeneration and mitigation 116
5.3 Materials and methodology 121
5.3.1 Lunar regolith simulant 121
5.3.2 Molten regolith electrolysis experiments 121
5.3.2.1 Electrolysis cell fabrication 122
5.3.2.2 Regeneration and mitigation testing 122

5.3.3 Characterization 125
5.4 Results and discussion 125
5.4.1 Electrolysis #1 data 125
5.4.2 Regeneration testing 128
5.4.3 Cell resistance testing 130
5.4.4 Mitigation experiments 132
5.4.5 Microscopy of cross-sectioned cell 134
5.5 Implications for hollow anode design 135
5.5.1 Regeneration vs. mitigation 135
5.5.2 YSZ wall recession 137
5.5.3 Refined anode mass payback ratio 138
5.6 Conclusion 140
References 141
Chapter 6: Discovery and characterization of a silicon aluminum scandate (SAS) material 143
6.1 Introduction 143
6.2 Materials and methods 145
6.2.1 Experimental methods 145
6.2.1.1 Powder synthesis 145
6.2.1.2 Pellet experiments 146
6.2.2 Microcrystal electron diffraction 147
6.2.3 X-ray diffraction 147
6.2.3.1 Ambient X-ray diffraction 147
6.2.3.2 High-temperature in situ X-ray diffraction 148
6.2.4 Electron-probe microanalysis 149
6.2.5 Scanning electron microscopy 149
6.2.6 Solid-state nuclear magnetic resonance 150
6.2.7 Differential thermal analysis 150
6.2.8 Laser flash analysis 151
6.3 Results 151
6.3.1 Structure determination 151
6.3.1.1 Microcrystal electron diffraction solution 151
6.3.1.2 Powder XRD refinement 152
6.3.1.3 Crystal structure 153
6.3.1.4 Solid-state NMR 156
6.3.2 Composition 158
6.3.2.1 Dopant site assignment 159
6.3.3 Material characterization 161
6.3.3.1 Theoretical density 161
6.3.3.2 Thermal expansion behavior 161
6.3.3.3 Thermal analysis 166
6.3.4 Reaction pathway 168
6.3.5 Thermal conductivity 170
6.4 Discussion 171
6.4.1 Implications of crystal structure 171

6.4.2 MicroED on inorganic materials 172
6.4.3 Potential applications 173
6.5 Conclusion 174
References 176
Chapter 7: Conclusions and future work 182
7.1 Conclusions 182
7.2 Suggestions for future work 185
7.2.1 YSZ hollow anodes 185
7.2.2 SAS material 188
Appendix A: Analysis of lunar oxygen production and refueling for Starship Human Landing System 190
Appendix B: Comparison of energy-dispersive X-ray spectroscopy vs. electron probe microanalysis for oxides 192
Appendix C: Estimating order of oxide electrolysis 210
Appendix D: Design, fabrication, and testing of inverted molten regolith electrolysis cell 213
Appendix E: Supporting material for Chapter 4 221
Appendix F: Proof-of-principle electrolysis of lunar maria regolith using zirconia-based hollow anodes 233
Appendix G: Supporting material for Chapter 6 241

LIST OF ILLUSTRATIONS

Number *Page*

1.1. Schematic of molten regolith electrolysis process 4
1.2. Schematic of cold-wall, Joule-heated MRE reactor built at NASA Kennedy Space Center 5
1.3. Schematic proposed hollow anode design for MRE 9
2.1. (a) XRD spectra of LHS-1 (highlands), starting ZrO_2 powder, and ZrO_2/LHS-1 mixture (50:50 molar ratio) before and after heat treatment. (b) XRD spectra of JSC-1A (maria), starting ZrO_2 powder, and ZrO_2/JSC-1A mixture (50:50 molar ratio) before and after heat treatment. Spectra show presence of anorthite (●) and monoclinic ZrO_2 (●) 24
2.2. BSE micrograph of (a) heat-treated, ZrO_2/LHS-1 (highlands) and (b) heat-treated, ZrO_2/JSC-1A (maria) 25
2.3. (a) XRD spectra of LHS-1 (highlands), starting HfO_2 powder, and HfO_2/LHS-1 mixture (50:50 molar ratio) before and after heat treatment. (b) XRD spectra of JSC-1A (maria), starting HfO_2 powder, and HfO_2/JSC-1A mixture (50:50 molar ratio) before and after heat treatment. Spectra show presence of anorthite (●) and monoclinic HfO_2 (●) 27
2.4. BSE micrograph of (a) heat-treated, HfO_2/LHS-1 (highlands) and (b) heat-treated, HfO_2/JSC-1A (maria) 28
2.5. (a) XRD spectra of LHS-1 (highlands), starting Y_2O_3 powder, and Y_2O_3/LHS-1 mixture (50:50 molar ratio) before and after heat treatment. (b) XRD spectra of JSC-1A (maria), starting Y_2O_3 powder, and Y_2O_3/JSC-1A mixture (50:50 molar ratio) before and after heat treatment. Spectra show presence of anorthite (●), cubic Y_2O_3 (●), and Ca/Y-cuspidine (●) 31
2.6. BSE micrograph of (a) heat-treated Y_2O_3/LHS-1 (highlands) and (b) heat-treated, Y_2O_3/JSC1A (maria) 32
2.7. Crystal structure of Ca/Y-cuspidine ($Ca_2Y_2Si_2O_9$) 34

2.8. (a) XRD spectra of LHS-1 (highlands), starting Sc_2O_3 powder, and Sc_2O_3/LHS-1 mixture (50:50 molar ratio) before and after heat treatment. (b) XRD spectra of JSC-1A (maria), starting Sc_2O_3 powder, and Sc_2O_3/JSC-1A mixture (50:50 molar ratio) before and after heat treatment. Spectra show presence of anorthite (●), cubic Sc_2O_3 (●), and Sc reaction phase (●)..... 36

2.9. BSE micrograph of (a) heat-treated, Sc_2O_3/LHS-1 (highlands) and (b) heat-treated, Sc_2O_3/JSC-1A (maria) 37

3.1. (a) XRD spectra of LHS-1 (highlands), starting YSZ powder, and YSZ/LHS-1 mixture (50:50 molar ratio) before and after heat treatment. (b) XRD spectra of JSC-1A (maria), starting YSZ powder, and YSZ/JSC-1A mixture (50:50 molar ratio) before and after heat treatment. Spectra show presence of anorthite (■), tetragonal YSZ (●), and cubic YSZ (▲) 58

3.2. BSE micrograph of (a) heat-treated, 50:50 molar ratio YSZ/LHS-1 (highlands) and (b) heat-treated, 50:50 molar ratio YSZ/JSC-1A (maria)..... 59

3.3. Optical and BSE images of the cross-sectioned heat-treated (a) YSZ/LHS-1 (highlands) crucible and (b) YSZ/JSC-1A (maria) crucible at 1600°C for 3 hours..... 63

3.4. Combined EDS/SEM/EBSD images of (a) YSZ/LHS-1 (highlands) interface and (b) YSZ/JSC-1A (maria) interface 67

3.5. Area-weighted histogram of grain diameters (5 μm bins) in the bulk and exterior regions of the crucible for (a) LHS-1 (highlands) and (b) JSC-1A (maria)..... 70

3.6. Area-weighted histogram of grain diameters (5 μm bins) in the bulk and surface regions of the crucible for (a) LHS-1 (highlands) and (b) JSC-1A (maria)..... 70

4.1. Schematic of (a) envisioned integration of hollow anode into existing MRE reactors and (b) inverted hollow anode used to perform proof-of-principle experiments..... 78

4.2. (a) O_2 content of outlet gas stream and (b) potential across electrolysis cell vs. elapsed time since start for all three electrolysis experiments 85

4.3. Optical microscopy of the 1-hour electrolysis cell and EDS elemental maps of the cathodic products generated. EDS analysis area is denoted with the orange box in the optical microscope image 89
4.4. Optical microscopy of the 3-hour electrolysis cell and EDS elemental maps of the cathodic products generated. EDS analysis area is denoted with the orange box in the optical microscope image 90
4.5. Optical microscopy of the 12-hour electrolysis cell and EDS elemental maps of the cathodic products generated. EDS analysis area is denoted with the orange box in the optical microscope image 91
4.6. FactSage predictions of (a) the percent atomic elemental composition of the remaining regolith and (b) the cathodic products composition vs. O_2 extraction efficiency. Dashed vertical lines in (a) and (b) represent the O_2 extraction efficiency achieved in the 1-hour (0.4%), 3-hour (1.2%), and 12-hour (3.7%) electrolysis cells 94
4.7. Area-weighted histogram of YSZ grain diameters (5 μm bins) at beginning-of-life (BOL), 1-hour electrolysis, 3-hour electrolysis, and 12-hour electrolysis 97
4.8. Raman spectra of YSZ from beginning-of-life (BOL), 1-hour, 3-hour, and 12-hour electrolysis cells 101
5.1. Schematic of ideal (fully ionic) YSZ hollow anode charge transport and resistor model 112
5.2. Schematic of degraded (ionic and electronic conduction) YSZ hollow anode charge transport and resistor model 113
5.3. Schematic of (a) envisioned integration of hollow anode into existing MRE reactors and (b) inverted hollow anode used to perform thesis experiments. Cathodic products are highlighted in red to show their position in the MRE reactor 115
5.4. Brouwer diagram for YSZ at 1600°C. Red dashed lines define the shift in pO_2 for the regeneration and mitigation techniques 120

5.5. (a) O_2 content of outlet gas stream and (b) potential across electrolysis cell vs. elapsed time since electrolysis start for electrolysis #1 and the 12-hour electrolysis cell from Chapter 4 126
5.6. (a) O_2 content of outlet gas stream and (b) potential across electrolysis cell vs. elapsed time since electrolysis start for electrolysis #2, #3, and #4 128
5.7. Cell resistance (left) and O_2 content of the outlet gas (right) vs. elapsed time since experiment start. Switchover from Ar to 10% O_2 flow occurs at 6 minutes 131
5.8. (a) O_2 content of outlet gas stream and (b) potential across electrolysis cell vs. elapsed time since electrolysis start for electrolysis #5 and #6 (10% O_2). The data from electrolysis #4 (Ar) are also shown for comparison..... 132
5.9. Optical microscopy of cross-sectioned YSZ inverted hollow anode used in regeneration and mitigation testing. The entire cell is shown on the left. The region near the cathode and anode with a cathodic product short is shown on the right 134
5.10. YSZ wall recession vs. exposure time. Error bars representing the standard deviation of recession measurements are shown. Linear fit shown as blue dashed line. Piecewise fit shown as orange dashed line 137
6.1. Image showing the pink color of the precursor mixture and the tan color of the converted doped SAS phase 146
6.2. (a) Transmission electron microscope image of doped SAS crystallites and (b) selected area diffraction still frame (from continuous diffraction dataset) of doped SAS crystallite, both from MicroED..... 152
6.3. XRD (Cu Kα) of doped SAS powder with simulated pattern after Rietveld refinement (red), calculated diffraction peaks (blue), and residual error (green). 153
6.4. Isometric view of $Si_2Al_2Sc_{14}O_{28}$ unit cell with views along the a-, b-, and c-axes..... 154
6.5. MAS NMR spectra for ^{45}Sc, ^{27}Al, and ^{29}Si. Simulated lineshapes and component curves, obtained from DMFit, are also presented 156

6.6. Room-temperature and high-temperature XRD (Co Kα) patterns of doped SAS of (a) the full 2θ range and temperatures between 25°C and 1500°C, and (b) an expanded view of (003) and $(03\bar{2})$ at 25°C, 1100°C, and 1500°C..... 162

6.7. (a) Lattice parameters (a, b, c, α, β, γ), (b) normalized unit cell lengths, (c) unit cell volume, and (d) calculated volumetric coefficient of thermal expansion obtained from high-temperature XRD as a function of temperature 163

6.8. SEM image of aligned parallel cracks observed in doped SAS pellet. Orange arrows mark the locations of the parallel cracks 164

6.9. EBSD spot analysis and grain orientation of doped SAS in a region exhibiting parallel cracks. Black vector in the unit cell represents the eigenvector of the thermal expansion tensor with the largest eigenvalue. The opposite direction of the black vector (not shown) represents the direction of largest thermal contraction due to cooling. The white regions are pores within the doped SAS material..... 166

6.10. Differential thermal analysis of (a) precursor mixture to 1600°C and (b) reacted, doped SAS to 2400°C 168

6.11. High-temperature XRD (Co Kα) scans of the precursor mixture (left) and weight percent of major crystalline phases at each temperature (right) 169

6.12. Thermal conductivity of doped SAS measured by laser flash analysis. Thermal conductivity of 3YSZ included for comparison 170

D.1. CAD model of inverted electrolysis cell. Major components are labeled..... 214

D.2. Quartz wool insulation locations in electrolysis cell design 217

D.3. Labeled images of assembled electrolysis cell, gas/electrical feedthroughs, and supporting equipment during molten regolith electrolysis testing..... 218

D.4. Temperature calibration of interior of YSZ tube (Calibration TC) and temperature of furnace (Control TC). Top graph shows the entirety of the heating and cooling profiles. Bottom graph provides a detailed view of the dwell segment at 1600°C 220

E.1. Thermal profile of all three electrolysis experiments from monitoring thermocouple in furnace. Top graph shows the entirety of the heating and cooling profiles. Bottom graph provides a detailed view of the dwell segment during which electrolysis is performed 222
E.2. Quantitative EDS summary of Mo oxides observed on interior of YSZ after electrolysis experiments. Data taken from 3-hour electrolysis cell. All values are in at% 223
E.3. Quantitative EDS summary of cathodic product region in 1-hour electrolysis cell (Figure 4.3). All values are in at% 224
E.4. Quantitative EDS summary of cathodic product region in 3-hour electrolysis cell (Figure 4.4). All values are in at% 225
E.5. Quantitative EDS summary of cathodic product region in 12-hour electrolysis cell (Figure 4.5). All values are in at% 226
E.6. FactSage predictions of the remaining regolith composition (full (left) and expanded (right)) vs. O_2 extraction efficiency. Dashed vertical lines represent the O_2 extraction efficiency achieved in the 1-hour (0.4%), 3-hour (1.2%), and 12-hour (3.7%) electrolysis cells.....227
E.7. FactSage predictions of the cathodic product composition (full (left) and expanded (right)) vs. O_2 extraction efficiency. Dashed vertical lines represent the O_2 extraction efficiency achieved in the 1-hour (0.4%), 3-hour (1.2%), and 12-hour (3.7%) electrolysis cells.....228
E.8. Backscattered electron (BSE) image and energy-dispersive X-ray spectroscopy (EDS) maps of YSZ particles at bottom of 1-hour electrolysis cell. EDS analysis area is denoted with the orange box in the optical microscope image 229
E.9. Backscattered electron (BSE) image and energy-dispersive X-ray spectroscopy (EDS) maps of YSZ particles at bottom of 3-hour electrolysis cell. EDS analysis area is denoted with the orange box in the optical microscope image 230

E.10. Backscattered electron (BSE) image and energy-dispersive X-ray spectroscopy (EDS) maps of YSZ particles at bottom of 12-hour electrolysis cell. EDS analysis area is denoted with the orange box in the optical microscope image 231

E.11. EBSD phase maps of beginning-of-life (BOL) YSZ and YSZ at regolith interface for the 1-hr, 3-hr and 12-hr cells 232

F.1. (a) O_2 content of outlet gas stream and (b) potential across electrolysis cell vs. elapsed time since electrolysis start for 1-hr electrolysis of LHS-1 and JSC-1A 234

F.2. Optical microscopy of the 1-hour JSC-1A electrolysis cell and EDS elemental maps of the cathodic products generated. EDS analysis area is denoted with the orange box in the optical microscope image 237

G.1. XRD (Cu Kα) of doped SAS powder with simulated pattern after Rietveld refinement (red) and calculated diffraction peaks (blue) of possible impurity phases 242

G.2. XRD (Cu Kα) of doped SAS powder with simulated pattern after Rietveld refinement without dopants (top) and with equally distributed dopants (bottom) 243

G.3. Laplacian $\nabla^2\rho(r)$ overlayed with bond path (brown solid line) and bond critical point (blue dot) obtained on each Sc site using experimental geometry of SAS. Logarithmic scale in the form of $\pm$ 1,2,4,8$\cdot 10^n$ ($-3 \leq n \geq 8$) eÅ^{-5} was adopted for drawing the contour map; blue and red colors correspond to positive and negative function values, respectively ..... 245 – 251

G.8. Full 2400°C differential thermal analysis (blue) and thermogravimetric analysis (orange) results of doped SAS 262

G.9. XRD (Cu Kα) patterns and SEM/BSE images of precursor pellets annealed at 1300°C, 1400°C, 1500°C, and 1600°C for 10 hours 264

LIST OF TABLES

Number *Page*

2.1. Manufacturer-provided compositions of lunar regolith simulants in wt%..... 22

2.2. Composition (at%) of solidified regolith in ZrO_2/LHS-1 and ZrO_2/JSC-1A specimens. Standard deviations are presented in parentheses 25

2.3. Composition (at%) of ZrO_2 particles in ZrO_2/LHS-1 and ZrO_2/JSC-1A specimens. Standard deviations are presented in parentheses 25

2.4. Composition (at%) of solidified regolith in HfO_2/LHS-1 and HfO_2/JSC-1A specimens. Standard deviations are presented in parentheses 29

2.5. Composition (at%) of HfO_2 particles in HfO_2/LHS-1 and HfO_2/JSC-1A specimens. Standard deviations are presented in parentheses 29

2.6. Composition (at%) of Ca/Y-cuspidine (reaction phase) in Y_2O_3/LHS-1 and Y_2O_3/JSC-1A specimens. Nominal composition of Ca/Y-cuspidine also shown. Standard deviations are presented in parentheses..... 33

2.7. Composition (at%) of Y_2O_3 particles in Y_2O_3/LHS-1 and Y_2O_3/JSC-1A specimens. Standard deviations are presented in parentheses 33

2.8. Ca/Y-cuspidine reaction phase formula unit for LHS-1 and JSC-1A using general cuspidine representation 35

2.9. Composition (at%) of solidified regolith in Sc_2O_3/LHS-1 and Sc_2O_3/JSC-1A specimens. Standard deviations are presented in parentheses 38

2.10. Composition (at%) of Sc_2O_3 particles in Sc_2O_3/LHS-1 and Sc_2O_3/JSC-1A specimens. Standard deviations are presented in parentheses 38

2.11. Composition (at%) of Sc reaction phase in Sc_2O_3/LHS-1 and Sc_2O_3/JSC-1A specimens. Standard deviations are presented in parentheses 39

3.1. Manufacturer-provided compositions of lunar regolith simulants in wt%..... 55

3.2. EPMA concentrations of Zr and Y in glassy matrix and YSZ particles of heat-treated YSZ/simulant samples. Standard deviations are presented in parentheses..... 60

4.1. Major abundances of LHS-1 simulant and highlands lunar regolith..... 80

4.2. Summary of cathodic products and regolith electrolysis efficiencies 87
4.3. Average regolith composition after melting and electrolysis (at%) 93
4.4. YSZ wall recession due to dissolution by molten LHS-1 96
4.5. Cell resistances at 1600°C before and after electrolysis 99
5.1. Resistor subscript definitions for Figures 5.1 – 5.2..... 114
5.2. Major abundances of LHS-1 simulant and highlands lunar regolith..... 121
5.3. Summary of regeneration and mitigation testing 124
5.4. Summary of each electrolysis segment and associated Faradaic efficiencies . 136
5.5. Summary of anode mass payback ratio calculations. Previous data is from Chapter 4 138
6.1. Binary oxide loading amount (grams) for producing doped SAS phase..... 146
6.2. Unit cell lattice parameters obtained from MicroED and powder XRD. Standard deviations are presented in parentheses 155
6.3. Average electron-probe microanalysis of doped SAS from 51 sites. Standard deviations are presented in parentheses..... 159
6.4. Fractional occupancy of Sc, Al, and Si coordination. Standard deviations for NMR coordination are presented in paratheses 160
B.1. EPMA and EDS composition of bright phase in 50:50 JSC-1A/ZrO_2 samples. EPMA used 3 sites. EDS used 9 sites 197
B.2. EPMA and EDS composition of regolith in 50:50 JSC-1A/ZrO_2 samples. EPMA used 10 sites. EDS used 31 sites 197
B.3. EPMA and EDS composition of bright phase in 50:50 LHS-1/ZrO_2 samples. EPMA used 3 sites. EDS used 10 sites 198
B.4. EPMA and EDS composition of regolith in 50:50 LHS-1/ZrO_2 samples. EPMA used 10 sites. EDS used 30 sites 198
B.5. EPMA and EDS composition of bright phase in 50:50 JSC-1A/HfO_2 samples. EPMA used 3 sites. EDS used 7 sites 199
B.6. EPMA and EDS composition of regolith in 50:50 JSC-1A/HfO_2 samples. EPMA used 10 sites. EDS used 16 sites 199

B.7. EPMA and EDS composition of bright phase in 50:50 LHS-1/HfO_2 samples. EPMA used 3 sites. EDS used 6 sites 200
B.8. EPMA and EDS composition of regolith in 50:50 LHS-1/HfO_2 samples. EPMA used 10 sites. EDS used 13 sites 200
B.9. EPMA and EDS composition of bright phase in 50:50 JSC-1A/Y_2O_3 samples. EPMA used 3 sites. EDS used 7 sites 201
B.10. EPMA and EDS composition of reaction phase in 50:50 JSC-1A/Y_2O_3 samples. EPMA used 5 sites. EDS used 7 sites 201
B.11. EPMA and EDS composition of bright phase in 50:50 LHS-1/Y_2O_3 samples. EPMA used 3 sites. EDS used 6 sites 202
B.12. EPMA and EDS composition of reaction phase in 50:50 LHS-1/Y_2O_3 samples. EPMA used 5 sites. EDS used 7 sites 202
B.13. EPMA and EDS composition of reaction phase in 50:50 JSC-1A/Sc_2O_3 samples. EPMA used 5 sites. EDS used 4 sites 203
B.14. EPMA and EDS composition of regolith in 50:50 JSC-1A/Sc_2O_3 samples. EPMA used 3 sites. EDS used 2 sites 203
B.15. EPMA and EDS composition of reaction phase in 50:50 LHS-1/Sc_2O_3 samples. EPMA used 5 sites. EDS used 4 sites 204
B.16. EPMA and EDS composition of regolith in 50:50 LHS-1/Sc_2O_3 samples. EPMA used 3 sites. EDS used 2 sites 204
B.17. EPMA and EDS composition of bright phase in 50:50 JSC-1A/Sc_2O_3 samples. EPMA used 3 sites. EDS used 2 sites 205
B.18. EPMA and EDS composition of bright phase in 50:50 LHS-1/Sc_2O_3 samples. EPMA used 3 sites. EDS used 2 sites 205
B.19. EPMA and EDS composition of bright phase in 50:50 JSC-1A/YSZ samples. EPMA used 5 sites. EDS used 5 sites 206
B.20. EPMA and EDS composition of regolith in 50:50 JSC-1A/YSZ samples. EPMA used 10 sites. EDS used 40 sites 206
B.21. EPMA and EDS composition of bright phase in 50:50 LHS-1/YSZ samples. EPMA used 5 sites. EDS used 6 sites 207

B.22. EPMA and EDS composition of regolith in 50:50 LHS-1/YSZ samples. EPMA used 10 sites. EDS used 36 sites 207
B.23. EPMA and EDS composition of bright phase in 25:75 JSC-1A/YSZ samples. EPMA used 3 sites. EDS used 6 sites 208
B.24. EPMA and EDS composition of regolith in 25:75 JSC-1A/YSZ samples. EPMA used 10 sites. EDS used 13 sites 208
B.25. EPMA and EDS composition of bright phase in 25:75 LHS-1/YSZ samples. EPMA used 3 sites. EDS used 6 sites 209
B.26. EPMA and EDS composition of regolith in 25:75 LHS-1/YSZ samples. EPMA used 10 sites. EDS used 13 sites 209
F.1. Manufacturer-provided compositions of lunar regolith simulants in wt%..... 233
F.2. Comparison of 1-hour JSC-1A and LHS-1 cathodic products and regolith electrolysis efficiencies.....238
F.3. Comparison of YSZ wall recession by molten JSC-1A or LHS-1 239
G.4. Electron-probe microanalysis of doped SAS pellets 252
G.6. Fit of thermal expansion tensor elements using the Coefficient of Thermal Expansion Analysis Suite (CTEAS) 255
G.7. Calculated eigenvalues and eigenvectors from the Coefficient of Thermal Expansion Analysis Suite (CTEAS) 259
G.9. Weight fraction and density of precursor pellets after 10-hour heat treatment in air 264

C h a p t e r 1

INTRODUCTION

1.1 Background

1.1.1 Motivation for in situ O_2 production on the lunar surface

Recent space exploration efforts have been focused on returning humans to the Moon, which serves as an ideal testing environment to validate new space technologies. NASA's Artemis program, in partnership with the European Space Agency (ESA), plans to land humans on the Moon by 2027, with the goal of establishing a sustained human presence on the lunar surface to support future Mars exploration programs [1]. The Chinese National Space Agency (CNSA) and Russia's Roscosmos have similar plans to establish a sustained human presence on the Moon through their International Lunar Research Station (ILRS) program [2]. Though there are numerous technological challenges to establishing a permanent lunar base, the cost of launching infrastructure and resupply cargo is considered the largest barrier [3]. Astrobotic, a space robotics company specializing in the development of lunar landers, provides a cost estimate of $1.2 billion per metric ton (mt) delivered to the lunar surface and $300 million per mt delivered to lunar orbit [4]. To put these numbers into perspective, the International Space Station (ISS) has an approximate mass of 400 mt [5]. Using Astrobotic's payload cost estimate, a lunar base similar in mass to the ISS would cost $480 billion in launch and delivery costs alone. This cost represents nearly 20 years of the entirety of NASA's annual budget (2024: ~$25 billion) [6].

The high cost of delivering materials and resources to the lunar surface has led to a renewed focus on in situ resource utilization (ISRU) technologies, which are techniques to extract and process extra-terrestrial resources to minimize the cost and mass requirements for lunar missions [7]. Of the resources that can be produced on the lunar surface, oxygen (O_2) is considered to one of the most important due to its usage in both life-support systems and as the oxidizer for spacecraft [8]. For chemical rockets, approximately 80% of the mass of

the propellant is O_2, serving as the oxidizer for either methalox (CH_4/O_2) or hydrolox (H_2/O_2) rockets [8]. Even in a fully fueled rocket, O_2 represents a significant amount of the total mass of the system. For example, O_2 comprises ~79% of the total mass of Space Launch System (SLS) core stage, NASA's primary launch vehicle for the Artemis missions [9]. Metzger investigated the economics of lunar-derived propellant and found that lunar-derived propellants can outcompete terrestrially supplied rocket propellants, even if launch costs are minimized with the development of more efficient launch vehicles [10]. Given that O_2 comprises 80% of the mass of the propellants, the analysis remains valid even if only the oxidizer of the propellants is considered. A cost analysis associated with lunar O_2 production and refueling for SpaceX's Starship Human Landing System (planned for use in Artemis 3 and 4) is provided in Appendix A and indicates that the cost per unit mass delivered to the lunar surface can be reduced by approximately 74%.

1.1.2 O_2 production through in situ resource utilization

ISRU processes target O_2 production from two specific lunar resources: lunar ice and lunar regolith. Lunar ice is likely found in the permanently shadowed regions, such as craters, at the lunar south pole [11]. O_2 production from lunar ice involves extracting the lunar ice, heating it until water vapor forms, and performing water electrolysis [12]. This method of O_2 production is desirable since terrestrial water electrolysis is well-studied and water electrolysis also generates H_2, which is the fuel for hydrolox rockets, such as NASA's SLS and Blue Origin's New Glenn. However, the main challenge for O_2 production from lunar ice is the availability of lunar ice. Though the existence of lunar ice was confirmed through spectroscopic measurements [13], there have been no in situ measurements of lunar ice. There is disagreement in the ISRU community about how much lunar ice exists and how easily accessible it is [14]. Additionally, even if significant amounts of lunar ice exist, it is likely located in a permanently shadowed region of the Moon, which represents a massive challenge for extraction [14]. These regions are generally the coldest regions of the lunar surface, with no access to solar radiation for photovoltaic power generation and situated at

the bottom of large craters. For these reasons, recent ISRU development efforts have moved away from lunar ice, in favor of lunar regolith.

Lunar regolith is the layer of granular oxide minerals and glasses that cover the top 10 meters of the lunar surface [11]. In contrast to lunar ice, lunar regolith is abundant everywhere on the lunar surface, eliminating the need for extensive resource prospecting [15]. Since lunar regolith is composed of oxide minerals and glasses, it contains approximately 45% O_2 by mass [11]. Lunar regolith is an ideal feedstock for O_2 production since it is widely accessible and contains a significant fraction of O_2. Several ISRU processes have been studied for generating O_2 from lunar regolith, including carbothermal reduction [16–18], hydrogen reduction [19–21], molten salt electrolysis [22–24], and molten regolith electrolysis [25–27]. Of these, molten regolith electrolysis is an attractive option since it also produces metals and metalloids, in addition to O_2, which has value for other in situ construction and manufacturing applications [28]. Guerrero-Gonzalez et al. performed a system analysis of these ISRU processes targeting O_2 and metals production and found that molten regolith electrolysis was the most effective ISRU process in terms of mass payback ratio [29]. Given its advantages, molten regolith electrolysis is the focus of this thesis.

1.1.3 Molten regolith electrolysis

Molten regolith electrolysis (MRE) uses molten lunar regolith as the working electrolyte and directly electrolyzes the oxide species in the molten regolith. In order to fully melt and dissociate lunar regolith, MRE requires an operating temperature of 1600°C [30]. To perform MRE, a cathode and anode are inserted into molten lunar regolith, and a potential is applied across the electrodes, producing molten metals and metalloids (Fe and Si) at the cathode surface and O_2 at the anode. A schematic of typical MRE operation is shown in Figure 1.1.

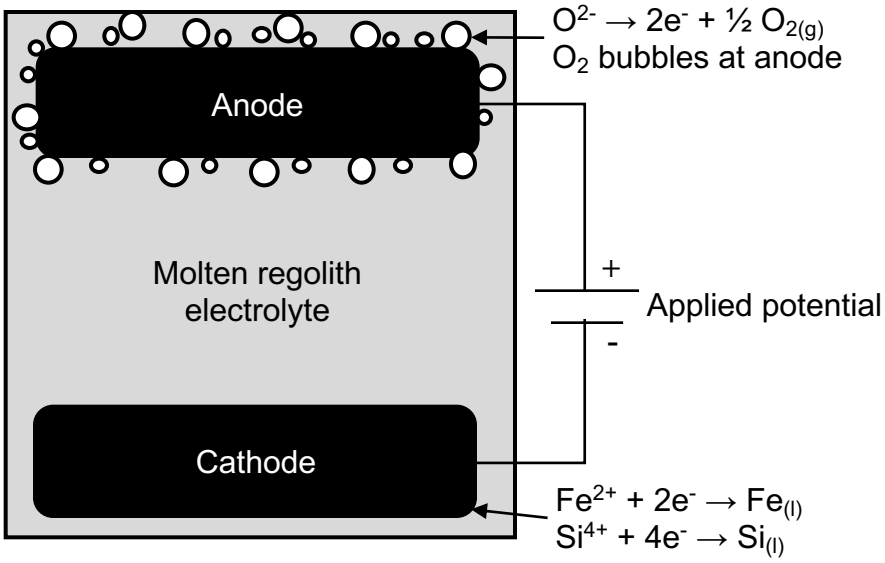

Figure 1.1. Schematic of molten regolith electrolysis process.

An ideal MRE reactor can produce O_2 and molten metals and metalloids without any additional consumables. This allows for MRE to operate without a consistent resupply of consumables, compared to hydrogen and carbothermal reduction, which require resupplies of hydrogen and methane, respectively [31]. Additionally, MRE can extract a higher amount of O_2 compared to hydrogen and carbothermal reduction methods. The extraction efficiency is defined as the mass of O_2 produced divided by the mass of regolith processed. The maximum theoretical value for extraction efficiency is approximately 45%, representing complete extraction of all the available O_2 in the regolith. For comparison, MRE can achieve extraction efficiencies of 15 – 40%, while hydrogen reduction and carbothermal reduction are limited to 1 – 5% and 10 – 20%, respectively [31]. Beyond the improved extraction efficiency, MRE also directly produces O_2, while hydrogen reduction and carbothermal reduction produce H_2O and CO/CO_2, respectively [31]. Both hydrogen and carbothermal reduction require a secondary electrolysis step to obtain O_2.

The cathodic products generated by MRE also have value for in situ construction and manufacturing of infrastructure components. Fe and Si are the first cathodic products generally produced by MRE, but other oxides in the molten regolith can also be electrolyzed,

producing Ti, Mg, and Al [31]. Patel et al. has shown that steel can be produced through post-processing of the Fe produced from MRE [32]. Grossman et al. demonstrated that wires of ferrosilicon can be produced, which serve as a feedstock for wire-based additive manufacturing methods to achieve complex part geometries [33]. The generation of cathodic products that can be used on the lunar surface further reduces the mass that needs to be delivered from Earth, which reduces the cost associated with a lunar settlement.

Previous development efforts for a flight-ready MRE system by NASA have produced a preliminary reactor design. NASA Kennedy Space Center (KSC) has investigated a Joule-heated, cold-wall reactor that uses loose regolith as the insulation to prevent the molten regolith from contacting the containment vessel [34]. Figure 1.2 shows a rendering of the KSC MRE reactor design. This reactor was operated successfully and demonstrated that a cold-walled, Joule-heated reactor design is feasible [34].

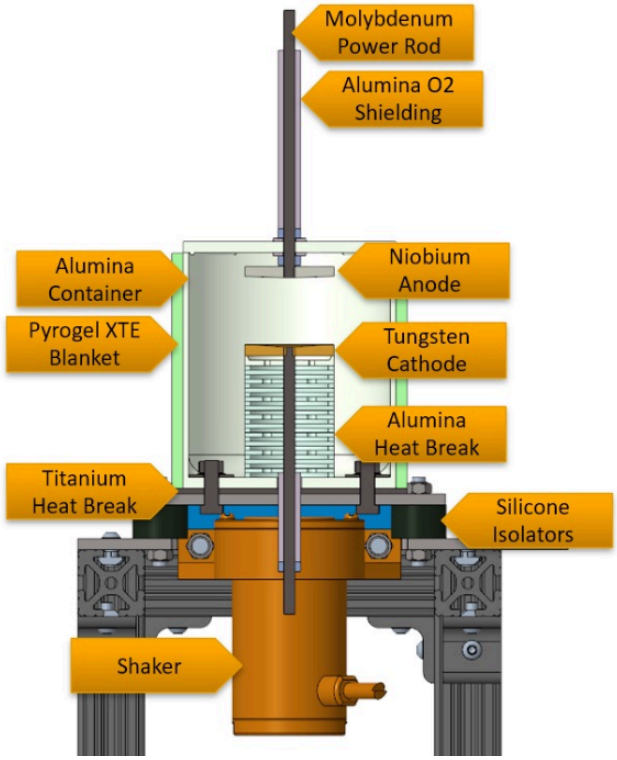

Figure 1.2. Schematic of cold-wall, Joule-heated MRE reactor built at NASA Kennedy Space Center. Reproduced from Ref. [34].

1.2 MRE challenges

Despite the previous MRE development effort discussed above, there are still challenges associated with performing MRE on the lunar surface. Two major design challenges that still need to be addressed are related to materials degradation under MRE conditions and efficient collection of the produced O_2 as are described here.

1.2.1 Materials degradation

MRE requires a high operational temperature of 1600°C and contact with the corrosive molten regolith. The specific composition of molten lunar regolith will be presented in the upcoming chapters, but it is generally a mixture of CaO-MgO-Al_2O_3-SiO_2 with a smaller concentration of Na_2O, K_2O, FeO, and TiO_2 [15]. Additionally, pure O_2 is generated in MRE reactors so materials in contact with molten regolith must also not oxidize, further limiting the materials that can be used. The oxidizing atmosphere is likely to exist in the entire MRE reactor, but the partial pressure of O_2 (pO_2) is highest at the anode, where pure O_2 is generated. The combination of these conditions can cause significant degradation to many commonly used refractory materials. As a result, materials selection for containment of the molten regolith and for the anode is nontrivial.

Platinum group metals have traditionally been used for containment of molten aluminosilicate-rich slags due to their relative stability in corrosive and oxidizing conditions [35]. In addition to their high cost and scarcity, these metals also form eutectics with the molten Si produced in MRE, precluding their use as a containment material for MRE [28]. For containment materials, electrical conductivity is not required, which allows electrically insulating materials to be used.

Standish et al. investigated refractory ceramics including Al_2O_3, ZrO_2 (CaO-, MgO-, and Y_2O_3-stabilized), and MgO plates in contact with molten lunar regolith simulants at 1600°C and concluded that Al_2O_3 exhibited the least degradation [36]. However, the porosity of the ceramics used in that study varied significantly, making it difficult to compare the degradation between ceramics. Rosenberg et al. studied crucible materials for carbothermal

reduction of lunar regolith simulants at 1650°C, including Al_2O_3, MgO, Y_2O_3-stabilized ZrO_2 (YSZ), Y_2O_3, and TaC; they concluded that yttria and YSZ were the only suitable materials for containing molten lunar regolith simulants [37]. Lensing et al. investigated the degradation of Al_2O_3, mixed-stabilized ZrO_2, and BN crucibles containing molten lunar regolith at 1600°C and found that BN is most suitable material under reducing conditions [38]. From these studies, there does not appear to be a refractory material that clearly outperforms others in the containment of molten lunar regolith. Additionally, all these studies were performed with bulk crucibles or plates of refractory material, where microstructural (porosity and grain size) and kinetic (dissolution and reaction) effects can influence the results, making it difficult to compare degradation behaviors. These considerations motivated a study of the equilibrium behavior between refractory materials and molten lunar regolith.

The anode must also be electrically conductive to allow electrolysis to be performed. An ideal MRE system would utilize inert anodes that do not degrade during operation. Unfortunately, there has not been a material identified that can completely resist corrosion by molten silicates at MRE operational temperature, while also being electrically conductive to enable electrolysis [39]. An alternative is to use a quasi-inert anode, with a controlled degradation rate, that would require periodic replacement. Reviews indicate that current MRE reactors utilize an Ir or Ir-coated quasi-inert anode to operate under these conditions [40,41]. In typical MRE reactor designs, the anode is placed such that it does not contact molten Si produced at the cathode (Figure 1.2), enabling the usage of platinum group metals at the anode. Wang et al. investigated Ir corrosion rates when used as the anode in MRE and measured a corrosion rate of ~8 mm/year, which is lost through dissolution to the molten regolith electrolyte [42]. Given the high cost and scarcity of Ir metal, it is unclear if Ir anodes are a cost-effective solution for long-term MRE reactors. As a result, electrically conductive refractory materials are evaluated in this thesis as a substitute for Ir at the anode.

1.2.2 O_2 collection in MRE reactors

During MRE, O_2 is produced at the anode surface, as shown in Figure 1.1. The production of gas at a solid-liquid interface results in the formation of O_2 bubbles. The molten regolith has a high viscosity and surface tension while operation on the lunar surface reduces the acceleration due to gravity, resulting in a lower buoyancy force [28]. The combination of these factors indicates that it is more difficult for bubbles to separate from the anode surface. This effectively decreases the surface area of the anode and can potentially cause electrolysis to stall [43]. Burke et al. investigated bubble separation in MRE reactors using computational fluid dynamics and found that bubbles generally become larger and bubble detachment time increases with the reduced lunar gravity [44]. Lomax et al. studied the effects of reduced gravity on bubble formation in H_2O electrolysis using parabolic flights and determined that the electrolysis efficiency decreases with operation in reduced lunar gravity [43]. These studies suggest that bubble separation is still a potential roadblock to efficient O_2 production through MRE on the lunar surface. Ideally, bubble formation should be avoided, but this is not possible in current MRE anode designs since O_2 is generated at a solid-liquid interface.

Beyond bubble separation, there is also a reduction in O_2 capture efficiency associated with bubbling O_2 through molten regolith into a shared reactor headspace. The O_2 can be reabsorbed into the molten lunar regolith before it is collected, causing a reduced effective O_2 generation efficiency. Additionally, O_2 can also reoxidize partially reduced Fe^{2+} species in the molten regolith electrolyte or gaseous reduced metal species, such as Na, K, or Mg in the reactor headspace, lowering the overall O_2 generation efficiency [28]. In the worst case scenario, O_2 can potentially contact the cathodic products and cause reoxidation of the reduced metals and metalloids generated at the cathode. However, the geometric design of MRE reactors (Figure 1.2) limits the likelihood of this happening, since cathodic products are denser than the molten regolith electrolysis and typically settle to the bottom of the reactor. All these potential issues can be avoided by collecting O_2 as it is produced rather than allowing it to bubble through the molten regolith before collection.

1.3 Hollow anode design

To address the challenges discussed in the previous section, a hollow anode design is proposed. The hollow anode design is comprised of an exterior solid electrolyte shell and an interior metallic current collector. Within this design, the goal is to force O^{2-} from the molten regolith to migrate through an oxygen-conducting solid electrolyte to the metallic current collector. Once O^{2-} reaches the current collector, electron transfer can occur, allowing for oxidation of O^{2-} into O_2. The generated O_2 is fully contained within the solid electrolyte shell, enabling the collection of O_2 without contact between the molten regolith and O_2. Additionally, O_2 is now generated at a solid/solid interface, eliminating the bubble formation challenges discussed earlier. The hollow anode design also prevents any volatile species from contaminating the electrolyzed, high-purity O_2. A schematic of the hollow anode design is presented in Figure 1.3.

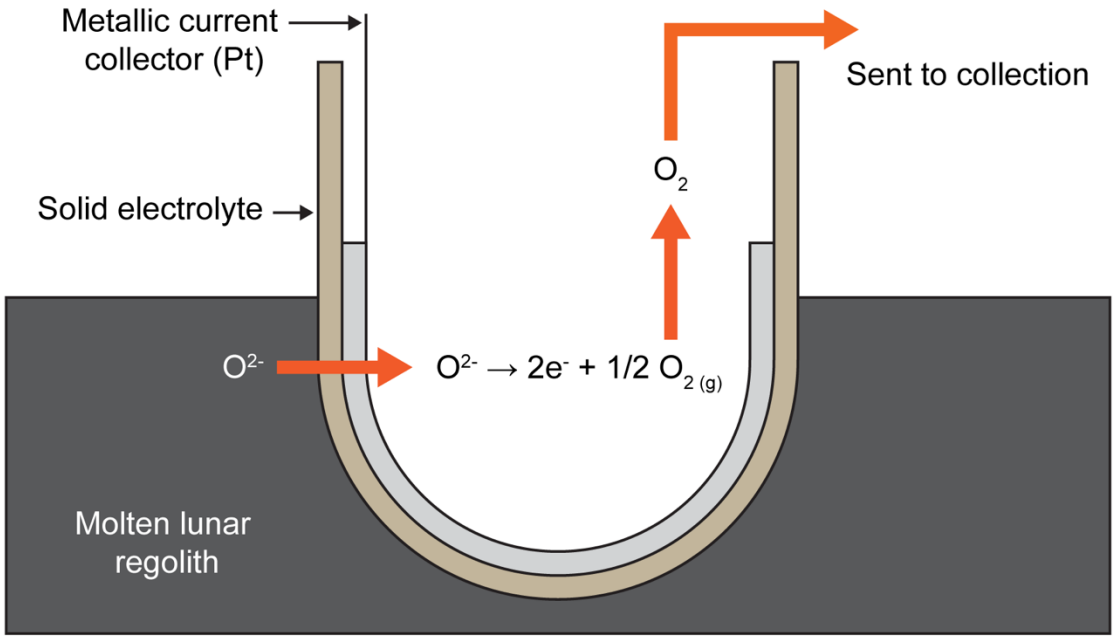

Figure 1.3. Schematic proposed hollow anode design for MRE.

Testing of the proposed hollow anode design is a significant focus of this thesis. The initial design for the hollow anode uses a fluorite-type O^{2-} conductor (either ZrO_2 or HfO_2) and Pt

as the current collector. ZrO_2- or HfO_2-based solid electrolytes generally have high ionic conductivity at elevated temperatures and high melting points. Pt is used as the current collector since it is relatively resistant to oxidizing environments at high temperatures [45]. Unlike the Ir anodes discussed earlier, the Pt used in the hollow anode does not directly contact molten regolith, avoiding the dissolution of Pt into the molten regolith electrolyte. Instead, the solid electrolyte is considered the consumable material in the hollow anode design. A successful demonstration of the hollow anode offers an alternative anode design to the currently used bare Ir anodes and is likely to enable the facile collection of the generated O_2.

1.4 Thesis outline

The purpose of this thesis is to establish a demonstration of oxygen production using the hollow anode design presented in Figure 1.3 and appropriate materials. Beyond this, the results presented in this thesis focus on characterization of thermochemical and electrochemical degradation mechanisms of the solid electrolyte in the MRE environment. It is paramount to determine the effects of material degradation on the electrolysis performance of the hollow anode to provide guidelines for integration into existing MRE reactors. In this work, a bottom-up approach, beginning with oxide powder experiments and then moving to bulk oxide component testing, is taken to investigate individual degradation mechanisms of solid electrolyte materials in the context of the MRE environment. From there, a laboratory-scale MRE reactor is constructed based on the observed degradation behavior of solid electrolyte materials. This MRE reactor becomes the testbed for electrolysis experiments that are used to determine if any additional degradation mechanisms are introduced from performing electrolysis. Finally, the degradation mechanisms are quantified based on several electrolysis experiments to provide a roadmap for hollow anode integration into industrial-scale MRE reactors.

First, Chapter 2 focuses on the evaluation of thermochemical degradation of unary oxides by molten lunar regolith simulants. The unary oxides investigated are Sc_2O_3, Y_2O_3, ZrO_2, and HfO_2 due to their usage in oxygen-conducting solid electrolytes. Powders are used for these experiments to limit kinetic effects so that the equilibrium condition of each unary oxide and regolith simulant system can be studied. Quenching is used to preserve the equilibrium state at 1600°C so that it can be evaluated at ambient temperature. These experiments provide a basis for evaluating the degradation of bulk oxide components, which introduce microstructural and kinetic effects. Ultimately, the YSZ is selected for the solid electrolyte in the hollow anode design.

In Chapter 3, YSZ (a binary oxide of Y_2O_3 and ZrO_2) is evaluated in both powder and crucible experiments. The powder experiments are similar to those performed in Chapter 2, but with a binary oxide instead of the unary oxide components. Crucible testing introduces the effects of microstructure and kinetics to determine if bulk YSZ parts are suitable for usage in the hollow anode. Microstructural evolution of YSZ, caused by contact with molten regolith simulants, is also characterized. The results reported in this chapter provide guidelines for the construction of a laboratory-scale MRE reactor.

Chapter 4 highlights the fabrication and testing of a laboratory-scale MRE cell incorporating a YSZ hollow anode. O_2 production is tested for varying durations of electrolysis, with a focus on determining how increasing electrolysis duration affects performance. Each electrolysis cell is analyzed by several material characterization techniques after electrolysis testing. The degradation mechanisms observed in Chapter 2 and 3 are used to support the post-electrolysis analysis of MRE cells. In addition to the expected thermochemical degradation of YSZ, a new electrochemically induced degradation mechanism is observed. Preliminary guidelines for YSZ hollow anode integration are presented based on the rates of each observed degradation mechanism.

Chapter 5 presents two different methods to address the electrochemically induced YSZ degradation mechanism observed in Chapter 4. Rationale for each method is provided. An additional electrolysis experiment is performed to evaluate each method and determine

which method offers the higher O_2 production rate. Based on the results of this experiment, the rates of each degradation mechanism are refined, and a final set of recommendations is provided for future YSZ hollow anode testing in industrial-scale MRE reactors.

In a shift away from MRE experiments, Chapter 6 centers on the discovery, synthesis, and characterization of a new Sc_2O_3-based material. The new material was initially observed in the unary oxide experiments (Chapter 2) and required identification of the crystal structure. A synthesis process is developed to produce crystallites that are phase pure. Microcrystal electron diffraction is performed on the phase pure material to solve the unknown structure, enabling several other material characterization techniques to be used, including high-temperature, in situ X-ray diffraction and solid state nuclear magnetic resonance. Characterization is focused on material properties relevant to both MRE and refractory oxides in general, such as thermal decomposition behavior and thermal expansion. Potential applications for this new material are also discussed.

Finally, Chapter 7 presents conclusions and suggestions for future work.

References

[1] NASA, Moon to Mars Architecture, NASA, n.d. https://www.nasa.gov/wp-content/uploads/2024/12/2024-architecture-executive-overview.pdf?emrc=4a55b3 (accessed August 29, 2025).

[2] X. Wu, The International Lunar Research Station: China's New Era of Space Cooperation and Its New Role in the Space Legal Order, Space Policy 65 (2023) 101537. https://doi.org/10.1016/j.spacepol.2022.101537.

[3] J. Robinot, S. Rodat, S. Abanades, A. Paillet, A. Cowley, Review of in-situ oxygen extraction from lunar regolith with focus on solar thermal and laser vacuum pyrolysis, Acta Astronautica 234 (2025) 242–259. https://doi.org/10.1016/j.actaastro.2025.05.008.

[4] Astrobotic, Astrobotic Lunar Landers Payload User's Guide, (2021). https://www.astrobotic.com/wp-content/uploads/2022/01/PUGLanders_011222.pdf (accessed August 29, 2025).

[5] NASA, International Space Station, NASA.Gov (2023). https://www.nasa.gov/reference/international-space-station/ (accessed August 30, 2025).

[6] C. Dreier, Your guide to NASA's budget, The Planetary Society (n.d.). https://www.planetary.org/space-policy/nasa-budget (accessed August 30, 2025).

[7] I.A. Crawford, Lunar resources: A review, Prog Phys Geog 39 (2015) 137–167. https://doi.org/10.1177/0309133314567585.

[8] D. Leger, F. Ghaffari-Tabrizi, M. Shaw, J. Rasera, D. Dickson, B. Valentin, A. Morlock, F. Thoresen, A. Cowley, Modeling energy requirements for oxygen production on the Moon, Proc. Natl. Acad. Sci. U.S.A. 122 (2025) e2306146122. https://doi.org/10.1073/pnas.2306146122.

[9] NASA, SLS (Space Launch System) Core Stage, (2024). https://www.nasa.gov/reference/sls-space-launch-system-core-stage/ (accessed December 23, 2024).

[10] P.T. Metzger, Economics of in-space industry and competitiveness of lunar-derived rocket propellant, Acta Astronautica 207 (2023) 425–444. https://doi.org/10.1016/j.actaastro.2023.03.014.

[11] L. Schlüter, A. Cowley, Review of techniques for In-Situ oxygen extraction on the moon, Planetary and Space Science 181 (2020) 104753. https://doi.org/10.1016/j.pss.2019.104753.

[12] R. Gustafson, E. Rice, Lunar polar ice - Methods for mining the new resource for exploration, in: 37th Aerospace Sciences Meeting and Exhibit, American Institute of Aeronautics and Astronautics, Reno,NV,U.S.A., 1999. https://doi.org/10.2514/6.1999-850.

[13] A. Colaprete, P. Schultz, J. Heldmann, D. Wooden, M. Shirley, K. Ennico, B. Hermalyn, W. Marshall, A. Ricco, R.C. Elphic, D. Goldstein, D. Summy, G.D. Bart, E. Asphaug, D. Korycansky, D. Landis, L. Sollitt, Detection of Water in the LCROSS Ejecta Plume, Science 330 (2010) 463–468. https://doi.org/10.1126/science.1186986.

[14] M. Anand, I.A. Crawford, M. Balat-Pichelin, S. Abanades, W. Van Westrenen, G. Péraudeau, R. Jaumann, W. Seboldt, A brief review of chemical and mineralogical resources on the Moon and likely initial in situ resource utilization (ISRU) applications, Planetary and Space Science 74 (2012) 42–48. https://doi.org/10.1016/j.pss.2012.08.012.

[15] G. Heiken, D. Vaniman, B.M. French, eds., Lunar sourcebook: a user's guide to the moon, Cambridge University Press, Cambridge [England] ; New York, 1991.

[16] R.J. Gustafson, B.C. White, M.J. Fidler, Oxygen Production via Carbothermal Reduction of Lunar Regolith, SAE International Journal of Aerospace 4 (2009) 311–316. https://doi.org/10.4271/2009-01-2442.

[17] I. Troisi, P. Lunghi, M. Lavagna, Oxygen extraction from lunar dry regolith: Thermodynamic numerical characterization of the carbothermal reduction, Acta Astronaut 199 (2022) 113–124. https://doi.org/10.1016/j.actaastro.2022.07.021.

[18] A. Paz, Carbothermal Reduction Demonstration (CaRD), (2023). https://ntrs.nasa.gov/api/citations/20230008393/downloads/SRR%202023-CaRD%20rev1.pdf.

[19] U. Hegde, R. Balasubramaniam, S. Gokoglu, Development and Validation of a Model for Hydrogen Reduction of JSC-1A, in: 47th AIAA Aerospace Sciences Meeting Including The New Horizons Forum and Aerospace Exposition, American Institute of Aeronautics and Astronautics, Orlando, Florida, 2009. https://doi.org/10.2514/6.2009-1389.

[20] Y. Lu, D. Mantha, R.G. Reddy, Thermodynamic Analysis on Lunar Soil Reduced by Hydrogen, Metall Mater Trans B 41 (2010) 1321–1327. https://doi.org/10.1007/s11663-010-9411-3.

[21] H.M. Sargeant, S.J. Barber, M. Anand, F.A.J. Abernethy, S. Sheridan, I.P. Wright, A.D. Morse, Hydrogen reduction of lunar samples in a static system for a water production demonstration on the Moon, Planet Space Sci 205 (2021) 105287. https://doi.org/10.1016/j.pss.2021.105287.

[22] B.A. Lomax, M. Conti, N. Khan, N.S. Bennett, A.Y. Ganin, M.D. Symes, Proving the viability of an electrochemical process for the simultaneous extraction of oxygen and production of metal alloys from lunar regolith, Planet Space Sci 180 (2020) 104748. https://doi.org/10.1016/j.pss.2019.104748.

[23] A. Meurisse, B. Lomax, Á. Selmeci, M. Conti, R. Lindner, A. Makaya, M.D. Symes, J. Carpenter, Lower temperature electrochemical reduction of lunar regolith simulants in molten salts, Planet Space Sci 211 (2022) 105408. https://doi.org/10.1016/j.pss.2021.105408.

[24] A. Ellery, I. Mellor, P. Wanjara, M. Conti, Metalysis Fray Farthing Chen Process As a Strategic Lunar *In Situ* Resource Utilization Technology, New Space 10 (2022) 224–238. https://doi.org/10.1089/space.2021.0047.

[25] A.H. Sirk, D.R. Sadoway, L. Sibille, Direct Electrolysis of Molten Lunar Regolith for the Production of Oxygen and Metals on the Moon, ECS Transactions 28 (2010) 367–373. https://doi.org/10.1149/1.3367929.

[26] K.D. Grossman, L. Sibille, E. Bell, E. Petersen, J.A. Toro Medina, H. Williams, T. Newbold, K. Zacny, I. Bates, GaLORE (Gaseous Lunar Oxygen from Regolith Electrolysis): Technology Advances for a Cold-Walled Molten Regolith Electrolysis Reactor, in: ASCEND 2021, American Institute of Aeronautics and Astronautics, Las Vegas, Nevada & Virtual, 2021. https://doi.org/10.2514/6.2021-4019.

[27] K.D. Runyon, J. Berdis, B. Summers, B. Clyde, K. Hibbitts, M. Nord, W. Fuhrman, A System-Level Approach to Extracting Oxygen from Lunar Regolith via Molten Regolith Electrolysis, in: 2022.

[28] M.S. Humbert, G.A. Brooks, A.R. Duffy, C. Hargrave, M.A. Rhamdhani, Thermophysical property evolution during molten regolith electrolysis, Planet Space Sci 219 (2022) 105527. https://doi.org/10.1016/j.pss.2022.105527.

[29] F.J. Guerrero-Gonzalez, P. Zabel, System analysis of an ISRU production plant: Extraction of metals and oxygen from lunar regolith, Acta Astronautica 203 (2023) 187–201. https://doi.org/10.1016/j.actaastro.2022.11.050.

[30] S.S. Schreiner, J.A. Hoffman, G.B. Sanders, K.A. Lee, Integrated modeling and optimization of lunar In-Situ Resource Utilization systems, in: 2015 IEEE Aerospace Conference, IEEE, Big Sky, MT, 2015: pp. 1–11. https://doi.org/10.1109/AERO.2015.7119077.

[31] S. Schreiner, Molten Regolith Electrolysis Reactor Modeling and Optimization of In-Situ Resource Utilization Systems, Massachusetts Institute of Technology, 2015.

[32] P.B. Patel, J. Soto, S. Koller, K. Latyshev, L. Sangabattula, Z. Adams, K. Misquitta, L. Jalil, A. Cooper, T. Nguyen, J. Fontanez, B. Ma, H. Na, J. Ramirez, C. Rissola, I. Subramanian, D. Bergman, A. Allanore, M. Culpepper, O.L. De Weck, G.C. Lordos, J.A. Hoffman, Producing Lunar Steel and Oxygen using Molten Regolith Electrolysis, in: ASCEND 2023, American Institute of Aeronautics and Astronautics, Las Vegas, Nevada, 2023. https://doi.org/10.2514/6.2023-4794.

[33] K.D. Grossman, T.S. Sakthivel, L. Sibille, J.G. Mantovani, S. Seal, Regolith-derived ferrosilicon as a potential feedstock material for wire-based additive manufacturing, Advances in Space Research 63 (2019) 2212–2219. https://doi.org/10.1016/j.asr.2018.12.002.

[34] K. Grossman, E. Petersen, E. Bell, J. Toro-Medina, L. Sibille, H. Williams, T. Newbold, K. Zacny, I. Bates, GaLORE (Gaseous Lunar Oxygen from Regolith Electrolysis): Successful Demonstration of a Cold-Walled Molten Regolith Electrolysis Reactor Design in a vacuum environment, (2023). https://isruinfo.com/public/docs/srr23/10-4%20Grossman-GALORE%20Demonstration%20of%20a%20Cold-Walled%20Molten%20Regolith%20Electrolysis%20Reactor%20Design%20in%20a%20Vacuum%20Environment.zip (accessed December 23, 2024).

[35] K. Morita, C. Wiraseranee, H. Shuto, S. Nakamura, K. Iwasawa, T.H. Okabe, N. Sano, Dissolution behaviour of platinum group metals into molten slags, Min Proc Ext Met 123 (2014) 29–34. https://doi.org/10.1179/0371955313Z.00000000070.

[36] E. Standish, D. Stefanescu, P. Curreri, Ceramics for Molten Materials Containment, Transfer and Handling on the Lunar Surface, in: 47th AIAA Aerospace Sciences Meeting Including The New Horizons Forum and Aerospace Exposition, American Institute of Aeronautics and Astronautics, Orlando, Florida, 2009. https://doi.org/10.2514/6.2009-1657.

[37] S.D. Rosenberg, O. Musbah, E.E. Rice, Carbothermal Reduction of Lunar Materials for Oxygen Production on the Moon: Reduction of Lunar Simulants with Carbon, Lunar and Planetary Science 27 (1996) 1103.

[38] M. Lensing, M. Sato, E. McMurchie, C.B. Dreyer, G.L. Brennecka, Corrosion and wetting behavior of monolithic refractory ceramics under molten lunar regolith electrolysis conditions, Acta Astronautica 236 (2025) 128–136. https://doi.org/10.1016/j.actaastro.2025.06.009.

[39] A. Allanore, Features and Challenges of Molten Oxide Electrolytes for Metal Extraction, J. Electrochem. Soc. 162 (2014) E13. https://doi.org/10.1149/2.0451501jes.

[40] H. Kim, J.D. Paramore, A. Allanore, D.R. Sadoway, Stability of Iridium Anode in Molten Oxide Electrolysis for Ironmaking: Influence of Slag Basicity, ECS Trans. 33 (2010) 219. https://doi.org/10.1149/1.3484779.

[41] H. Kim, J. Paramore, A. Allanore, D.R. Sadoway, Electrolysis of Molten Iron Oxide with an Iridium Anode: The Role of Electrolyte Basicity, J Electrochem Soc 158 (2011) E101. https://doi.org/10.1149/1.3623446.

[42] D. Wang, A.J. Gmitter, D.R. Sadoway, Production of Oxygen Gas and Liquid Metal by Electrochemical Decomposition of Molten Iron Oxide, J. Electrochem. Soc. 158 (2011) E51. https://doi.org/10.1149/1.3560477.

[43] B.A. Lomax, G.H. Just, P.J. McHugh, P.K. Broadley, G.C. Hutchings, P.A. Burke, M.J. Roy, K.L. Smith, M.D. Symes, Predicting the efficiency of oxygen-evolving electrolysis on the Moon and Mars, Nat Commun 13 (2022) 583. https://doi.org/10.1038/s41467-022-28147-5.

[44] P.A. Burke, M.E. Nord, C.A. Hibbitts, J.R. Berdis, Modeling electrolysis in reduced gravity: producing oxygen from in-situ resources at the moon and beyond, Front. Space Technol. 5 (2024). https://doi.org/10.3389/frspt.2024.1304579.

[45] C.A. Krier, R.I. Jaffee, Oxidation of the platinum-group metals, Journal of the Less Common Metals 5 (1963) 411–431. https://doi.org/10.1016/0022-5088(63)90055-9.

Chapter 2

EVALUATION OF UNARY OXIDES WITH MOLTEN REGOLITH SIMULANTS

Portions of the introduction and experimental methodology of this chapter are presented in "Thermochemical interactions between yttria-stabilized zirconia and molten lunar regolith simulants" by K. Yu, J. Stokes, B. Harder, L. Reidy, and K. T. Faber, which was published in the Journal of the American Ceramic Society in 2024. K. Yu led the experimental portion of this work. J. Stokes, B. Harder, and L. Reidy provided resources and subject matter expertise to design the experiments and assist in analyzing the results. K. T. Faber supervised the work.

K. Yu, J. Stokes, B. Harder, L. Reidy, K.T. Faber (2024). "Thermochemical interactions between yttria-stabilized zirconia and molten lunar regolith simulants". In: *Journal of the American Ceramic Society* 107(11), pp. 7119-7130. DOI: 10.1111/jace.19821

2.1 Introduction

The hollow anode design presented in the Introduction chapter requires an oxygen anion conductor, while building a molten regolith electrolysis (MRE) reactor will require some type of containment vessel. Containment and anode materials selection is challenging due to the harsh MRE environment, which includes an oxidizing atmosphere, contact with corrosive molten regolith, and a high operational temperature of 1600°C [1]. Platinum group metals have been traditionally used in applications with similar harsh environments [2]. However, these metals have high cost, while also forming eutectics with the molten silicon produced during MRE, precluding their use in MRE reactors [3]. Based on conditions described above, refractory oxide ceramics were determined to be promising candidates for containment materials, while some oxide ceramics can also act as oxygen anion conductors.

Oxygen anion conductors, which serve as the solid state electrolyte in the hollow anode, are typically oxide materials with the fluorite or perovskite structure [4]. These structures contain oxygen anion transport channels, caused by a high concentration of oxygen vacancies, resulting in high ionic conductivities [4]. Oxygen-conducting fluorite materials generally refer to stabilized ZrO_2 systems, where the stabilizer (dopant) can be CaO, MgO, Sc_2O_3, or Y_2O_3 [5]. Several different perovskites have been investigated as oxygen conductors, with the general formula ABO_3, in which A and B sites can contain multiple aliovalent cations to increase the number of oxygen vacancies [4]. Both ZrO_2-based and perovskite-based oxygen conductors are typically used at lower temperatures (800-1000°C) than the operational temperature of MRE (1600°C) [4]. ZrO_2-based oxygen conductors are estimated to be more likely to survive extended operation at 1600°C since ZrO_2 has a melting point of 2715°C, while oxide perovskites have melting points in the range of 1900°C-2370°C [6,7].

For containment applications, Standish et al. investigated refractory ceramics including Al_2O_3, stabilized ZrO_2 (CaO-ZrO_2, MgO- ZrO_2, and Y_2O_3- ZrO_2), and MgO plates in contact with molten lunar regolith simulants at 1600°C and concluded that Al_2O_3 exhibited the least degradation [8]. However, the porosity of the ceramics used in that study varied significantly, making it difficult to compare the degradation between ceramics. Rosenberg et al. studied crucible materials for carbothermal reduction of lunar regolith simulants at 1650°C, including Al_2O_3, MgO, Y_2O_3-ZrO_2 (YSZ), Y_2O_3, and TaC; they concluded that Y_2O_3 and YSZ were the only suitable materials for containing molten lunar regolith simulants [9]. Both of the aforementioned studies did not investigate the degradation mechanisms of these refractory ceramics in contact with molten regolith simulants and focused only on evaluating these materials from an engineering perspective, thereby motivating this investigation.

Based on the presented information, it appears that stabilized ZrO_2 materials are the most promising material for use as both the solid state electrolyte in the hollow anode design and as a containment material for molten regolith. HfO_2 is another candidate material for these applications. It possesses a similar melting point to ZrO_2 at 2758°C [6]. HfO_2 can also function as an oxygen conductor, since it also possesses the fluorite structure when doped [10]. Both ZrO_2 and HfO_2 rely on stabilizers to induce the fluorite structure. Stabilizers are

generally selected to be cause aliovalent substitutions for Zr and Hf, causing the formation of oxygen vacancies that enable high oxygen anion conductivity [5,10]. Since these stabilizers also interact with the molten regolith, it is important to evaluate the interactions between the stabilizer and molten regolith. Sc_2O_3 and Y_2O_3 were selected as they are commonly used stabilizers for ZrO_2 and HfO_2 [11]. CaO and MgO are also commonly used stabilizers for ZrO_2, but both are present in the molten regolith simulants. Thus, CaO-ZrO_2 and MgO-ZrO_2 can be evaluated based on the interactions of molten regolith with ZrO_2 and HfO_2.

This thesis chapter focuses on an investigation of the equilibrium state of ZrO_2, HfO_2, Y_2O_3, and Sc_2O_3 in contact with molten regolith simulants at 1600°C. This is accomplished through mixing unary oxide powders with regolith simulants, heat-treating the mixture to 1600°C, and quenching the sample. The use of powders allows for a high surface area of each oxide to be in contact with the molten regolith simulant, preventing kinetic limitations from influencing the results so that equilibrium can be achieved quickly. Quenching after heat treatment is necessary to lock in the equilibrium state at 1600°C. This allows for a determination of the degradation mechanisms at work at 1600°C, which will be evaluated for how they may impact MRE. Additionally, it has been shown by others that the type of regolith simulant (highlands vs maria) used can have a large effect on the degradation [12]. This work uses two regolith simulants, representative of the highlands and maria regions of the lunar surface. Ultimately, the results of this thesis chapter will be used to inform material selection for building a MRE reactor incorporating the hollow anode design.

2.2. Experimental procedures and materials

2.2.1 Lunar regolith simulants

Two lunar regolith simulants were selected to represent the two geologically distinct regions of the lunar surface: the lunar highlands and maria. The lunar highlands are the brighter regions of the lunar surface and compositionally dominated by feldspar, while the lunar maria are the darker regions of the lunar surface and mostly composed of basaltic lavas and pyroxene [13]. LHS-1 (Space Resource Technologies, FL) was selected as the highlands regolith simulant and JSC-1A (NASA) was selected as the maria regolith simulant [14,15]. The compositions of both regolith simulants are summarized in Table 2.1. The SiO_2 content of both simulants is similar, with JSC-1A having a higher concentration of FeO and MgO and a lower concentration of CaO and Al_2O_3 compared to LHS-1.

Table 2.1. Manufacturer-provided compositions of lunar regolith simulants in wt%. [14,15]

Species	SiO_2	FeO	MgO	CaO	Al_2O_3	TiO_2	Na_2O	K_2O
JSC-1A (Maria)	48.7	11.0	9.2	10.6	15.3	1.6	2.8	0.8
LHS-1 (Highlands)	51.8	2.7	1.6	12.9	26.9	0.6	2.9	0.8

2.2.2 Powder experiments

Sc_2O_3 (HEFA Rare Earth Canada Co. Ltd.), Y_2O_3 (Praxair Inc.), ZrO_2 (Cerac Inc.), and HfO_2 (Cerac Inc.) powders were mixed individually with each regolith simulant on a ball mill in ethanol using 10 mm cylindrical yttria-stabilized zirconia media for 16 hours. A molar ratio of 50:50 for the unary oxide powders to regolith simulant was used. Approximately 1 g of each of the resulting mixed powders were uniaxially pressed into 12.7 mm diameter pellets. The pellets were placed in platinum crucibles and heat treated at a ramp rate of 10°C/min to

1600°C in air and held at temperature for 3 hours. After the heat treatments, the pellets were air quenched using a cooling fan, reaching room temperature after approximately 10 minutes. The samples were then cross sectioned in half, with one half polished for scanning electron microscopy (SEM) analysis. The other half was crushed and ground in an alumina mortar and pestle for powder X-ray diffraction (XRD) analysis.

XRD analysis (Cu K-α source, D8 Advance, Bruker) was performed on the starting powders, both regolith simulants prior to mixing, the oxide/simulant mixtures, and the final reground, heat-treated oxide/simulant mixtures. SEM (1550VP FESEM, ZEISS) was used with the backscattered electron (BSE) detector to observe thermochemical changes in the heat-treated mixtures. For more accurate compositional analysis, electron-probe microanalysis (EPMA) (JXA-iHP200F, JEOL) was performed on the heat-treated samples using standards for Si, Al, Ti, Ca, K, Na, Mg, Fe, Mn, Zr, Hf, Sc, and Y. Oxygen content was obtained based on stoichiometry assuming all species are fully oxidized.

2.3 Results

2.3.1 ZrO_2

XRD spectra for the starting regolith simulant and ZrO_2 powders, the mixed ZrO_2/simulant powder (50:50 molar ratio), and the heat-treated ZrO_2/simulant powder (50:50 molar ratio) are presented in Figure 2.1. The starting ZrO_2 powder possesses the monoclinic crystal structure since there are no stabilizers present [5]. Both regolith simulants contain anorthite ($Ca_2Al_2Si_2O_8$) as the dominant crystalline phase based on the starting regolith simulant XRD spectra. It is noted that the XRD data for JSC-1A have a lower signal-to-noise ratio compared to LHS-1. This is attributed to LHS-1 being primarily a mixture of minerals, whereas JSC-1A contains a significant portion of basaltic glass [14,15]. Anorthite peaks are labeled only if they are observed in the ZrO_2/simulant mixture. The lower intensity of this anorthite peak is attributed to the lower atomic scattering factor of anorthite's constituent cations (Ca, Al, Si) compared to Zr [16].

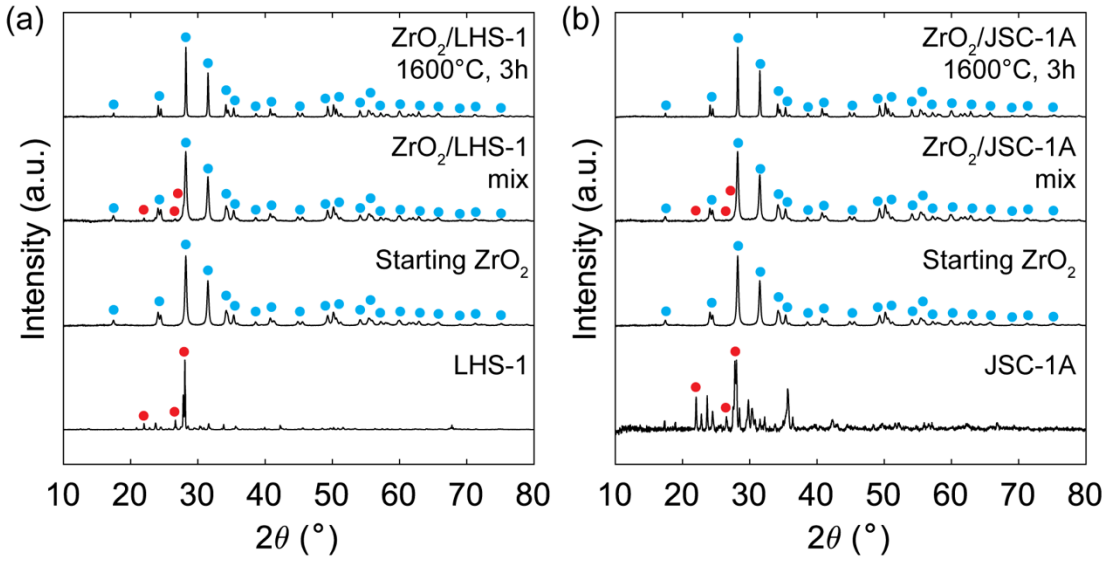

Figure 2.1. (a) XRD spectra of LHS-1 (highlands), starting ZrO_2 powder, and ZrO_2/LHS-1 mixture (50:50 molar ratio) before and after heat treatment. (b) XRD spectra of JSC-1A (maria), starting ZrO_2 powder, and ZrO_2/JSC-1A mixture (50:50 molar ratio) before and after heat treatment. Spectra show presence of anorthite (●) and monoclinic ZrO_2 (●).

After heat-treating and quenching, the ZrO_2/simulant XRD patterns no longer contain the anorthite peaks, indicating that the regolith simulant had melted in both samples, and remained amorphous through solidification due to rapid quenching. In both samples, the original monoclinic ZrO_2 peaks are still present, with no additional crystalline phases observed. These XRD scans indicate that ZrO_2 did not form additional crystalline reaction products with exposure to either LHS-1 or JSC-1A.

SEM micrographs of the heat-treated ZrO_2/LHS-1 and ZrO_2/JSC-1A samples, obtained using the backscatter electron (BSE) detector, are shown in Figure 2.2. There are two distinct phases in both samples – a bright ZrO_2 phase and a dark simulant glass matrix. These results are consistent with the XRD spectra of the heat-treated samples in that ZrO_2 is the only observed crystalline phase. Since no reaction phase was detected by XRD and SEM, dissolution (by either LHS-1 or JSC-1A) is predicted to be the dominant degradation mechanism in both ZrO_2/simulant samples. Large (~10-50 μm) pores are observed in both samples and are attributed to gas evolution during the heat-treatment process.

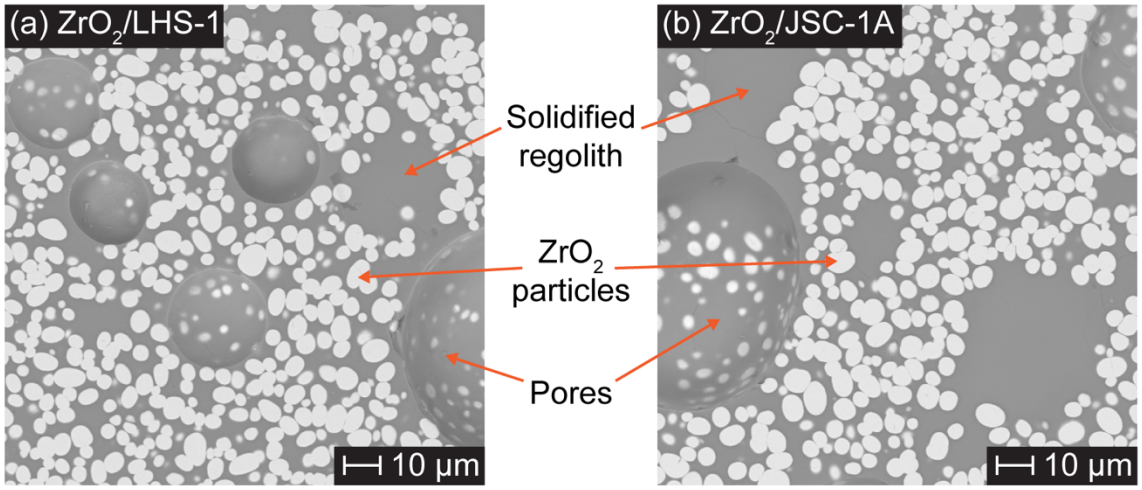

Figure 2.2. BSE micrograph of (a) heat-treated, ZrO_2/LHS-1 (highlands) and (b) heat-treated, ZrO_2/JSC-1A (maria).

Table 2.2. Composition (at%) of solidified regolith in ZrO_2/LHS-1 and ZrO_2/JSC-1A specimens. Standard deviations are presented in parentheses.

	Si	**Al**	**Ti**	**Ca**	**K**	**Na**	**Mg**	**Fe**	**Mn**	**Zr**	**O**
LHS-1	17.36 (0.11)	11.00 (0.06)	0.13 (0.01)	5.14 (0.06)	0.23 (0.01)	1.70 (0.03)	1.10 (0.02)	0.71 (0.01)	0.01 (0.00)	**1.07 (0.18)**	61.55 (0.03)
JSC-1A	17.11 (0.11)	6.41 (0.05)	0.33 (0.01)	4.18 (0.03)	0.29 (0.01)	1.92 (0.05)	4.85 (0.04)	3.09 (0.03)	0.05 (0.01)	**1.30 (0.13)**	60.43 (0.03)

Table 2.3. Composition (at%) of ZrO_2 particles in ZrO_2/LHS-1 and ZrO_2/JSC-1A specimens. Standard deviations are presented in parentheses.

	Ti	**Ca**	**Fe**	**Zr**	**Hf**	**O**
LHS-1	0.05 (0.02)	0.03 (0.00)	0.09 (0.04)	32.81 (0.06)	0.38 (0.02)	66.63 (0.01)
JSC-1A	0.10 (0.01)	0.04 (0.01)	0.33 (0.04)	32.60 (0.03)	0.39 (0.01)	66.54 (0.02)

EPMA compositional analysis is provided in Tables 2.2 and 2.3 for the solidified regolith and ZrO_2 particles, respectively. Compositional analysis of the solidified regolith revealed that Zr is observed in both regolith simulants. These results confirmed that ZrO_2 is undergoing dissolution in both molten regolith simulants since Zr is not present in either regolith simulant at beginning-of-life (BOL). Based on Table 2.2, it appears that there is a higher content of Zr in JSC-1A then in LHS-1, indicating that either the equilibrium solubility of Zr is higher in JSC-1A or the kinetics of ZrO_2 dissolution are faster in JSC-1A. This observation suggests that JSC-1A may cause accelerated degradation of bulk ZrO_2 compared to LHS-1. This hypothesis is explored further in Chapter 3. The concentrations of Zr in Table 2.2 are consistent with those reported in literature for pure ZrO_2 in aluminosilicate glasses at similar temperatures, which range from 1.3 at% to 3.3 at%, depending on the composition of the glass [17,18].

Compositional analysis of the remaining ZrO_2 particles indicated that Ti, Ca, Fe, and Hf are present. Hf is a common impurity in ZrO_2 and is present before the heat treatments. The remaining metals are likely diffusing into ZrO_2 from the regolith simulants at 1600°C. Ti and Fe possess relatively small ionic radii compared to Zr, which allows them to substitute for Zr [19]. Surprisingly, Ca is also detected, while no Mg was detected, even though Ca possesses a larger ionic radii [19]. Both CaO and MgO are common stabilizers for the ZrO_2 crystal structure and are present in both regolith simulants [5]. However, based on the XRD data and EPMA composition, it does not appear that either species is diffusing into the ZrO_2 crystal structure in quantities large enough to cause a transformation into either the tetragonal or cubic polymorphs of ZrO_2. This behavior suggests that both CaO-ZrO_2 and MgO-ZrO_2 are not thermodynamically stable in contact with either molten regolith simulant. If they were thermodynamically stable, the expected behavior is that CaO and MgO from the regolith would have higher concentrations in ZrO_2 than what is observed in EPMA. Ultimately, these results indicate that CaO-ZrO_2 and MgO-ZrO_2 are not suitable for contact/containment of either regolith simulant, since prolonged exposure would cause Ca and Mg to diffuse into the regolith simulant, causing ZrO_2 to become destabilized.

2.3.2 HfO_2

XRD spectra for the starting regolith simulant and HfO_2 powders, the mixed HfO_2/simulant powder (50:50 molar ratio), and the heat-treated HfO_2/simulant powder (50:50 molar ratio) are presented in Figure 2.3. Like ZrO_2, the starting HfO_2 powder possesses the monoclinic crystal structure since there are no stabilizers present [10]. Both regolith simulants contain anorthite ($Ca_2Al_2Si_2O_8$) as the dominant crystalline phase based on their starting XRD spectra. It is noted that the XRD data for JSC-1A has a lower signal-to-noise ratio compared to LHS-1. This is attributed to LHS-1 being primarily a mixture of minerals, whereas JSC-1A contains a significant portion of basaltic glass [14,15]. Anorthite peaks are labeled only if they are observed in the HfO_2/simulant mixture. In contrast to the ZrO_2/simulant mixtures, the anorthite crystalline peaks in the HfO_2/simulant mixtures are barely detectable. This is attributed to the higher atomic scattering factor of Hf relative to Zr [16].

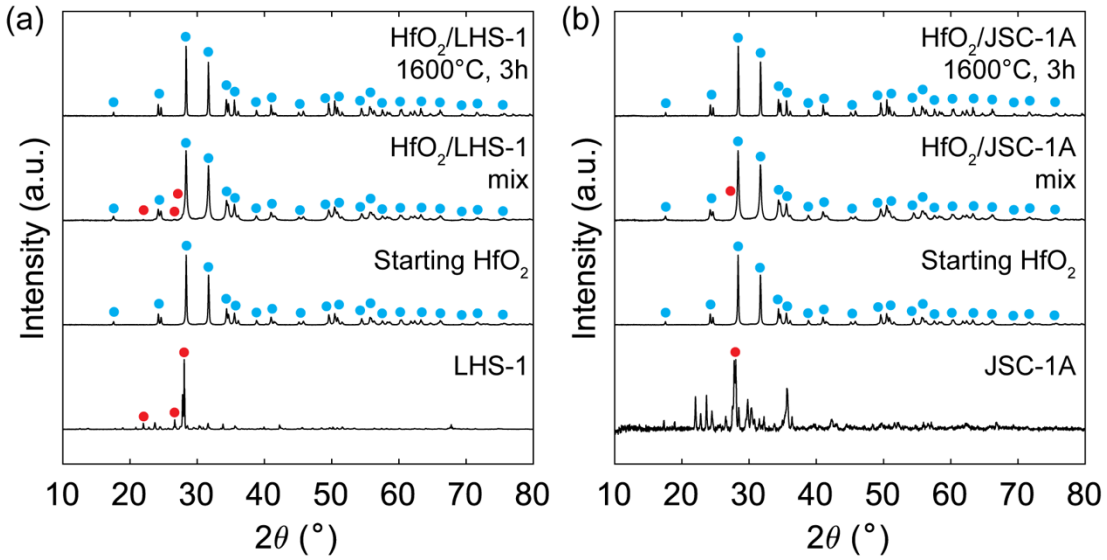

Figure 2.3. (a) XRD spectra of LHS-1 (highlands), starting HfO_2 powder, and HfO_2/LHS-1 mixture (50:50 molar ratio) before and after heat treatment. (b) XRD spectra of JSC-1A (maria), starting HfO_2 powder, and HfO_2/JSC-1A mixture (50:50 molar ratio) before and after heat treatment. Spectra show presence of anorthite (●) and monoclinic HfO_2 (●).

After heat-treating and quenching, the HfO_2/simulant XRD patterns no longer contain the anorthite peaks, indicating that the regolith simulant had melted in both samples, and remained amorphous through solidification due to rapid quenching. In both samples, the original monoclinic HfO_2 peaks are still present, with no additional crystalline phases observed. This is similar behavior to what was observed with the ZrO_2/simulant experiments. This behavior is expected since ZrO_2 and HfO_2 possess similar material properties due to both Zr and Hf being Group 4 transition metals. These XRD scans indicate that HfO_2 did not form additional crystalline reaction products with exposure to either LHS-1 or JSC-1A.

SEM micrographs of the heat-treated HfO_2/LHS-1 and HfO_2/JSC-1A samples, obtained using the backscatter electron (BSE) detector, are shown in Figure 2.4. There are two distinct phases in both samples: a bright HfO_2 phase and a dark simulant glass matrix. These results are consistent with the XRD spectra of the heat-treated samples in that HfO_2 is the only observed crystalline phase. Since no reaction phase was detected by XRD and SEM, dissolution (by either LHS-1 or JSC-1A) is predicted to be the dominant degradation mechanism in both HfO_2/simulant samples. The HfO_2 particles are more faceted compared to the ZrO_2 (Figure 2.1). This behavior will be discussed in Section 2.4.1.

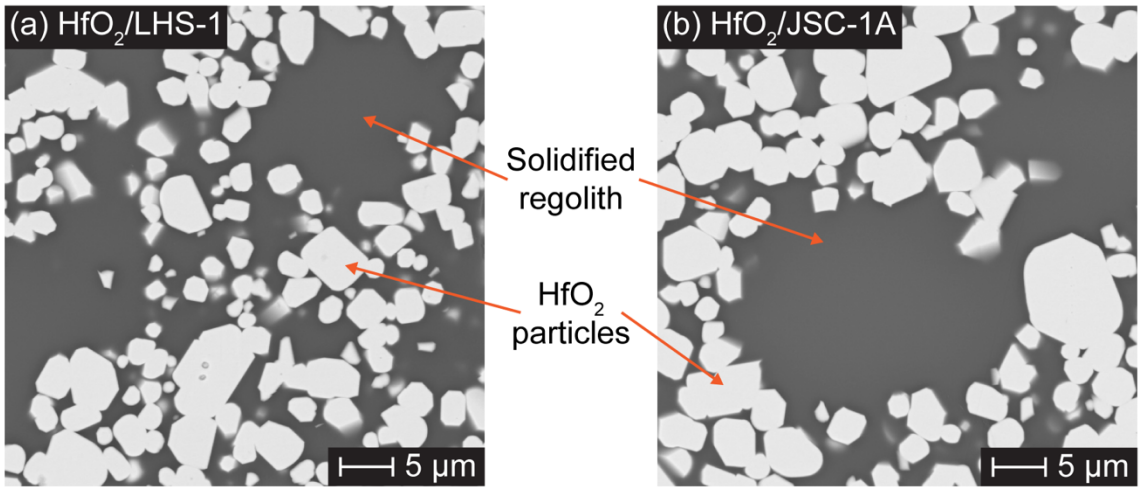

Figure 2.4. BSE micrograph of (a) heat-treated, HfO_2/LHS-1 (highlands) and (b) heat-treated, HfO_2/JSC-1A (maria).

EPMA compositional analysis is provided in Tables 2.4 and 2.5 for the solidified regolith and HfO_2 particles, respectively. Compositional analysis of the solidified regolith revealed that Hf is observed in both regolith simulants. These results confirmed that HfO_2 is undergoing dissolution in both molten regolith simulants since Hf is not present in either regolith simulant at BOL. Based on Table 2.4, it appears that Hf concentration in LHS-1 and JSC-1A are comparable. This behavior differs from ZrO_2, where JSC-1A contained a higher concentration of Zr compared to LHS-1 (Table 2.2). These results suggest that either the equilibrium solubility of Hf is similar in both JSC-1A and LHS-1 or the kinetics of HfO_2 dissolution are similar in both JSC-1A and LHS-1. Unlike ZrO_2, it does not appear that HfO_2 dissolution is impacted by the type of regolith simulant used.

Table 2.4. Composition (at%) of solidified regolith in HfO_2/LHS-1 and HfO_2/JSC-1A specimens. Standard deviations are presented in parentheses.

	Si	**Al**	**Ti**	**Ca**	**K**	**Na**	**Mg**	**Fe**	**Mn**	**Hf**	**O**
LHS-1	17.61 (0.04)	10.77 (0.06)	0.12 (0.01)	5.06 (0.04)	0.20 (0.01)	1.72 (0.02)	1.11 (0.01)	0.75 (0.02)	0.01 (0.00)	**1.03 (0.11)**	61.60 (0.03)
JSC-1A	17.58 (0.07)	6.32 (0.07)	0.33 (0.01)	4.11 (0.02)	0.25 (0.01)	1.84 (0.04)	4.84 (0.04)	3.09 (0.04)	0.05 (0.00)	**1.03 (0.13)**	60.54 (0.03)

Table 2.5. Composition (at%) of HfO_2 particles in HfO_2/LHS-1 and HfO_2/JSC-1A specimens. Standard deviations are presented in parentheses.

	Ti	**Mn**	**Hf**	**O**
LHS-1	0.15 (0.01)	0.06 (0.02)	33.14 (0.00)	66.65 (0.01)
JSC-1A	0.20 (0.07)	0.06 (0.01)	33.09 (0.06)	66.65 (0.02)

Chevreux et al. investigated Hf solubility in CaO-Na_2O-Al_2O_3-SiO_2 and CaO-Al_2O_3-SiO_2 glasses at 1400°C [20]. The authors measured a Hf solubility of ~2 at%, which is approximately double the Hf concentration presented in Table 2.4 (~1 at%). However, it is noted that the glasses used in Chevreux's experiments contained significantly higher amounts of glass network modifiers in CaO or ($CaO+Na_2O$). The two glasses investigated contained ~33 wt% CaO or ($CaO+Na_2O$), while the lunar regolith simulants in this study contained either 13.4 wt% of ($CaO+Na_2O$) for LHS-1 or 15.8 wt% of ($CaO+Na_2O$) for JSC-1A. Chevreux et al. showed that Hf solubility is positively correlated with the amount of network modifiers in the molten glass and with increasing exposure temperature [20]. Given the lower Hf concentration observed in regolith simulant experiments (Table 2.4), it appears that the effect of decreasing the amount of network modifiers dominates over the effect of increased exposure temperature (1600°C in regolith simulant experiments vs 1400°C in Chevreux's experiment).

It is noted that the Hf concentration presented in Table 2.4 may not be the equilibrium solubility of Hf in molten regolith simulants. However, the duration of the regolith simulant experiments matches Chevreux's glass experiments (3 hours for both), so a direct comparison can be made. Chevreux et al. showed that solution equilibrium is reached in their experiments at both 1250°C and 1400°C. Given the higher temperature of the molten regolith simulant experiments, it is likely that solution equilibrium has been reached and the results from Table 2.4 are the Hf equilibrium solubility in LHS-1 and JSC-1A. However, additional experiments that extend the exposure duration are required to confirm this.

Compositional analysis of the remaining HfO_2 particles indicate that Ti and Mn are present. Ti is also observed in ZrO_2, but Mn is not. Ti is also a Group 4 transition metal, with a smaller ionic radii than Hf and Zr, so it is not surprising to see Ti diffusing into both HfO_2 and ZrO_2 [19]. The EPMA results (Tables 2.3 and 2.5) suggest that Ca and Fe preferentially diffuse into ZrO_2, while Mn preferentially diffuses into HfO_2. This behavior is unexpected, since HfO_2 and ZrO_2 possess similar lattice parameters, bond lengths, and metal-oxygen coordination [21]. There does not appear to be a clear reason for this difference. Further thermochemical investigation is necessary to better understand this behavior.

2.3.3 Y_2O_3

XRD spectra for the starting regolith simulant and Y_2O_3 powders, the mixed Y_2O_3/simulant powder (50:50 molar ratio), and the heat-treated Y_2O_3/simulant powder (50:50 molar ratio) are presented in Figure 2.5. Bulk Y_2O_3 possesses a cubic crystal structure at all temperatures until its melting point [22]. Both regolith simulants contain anorthite ($Ca_2Al_2Si_2O_8$) as the dominant crystalline phase based on the starting regolith simulant XRD spectra. It is noted that the XRD data for JSC-1A has a lower signal-to-noise ratio compared to LHS-1. This is attributed to LHS-1 being primarily a mixture of minerals, whereas JSC-1A contains a significant portion of basaltic glass [14,15]. Anorthite peaks are labeled only if they are observed in the Y_2O_3/simulant mixture. The lower intensity of this anorthite peak is attributed to the lower atomic scattering factor of anorthite's constituent cations (Ca, Al, Si) compared to Y [16].

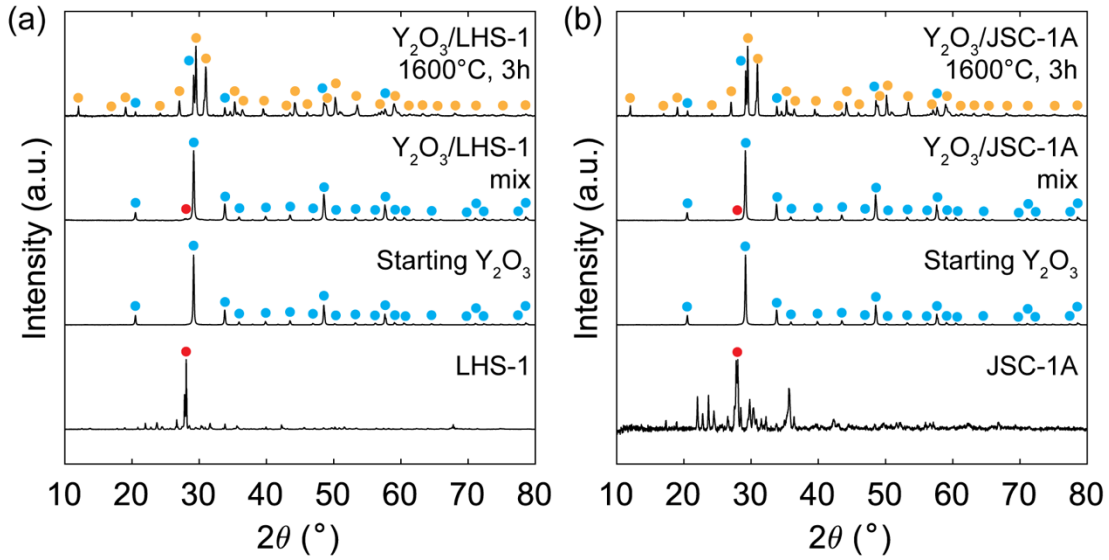

Figure 2.5. (a) XRD spectra of LHS-1 (highlands), starting Y_2O_3 powder, and Y_2O_3/LHS-1 mixture (50:50 molar ratio) before and after heat treatment. (b) XRD spectra of JSC-1A (maria), starting Y_2O_3 powder, and Y_2O_3/JSC-1A mixture (50:50 molar ratio) before and after heat treatment. Spectra show presence of anorthite (●), cubic Y_2O_3 (●), and Ca/Y-cuspidine (●).

After heat treating and quenching, both Y_2O_3/LHS-1 and Y_2O_3/JSC-1A samples exhibit a significant number of additional peaks in their XRD patterns. The presence of these peaks suggests that there is a crystalline reaction product that formed during the heat treatment of the samples. This behavior is completely different from both the ZrO_2 and HfO_2 experiments discussed previously, where no crystalline reaction products are observed. Phase identification of these additional peaks indicates that the crystalline reaction product is a Ca/Y-cuspidine phase, with the nominal formula of $Ca_2Y_2Si_2O_9$. This Ca/Y-cuspidine phase is formed in both the Y_2O_3/LHS-1 and Y_2O_3/JSC-1A samples, revealing that the crystalline reaction product, formed from either regolith simulant, possesses the same structure.

SEM micrographs of the heat-treated Y_2O_3/LHS-1 and Y_2O_3/JSC-1A samples, obtained using the backscatter electron (BSE) detector, are shown in Figure 2.6. There are two distinct phases in both samples – a bright Y_2O_3 phase and a dark reaction phase, identified by XRD to be Ca/Y-cuspidine. The darkest regions of the sample are pores, and no residual solidified regolith simulant was observed in either sample. The observation of two crystalline phases is consistent with the XRD data for these samples.

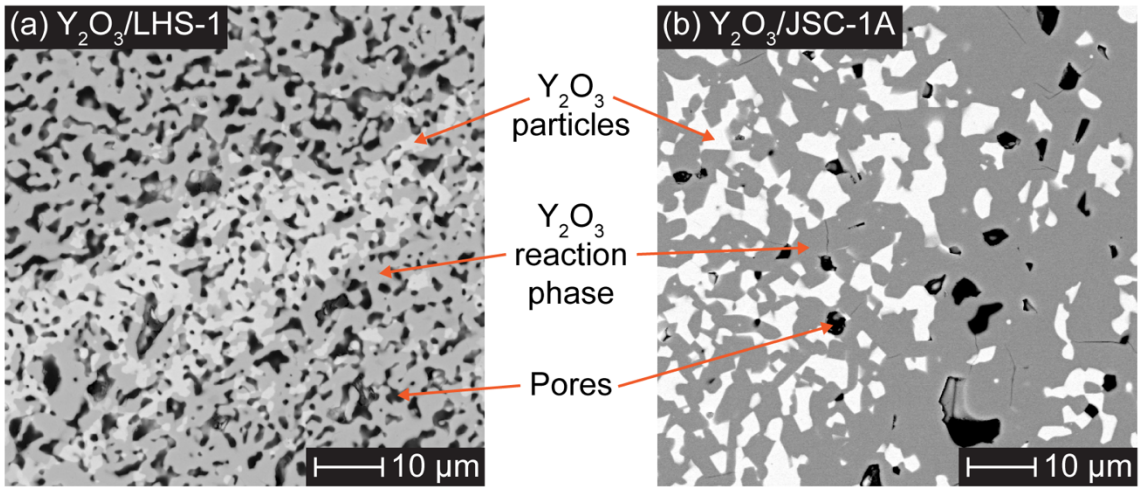

Figure 2.6. BSE micrograph of (a) heat-treated Y_2O_3/LHS-1 (highlands) and (b) heat-treated, Y_2O_3/JSC1A (maria).

EPMA compositional analysis is provided in Tables 2.6 and 2.7 for the Ca/Y-cuspidine phase and remaining Y_2O_3 particles, respectively. The nominal composition of Ca/Y-cuspidine is also presented in Table 2.6 for comparison. Based on Table 2.6, it appears that the Ca/Y-cuspidine reaction product can accommodate several cation substitutions with the cations found in the lunar regolith simulants. The ratios of Ca:Y:Si are not consistent with the nominal composition of Ca/Y-cuspidine, suggesting that there is likely some solubility range of $CaO:Y_2O_3$. The reaction product that forms from both LHS-1 and JSC-1A is significantly higher in Y_2O_3. This behavior will be discussed in the next paragraph. Table 2.7 indicates that the remaining Y_2O_3 is relatively pure, with most of the measured impurities near the EPMA detection limit. Si in the LHS-1 sample is likely due to interaction volume effects.

Table 2.6. Composition (at%) of Ca/Y-cuspidine (reaction phase) in Y_2O_3/LHS-1 and Y_2O_3/JSC-1A specimens. Nominal composition of Ca/Y-cuspidine also shown. Standard deviations are presented in parentheses.

	Si	**Al**	**Ti**	**Ca**	**Na**	**Mg**	**Fe**	**Y**	**O**
LHS-1	7.03 (0.13)	5.15 (0.18)	0.08 (0.02)	2.17 (0.08)	0.02 (0.02)	0.43 (0.04)	0.32 (0.06)	23.98 (0.12)	60.83 (0.02)
JSC-1A	7.29 (0.06)	2.86 (0.04)	0.16 (0.01)	1.73 (0.01)	0.24 (0.09)	1.89 (0.05)	1.35 (0.03)	24.07 (0.07)	60.40 (0.04)
$Ca_2Y_2Si_2O_9$	13.33	-	-	13.33	-	-	-	13.33	60.00

Table 2.7. Composition (at%) of Y_2O_3 particles in Y_2O_3/LHS-1 and Y_2O_3/JSC-1A specimens. Standard deviations are presented in parentheses.

	Si	**Al**	**Ti**	**Ca**	**Fe**	**Mn**	**Y**	**O**
LHS-1	0.09 (0.07)	0.01 (0.01)	0.01 (0.01)	0.05 (0.01)	-	0.01 (0.01)	39.82 (0.09)	60.01 (0.01)
JSC-1A	-	-	0.01 (0.01)	0.03 (0.00)	0.02 (0.01)	-	39.94 (0.02)	59.99 (0.00)

The general formula for the cuspidine family of phases is $M_4(T_2O_7\square)X_2$ [23]. The cuspidine family can have either monoclinic or orthorhombic unit cells, depending on the cations in the structure [23]. For the Ca/Y-cuspidine ($Ca_2Y_2Si_2O_9$), the unit cell is orthorhombic, which is consistent with the XRD data presented in Figure 2.5. In this structure, the M site is shared by Ca and Y, the T site is occupied by Si, and the X site is occupied by O. Poerschke et al. investigated the CaO-SiO_2-Y_2O_3 system and observed the formation of Ca/Y-cuspidine at 1400°C and 1600°C [24]. The authors provided the crystal structure of Ca/Y-cuspidine, which is shown below in Figure 2.7 [24]. In this nominal structure, there is a normally vacant anion site (□) that can accommodate additional O anions to charge balance the structure if there are aliovalent cation substitutions.

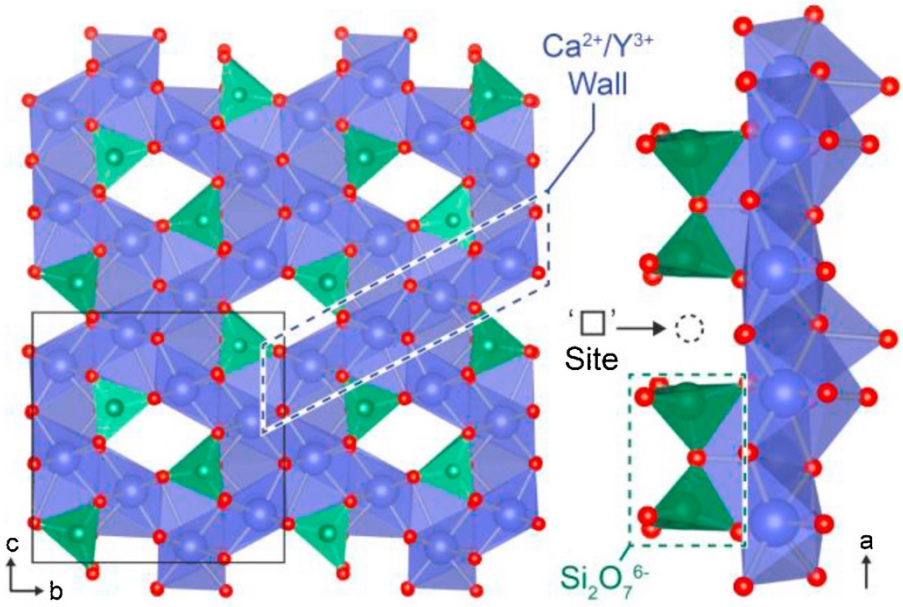

Figure 2.7. Crystal structure of Ca/Y-cuspidine ($Ca_2Y_2Si_2O_9$). Reproduced from Ref. [24] with permission from Elsevier.

Kolitsch et al. investigated the Y_2O_3-Al_2O_3-SiO_2 system and observed a different cuspidine phase, with the nominal formula $Y_4(Al_2O_7)O_2$ [25]. This yttrium aluminate cuspidine possesses a monoclinic unit cell. The authors showed that Si can substitute for Al in the yttrium aluminate cuspidine, up to ~30% on the Al site [25]. Based on this result, it is assumed that Al can also substitute for Si in the Ca/Y-cuspidine observed in this work.

Poerschke et al. did not determine the solubility range of $Ca_2Y_2Si_2O_9$, but proposed that $YO_{1.5}$ substitutions for CaO, beyond the 1:1 ratio in the nominal formula, are likely possible due to the presence of the normally vacant anion site (□) [24]. These vacant anion can accommodate the additional O anions necessary to charge balance the structure [24]. The authors proposed the following formula to describe these substitutions: $(Ca_{2-x}Y_{2+x})(Si_2O_7O_{x/2})O_2$ [24]. This is consistent with Table 2.6, which shows that both Ca/Y-cuspidine phases that form have a significantly higher concentration of Y and lower concentration of Ca than the nominal formula possesses. The cations that are still unaccounted for are Ti, Na, Mg, and Fe. Based on their ionic radii, Ti, Mg, and Fe are similar to Si/Al, while Na is similar to Ca/Y [19]. It is assumed that Ti, Mg, and Fe substitute for Si on the T site, while Na substitutes for Ca/Y on M site. The data from Table 2.6 can be renormalized so that the (Na+Ca+Y) is set to the number of M site cations (4). By applying these assumptions, the Ca/Y-cuspidine reaction product from LHS-1 and JSC-1A can be represented using the general formula of cuspidine ($M_4(T_2O_7□)X_2$), which is shown in Table 2.8.

Table 2.8. Ca/Y-cuspidine reaction phase formula unit for LHS-1 and JSC-1A using general cuspidine representation.

	M_4			T_2O_7						□		X_2
	Na	Ca	Y	Si	Al	Mg	Fe	Ti	O	□	O	O
LHS-1	0.003	0.332	3.665	1.075	0.787	0.066	0.049	0.012	7	0.702	0.298	2
JSC-1A	0.037	0.266	3.697	1.120	0.439	0.290	0.207	0.025	7	0.722	0.278	2

The sum of the M site cations is 4 due to the normalization method. The sum of T site cations is 1.989 for the LHS-1 Ca/Y-cuspidine and 2.081 for the JSC-1A Ca/Y-cuspidine. The LHS-1 value is within 1% of the ideal value of 2, suggesting that this analysis is likely accurate. The JSC-1A value is roughly 4% higher than the ideal value, indicating that there are likely cations that are incorrectly assigned to the T site and partially substitute on the M site. However, this behavior is beyond the scope of this work and requires additional experiments.

2.3.4 Sc_2O_3

XRD spectra for the starting regolith simulant and Sc_2O_3 powders, the mixed Sc_2O_3/simulant powder (50:50 molar ratio), and the heat-treated Sc_2O_3/simulant powder (50:50 molar ratio) are presented in Figure 2.8. Bulk Sc_2O_3 possesses a cubic crystal structure at all temperatures until its melting point [26]. Both regolith simulants contain anorthite ($Ca_2Al_2Si_2O_8$) as the dominant crystalline phase based on the starting regolith simulant XRD spectra. It is noted that the XRD data for JSC-1A has a lower signal-to-noise ratio compared to LHS-1. This is attributed to LHS-1 being primarily a mixture of minerals, whereas JSC-1A contains a significant portion of basaltic glass [14,15]. Anorthite peaks are labeled only if they are observed in the Sc_2O_3/simulant mixture. Compared to ZrO_2, HfO_2, and Y_2O_3, the Sc_2O_3/simulant mixture has the largest intensity peaks for anorthite. This is attributed to the lower atomic scattering factor of Sc compared to Zr, Hf, and Y [16].

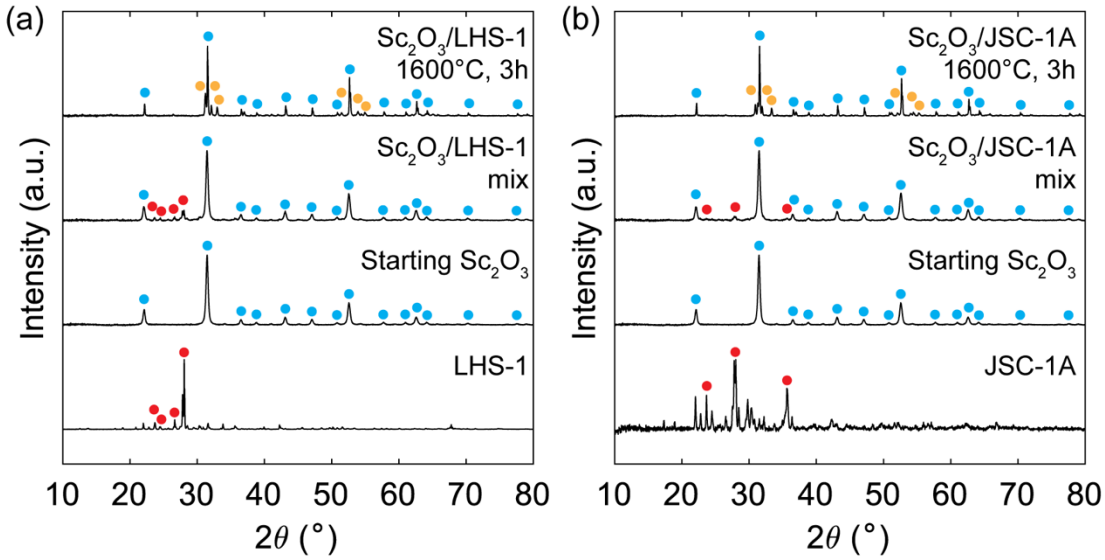

Figure 2.8. (a) XRD spectra of LHS-1 (highlands), starting Sc_2O_3 powder, and Sc_2O_3/LHS-1 mixture (50:50 molar ratio) before and after heat treatment. (b) XRD spectra of JSC-1A (maria), starting Sc_2O_3 powder, and Sc_2O_3/JSC-1A mixture (50:50 molar ratio) before and after heat treatment. Spectra show presence of anorthite (●), cubic Sc_2O_3 (●), and Sc reaction phase (●).

After heat treating and quenching, both Sc_2O_3/LHS-1 and Sc_2O_3/JSC-1A samples exhibit a number of additional peaks in their XRD patterns. The presence of these peaks suggests that there is a crystalline reaction product that formed during the heat treatment of the samples. This behavior is similar to the Y_2O_3 results discussed previously, where a crystalline reaction product was observed. However, unlike the Y_2O_3/simulant XRD, the Sc reaction product peaks are lower in intensity and the pure Sc_2O_3 peaks are still present and dominate the XRD pattern, indicating that there is still a significant amount of Sc_2O_3 left in both samples. Phase identification of these additional peaks did not match any known phases or minerals. The unidentified peaks have the same position between the Sc_2O_3/LHS-1 and Sc_2O_3/JSC-1A samples, indicating that the reaction products possess the same structure.

SEM micrographs of the heat-treated Sc_2O_3/LHS-1 and Sc_2O_3/JSC-1A samples, obtained using the backscatter electron (BSE) detector, are shown in Figure 2.9. There are three distinct phases in both samples: a bright Sc_2O_3 phase, a gray Sc reaction product, and a dark solidified simulant phase. This is unlike the Y_2O_3/simulant samples since a residual, solidified simulant matrix still exists in these Sc_2O_3/simulant samples. Pores are also observed in the sample, which are attributed to gas evolution during the experiment. The solidified simulant is amorphous due to quenching since it is not detected in the XRD data.

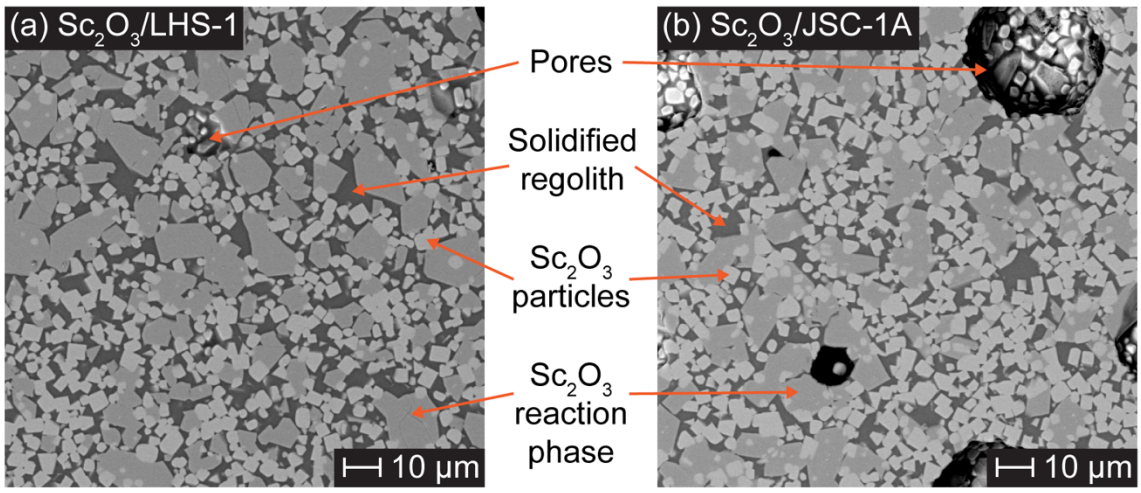

Figure 2.9. BSE micrograph of (a) heat-treated, Sc_2O_3/LHS-1 (highlands) and (b) heat-treated, Sc_2O_3/JSC-1A (maria).

EPMA compositional analysis is provided in Tables 2.9, 2.10, 2.11 for the solidified regolith simulant, remaining Sc_2O_3 particles, and the Sc reaction phase, respectively. Based on Table 2.9, the measured concentration of Sc in the remaining regolith is higher for LHS-1 than JSC-1A. This measurement suggests that LHS-1 has a higher solubility for Sc than JSC-1A. However, the solubility of Sc in regolith simulants is not expected to be accurate since a Sc reaction product forms. Given the 50:50 molar ratio used, and the amount of Sc reaction product observed by SEM, the remaining regolith composition is no longer representative of the BOL regolith simulant. Based on Table 2.11, SiO_2 and Al_2O_3 are preferentially removed from the molten regolith simulant in the reaction between Sc_2O_3 and the regolith simulants. An accurate determination of the solubility limit of Sc in regolith simulants requires increasing the Sc_2O_3 content until the first crystallites of the Sc reaction product are observed.

Table 2.9. Composition (at%) of solidified regolith in Sc_2O_3/LHS-1 and Sc_2O_3/JSC-1A specimens. Standard deviations are presented in parentheses.

	Si	**Al**	**Ti**	**Ca**	**K**	**Na**	**Mg**	**Fe**	**Mn**	**Sc**	**O**
LHS-1	16.45 (0.09)	8.59 (0.04)	0.10 (0.00)	6.72 (0.01)	0.20 (0.01)	1.80 (0.04)	0.69 (0.01)	0.26 (0.01)	0.01 (0.00)	**4.20 (0.12)**	60.97 (0.03)
JSC-1A	16.29 (0.04)	6.52 (0.08)	0.14 (0.01)	6.50 (0.10)	0.37 (0.02)	2.80 (0.08)	3.54 (0.05)	1.08 (0.02)	0.04 (0.01)	**2.92 (0.15)**	59.79 (0.03)

Table 2.10. Composition (at%) of Sc_2O_3 particles in Sc_2O_3/LHS-1 and Sc_2O_3/JSC-1A specimens. Standard deviations are presented in parentheses.

	Si	**Al**	**Ti**	**Ca**	**K**	**Mg**	**Fe**	**Mn**	**Sc**	**O**
LHS-1	0.04 (0.01)	0.51 (0.04)	0.40 (0.01)	0.24 (0.01)	0.01 (0.00)	0.07 (0.00)	0.27 (0.03)	-	38.49 (0.02)	59.97 (0.00)
JSC-1A	0.04 (0.00)	0.36 (0.01)	0.50 (0.02)	0.18 (0.03)	0.01 (0.04)	0.21 (0.02)	1.14 (0.10)	0.01 (0.00)	37.75 (0.14)	59.79 (0.03)

Table 2.11. Composition (at%) of Sc reaction phase in Sc_2O_3/LHS-1 and Sc_2O_3/JSC-1A specimens. Standard deviations are presented in parentheses.

	Si	**Al**	**Ti**	**Ca**	**Na**	**Mg**	**Fe**	**Mn**	**Sc**	**O**
LHS-1	5.25 (0.03)	4.60 (0.02)	0.26 (0.00)	0.33 (0.02)	0.01 (0.00)	0.48 (0.01)	0.29 (0.01)	0.01 (0.01)	27.90 (0.03)	60.88 (0.01)
JSC-1A	6.99 (0.05)	2.15 (0.03)	0.26 (0.01)	0.27 (0.04)	0.01 (0.04)	2.14 (0.03)	0.94 (0.00)	0.01 (0.00)	26.44 (0.09)	60.77 (0.01)

Table 2.10 indicates that the remaining Sc_2O_3 particles contain impurities, likely stemming from the molten regolith simulants. It is noted that the concentration of these impurities is approximately an order-of-magnitude higher than the impurities observed in the remaining Y_2O_3 particles (Table 2.7). Of the impurities observed, it appears that Al, Ti, and Fe have the highest concentration. Al_2O_3 has a high solid solubility in Sc_2O_3, so a high concentration of Al in the remaining Sc_2O_3 particle is not surprising [27]. Ti and Fe possess similar ionic radii to Sc, so it is expected that both can substitute for Sc in Sc_2O_3 [19].

Based on Table 2.11, the composition of the unidentified Sc reaction phase shows that Si and Al are the primary cations other than Sc. Zhi et al. investigated the Sc_2O_3-SiO_2-Al_2O_3 system and did not observe a stable ternary oxide comprised of Sc_2O_3, SiO_2, Al_2O_3 [28]. It is hypothesized that the reaction phase observed in Sc_2O_3/simulant samples may be stabilized by the six other cations detected by EPMA. It was initially believed that the compositional analysis on the Sc reaction product could provide guidance on phase identification using the Powder Diffraction File 4+ database (International Centre for Diffraction Data) and the Inorganic Crystal Structure Database. However, there were still no structures found that matched the observed peaks in the XRD data. Further characterization and structure determination of the Sc reaction phase are the focus of Chapter 6.

2.3.5 EDS vs. EPMA

The composition of all phases in all experiments presented in this chapter were determined by EPMA. Prior to EPMA analysis, energy-dispersive X-ray spectroscopy (EDS) was also performed on the same materials. Having both EDS and EPMA data on the same phases present an opportunity to evaluate the accuracy of EDS vs. EPMA for the two systems in Caltech's Geology and Planetary Sciences Division Analytical Facility. A comparison is provided in Appendix B (Tables B.1 – B.18). This comparison indicates that EDS-measured compositions are, on average, within 0.07 at% of EPMA-measured results for the multicomponent crystalline and amorphous oxide phases presented in this thesis chapter. Due to the close agreement between EDS and EPMA measurements, EDS composition analysis is used in the upcoming thesis chapters.

2.4 Discussion

2.4.1 ZrO_2 and HfO_2 particle morphology

The ZrO_2 (Figure 2.2) and HfO_2 (Figure 2.4) particles observed under SEM possess different particle morphology. The ZrO_2 particles are roughly ellipsoidal in shape and have curved surfaces. In contrast, the HfO_2 particles are faceted and have straight edges. Given the similarity of the crystal structures of ZrO_2 and HfO_2, the difference in their particle morphology is unexpected [21]. Both oxides were exposed to molten regolith simulants, which provides a new mechanism for surface rearrangement for these particles, facilitated by diffusion in the molten regolith simulants. The difference in their particle morphology suggests that the surface energies of specific crystallographic planes in ZrO_2 and HfO_2 must be significantly different. Based on the observed behavior, it is hypothesized that HfO_2 must have a larger difference in the surface energy of its low-index planes compared to ZrO_2, since HfO_2 surface rearrangement results in certain crystal planes being preferred, while ZrO_2 maintains an ellipsoidal shape.

Literature-reported surface energies of ZrO_2 and HfO_2 have been investigated using density functional theory [29,30]. For the monoclinic ZrO_2 system, Christensen et al. determined that the largest surface energy difference between low-index planes is ~1.22 J/m^2, between (010) and $(\bar{1}11)$ [29]. For the monoclinic HfO_2 system, Mukhopadhyay et al. found that the largest surface energy difference between low-index planes is ~0.89 J/m^2, also between (010) and $(\bar{1}11)$ [30]. Based on these investigations, it appears that ZrO_2 has higher anisotropy in surface energy and should produce more faceted crystallites compared to HfO_2. This is the opposite of the behavior observed in the samples under SEM. Thus, the comparison of surface energy for the monoclinic ZrO_2 and HfO_2 structures does not appear to be the correct method to evaluate the differences in particle morphology.

Despite the similarities between the monoclinic ZrO_2 and HfO_2 structures, there is a key difference between the two structures. Both structures undergo a diffusionless phase transformation from the monoclinic to tetragonal phase with increasing temperature [31]. Wolten investigated this monoclinic-tetragonal phase transformation for both ZrO_2 and HfO_2, finding that the ZrO_2 transformation occurs between 1050°C-1100°C, while the HfO_2 transformation occurs between 1640°C-1720°C [31]. Wolten's results indicate that ZrO_2 is in the tetragonal phase during the 3 hour heat-treatments with molten regolith simulants at 1600°C, while HfO_2 is still in the monoclinic phase. This suggests that the correct surface energy comparison is between tetragonal ZrO_2 and monoclinic HfO_2. Christensen et al. also investigated the surface energies of tetragonal ZrO_2, calculating that the largest surface energy difference between low-index planes is ~0.46 J/m^2, between (111) and (101) [29]. This value is roughly half of the surface energy difference for monoclinic HfO_2 (~0.89 J/m^2). Thus, the faceted HfO_2 particle morphology is attributed to its larger surface energy difference between low-index planes when compared to tetragonal ZrO_2.

2.4.2 Lack of zircon and hafnon

XRD data of the ZrO_2/simulant and HfO_2/simulant samples indicate that there are no crystalline reaction products formed, as discussed in Sections 2.3.1 and 2.3.2. Since both regolith simulants contain SiO_2 as the dominant oxide species, zircon ($ZrSiO_4$) and hafnon

($HfSiO_4$) were considered possible reaction products. Holgate et al. investigated both ZrO_2 and HfO_2 degradation and reaction behavior in contact with two molten aluminosilicates of similar composition to the molten regolith simulants used in this study at 1300°C [32]. The authors also performed a thermodynamic assessment of phase equilibria for ZrO_2 and the molten aluminosilicates, finding that zircon is not stable above 1400°C. Instead, the phase equilibria analysis above 1400°C indicates that saturation of the molten aluminosilicate causes reprecipitation of ZrO_2. Holgate's thermodynamic analysis is consistent with the ZrO_2/LHS-1 and ZrO_2/JSC-1A results, in which ZrO_2 is the only crystalline phase observed by XRD. Thus, it seems that zircon will not form as a reaction product of ZrO_2 and the molten regolith simulants at the operating temperature of MRE (1600°C).

Holgate et al. did not perform the same thermodynamic assessment on HfO_2, due to limited thermochemical data availability . The authors made the argument that the similarity between the melting points (ΔT_M = 43°C) and observed phase equilibria of HfO_2 and ZrO_2 suggest that hafnon will also not form at temperature at or above 1400°C [32]. This argument appears to be valid for the HfO_2/simulant results presented in this work. HfO_2 is the only crystalline phase detected by XRD after the heat-treatments with both molten regolith simulants. As a result, it also seems that hafnon will not form as a reaction product of HfO_2 and the molten regolith simulants at the operating temperature of MRE (1600°C).

2.4.3 Dissolution during MRE

The two degradation mechanisms observed for oxides interacting with molten regolith simulants are reactive crystallization and dissolution. Reactive crystallization results from a reaction between molten regolith simulants and the unary oxides, causing the formation of a solid, crystalline phase at 1600°C. This behavior was observed for Y_2O_3 and Sc_2O_3, with Y_2O_3 undergoing full reactive crystallization (no molten regolith simulant left) and Sc_2O_3 undergoing partial reactive crystallization (some molten regolith simulant left as a matrix). In contrast to this reactive crystallization, dissolution of unary oxides causes the some of the unary oxide particles to dissolve into the molten regolith simulant, without the formation of a reaction product, which was observed for both ZrO_2 and HfO_2. Dissolution behavior

suggests that the equilibrium of the system has two stable phases, the original unary oxide (potentially with impurities) and a molten regolith simulant at saturation with the unary oxide. The ideal material for use in either containment vessels or as a hollow anode should exhibit no degradation during operation. However, no material has been discovered that can prevent degradation in molten regolith at 1600°C [33]. Hence, an evaluation of which degradation mechanism is less detrimental is a necessity.

For usage in a MRE system, dissolution is the preferred behavior since it allows for preservation of the initial oxide phase for longer periods of time, while only adding oxide species to the molten regolith. Reactive crystallization is not desirable since it causes both the oxide phase and the remaining regolith to change in composition and properties, making it difficult to perform electrolysis for long periods of time. For the case of full reactive crystallization, there is no remaining molten regolith, like the results shown for the Y_2O_3/simulants experiment. Instead, a solid Ca/Y-cuspidine phase formed from the reaction. If this occurs in a MRE reactor, there would be no working electrolyte (molten regolith) left to perform electrolysis on. For the case of partial reactive crystallization, a smaller amount of molten regolith is left, as shown in Sc_2O_3/simulant experiment. However, the composition of the remaining regolith is altered from the BOL composition. This can have a substantial effect on the electrolysis process as the molten regolith may not have as high of a concentration of reducible oxide species. Specifically, for the Sc_2O_3/simulant experiments, compositional analysis indicates that SiO_2 and Al_2O_3 are preferentially reacting with Sc2O3 (Table 2.11). The loss of SiO_2 is the most concerning since it is typically the second oxide species to be electrolyzed and reduces the extraction yield of both oxygen and silicon that is produced during electrolysis [34]. As a result, dissolution is likely the less detrimental degradation mechanism for MRE applications.

It is paramount that the dissolved species do not interfere with the electrolysis process. This interference can manifest in two ways. The first is that the addition of a dissolved oxide species introduces a new electrochemically active species into the working electrolyte (the molten regolith). Since the MRE process produces oxygen (anode) and reduced metals (cathode), it is critical to ensure that the dissolved oxide species is not electrolyzed prior to

the end of the designed electrolysis process. The second type of interference is through altering the molten regolith viscosity. MRE is dependent on mass transport of metallic cations to the cathode and oxygen anions to the anode. The viscosity of the molten regolith must remain as low as possible to reduce the overpotential required to perform electrolysis. ZrO_2 will be examined in the context of these potential challenges resulting from dissolution since there is comparatively little data available for HfO_2. However, Ellison et al. showed that Zr and Hf possess similar solution behavior in high silicate melts, suggesting that HfO_2 is likely to follow the same trends as ZrO_2 when dissolved into molten regolith [35].

To evaluate whether the introduction of ZrO_2 into molten regolith causes ZrO_2 to become electrolyzed prior to the desired oxides, it is important to define the end of the MRE process. Based on a literature review, it appears that liquidus temperature of the molten regolith working electrolyte is the major limitation preventing full electrolysis of all oxide species in the regolith [3,34,36]. MRE reactors generally target an operational temperature of 1600°C, since higher temperatures are generally not practically achievable due to material degradation [33]. However, the liquidus temperature of both highlands and maria regolith increases with increasing oxygen removal from the molten regolith through electrolysis. The removal of oxygen is commonly normalized to give oxygen extraction efficiency, defined as the mass of O_2 produced divided by the mass of the starting molten regolith. Schreiner et al. calculated a maximum oxygen extraction efficiency of ~20% for maria regolith before the liquidus temperature exceeds the reaction operational temperature of 1600°C [34]. Schneiderman et al. calculated a similar maximum oxygen extraction efficiency of ~20% for highlands regolith before the liquidus temperature exceeds 1600°C [36]. Hence, the end of electrolysis for both types of molten regolith is at an oxygen extraction efficiency of ~20%, if the reactor temperature cannot exceed 1600°C. It is noted that a modest increase in reactor temperature, from 1600°C to 1675°C can enable a maximum extraction efficiency of ~37% for highlands regolith [36].

For the case of 20% oxygen extraction efficiency, FeO and SiO_2 are predicted to be electrolyzed in maria regolith, while FeO, SiO_2, and TiO_2 are predicted to be electrolyzed in highlands regolith [34,36]. For the case of 37% oxygen extraction efficiency (1675°C

operational temperature), FeO, SiO_2, TiO_2, MnO, MgO, Na_2O, and Al_2O_3 are predicted to be electrolyzed in the highlands regolith. It can be shown that the order of oxide electrolysis is the approximately the same as the order of oxide stability given by the Ellingham diagram (Appendix C). This estimate has also been used previously by Humbert [37]. Consequently, the Ellingham diagram can be used to predict where ZrO_2 falls in the order of oxide electrolysis by comparing the oxide stability of ZrO_2 to other oxides in the molten regolith.

The Ellingham diagram reveals that ZrO_2 has a higher oxide stability than Al_2O_3 [38,39]. As a result, ZrO_2 is not expected to be electrolyzed until Al_2O_3 is electrolyzed when performing MRE. The 20% oxygen extraction efficiency calculations for highlands and maria regolith did not predict Al_2O_3 electrolysis, so it is probable that ZrO_2 will also not be electrolyzed in these conditions [34,36]. The 37% oxygen extraction efficiency calculations predict that Al_2O_3 electrolysis begins at ~30% oxygen extraction efficiency. Thus, this analysis indicates that ZrO_2 will not be electrolyzed until at least 30% extraction efficiency is achieved. Therefore, ZrO_2 dissolution is not expected to alter the order of oxide electrolysis when operating the reactor at 1600°C but may be electrolyzed above 30% oxygen extraction efficiency at 1675°C.

The effect of ZrO_2 dissolution on molten regolith viscosity must also be evaluated. In general, ZrO_2 can act as both a network modifier (decreasing glass viscosity) or an intermediate network former (increasing glass viscosity), depending on its local environment and the glass composition [40]. Ficheux investigated the viscosity of Na_2O-CaO-Al_2O_3-SiO_2-ZrO_2 glasses across several different compositions at 1500°C and determined that substituting 2.3 mol% ZrO_2 for the other oxides can result in either an increase or decrease in viscosity, depending on the substitute, supporting the idea that ZrO_2 can serve as either a network modifier or intermediate network former [41]. The partial substitution of SiO_2 with ZrO_2 resulted in the largest decrease in viscosity from 13.5 Pa*s to 6.5 Pa*s, while the partial substitution of Na_2O with ZrO_2 produced the largest increase in viscosity from 7.4 Pa*s to 11.4 Pa*s [41]. Based on these results, it is not clear how the viscosity of the molten regolith will change with increasing ZrO_2 content. However, the viscosity changes are relatively small, indicating that ZrO_2 is unlikely to cause a drastic change in the regolith viscosity. Schneiderman et al.

measured the viscosity of highlands regolith at 1600°C as the composition changes due to electrolysis by producing glasses of the predicted composition at several different oxygen extraction efficiencies [36]. They measured 40 Pa*s at 0% oxygen extraction, which decreases to 1.2 Pa*s at 20% oxygen extraction [36]. Their results suggest that the magnitude of viscosity change of the molten regolith, due to electrolysis changing the regolith composition, is larger than the change in viscosity that could occur from the dissolution of ZrO_2.

From analyzing the effects of ZrO_2 dissolution on the order of oxide electrolysis and on the molten regolith viscosity, it does not appear that ZrO_2 dissolution will adversely affect the MRE process. It was estimated that ZrO_2 is likely one of the last oxides to be electrolyzed, occurring after Al_2O_3. A MRE reactor is unlikely to achieve Al_2O_3 electrolysis (starting at 30% oxygen extraction) unless the operational temperature of the reactor is increased from 1600°C, and even then, it is not clear that ZrO_2 will be electrolyzed since Al_2O_3 has a lower oxide stability than ZrO_2. The dissolution of ZrO_2 is also predicted to have an insignificant effect on the molten regolith viscosity compared to the decrease in viscosity that results from electrolysis. Ultimately, the main drawback of ZrO_2 dissolution is likely corrosion of the containment vessel or hollow anode. As stated previously, it is expected that HfO_2 would have similar behavior to ZrO_2 for both effects discussed in this section.

2.5 Conclusion

The results presented in this thesis chapter shed light on the equilibrium behavior of ZrO_2, HfO_2, Sc_2O_3, Y_2O_3 with highlands (LHS-1) and maria (JSC-1A) regolith simulants at 1600°C. ZrO_2 and HfO_2 undergo dissolution in contact with molten regolith, while Y_2O_3 and Sc_2O_3 react with the molten regolith to form solid crystalline phases, in a process known as reactive crystallization. The ideal material for containment of molten regolith and for use as a solid state electrolyte in the hollow anode design should remain indefinitely inert in contact with molten regolith at 1600°C. However, such a material has not been identified and may not exist. Section 2.4.3 evaluates the dissolution vs. reactive crystallization degradation

behavior in the context of MRE applications, indicating that dissolution is the preferred degradation mechanism. Dissolution is preferred because the dissolved ZrO_2 or HfO_2 does not impact the order of oxide electrolysis or the viscosity of molten regolith. Thus, it appears that ZrO_2 and HfO_2 are promising candidates for use as both a containment material and as the solid electrolyte in the hollow anode.

ZrO_2 and HfO_2 exhibited similar dissolution behavior in contact with both LHS-1 and JSC-1A. Based on Tables 2.2 (ZrO_2) and 2.4 (HfO_2), both oxides have similar solubilities in LHS-1 and ZrO_2 having a higher solubility in JSC-1A compared to HfO_2. These results suggest that HfO_2 may have slightly lower degradation compared to ZrO_2. However, commercial sources of dense HfO_2 parts are comparatively limited. Thus, despite the potentially lower degradation associated with HfO_2, the decision was made to move forward with a ZrO_2-based solid electrolyte for hollow anodes. Analysis of the ZrO_2 particles revealed that CaO and MgO will likely diffuse out of ZrO_2 if they are used as stabilizers. Thus, CaO-ZrO_2 and MgO-ZrO_2 were found to be unsuitable for contact with molten regolith (Section 2.3.1).

Both Sc_2O_3 and Y_2O_3 are also stabilizers for ZrO_2. While pure Sc_2O_3 and Y_2O_3 were determined to be incompatible in contact with molten regolith due to reactive crystallization, it is possible that they can still be used as stabilizers for ZrO_2 in contact with molten regolith. There are several thermochemical investigations of Y_2O_3 with other oxides found in the regolith, including SiO_2, Al_2O_3, and CaO (Section 2.3.3). In contrast, there are comparatively few thermochemical studies targeting Sc_2O_3 with other oxides in the regolith (Section 2.3.4). This difference in the thermochemical data available for Y_2O_3 and Sc_2O_3 is highlighted with the observation of a previously unreported Sc reaction phase, forming in the Sc_2O_3/simulant samples. Due to the limited thermochemical data available for Sc_2O_3, the decision was made to move forward with Y_2O_3-ZrO_2 (YSZ) as both the containment material and solid state electrolyte in the hollow anode design. The next thesis chapter will explore the degradation of YSZ, both in both powder and bulk form, in contact with molten regolith simulants.

References

[1] S.S. Schreiner, J.A. Hoffman, G.B. Sanders, K.A. Lee, Integrated modeling and optimization of lunar In-Situ Resource Utilization systems, in: 2015 IEEE Aerospace Conference, IEEE, Big Sky, MT, 2015: pp. 1–11. https://doi.org/10.1109/AERO.2015.7119077.

[2] K. Morita, C. Wiraseranee, H. Shuto, S. Nakamura, K. Iwasawa, T.H. Okabe, N. Sano, Dissolution behaviour of platinum group metals into molten slags, Min Proc Ext Met 123 (2014) 29–34. https://doi.org/10.1179/0371955313Z.00000000070.

[3] M.S. Humbert, G.A. Brooks, A.R. Duffy, C. Hargrave, M.A. Rhamdhani, Thermophysical property evolution during molten regolith electrolysis, Planet Space Sci 219 (2022) 105527. https://doi.org/10.1016/j.pss.2022.105527.

[4] W. Li, J. Sunarso, Y. Yang, Y. Chen, C. Ge, W. Wang, Y. Guo, R. Ran, W. Zhou, Strategies for improving oxygen ionic conducting in perovskite oxides and their practical applications, Energy Reviews 3 (2024) 100085. https://doi.org/10.1016/j.enrev.2024.100085.

[5] S. Badwal, Zirconia-based solid electrolytes: microstructure, stability and ionic conductivity, Solid State Ionics 52 (1992) 23–32. https://doi.org/10.1016/0167-2738(92)90088-7.

[6] R. Ruh, H.J. Garrett, R.F. Domagala, V.A. Patel, The System Zirconia-Scandia, Journal of the American Ceramic Society 60 (1977) 399–403. https://doi.org/10.1111/j.1151-2916.1977.tb15521.x.

[7] J.P. Poirier, Lindemann law and the melting temperature of perovskites, Physics of the Earth and Planetary Interiors 54 (1989) 364–369. https://doi.org/10.1016/0031-9201(89)90253-7.

[8] E. Standish, D. Stefanescu, P. Curreri, Ceramics for Molten Materials Containment, Transfer and Handling on the Lunar Surface, in: 47th AIAA Aerospace Sciences Meeting Including The New Horizons Forum and Aerospace Exposition, American Institute of Aeronautics and Astronautics, Orlando, Florida, 2009. https://doi.org/10.2514/6.2009-1657.

[9] S.D. Rosenberg, O. Musbah, E.E. Rice, Carbothermal Reduction of Lunar Materials for Oxygen Production on the Moon: Reduction of Lunar Simulants with Carbon, Lunar and Planetary Science 27 (1996) 1103.

[10] L. Sévin, L. Audouard, V. Razafindramanana, F. Mauvy, L. Galzin, J.-F. Justin, P. Bertrand, C. Langlade, M. Garcia, A. Julian-Jankowiak, Phase stabilisation, thermal expansion and ionic conductivity of high content rare earth oxide (Lu_2O_3, Y_2O_3 and Gd_2O_3) stabilised cubic hafnia, Journal of the European Ceramic Society 43 (2023) 4153–4166. https://doi.org/10.1016/j.jeurceramsoc.2023.03.006.

[11] P. Simoncic, A. Navrotsky, Systematics of Phase Transition and Mixing Energetics in Rare Earth, Yttrium, and Scandium Stabilized Zirconia and Hafnia, Journal of the American Ceramic Society 90 (2007) 2143–2150. https://doi.org/10.1111/j.1551-2916.2007.01678.x.

[12] H. Kim, J. Paramore, A. Allanore, D.R. Sadoway, Electrolysis of Molten Iron Oxide with an Iridium Anode: The Role of Electrolyte Basicity, J Electrochem Soc 158 (2011) E101. https://doi.org/10.1149/1.3623446.

[13] G. Heiken, D. Vaniman, B.M. French, eds., Lunar sourcebook: a user's guide to the moon, Cambridge University Press, Cambridge [England] ; New York, 1991.

[14] Exolith Lab, LHS-1 Lunar Highlands Simulant Fact Sheet (002-01-001-0621), (2021). https://cdn.shopify.com/s/files/1/0398/9268/0862/files/lhs-1-spec-sheet-Dec2022.pptx.pdf?v=1688051876.

[15] D.S. McKay, J.L. Carter, W.W. Boles, C.C. Allen, J.H. Allton, JSC-1: A New Lunar Soil Simulant, in: Engineering, Construction, and Operations in Space IV, American Society of Civil Engineers, Albuquerque, NM, 1994: pp. 857–866. https://www.lpi.usra.edu/lunar/strategies/jsc_lunar_simulant.pdf.

[16] B.L. Henke, E.M. Gullikson, J.C. Davis, X-Ray Interactions: Photoabsorption, Scattering, Transmission, and Reflection at E = 50-30,000 eV, Z = 1-92, Atom Data Nucl Data 54 (1993) 181–342. https://doi.org/10.1006/adnd.1993.1013.

[17] K. Kato, N. Araki, The corrosion of zircon and zirconia refractories by molten glasses, J Non-Cryst Solids 80 (1986) 681–687. https://doi.org/10.1016/0022-3093(86)90462-X.

[18] M. Ficheux, E. Burov, G. Aquilanti, N. Trcera, V. Montouillout, L. Cormier, Structural evolution of high zirconia aluminosilicate glasses, J Non-Cryst Solids 539 (2020) 120050. https://doi.org/10.1016/j.jnoncrysol.2020.120050.

[19] R.D. Shannon, Revised effective ionic radii and systematic studies of interatomic distances in halides and chalcogenides, Acta Cryst A 32 (1976) 751–767. https://doi.org/10.1107/S0567739476001551.

[20] P. Chevreux, A. Laplace, E. Deloule, L. Tissandier, N. Massoni, Hafnium solubility determination in soda-lime aluminosilicate glass, Journal of Non-Crystalline Solids 457 (2017) 13–24. https://doi.org/10.1016/j.jnoncrysol.2016.11.009.

[21] R. Ruh, P.W.R. Corfield, Crystal Structure of Monoclinic Hafnia and Comparison with Monoclinic Zirconia, J American Ceramic Society 53 (1970) 126–129. https://doi.org/10.1111/j.1151-2916.1970.tb12052.x.

[22] İ. Şavklıyıldız, Thermal equation of state study of polymorphic phases of Y_2O_3, Journal of Applied Physics 129 (2021). https://doi.org/10.1063/5.0043704.

[23] S. Merlino, N. Perchiazzi, Modular mineralogy in the cuspidine group of minerals, The Canadian Mineralogist 26 (1988) 933–943.

[24] D.L. Poerschke, T.L. Barth, O. Fabrichnaya, C.G. Levi, Phase equilibria and crystal chemistry in the calcia–silica–yttria system, Journal of the European Ceramic Society 36 (2016) 1743–1754. https://doi.org/10.1016/j.jeurceramsoc.2016.01.046.

[25] U. Kolitsch, H.J. Seifert, T. Ludwig, F. Aldinger, Phase equilibria and crystal chemistry in the Y_2O_3–Al_2O_3–SiO_2 system, J. Mater. Res. 14 (1999) 447–455. https://doi.org/10.1557/jmr.1999.0064.

[26] M. Zinkevich, Thermodynamics of rare earth sesquioxides, Progress in Materials Science 52 (2007) 597–647. https://doi.org/10.1016/j.pmatsci.2006.09.002.

[27] W. Zhi, F. Wang, X. Chen, Y. Tian, B. Yang, Thermodynamic assessment of the CaO–Al_2O_3–Sc_2O_3 ternary system, Calphad 78 (2022) 102454. https://doi.org/10.1016/j.calphad.2022.102454.

[28] W. Zhi, F. Wang, X. Chen, Y. Tian, B. Yang, Phase equilibria and thermodynamic assessment of the Al_2O_3-SiO_2-Sc_2O_3 system, Ceramics International 49 (2023) 9735–9747. https://doi.org/10.1016/j.ceramint.2022.11.147.

[29] A. Christensen, E.A. Carter, First-principles study of the surfaces of zirconia, Phys. Rev. B 58 (1998) 8050–8064. https://doi.org/10.1103/physrevb.58.8050.

[30] A.B. Mukhopadhyay, J.F. Sanz, C.B. Musgrave, First-principles calculations of structural and electronic properties of monoclinic hafnia surfaces, Phys. Rev. B 73 (2006). https://doi.org/10.1103/physrevb.73.115330.

[31] G.M. Wolten, Diffusionless Phase Transformations in Zirconia and Hafnia, Journal of the American Ceramic Society 46 (1963) 418–422. https://doi.org/10.1111/j.1151-2916.1963.tb11768.x.

[32] C.S. Holgate, Y. Yang, C.G. Levi, Reactive crystallization in HfO_2 exposed to molten silicates, Journal of the European Ceramic Society 41 (2021) 5686–5695. https://doi.org/10.1016/j.jeurceramsoc.2021.03.025.

[33] C. Schwandt, J.A. Hamilton, D.J. Fray, I.A. Crawford, The production of oxygen and metal from lunar regolith, Planetary and Space Science 74 (2012) 49–56. https://doi.org/10.1016/j.pss.2012.06.011.

[34] S.S. Schreiner, L. Sibille, J.A. Dominguez, J.A. Hoffman, A parametric sizing model for Molten Regolith Electrolysis reactors to produce oxygen on the Moon, Advances in Space Research 57 (2016) 1585–1603. https://doi.org/10.1016/j.asr.2016.01.006.

[35] A.J. Ellison, P.C. Hess, Solution behavior of +4 cations in high silica melts: petrologic and geochemical implications, Contr. Mineral. and Petrol. 94 (1986) 343–351. https://doi.org/10.1007/bf00371443.

[36] B. Schneiderman, M. Lensing, E. McMurchie, J. Stokes, G. Brennecka, C. Dreyer, C. Brice, Z. Yu, J. Kim, Evolution of oxide composition, liquidus temperature, and viscosity during lunar molten regolith electrolysis, Acta Astronautica 234 (2025) 1–12. https://doi.org/10.1016/j.actaastro.2025.04.055.

[37] M. Humbert, Electrolysis of Silicate Minerals in Reduced Gravity for Metal and Oxygen Production, (2024) 12445858 Bytes. https://doi.org/10.25916/SUT.28031294.V1.

[38] H. Ellingham, Transactions and Communications, J. Soc. Chem. Ind. 63 (1944) 125–160. https://doi.org/10.1002/jctb.5000630501.

[39] T.B. Reed, Free energy of formation of binary compounds: an atlas of charts for high-temperature chemical calculations, MIT Press, Cambridge, Mass, 1971.

[40] A. Shearer, M. Montazerian, B. Deng, J.J. Sly, J.C. Mauro, Zirconia-containing glass-ceramics: From nucleating agent to primary crystalline phase, Int J Ceramic Engine & Sci 6 (2024). https://doi.org/10.1002/ces2.10200.

[41] M. Fichuex, Diffusion multicomp lticomposante et environnement s ment structural dans le verre Na rre Na_2O-CaO-Al_2O_3-SiO_2 contenan ontenant du zirconium, Sorbonne Université, 2018. https://theses.hal.science/tel-02924994/preview/These_Ficheux_Maxime_2018.pdf.

Chapter 3

DEGRADATION OF YTTRIA-STABILIZED ZIRCONIA BY MOLTEN REGOLITH SIMULANTS

The majority of this chapter is presented in "Thermochemical interactions between yttria-stabilized zirconia and molten lunar regolith simulants" by K. Yu, J. Stokes, B. Harder, L. Reidy, and K. T. Faber, which was published in the Journal of the American Ceramic Society in 2024. K. Yu led the experimental portion of this work and wrote the original draft of the manuscript. J. Stokes, B. Harder, and L. Reidy provided resources and subject matter expertise to design the experiments and assist in analyzing the results. K. T. Faber supervised the work. All authors were involved in editing the manuscript.

K. Yu, J. Stokes, B. Harder, L. Reidy, K.T. Faber (2024). "Thermochemical interactions between yttria-stabilized zirconia and molten lunar regolith simulants". In: *Journal of the American Ceramic Society* 107(11), pp. 7119-7130. DOI: 10.1111/jace.19821

3.1 Introduction

The results of Chapter 2 indicated that yttria-stabilized zirconia (YSZ) is a promising material for usage in molten regolith electrolysis (MRE) systems as a containment material and as a solid electrolyte. This chapter focuses on the evaluation of YSZ as a containment material in contact with molten regolith simulants.

Platinum group metals have traditionally been used for containment of molten aluminosilicate-rich slags due to their relative stability in corrosive and oxidizing conditions [1]. In addition to their high cost and scarcity, these metals also form eutectics with the molten silicon produced in MRE, precluding their use as a containment material for MRE [2]. Kim et al. investigated the use of iridium as an anode for MRE in different compositions of slag; the iridium is only used at the anode and does not contact the molten silicon produced

at the cathode, avoiding the formation of eutectics between iridium and silicon [3]. However, the authors found that the composition of the slag, and its subsequent optical basicity, had a significant effect on the corrosion rate of iridium. The more acidic slag (higher in silica) resulted in roughly an order-of-magnitude reduction in the corrosion rate of iridium compared to the more basic slag (higher in calcia). Based on these results, variations in the composition of molten lunar regolith should result in differences in the corrosion rates of containment materials.

Standish et al. investigated refractory ceramics including alumina, zirconia (calcia-, magnesia-, and yttria-stabilized), and magnesia plates in contact with molten lunar regolith simulants at 1600°C and concluded that alumina exhibited the least degradation [4]. However, the porosity of the ceramics used in that study varied significantly, making it difficult to compare the degradation between ceramics. Rosenberg et al. studied crucible materials for carbothermal reduction of lunar regolith simulants at 1650°C, including alumina, magnesia, yttria-stabilized zirconia (YSZ), yttria, and tantalum carbide; they concluded that yttria and YSZ were the only suitable materials for containing molten lunar regolith simulants [5]. Both of the aforementioned studies did not investigate the degradation mechanisms of these refractory ceramics in contact with molten regolith simulants and focused only on evaluating these materials from an engineering perspective, thereby motivating this investigation.

The current chapter seeks to elucidate the degradation mechanisms of YSZ in contact with two representative lunar regolith simulants and evaluate YSZ's ability to contain these molten simulants. YSZ was selected due to the results presented in Chapter 2. The thermochemical equilibrium state of YSZ in molten lunar regolith simulants was determined through YSZ powder experiments. YSZ crucible experiments further extend these results by introducing microstructural effects to the system. Ultimately, this study will inform and guide materials design for a MRE reactor incorporating the hollow anode design.

3.2. Experimental procedures and materials

3.2.1 Lunar regolith simulants

Two lunar regolith simulants were selected to represent the two geologically distinct regions of the lunar surface – the lunar highlands and maria. The lunar highlands are the brighter regions of the lunar surface and compositionally dominated by feldspar, while the lunar maria are the darker regions of the lunar surface and mostly composed of basaltic lavas and pyroxene [6]. LHS-1 (Space Resource Technologies, FL) was selected as the highlands regolith simulant and JSC-1A (NASA) was selected as the maria regolith simulant [7,8]. The compositions of both regolith simulants are summarized in Table 3.1. The SiO_2 content of both simulants is similar, with JSC-1A having a higher concentration of FeO and MgO and a lower concentration of CaO and Al_2O_3 compared to LHS-1.

Table 3.1. Manufacturer-provided compositions of lunar regolith simulants in wt%. [7,8]

Species	SiO_2	FeO	MgO	CaO	Al_2O_3	TiO_2	Na_2O	K_2O
JSC-1A (Maria)	48.7	11.0	9.2	10.6	15.3	1.6	2.8	0.8
LHS-1 (Highlands)	51.8	2.7	1.6	12.9	26.9	0.6	2.9	0.8

3.2.2 Powder experiments

YSZ (11wt%/6.3mol% Y_2O_3) powder (Hermann C. Starck, Berlin) was mixed individually with each regolith simulant on a ball mill in ethanol using 10 mm cylindrical YSZ media for 16 hours. A total of four mixtures were produced; two at a 25:75 molar ratio of simulant to YSZ and two at a 50:50 molar ratio of simulant to YSZ. Approximately 1 g each of the resulting mixed powders was uniaxially pressed into 12.7 mm diameter pellets. The pellets were placed in platinum crucibles and heat treated at a ramp rate of 10°C/min to 1600°C in air and held at temperature for 3 hours. After the heat treatments, the pellets were air

quenched using a cooling fan, reaching room temperature after approximately 10 minutes. The samples were then cross-sectioned in half, with one half polished for scanning electron microscopy (SEM) analysis. The other half was crushed and ground in an alumina mortar and pestle for powder X-ray diffraction (XRD) analysis.

XRD analysis (Cu K-α source, D8 Advance, Bruker) was performed on the starting YSZ powders, both regolith simulants prior to mixing, the YSZ/simulant mixtures, and the final reground, heat-treated YSZ/simulant mixtures. SEM (1550VP FESEM, ZEISS) was used with the backscattered electron (BSE) detector to observe thermochemical changes in the heat-treated mixtures. For more accurate compositional analysis, electron-probe microanalysis (EPMA) (JXA-iHP200F, JEOL) was performed on the heat-treated samples using standards for Si, Al, Ti, Ca, K, Na, Mg, Fe, Mn, Zr, Hf, and Y. Oxygen content was obtained based on stoichiometry assuming all species are fully oxidized.

3.2.3 Crucible experiments

YSZ (14wt%/8.2mol% Y_2O_3) crucibles (40mm OD x 40mm tall) were obtained from Edgetech Industries. Each crucible was loaded with approximately 30 grams of LHS-1 or JSC-1A, filling half of the available volume. Alumina lids, coated in calcia-stabilized zirconia (ZYP Coatings), were used to prevent the regolith simulants from spilling over the top of the crucibles. Both crucibles were heat treated in an alumina tube furnace under flowing argon. The samples were ramped at 2°C/min up to 1600°C, held for 3 hours, and then cooled back to ambient temperature at 2°C/min. Both regolith simulants melted into a glassy phase during the heat treatment and were bonded to the YSZ crucibles. The entire assembly was mounted in epoxy, cross-sectioned to the center of crucible, and polished for SEM analysis. Optical microscopy (VHX-2000, Keyence) was performed on the polished cross-sections to observe macroscopic (>1 mm) phenomena of the YSZ, solidified regolith simulants, and the YSZ/simulant interface. SEM (1550VP FESEM, ZEISS) and energy dispersive spectroscopy (EDS) (X-Max EDS, Oxford Instruments) were used to assess the compositional and microstructural changes at the YSZ/simulant interface. Electron backscatter diffraction (EBSD) (HKL EBSD) was employed to evaluate the phases and grain

sizes of YSZ at the YSZ/simulant interface. MTEX, an EBSD analysis software package, was used for segmentation and grain size analysis on the EBSD maps to provide statistical data on grain sizes [9].

3.2.4 FactSage thermochemistry model

A FactSage model was created to thermodynamically predict possible reaction phases and estimate Zr solubility at 1600°C in both molten regolith simulants using the FToxid database [10]. Y was not included in this analysis since it is not optimized in the FToxid database. Both regolith simulant systems were modeled using the oxide chemistry provided in Table 3.1. The Equilib module was used to find the Zr solubility in both regolith simulants. The amount of ZrO_2 was added to the regolith compositions as a variable term, with tetragonal ZrO_2 set as a formation target. FactSage calculations then provided the amount of ZrO_2 needed to form the tetragonal ZrO_2 phase. The Equilib module was also used to identify any phases, other than a slag phase, that might precipitate from the regolith simulant compositions. Finally, the Viscosity module was used with the melt database to estimate the viscosity of both regolith simulants at 1600°C.

3.3 Results and discussion

3.3.1 Powder experiments

XRD spectra for the starting regolith simulant and YSZ powders, the mixed YSZ/simulant powder (50:50 molar ratio), and the heat-treated YSZ/simulant powder (50:50 molar ratio) are presented in Figure 3.1. Both regolith simulants contain anorthite ($Ca_2Al_2Si_2O_8$) as the dominant crystalline phase based on the starting regolith simulant XRD spectra. The starting YSZ powder is primarily a mixture of the cubic and tetragonal zirconia crystal structures. After ball milling to mix the YSZ and simulant powders, there is a small anorthite peak (28°) observed in both mixtures, indicating that the powders were well mixed. The lower intensity

of this anorthite peak is attributed to the lower atomic scattering factor of anorthite's constituent cations (Ca, Si) compared to YSZ's cations (Y, Zr) [11].

After heat treating and quenching, the YSZ/simulant XRD patterns no longer contain the anorthite peak at 28°, indicating that the regolith simulant had melted in both samples, and remained amorphous through solidification due to rapid quenching. In both samples, the original YSZ peaks (mixture of tetragonal and cubic YSZ) are still present, with no additional crystalline phases observed. These XRD scans indicate that YSZ did not form additional crystalline reaction products with exposure to either LHS-1 or JSC-1A.

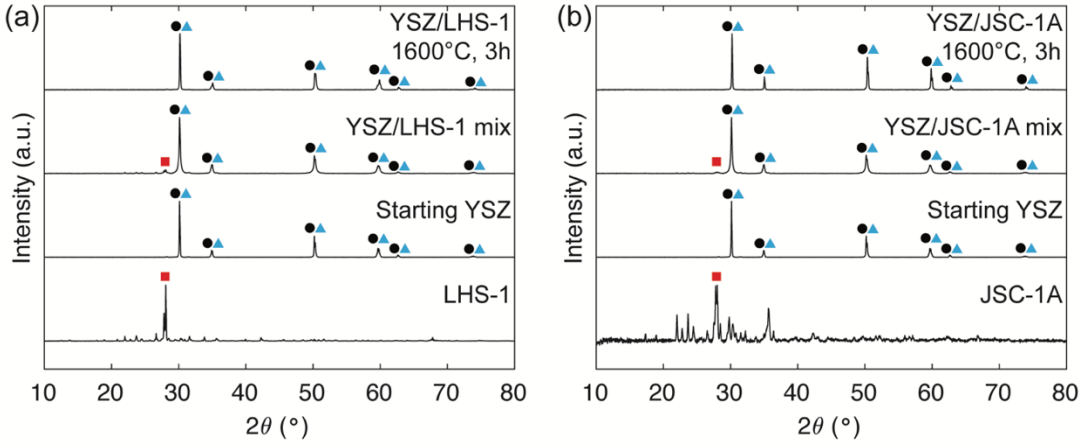

Figure 3.1. (a) XRD spectra of LHS-1 (highlands), starting YSZ powder, and YSZ/LHS-1 mixture (50:50 molar ratio) before and after heat treatment. (b) XRD spectra of JSC-1A (maria), starting YSZ powder, and YSZ/JSC-1A mixture (50:50 molar ratio) before and after heat treatment. Spectra show presence of anorthite (■), tetragonal YSZ (●), and cubic YSZ (▲).

SEM micrographs of the 50:50 molar ratio heat-treated YSZ/LHS-1 and YSZ/JSC-1A samples, obtained using the backscatter electron (BSE) detector, are shown in Figure 3.2. There are two distinct phases in both samples: a brighter YSZ phase and a darker simulant glass matrix. These results are consistent with the XRD spectra of the heat-treated samples in that YSZ is the only observed crystalline phase. Since no reaction phase was detected by XRD and SEM, dissolution/reprecipitation is predicted to be the dominant degradation mechanism in both YSZ/simulant samples. The YSZ particles in the JSC-1A system are

larger than those in the LHS-1 system. This difference in particle size is attributed to the ball milling used to mix these powders. The LHS-1 system contained a higher content of harder minerals such as anorthite and may cause a faster rate of YSZ particle size reduction compared to JSC-1A. EPMA compositional analysis (Table 3.2) confirms that both sets of YSZ/LHS-1 and YSZ/JSC-1A powder samples are at equilibrium. Thus, the difference in YSZ particle sizes is not believed to be significant for this analysis.

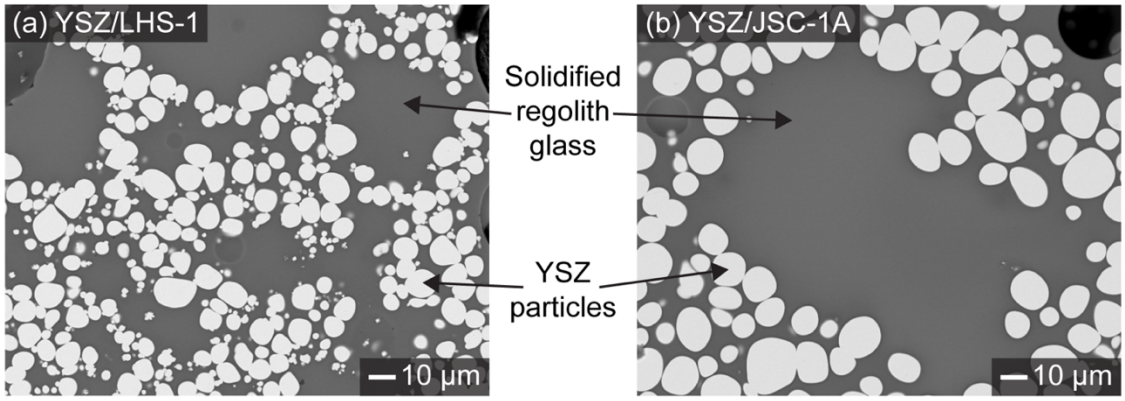

Figure 3.2. BSE micrograph of (a) heat-treated, 50:50 molar ratio YSZ/LHS-1 (highlands) and (b) heat-treated, 50:50 molar ratio YSZ/JSC-1A (maria).

The dissolution should result in a measurable concentration of Zr and Y within the glassy matrix. Additionally, metal ions, such as Ca, Mg, Fe, and Ti, in the molten regolith simulant are soluble in YSZ and are likely to diffuse into the YSZ particles at 1600°C. Low concentrations (<0.5 at%) of these cations are detected in the YSZ particles. EPMA composition analysis of Zr and Y in both the glassy matrix and YSZ particles are provided in Table 3.2. The nominal composition of the starting YSZ powder is also provided in Table 3.2. Full EPMA compositions of both the glassy matrix and YSZ particles are provided in Appendix B (Tables B.19 – B.26).

Table 3.2. EPMA concentrations of Zr and Y in glassy matrix and YSZ particles of heat-treated YSZ/simulant samples. Standard deviations are presented in parentheses.

		LHS-1 (Highlands)		JSC-1A (Maria)	
Phase	Molar ratio (simulant:YSZ)	Zr at%	Y at%	Zr at%	Y at%
Glassy matrix	25:75	1.09 (0.06)	1.50 (0.04)	1.27 (0.16)	1.78 (0.03)
	50:50	1.38 (0.18)	1.27 (0.02)	1.65 (0.44)	1.38 (0.04)
YSZ particles	25:75	29.36 (0.25)	4.09 (0.35)	29.24 (0.09)	3.86 (0.02)
	50:50	29.72 (0.15)	3.53 (0.18)	29.34 (0.20)	3.39 (0.33)
	Nominal composition	30.00	4.00	30.00	4.00

The measured concentrations of Zr and Y in the glassy matrix are in close agreement between the 25:75 and 50:50 molar ratio samples for both regolith simulants, indicating that the samples have reached solubility equilibrium. Based on FactSage results, it is determined that the system would not produce any high-temperature reaction phases, which is consistent with the XRD (Figure 3.1) and SEM (Figure 3.2) results. Additionally, FactSage predictions include a 1.96 at% Zr and 1.95 at% Zr solubility for LHS-1 and JSC-1A, respectively, which is consistent with the measured solubilities of Zr. Based on combined experimental results, the two regolith simulants have similar solubilities for Zr and Y, with molten JSC-1A having marginally higher solubilities than molten LHS-1. The solubilities of Zr in Table 3.2 are consistent with those reported in literature for pure ZrO_2 (no Y_2O_3) in aluminosilicate glasses at similar temperatures, which range from 1.3 at% to 3.3 at%, depending on the composition of the glass [12,13].

Measured Y concentrations in the glassy matrix for each sample are also similar to the Zr concentrations even though the starting YSZ material is only 8.2 mol% Y_2O_3. Since YSZ dissolution should result in a concentration of Zr and Y that maintains the same ratio as the starting material, Y must also be diffusing out of the YSZ. The measured Y concentration in the YSZ particles decreased with increasing regolith simulant, which supports the idea of Y diffusion out of the starting YSZ material. As more molten regolith is available for Y to diffuse into, more Y is depleted from the YSZ particles until the Y solubility limit is reached.

Guo et al. investigated the effect of varying optical basicity of an oxy-fluoride flux to understand Y depletion from YSZ. Their results indicate that Y depletion will occur when the optical basicity (Λ) of the flux is lower than that of Y_2O_3 ($\Lambda = 0.72$) [14]. The optical basicities of LHS-1 and JSC-1A were calculated based on the compositions presented in Table 3.1, resulting in $\Lambda_{LHS\text{-}1} = 0.57$ and $\Lambda_{JSC\text{-}1A} = 0.60$, respectively. Thus, both regolith simulants are lower (more acidic) in optical basicity than Y_2O_3, and therefore, Y depletion from YSZ is expected to occur in the presence of both molten regolith simulants. The observed Y depletion behavior in an oxide melt is consistent with previously reported results in an oxy-fluoride melt [14].

The Y depletion from YSZ in turn increases the Y content in both molten regolith simulants, resulting in comparable solubilities for Zr and Y shown in Table 3.2. The similarity of Zr and Y solubilities observed is consistent with the observations of Krämer et al. at 1300°C [15]. However, this combined YSZ dissolution and Y depletion from YSZ, in both cases, appears to occur at temperatures higher than the liquidus temperature of the glass. In contrast, Zhao et al. investigated YSZ degradation at 1250°C, just above the liquidus temperature of the aluminosilicate glass used in their system and observed the formation of Y-enriched YSZ instead of Y depletion into the glass phase [16]. This difference is attributed to the temperature at which these experiments were performed.

3.3.2 Crucible experiments

3.3.2.1 Bulk regolith behavior

Optical and scanning electron microscopy was performed on the cross-sectioned YSZ crucible samples and is presented in Figure 3.3. The solidified LHS-1 in the YSZ crucible (Figure 3.3(a)) contains minimal microstructural features, with most of the solidified LHS-1 appearing dark and glassy. YSZ dendrites grow from the bottom YSZ/LHS-1 interface. Other than the dendrite formation, optical and electron microscopy do not reveal any additional YSZ particles within the bulk of the solidified LHS-1. In contrast to LHS-1, the solidified JSC-1A (Figure 3.3(b)) exhibits more microstructural features within the bottom half of the sample. The region closest to the YSZ/JSC-1A interface contains larger and coarser dendrites compared to the YSZ/LHS-1 interface. The dendrite size decreases with increasing distance from the YSZ/JSC-1A interface. An optical micrograph is inset in Figure 3.3(b) to highlight the dendritic features spanning roughly the bottom half of the sample. The top half of this sample is similar to the LHS-1 crucible in that there are no observed YSZ dendrites in the solidified JSC-1A. EDS analysis of different regions in the solidified regolith indicates that the Zr and Y content is not homogenous and is generally higher near the YSZ interface, suggesting that equilibrium has not been reached in these crucible experiments, unlike the YSZ powder experiments described in Section 3.3.1.

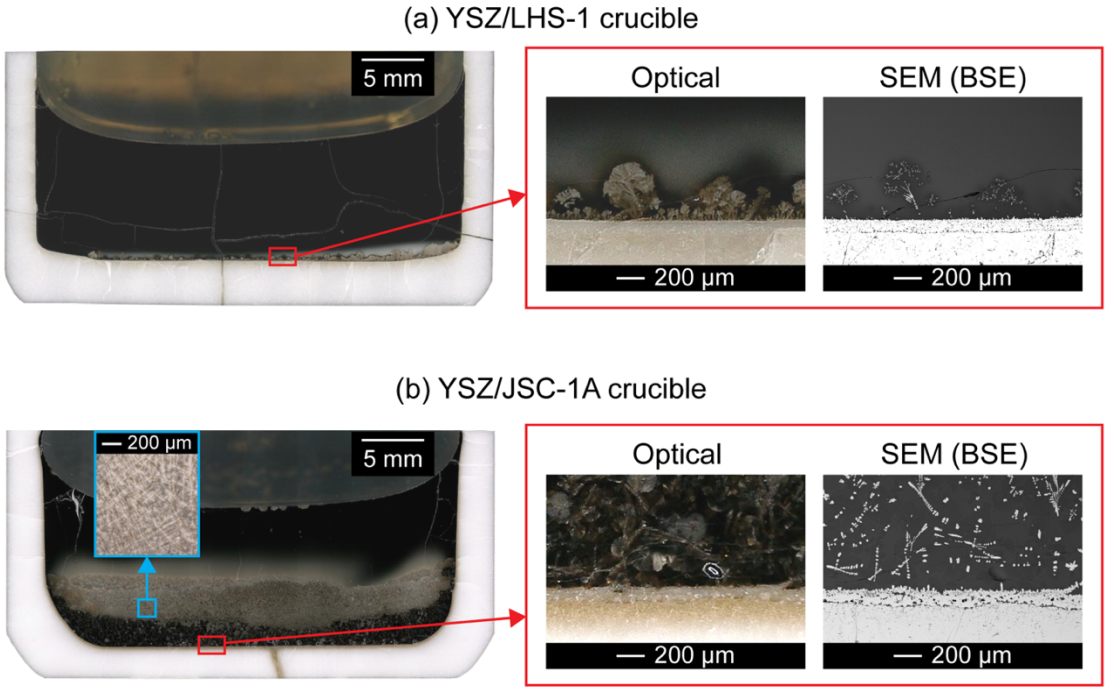

Figure 3.3. Optical and BSE images of the cross-sectioned heat-treated (a) YSZ/LHS-1 (highlands) crucible and (b) YSZ/JSC-1A (maria) crucible at 1600°C for 3 h.

YSZ dendrite formation in both regolith simulants was hypothesized to be caused by the slow cooling of the crucibles from 1600°C to ambient temperature compared to the quenched powder samples described previously. YSZ dissolves into the molten regolith simulants at 1600°C according to the solubility limits observed in the powder experiments. As the temperature of the sample is slowly decreased, the solubility limit of Zr and Y decreases until YSZ nucleated in the molten regolith simulant, forming dendrites in the process. The larger number of dendrites observed in the JSC-1A sample suggests that more Zr and Y have dissolved into JSC-1A as compared to LHS-1. There is also higher localized corrosion at the triple boundary between the YSZ crucible, molten regolith simulant, and argon. This type of corrosion is accelerated by Marangoni convection at this interface, which has been observed in other experiments with molten lunar regolith simulants [17]. The Marangoni-mediated corrosion in the JSC-1A sample is also more severe than for LHS-1. Both results suggest that the dissolution rate of YSZ in JSC-1A is higher than the dissolution rate of YSZ in LHS-1.

The powder experiments (Table 3.2) reveal comparable solubility limits of Zr and Y in molten JSC-1A and LHS-1 at equilibrium, but a higher dissolution rate of YSZ in JSC-1A is observed in the larger scale crucible experiments. This behavior is attributed to the difference in viscosities between JSC-1A and LHS-1. From the FactSage viscosity model, approximately an order of magnitude difference between the two molten regolith simulants (without dissolved Zr or Y) at 1600°C is computed ($\eta_{JSC\text{-}1A}$: 0.7 Pa*s, $\eta_{LHS\text{-}1}$: 6.7 Pa*s). This is likely due to the higher content of silica network modifiers such as FeO and MgO in JSC-1A compared to LHS-1 [18]. Humbert et al. modeled regolith thermophysical properties for measured compositions of lunar regolith at 1850°C and predicted a similar order-of-magnitude increase in viscosity for the highlands (LHS-1) compared to the maria (JSC-1A) [2].

Kato and Araki investigated the effect of glass composition on the dissolution behavior of zirconia at 1500°C and found similar results; the overall dissolution/corrosion loss of zirconia was higher with decreasing molten glass viscosity [12]. Additionally, they discovered that the dissolution rate of zirconia is controlled by the rate of dissolved Zr transport into the bulk molten glass. The Noyes-Whitney-Nernst equation can be used to describe dissolution dominated by solute (Zr) diffusion away from the dissolving surface:

$$j = \frac{D}{\delta^*}(C_i - C_\infty) \tag{3.1}$$

where j is the dissolution flux, D is the diffusivity of the dissolved species, C_i is the concentration of the dissolved species at the interface, C_∞ is the concentration of the dissolved species in the bulk molten glass, and δ^* is the diffusion layer thickness, which is defined as:

$$\delta^* = (C_i - C_\infty)/(dC/dy)_i$$

where $(dC/dy)_i$ is the concentration gradient at the interface and y is the position along the direction normal to the interface [19]. For a given temperature and solute, the Stokes-Einstein equation, relating viscosity to diffusivity, can be reduced to:

$$D\,\eta = k \tag{3.2}$$

where η is the viscosity of the glass and k is a constant that varies with temperature and size of the diffusing species. By combining the previous equations, the following relation is obtained:

$$j = \frac{k}{\delta^{*}\eta}(C_i - C_\infty) \tag{3.3}$$

Based on the powder experiments, C_i (solubility concentration of Zr) is similar for JSC-1A and LHS-1, while C_∞ is zero for both regolith simulants. This implies that δ^* is also similar between the two regolith simulants at the start of dissolution. The constant k, in the context of these crucible experiments, is the same for JSC-1A and LHS-1 since the diffusing species and temperature are identical. Thus, changes in the dissolution flux j are dominated by the viscosity term and j is inversely proportional to the viscosity of the melt. For a glass-forming melt, the Stokes-Einstein relation is inaccurate due to the coexistence of various silicon-oxygen complexes in the glass, and a more suitable model can be expressed as:

$$D^m\,\eta = k \tag{3.4}$$

where m is a positive coefficient and is the ratio of the activation energies of viscous flow and diffusion [20]. However, the same overall trend applies in that the dissolution flux j will be dependent on the inverse of η raised to a positive exponent.

As a result of this analysis and given the lower viscosity of JSC-1A compared to LHS-1, the dissolution rate of YSZ in JSC-1A is expected to be higher than that of YSZ in LHS-1. The greater volume of recrystallized dendrites observed in the JSC-1A sample indicates that more YSZ is dissolved into JSC-1A compared to the LHS-1 sample, which is consistent with the expected dissolution behavior of the molten regolith simulants based on their viscosities. The composition of the lunar regolith simulant, and resulting viscosity, has a significant effect on the overall corrosion of the YSZ crucible. This suggests that lunar maria regolith, which has

a higher concentration of network modifiers, will degrade crucibles faster than lunar highlands regolith.

3.3.2.2 YSZ/regolith interfacial behavior

To better understand the microstructural and compositional changes that occur due to interactions between the YSZ and molten regolith simulants, further analysis of the YSZ/simulant interface were required. Combined SEM images, EDS line scans, and EBSD maps were collected at the bottom YSZ/simulant interface, over a width of 200 μm and extending approximately 650 μm into the YSZ. These results are presented in Figure 3.4. Both samples contain three distinct regions based on the changes of Y content in EDS line scans and are demarcated by horizontal green lines. These three areas will be referred to as the reprecipitation region (top), surface region (middle), and bulk region (bottom) in the upcoming discussions.

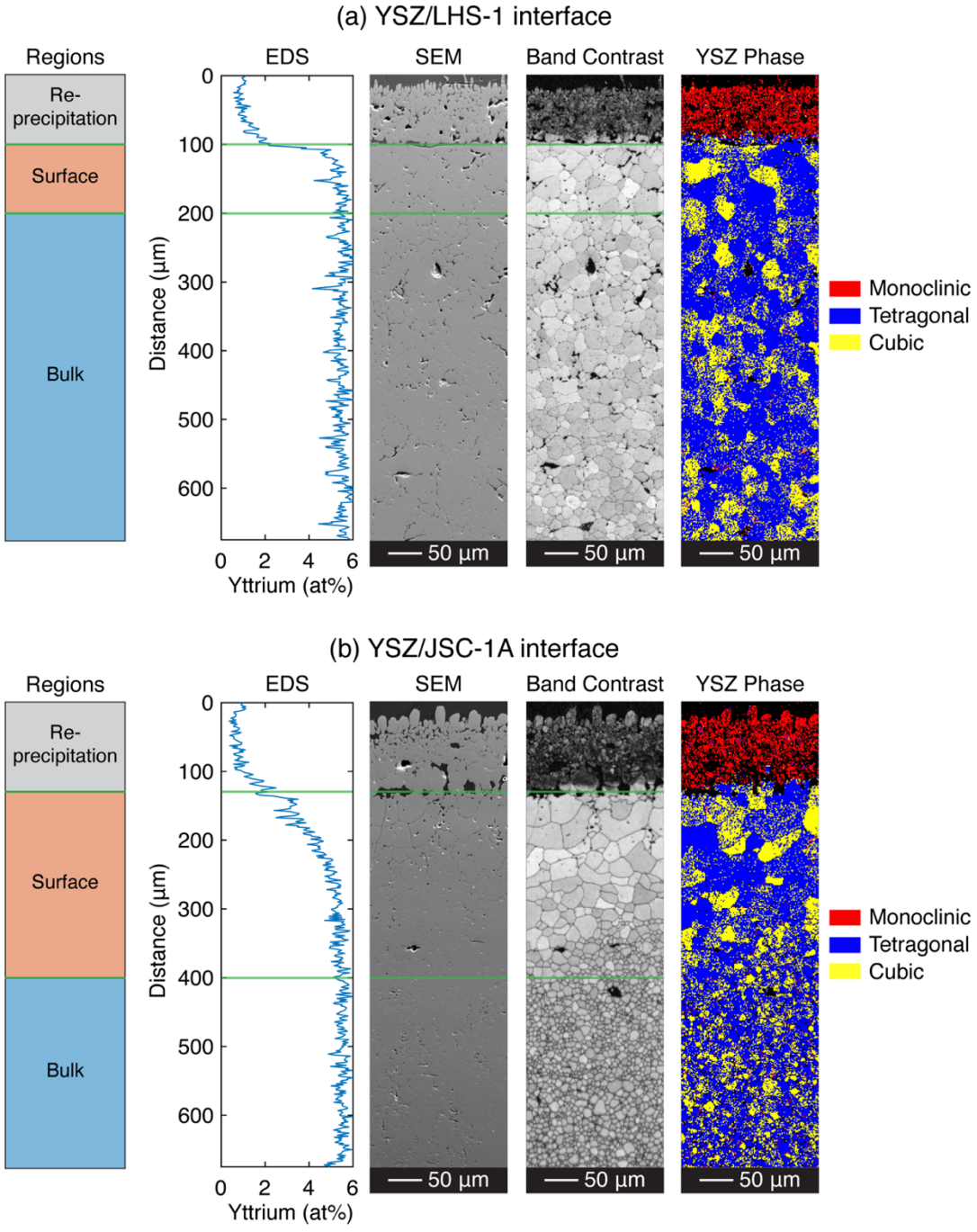

Figure 3.4. Combined EDS/SEM/EBSD images of (a) YSZ/LHS-1 (highlands) interface (crucible bottom) and (b) YSZ/JSC-1A (maria) interface (crucible bottom).

The reprecipitation region (top) exhibits decreased Y content with respect to the starting YSZ crucible material (5.2 at% Y) and is approximately 100-150 μm thick for both regolith simulants. EBSD phase mapping indicates that this region contains mostly monoclinic YSZ as well as pockets of amorphous, solidified regolith simulant. A dissolution-reprecipitation mechanism is responsible for producing the monoclinic YSZ phase. As the regolith simulants melt, YSZ begins to dissolve from the crucible wall until the local molten regolith environment is saturated with Zr. At this point, Y-depleted (~1 at% Y) YSZ particles begin to reprecipitate into smaller grain sizes compared to those in the original YSZ crucible. The effect is exacerbated on cooling as the solubility of Zr decreases with temperature, and a higher degree of undercooling is experienced. The grains in direct contact with the molten regolith simulants demonstrate cellular growth that eventually transitions to dendrites observed in Figure 3.3. These Y-depleted particles are tetragonal at high temperature, but do not contain sufficient Y to stabilize the tetragonal phase and ultimately transform into the monoclinic phase on cooling. This effect has been observed in YSZ interactions with molten silicates at temperatures lower than 1600°C [13,21]. The tetragonal-to-monoclinic transformation causes significant stress on the crucible walls and likely gives rise to the crucible cracks that are observed in Figure 3.3. Based on the measured Y content in the monoclinic region, the tetragonal-to-monoclinic transformation is expected to occur around 1100°C, while the liquidus temperature of the regolith simulants is predicted to be between 1450°C and 1550°C [22,2]. Thus, it is concluded that the cracks in the YSZ crucible form after the molten regolith simulant has solidified, which is supported by the lack of molten regolith penetration along the majority of cracks in the YSZ crucible wall.

The surface region (middle) is the interior of the YSZ crucible wall after the initial dissolution of YSZ occurs and the molten regolith near the interface is locally saturated with Zr and Y. For both LHS-1 and JSC-1A, this region exhibits an increase in Y content (from top to bottom) that eventually returns to the nominal Y content of the YSZ crucible. EDS line scans elucidate the diffusion profile of Y from the bulk YSZ into the molten regolith simulant. This is consistent with the previous EPMA powder results that also exhibit Y depletion in the YSZ particles (Table 3.2). In addition to the greater amount of YSZ dissolution observed with

JSC-1A vis-à-vis LHS-1, more Y depletion is observed in the YSZ exposed to JSC-1A. The lower viscosity of JSC-1A likely allowed for faster transport of Y out of YSZ and into the bulk of the molten JSC-1A, resulting in a more extensive Y depletion region compared to that in the LHS-1 sample. In contrast to the reprecipitation region, the thickness of the surface region varies between the two regolith simulants and is approximately 100 μm for LHS-1 and 380 μm for JSC-1A. EBSD phase mapping of the surface region reveals that this region is largely a mixture of cubic and tetragonal YSZ, with no monoclinic YSZ content. Additionally, the YSZ grains in the surface region are larger than those in the bulk region below it, suggesting that interactions between YSZ and both molten regolith simulants are accelerating grain coarsening, being more pronounced in the case of JSC-1A.

The bulk region (bottom) is representative of the remaining YSZ crucible material. The Y level is consistent with the nominal Y content of the starting YSZ crucible material and does not vary in the EDS line scan. Similar to the surface region, EBSD mapping of the bulk region reveals that it is also a mixture of cubic and tetragonal YSZ, with no monoclinic YSZ content. EBSD scans on the exterior crucible wall (~2.5 mm below the regions in Figure 3.4) for each crucible are consistent with the bulk region of each crucible, allowing the designated bulk region to be used as a baseline for grains that are far from the YSZ/simulant interface and unaffected by interactions with the molten regolith simulant. A comparison of YSZ grain sizes in the bulk region and the exterior crucible for both LHS-1 and JSC-1A is provided in Figure 3.5. There are small differences (~5% on average) in the bulk region grain sizes between JSC-1A and LHS-1, but this is attributed to manufacturing variations during YSZ crucible production.

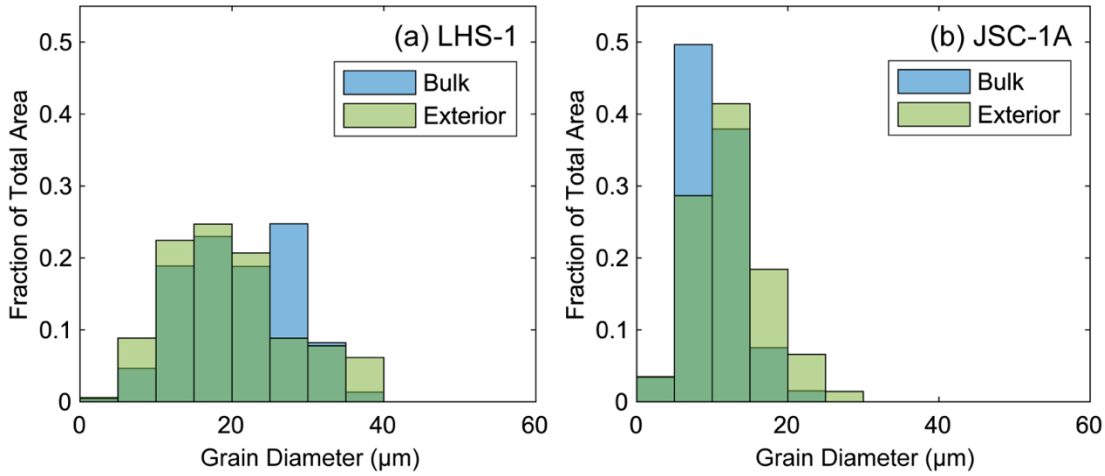

Figure 3.5. Area-weighted histogram of grain diameters (5 μm bins) in the bulk and exterior regions of the crucible for (a) LHS-1 (highlands) and (b) JSC-1A (maria).

Using the bulk region as a baseline, it is clear that YSZ grain coarsening had occurred in the surface region for both regolith simulants. Grain segmentation and size analysis were performed on the grains within surface and bulk regions of both samples. Grains intersecting the map boundaries were not included to avoid skewing the data based on arbitrary locations. An area-weighted histogram of the equivalent grain diameters is presented in Figure 3.6.

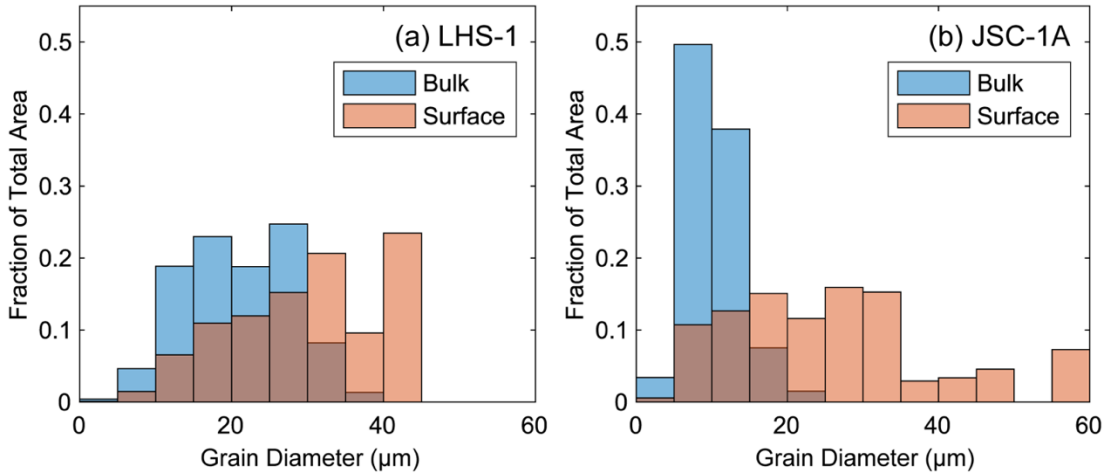

Figure 3.6. Area-weighted histogram of grain diameters (5 μm bins) in the bulk and surface regions of the crucible for (a) LHS-1 (highlands) and (b) JSC-1A (maria).

Grain coarsening occurs in both samples as shown in Figure 3.6. For both regolith simulants, there is a decrease in the fractional area of smaller grains and an increase in the fractional area of larger grains in the surface region compared to the bulk region. In the YSZ/LHS-1 bulk region, grains larger than 30 μm make up ~10% of the area, while in the surface region, grains larger than 30 μm make up ~55% of the area. Additionally, there is a clear decrease in the fractional area of all grain sizes smaller than 30 μm in the surface region compared to the bulk region. In the YSZ/JSC-1A bulk region, there are no grains larger than 25 μm (0% area), but in the surface region, grains larger than 25 μm make up ~50% of the area. Similar to the YSZ/LHS-1 crucible, there is a decrease in the fractional area of all grain sizes smaller than 15 μm in the surface region compared to the bulk region. These results are consistent with the visibly larger grains in the surface regions of Figure 3.4 and indicate that grain coarsening was accelerated in the surface region of both YSZ crucibles. However, JSC-1A cause grain coarsening to occur more quickly compared to LHS-1.

Since the bulk region of YSZ grains underwent the same thermal treatment as the surface region, it is imperative to consider mechanisms that facilitate grain coarsening locally at the YSZ/simulant interface. Large pockets of regolith simulant in the surface region of either crucible are not detected in EDS scans. This suggests that the regolith simulant is penetrating the YSZ crucible wall along the YSZ grain boundaries. This mechanism of grain boundary dissolution and penetration has been observed in YSZ interactions with molten silicates [21,23,24]. The molten regolith simulant increases the diffusivity of Zr and Y along grain boundaries, accelerating the rate at which grains can coarsen compared to the bulk of the YSZ. Furthermore, the YSZ/JSC-1A sample exhibits a higher degree of coarsening, almost certainly due to its lower viscosity at 1600°C. The diffusivities of Zr and Y are expected to be higher in JSC-1A (Section 3.3.2.1), so YSZ grain coarsening should also occur faster than in LHS-1 as a result. Additionally, the lower viscosity of JSC-1A results in a higher degree of penetration into the YSZ material, allowing coarsening to occur deeper into the YSZ material compared to LHS-1.

The grain coarsening behavior in both samples has important implications for the long-term degradation behavior of YSZ in contact with molten regolith simulants. If the molten regolith

simulant is dissolving and penetrating along grain boundaries, then grain coarsening should slow the rate of penetration by reducing the number of grain boundaries at the YSZ/simulant interface. Kowalski et al. investigated the effect of YSZ grain size on molten silicate degradation and found that larger grain sizes can slow the rate of penetration into YSZ significantly; they attribute this behavior to a change in grain boundary density, width, and shape associated with the change in YSZ grain size [25]. Additionally, the authors concluded that for a finite amount of molten silicate and given enough time, the depth of penetration will be equal regardless of the grain size and grain boundary morphology. In containment applications, the amount of molten lunar regolith will be much larger compared to that of the YSZ crucible walls, so the molten lunar regolith will eventually penetrate the YSZ crucible wall and cause crucible failure. However, the Kowalski et al. results suggest that it is possible that YSZ grain coarsening can slow the degradation rate of YSZ and extend the usable life of a YSZ crucible for containing molten lunar regolith.

3.4 Conclusion

High-temperature YSZ degradation by molten lunar regolith simulants was evaluated by powder and crucible experiments. Two different lunar regolith simulants were tested, representing the highlands (LHS-1) and maria (JSC-1A) regions of the lunar surface. Based on the YSZ powder experiments, both molten lunar regolith simulants had a comparable equilibrium solubility for Zr and Y, with JSC-1A having marginally higher solubility for Zr and Y. Two degradation mechanisms were observed in the powder experiments: YSZ dissolution and Y depletion in the YSZ. Based upon YSZ crucible experiments, greater amounts of recrystallized YSZ were observed in the solidified JSC-1A regolith simulant than in LHS-1, indicating that more YSZ had dissolved. However, this increase in YSZ dissolution was not fully accounted for by the marginal difference in Zr and Y solubilities between LHS-1 and JSC-1A. Instead, the higher degradation observed with JSC-1A stemmed from its lower viscosity compared to LHS-1, which was credited to higher FeO and MgO contents that disrupt the silica network at high temperatures. In addition to causing a

higher YSZ dissolution rate, the lower viscosity of the JSC-1A allowed it to penetrate further into the YSZ crucible wall, enabling significant grain coarsening deeper into the sample.

Overall, YSZ crucibles successfully contained both molten lunar regolith simulants at 1600°C for 3 hours, but ultimately cracked on cooldown. This cracking behavior is attributed to the formation of Y-depleted YSZ at the YSZ/simulant interface which undergoes a phase transformation from tetragonal to monoclinic phases. Based on the crucible experiments, YSZ may be well suited for containment or contact with molten lunar highlands regolith for longer times than explored in this work, since the LHS-1 regolith simulant suffered less degradation than JSC-1A. However, the formation of Y-depleted YSZ and subsequent transformation-induced cracking, may limit YSZ to single use applications to support oxygen extraction ISRU processes. The ultimate goal of lunar ISRU for oxygen extraction is to scale up to continuous oxygen production, in which case, YSZ may be a promising containment material for high-temperature processes involving molten lunar regolith such as molten regolith electrolysis and carbothermal reduction.

The results of this chapter support the design and fabrication of a molten regolith electrolysis reactor incorporating a hollow anode design. From the observed degradation mechanisms, it appears that YSZ will survive contact with molten regolith simulants at 1600°C for at least 3 hours. This allows enough time to test the feasibility of YSZ as a solid-state electrolyte in the hollow anode design. Unfortunately, cracking will occur on cooling, so the YSZ must be replaced between electrolysis experiments. Chapter 4 will focus on the design and proof-of-principle testing of a YSZ hollow anode for performing molten regolith electrolysis.

References

[1] K. Morita, C. Wiraseranee, H. Shuto, S. Nakamura, K. Iwasawa, T.H. Okabe, N. Sano, Dissolution behaviour of platinum group metals into molten slags, Min Proc Ext Met 123 (2014) 29–34. https://doi.org/10.1179/0371955313Z.00000000070.

[2] M.S. Humbert, G.A. Brooks, A.R. Duffy, C. Hargrave, M.A. Rhamdhani, Thermophysical property evolution during molten regolith electrolysis, Planet Space Sci 219 (2022) 105527. https://doi.org/10.1016/j.pss.2022.105527.

[3] H. Kim, J. Paramore, A. Allanore, D.R. Sadoway, Electrolysis of Molten Iron Oxide with an Iridium Anode: The Role of Electrolyte Basicity, J Electrochem Soc 158 (2011) E101. https://doi.org/10.1149/1.3623446.

[4] E. Standish, D. Stefanescu, P. Curreri, Ceramics for Molten Materials Containment, Transfer and Handling on the Lunar Surface, in: 47th AIAA Aerospace Sciences Meeting Including The New Horizons Forum and Aerospace Exposition, American Institute of Aeronautics and Astronautics, Orlando, Florida, 2009. https://doi.org/10.2514/6.2009-1657.

[5] S.D. Rosenberg, O. Musbah, E.E. Rice, Carbothermal Reduction of Lunar Materials for Oxygen Production on the Moon: Reduction of Lunar Simulants with Carbon, Lunar and Planetary Science 27 (1996) 1103.

[6] G. Heiken, D. Vaniman, B.M. French, eds., Lunar sourcebook: a user's guide to the moon, Cambridge University Press, Cambridge [England] ; New York, 1991.

[7] Exolith Lab, LHS-1 Lunar Highlands Simulant Fact Sheet (002-01-001-0621), (2021). https://cdn.shopify.com/s/files/1/0398/9268/0862/files/lhs-1-spec-sheet-Dec2022.pptx.pdf?v=1688051876.

[8] D.S. McKay, J.L. Carter, W.W. Boles, C.C. Allen, J.H. Allton, JSC-1: A New Lunar Soil Simulant, in: Engineering, Construction, and Operations in Space IV, American Society of Civil Engineers, Albuquerque, NM, 1994: pp. 857–866. https://www.lpi.usra.edu/lunar/strategies/jsc_lunar_simulant.pdf.

[9] F. Bachmann, R. Hielscher, H. Schaeben, Grain detection from 2d and 3d EBSD data—Specification of the MTEX algorithm, Ultramicroscopy 111 (2011) 1720–1733. https://doi.org/10.1016/j.ultramic.2011.08.002.

[10] C.W. Bale, E. Bélisle, P. Chartrand, S.A. Decterov, G. Eriksson, A.E. Gheribi, K. Hack, I.-H. Jung, Y.-B. Kang, J. Melançon, A.D. Pelton, S. Petersen, C. Robelin, J. Sangster, P. Spencer, M.-A. Van Ende, FactSage thermochemical software and databases, 2010–2016, Calphad 54 (2016) 35–53. https://doi.org/10.1016/j.calphad.2016.05.002.

[11] B.L. Henke, E.M. Gullikson, J.C. Davis, X-Ray Interactions: Photoabsorption, Scattering, Transmission, and Reflection at E = 50-30,000 eV, Z = 1-92, Atom Data Nucl Data 54 (1993) 181–342. https://doi.org/10.1006/adnd.1993.1013.

[12] K. Kato, N. Araki, The corrosion of zircon and zirconia refractories by molten glasses, J Non-Cryst Solids 80 (1986) 681–687. https://doi.org/10.1016/0022-3093(86)90462-X.

[13] M. Ficheux, E. Burov, G. Aquilanti, N. Trcera, V. Montouillout, L. Cormier, Structural evolution of high zirconia aluminosilicate glasses, J Non-Cryst Solids 539 (2020) 120050. https://doi.org/10.1016/j.jnoncrysol.2020.120050.

[14] J. Guo, T. Villalon, U. Pal, S. Basu, Effect of optical basicity on the stability of yttria-stabilized zirconia in contact with molten oxy-fluoride flux, J Am Ceram Soc 101 (2018) 3605–3616. https://doi.org/10.1111/jace.15496.

[15] S. Krämer, J. Yang, C.G. Levi, C.A. Johnson, Thermochemical Interaction of Thermal Barrier Coatings with Molten CaO–MgO–Al_2O_3–SiO_2 (CMAS) Deposits, J Am Ceram Soc 89 (2006) 3167–3175. https://doi.org/10.1111/j.1551-2916.2006.01209.x.

[16] H. Zhao, C.G. Levi, H.N.G. Wadley, Molten silicate interactions with thermal barrier coatings, Surf Coat Tech 251 (2014) 74–86. https://doi.org/10.1016/j.surfcoat.2014.04.007.

[17] J.A. Dominguez, J. Whitlow, Marangoni effect and its potential utilization in supporting lunar habitats and other extraterrestrial endeavors, Adv Space Res 69 (2022) 2259–2267. https://doi.org/10.1016/j.asr.2021.12.023.

[18] R.I. Webster, E.J. Opila, Viscosity of CaO–MgO–Al_2O_3–SiO_2 (CMAS) melts: Experimental measurements and comparison to model calculations, J Non-Cryst Solids 584 (2022) 121508. https://doi.org/10.1016/j.jnoncrysol.2022.121508.

[19] A.R. Cooper, W.D. Kingery, Dissolution in Ceramic Systems: I, Molecular Diffusion, Natural Convection, and Forced Convection Studies of Sapphire Dissolution in Calcium Aluminum Silicate, J Am Ceram Soc 47 (1964) 37–43. https://doi.org/10.1111/j.1151-2916.1964.tb14638.x.

[20] Y.A. Guloyan, O.M. Pustyl'nikov, Physical-chemical interactions during contact between molten glass and refractories, Glass Ceram 67 (2011) 297–303. https://doi.org/10.1007/s10717-011-9283-2.

[21] C.S. Holgate, G.G.E. Seward, A.R. Ericks, D.L. Poerschke, C.G. Levi, Dissolution and diffusion kinetics of yttria-stabilized zirconia into molten silicates, J Eur Ceram Soc 41 (2021) 1984–1994. https://doi.org/10.1016/j.jeurceramsoc.2020.10.056.

[22] R.W. Trice, Y.J. Su, J.R. Mawdsley, K.T. Faber, A.R. De Arellano-López, H. Wang, W.D. Porter, Effect of heat treatment on phase stability, microstructure, and thermal conductivity of plasma-sprayed YSZ, J Mater Sci 37 (2002) 2359–2365. https://doi.org/10.1023/A:1015310509520.

[23] D. Wu, X. Shan, H. Cai, F. Yang, X. Zhao, Grain boundary corrosion mechanism of YSZ thermal barrier oxides under CMAS attack, Corros Sci 209 (2022) 110803. https://doi.org/10.1016/j.corsci.2022.110803.

[24] S. Morelli, V. Testa, G. Bolelli, O. Ligabue, E. Molinari, N. Antolotti, L. Lusvarghi, CMAS corrosion of YSZ thermal barrier coatings obtained by different thermal spray processes, J Eur Ceram Soc 40 (2020) 4084–4100. https://doi.org/10.1016/j.jeurceramsoc.2020.04.058.

[25] B. Kowalski, J. Stokes, P.E. Albert, P.E. Lauer, D.E. Wolfe, Effect of test parameters in the exposure of Ca–Mg–Al–silicate on yttria stabilized zirconia, J Am Ceram Soc 106 (2023) 3911–3921. https://doi.org/10.1111/jace.19025.

Chapter 4

ELECTROLYSIS OF LUNAR HIGHLANDS REGOLITH USING ZIRCONIA-BASED HOLLOW ANODES

The contents of this chapter are also presented in "Improving molten regolith electrolysis with zirconia-based hollow anode technology" by K. Yu, W. West, J. Stokes, B. Harder, L. Reidy, J. Dominguez, and K. T. Faber, which was published in Acta Astronautica in 2025. K. Yu led the experimental portion of this work and wrote the original draft of the manuscript. J. Stokes, B. Harder, L. Reidy, and J. Dominguez provided resources and subject matter expertise to design the experiments and assist in analyzing the results. K. T. Faber supervised the work. All authors were involved in editing the manuscript.

K. Yu, W. West, J. Stokes, B. Harder, L. Reidy, J. Dominguez, K.T. Faber (2025). "Improving molten regolith electrolysis with zirconia-based hollow anode technology". In: *Acta Astronautica* 235, pp. 723-735. DOI: 10.1016/j.actaastro.2025.06.028

4.1 Introduction

This chapter focuses on the evaluation a new type of anode, known as the hollow anode, that can mitigate some of the risks associated with molten regolith electrolysis (MRE), as discussed in the Introduction chapter. The hollow anode is designed to allow for the facile collection of O_2 after it has been produced through MRE. Figure 4.1(a) provides a schematic of the envisioned integration of a hollow anode in a MRE reactor, based on the work of Grossman et al. [1]. The hollow anode contains a solid electrolyte shell and a metallic current collector. Within this design, the goal is to force O^{2-} from the molten regolith to migrate through an oxygen-conducting solid electrolyte to the metallic current collector. Once O^{2-} reaches the current collector, electron transfer can occur, allowing for oxidation of O^{2-} into O_2. The generated O_2 is fully contained within the solid electrolyte shell, enabling the collection of O_2 without contact between the molten regolith and O_2. Additionally, O_2 is now

generated at a solid/solid interface, eliminating the bubble formation challenges discussed earlier. The hollow anode design also prevents any volatile species from contaminating the electrolyzed, high-purity O_2.

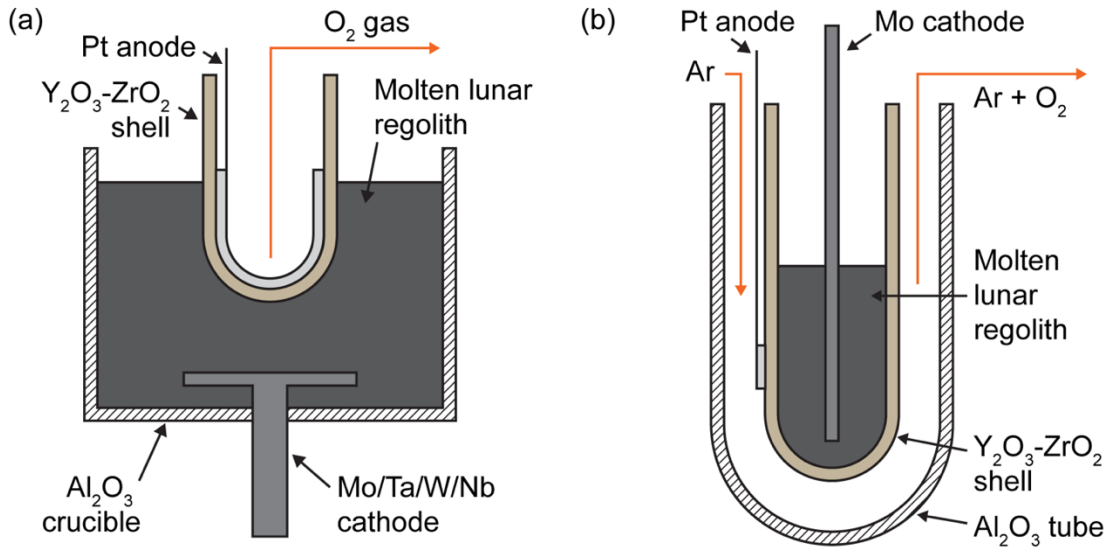

Figure 4.1. Schematic of (a) envisioned integration of hollow anode into existing MRE reactors and (b) inverted hollow anode used to perform proof-of-principle experiments.

The materials used for the hollow anode are yttria-stabilized zirconia (YSZ) for the solid electrolyte shell and Pt for the metallic current collector. YSZ is a well-known oxygen-ion conductor, as well as a refractory oxide ceramic. The results from the Chapter 3 have shown that YSZ demonstrates controlled degradation in contact with molten regolith simulants at 1600°C [2]. Pt is used as the current collector since it is relatively resistant to oxidizing environments at high temperatures [3]. Unlike the Ir anodes discussed in the introductory chapter, the Pt used in the hollow anode does not directly contact molten regolith, avoiding the dissolution of Pt into the molten regolith electrolyte. The combined YSZ/Pt anode shown in Figure 4.1(a) is referred to as the hollow anode.

Anodes with a similar design to the hollow anode have been used previously in lower temperature applications. Guo et al. studied the use of YSZ/Ag anodes in oxy-fluoride fluxes at 1200°C and found that the optical basicity of the oxy-fluoride flux has a significant effect

on YSZ degradation [4]. Gao et al. investigated the use of magnesia-stabilized zirconia (MSZ)/Pt anodes in FeO-containing slags at 1450°C and found that the inclusion of MSZ as a solid electrolyte does not negatively impact the performance of their electrolysis cell [5,6]. Both experiments were performed at lower temperatures than the MRE operational temperature of 1600°C. Moreover, the flux (Ca^{2+}, Mg^{2+}, Si^{4+}, Y^{3+}) or slag (Ca^{2+}, Mg^{2+}, Si^{4+}, Al^{3+}, Fe^{2+}/Fe^{3+}) used contained relatively few cationic species compared to the 10-component molten regolith simulant used in these studies.

This chapter presents the design, fabrication and testing of a laboratory-scale MRE cell, utilizing an inverted hollow anode (Figure 4.1(b)), which successfully demonstrates that MRE can be performed with a hollow anode for up to 12 hours. Residual gas analysis confirms the production of O_2 when potential is applied to the cell. The elemental composition of both the cathodic products and solidified regolith simulant are presented, indicating that FeO and SiO_2 are the primary oxide species being electrolyzed. A FactSage thermochemical model was also built to predict the cathodic products and remaining regolith simulant compositions, which is compared to the experimentally measured compositions from the MRE cells. The results of laboratory-scale testing reveal interactions between YSZ and molten regolith simulant that will be discussed and extended to provide design considerations for a hollow anode in full-scale MRE reactors.

4.2 Materials and methodology

4.2.1 Lunar regolith simulant

The lunar south pole is the targeted landing site for NASA's Artemis missions and could potentially be suitable for a permanent lunar settlement [7]. As a result, MRE experiments were performed on lunar highlands regolith simulant, which is more representative of the regolith at the lunar south pole [8]. LHS-1 (Space Resource Technologies) was selected as the highlands regolith simulant. The composition of LHS-1 [9], and a comparison to lunar highlands regolith returned from Apollo 16 [10], are presented in Table 4.1. Though there are some compositional variations in specific oxides (CaO, MgO, Na_2O), the terrestrially produced LHS-1 is comparable in the major oxides, SiO_2 and Al_2O_3, to the lunar regolith

returned by Apollo 16. It is noted that though Table 4.1 presents the composition using a binary oxide basis, both the lunar regolith and regolith simulant are comprised of mixtures of oxide glasses and minerals. However, MRE seeks to fully melt the regolith to form an ionic liquid electrolyte and does not require the presence of specific minerals, such as ilmenite ($FeTiO_3$) for hydrogen reduction [11].

Table 4.1. Major abundances of LHS-1 simulant and highlands lunar regolith (wt%) [9,10]

Species	SiO_2	FeO	MgO	CaO	Al_2O_3	TiO_2	Na_2O	K_2O	MnO	P_2O_5
LHS-1 (Simulant)	51.2	2.7	1.6	12.8	26.6	0.6	2.9	0.5	0.1	0.1
Apollo 16 (#64501)	45.3	4.2	4.9	17.2	27.7	0.4	0.4	0.1	< 0.1	-

4.2.2 Molten regolith electrolysis experiments

All MRE runs were performed in the inverted hollow anode configuration, shown in Figure 4.1(b). In this design, the YSZ tube functioned as both the primary containment vessel and as the solid electrolyte for O^{2-}. An outer alumina tube was used to isolate the gaseous environment around the cell and acted as a secondary containment vessel. A mass flow controller (FMA series, OMEGA) was used to provide a consistent Ar flow to serve as the carrier gas. The gas outlet was connected to a residual gas analyzer (HPR-20, Hiden Analytical) for compositional analysis to track the production of O_2. The sealed electrolysis reactor was placed into a high-temperature box furnace (Rapid Temp Furnace, CM Furnaces) for heating to the operational temperature. The electrolysis cell was designed such that the lower quarter-portion of the cell containing LHS-1 was exposed to operational temperature, as shown in Figure 4.1(b). The upper portion of the electrolysis reactor with electrical leads, gas fittings, and tube gaskets (not shown) remained near ambient temperature. A potentiostat (VersaStat 4, Princeton Applied Research) was attached to the cathode and anode leads to perform electrolysis. Additional images and details of the electrolysis cell design, fabrication, and shakedown testing are provided in Appendix D.

4.2.2.1 Electrolysis cell fabrication

A custom stainless steel endplate was designed and machined to provide a mounting point for the interior 10.5 wt% YSZ tube and a sealing surface for the exterior alumina tube (McDanel Advanced Material Technologies). The endplate also contained feedthroughs for the cathode, anode, gas inlet tube, and gas outlet tube. To fabricate the electrolysis cell, a YSZ tube was loaded with approximately 20 grams of LHS-1 and mounted onto the endplate. The cathode was an alumina-sheathed Mo rod that was inserted into the center of the endplate and pushed down the YSZ tube through the loose regolith simulant. The anode consisted of a Pt wire mesh that was adhered to the exterior of the YSZ tube with Pt ink (Fuel Cell Store). The gas inlet and outlet tubes were then attached to the endplate. Finally, the entire assembly was lowered into the exterior alumina tube and sealed off by a Viton gasket at the endplate.

4.2.2.2 Electrolysis conditions

MRE was performed for three different durations: 1 hour, 3 hours, and 12 hours. The operational temperature of the electrolysis cell was 1600°C for all three durations. The cell was held at temperature for an additional hour before electrolysis to allow the cell to stabilize. After each electrolysis period, the cell was held at temperature for another hour to perform electrochemical characterization such as cell resistance determination. The thermal profile of all three electrolysis durations is provided in Appendix E (E.1). All experiments were run under 100 sccm of flowing Ar. The experiments were performed with a constant current set at 0.5 A on the potentiostat. The cathode surface area was ~10 cm^2 and the anode pad surface area was ~1 cm^2, giving an anodic current density of ~0.5 A/cm^2. The YSZ tube, LHS-1 regolith simulant, Mo cathode, and Pt anode were replaced between each electrolysis test.

4.2.3 Characterization

The geometry of the MRE cells was designed to allow for characterization of all heated cell components, including the YSZ solid electrolyte, cathodic products, and solidified regolith simulant, after each experiment. After cooling, each cell was mounted in epoxy and cross-

sectioned down the middle of the cell. One half of each cell was polished to 0.05 μm to prepare for subsequent characterization.

4.2.3.1 Optical microscopy

All cells were optically imaged at 30x (VHX-7000, Keyence) and stitched together to capture macroscopic changes resulting from high-temperature operation and electrolysis. Further investigation of regions of interest was performed at 50x – 200x (VHX-2000, Keyence). These regions provided guidance for higher-magnification electron microscopy. ImageJ was used to measure YSZ wall recession from these images [12].

4.2.3.2 Electron microscopy

Scanning electron microscopy (SEM; 1550VP FESEM, ZEISS) was used with the backscattered electron (BSE) detector to image the cathodic products and solidified regolith simulant within each cell. BSE image brightness was determined by the average atomic number of the elements present, with lighter elements appearing darker. Since O has a low atomic number, BSE images can provide an initial analysis of which regions were metallic (the cathode and cathodic products) vs. oxide (the remaining LHS-1). Energy dispersive X-ray spectroscopy (EDS; X-Max EDS, Oxford Instruments) was used to assess the elemental composition of the cathodic products and solidified regolith simulant using EDS mapping and point analysis.

Beyond SEM and EDS, electron backscatter diffraction (EBSD; HKL EBSD, Oxford Instruments) was used to determine the grain structure and phase of YSZ. Specifically, regions of YSZ in contact with molten regolith were analyzed to elucidate the compositional and microstructural changes of YSZ for each electrolysis cell. Each EBSD analysis region was 300 μm wide (along a YSZ/LHS-1 interface) and 700 μm deep (from YSZ/LHS-1 interface into YSZ interior) with a 1.5 μm step size. All electrolysis cells and a polished fragment of the beginning-of-life (BOL) YSZ were analyzed using EBSD. MTEX, an EBSD analysis software package, was used for grain segmentation and grain size analysis on the collected EBSD maps to provide statistical data on grain sizes [13].

4.2.3.3 Raman spectroscopy

A confocal Raman microscope (inVia Raman, Renishaw) was used on the center of the YSZ walls to qualitatively determine the effect of extended electrolysis on YSZ. All electrolysis cells and a fragment of the BOL YSZ were characterized by Raman spectroscopy. For this analysis, a 20x lens was used with 10% laser power, a 30-second acquisition time, with three total accumulations. Background subtraction was performed using the WiRE software package (Renishaw). The resulting data were normalized for intensity by MATLAB.

4.2.3.4 FactSage analysis

FactSage 8.3 was used to construct a thermochemical model for the removal of O_2 from molten lunar regolith at 1600°C [14]. The LHS-1 composition from Table 4.1 was input as the initial composition for the system, totaling 1 gram. The FToxid and FTlite databases were used to determine the equilibrium slag (regolith simulant) and metal (cathodic products) compositions, respectively. Data for all solid and liquid solutions/compounds containing the species in Table 4.1 were added from both the FToxid and FTlite databases; however, only the slag and liquid metal phases were predicted to be thermodynamically stable at 1600°C. The goal of this FactSage analysis was to predict the compositional variations of the molten regolith and cathodic products with increasing electrolysis duration. Thus, the gas phase was omitted to reduce the model computation time. The basis for O_2 removal was extraction efficiency and was defined as the mass of O_2 produced divided by the mass of regolith. The model was used to generate the equilibrium slag and metal compositions from an extraction efficiency of 0% (representing BOL) to 5%, in 0.1% increments. This was accomplished by setting O_2 as a variable species and allowing it to vary from 0 to -0.05 grams, representing 0% and 5% extraction efficiency. It is noted that these results do not account for the kinetics of electrolysis and are only able to determine the thermodynamic equilibrium composition assuming that O_2 is removed from the system. As a result, Mo (cathode) and YSZ/Pt (anode) were not included in this analysis since their dissolution into the molten LHS-1 is a kinetically limited process.

4.3 Results

4.3.1 Electrolysis data

The volumetric percentage of O_2 in the outlet gas stream and the potential required to maintain 0.5 A of current through the cell are presented in Figure 4.2. Elapsed time in these plots is counted from the application of constant current to the cell. In all cells, the O_2 content increases from ~0.005 vol% (background O_2) to ~1 vol% within a few minutes of starting electrolysis. The constant current condition was applied for 1 hour, 3 hours, and 12 hours. The time at which the potential curve terminates denotes the end of electrolysis. Within a few minutes of ending electrolysis, the O_2 content decreases to ~0.005 vol%. These results indicate that O_2 is being produced when current is applied to the cell, providing a proof-of-principle validation that MRE can be performed through the YSZ solid electrolyte and demonstrating that the hollow anode design is feasible.

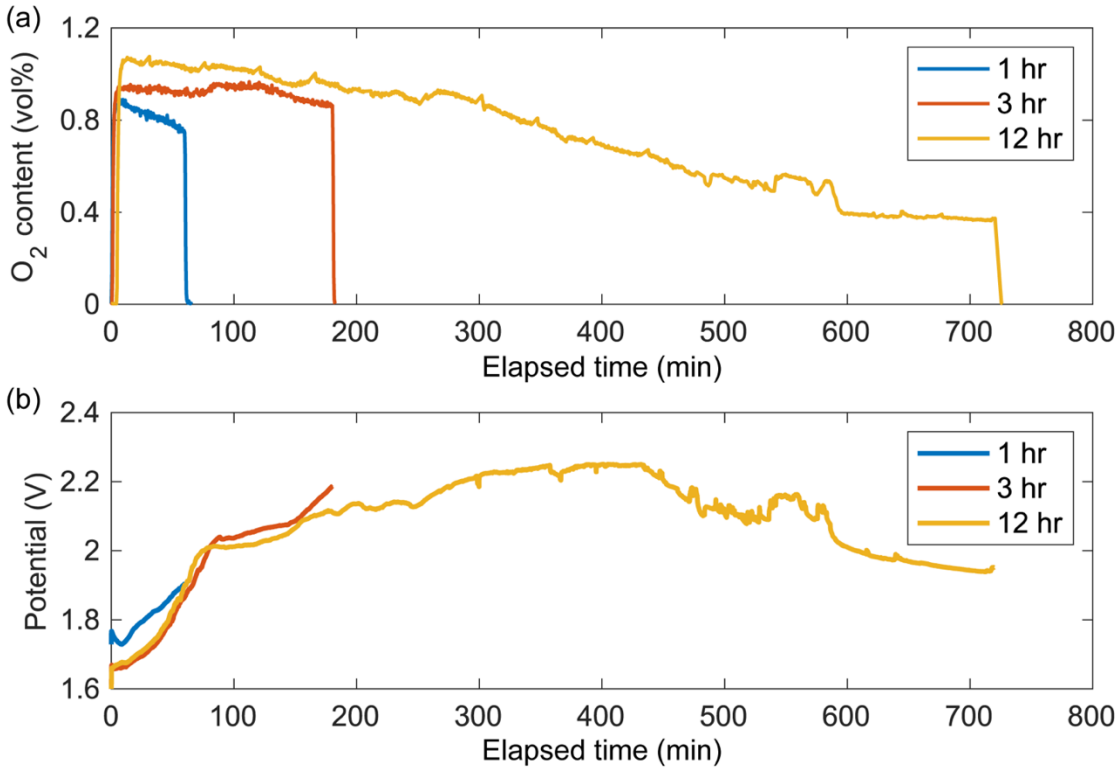

Figure 4.2. (a) O_2 content of outlet gas stream and (b) potential across electrolysis cell vs. elapsed time since electrolysis start for all three electrolysis experiments.

The initial potential behavior for the three electrolysis cells is comparable, suggesting that the electrolysis cell fabrication procedure is robust. All three cells exhibited an increase in potential over the first ~80 minutes of operation. In this initial period, the expected cathodic reaction is the reduction of Fe^{2+}/Fe^{3+}, coming from FeO/Fe_2O_3 in the regolith. The increase in potential is attributed to two factors: the mass transport limitation of FeO/Fe_2O_3 and the increase in regolith viscosity. When electrolysis first occurs, the molten regolith is well-mixed, with FeO/Fe_2O_3 available at the cathode surface for reduction. As electrolysis continues, the FeO/Fe_2O_3 concentration near the cathode surface is depleted as it is reduced to Fe^0, requiring a larger potential to cause FeO/Fe_2O_3 to migrate to the cathode. In addition to this effect, FeO/Fe_2O_3 is also a glass network modifier which increases regolith viscosity with decreasing concentration [15]. Thus, as FeO/Fe_2O_3 is depleted from the molten regolith, the viscosity of the remaining molten regolith increases, which requires the potential to

further increase in order to maintain a consistent rate of FeO/Fe_2O_3 diffusion to the cathode surface.

In the 3-hour and 12-hour electrolysis cells, there is an inflection point in the potential curve at approximately 90 minutes. Based on FactSage predictions (Section 4.3.4), this inflection point is an indication that nearly all the FeO/Fe_2O_3 in LHS-1 has been electrolyzed. After this point, Si^{4+} reduction, from SiO_2, becomes the dominant cathodic reaction, which is consistent with previously reported models [16]. Due to the significantly higher concentration of SiO_2 compared to FeO in LHS-1, the limitation on mass transport is diminished, causing the potential to increase at a slower rate after the inflection point. In contrast to FeO/Fe_2O_3, SiO_2 is a glass network former. The continued removal of SiO_2 through electrolysis causes the regolith viscosity to decrease, thereby increasing the diffusivity of cations in the remaining regolith, allowing more SiO_2 to diffuse to the cathode surface. These two effects result in a slower increase in the potential applied after the inflection point in both the 3-hour and 12-hour electrolysis cells.

The 12-hour electrolysis cell potential alone indicates that its slower rate of increase continues until ~420 minutes (7 hours) of electrolysis. At this point, the potential starts to decrease and contains more noise. The decrease in potential is associated with a lower cell resistance, which is attributed to the onset of electronic conductivity in YSZ and will be discussed in more detail in Section 4.3.5.2. The noise in the data is attributed to the expanding cathodic products. As more cathodic products are generated, its volume increases until an electronic short between the cathode and the YSZ wall is formed. Since the cathodic products are liquid at operational temperature, the noise in the potential originates from shorts forming and disappearing as the liquid cathodic products are repositioned by natural convection within the cell.

In all three electrolysis experiments, the highest O_2 content measured occurs at the start of electrolysis and decreases over time. This behavior is also attributed to the onset of electronic conductivity in YSZ and is discussed in more detail in Section 4.3.5.2 [17–19]. As YSZ becomes more electronically conductive, O_2 is not solely generated on the exterior of the

YSZ but can also be generated on the interior of the inverted hollow anode. The gas outlet tube samples from the exterior of the YSZ. Any O_2 that is produced on the interior of the cell will likely oxidize the exposed portion of the alumina-sheathed Mo cathode. Evidence of this behavior has been observed in the interior of the YSZ (Appendix E.2). The oxidation of Mo produces volatile MoO_x, which then condenses in cold regions of the cell. Therefore, it is assumed that the O_2 measured by the residual gas analyzer is the lower bound of O_2 produced since it cannot detect the Mo oxidation products that have condensed on cold spots in the electrolysis cell.

The volume of O_2 produced can be calculated by integrating the O_2 content data with a known gas flow rate from the mass flow controller. The electrolysis duration can be used in conjunction with the known current applied to the cell to calculate the total charge transferred during electrolysis. The anodic half-reaction is assumed to be:

$$2\ O^{2-} \rightarrow O_{2(g)} + 4\ e^-$$

The total charge transferred can be used to determine the maximum O_2 that could be produced by assuming that every e^- participates in the Faradaic reaction. The anodic Faradaic efficiency then can be calculated by dividing the measured O_2 produced by the theoretical maximum O_2 produced. Extraction efficiency is defined as the mass of O_2 produced divided by the mass of regolith processed, with the maximum possible extraction efficiency for LHS-1 being approximately 46%. A summary of the aforementioned calculations and experimental measurements for each electrolysis experiment is presented in Table 4.2.

Table 4.2. Summary of cathodic products and regolith electrolysis efficiencies

Electrolysis duration	Cathodic products observed	Anodic Faradaic efficiency	Mass of O_2 produced	Extraction efficiency
1 hr	Fe	47%	0.070 g	0.4%
3 hr	Fe, P, Si	53%	0.237 g	1.2%
12 hr	Fe, P, Si, Ti, Mn	42%	0.749 g	3.7%

Hollow anodes incorporating an ideal O^{2-} ion conductor as the solid electrolyte would result in a Faradaic efficiency of 100% since the solid electrolyte blocks e^- transport. However, the onset of electronic conductivity in the YSZ used in these experiments causes the Faradaic efficiency to be lower than 100% since e^- are no longer blocked. Despite this behavior, the calculated anodic Faradaic efficiencies are in line with those reported in studies utilizing a bare Ir anode instead of a hollow anode. Sirk et al. performed MRE with a Mo cathode and Ir anode, reporting Faradaic efficiencies of approximately 30-60% when electrolyzing an FeO-containing molten regolith [20]. This suggests that the increased electronic conductivity of YSZ does not significantly reduce the Faradaic efficiency of MRE when compared to an Ir anode. However, it is noted that the inclusion of YSZ as a solid electrolyte may require a higher overpotential compared to an exposed Ir anode.

4.3.2 Cathodic products

Optical microscope images of each electrolysis cell and EDS elemental maps of the cathodic products generated in each electrolysis cell are presented in Figures 4.3 (1-hour electrolysis), 4.4 (3-hour electrolysis), and 4.5 (12-hour electrolysis). A quantitative EDS point analysis of each region is provided in Appendix E (E.3 – E.5). The observed cathodic products are also summarized in Table 4.2. The EDS maps presented consist of the observed cathodic products, except for O and Al. Al_2O_3 is not able to be electrolyzed at these durations, so the O and Al maps are provided as an indication of the position of the remaining regolith in each EDS region.

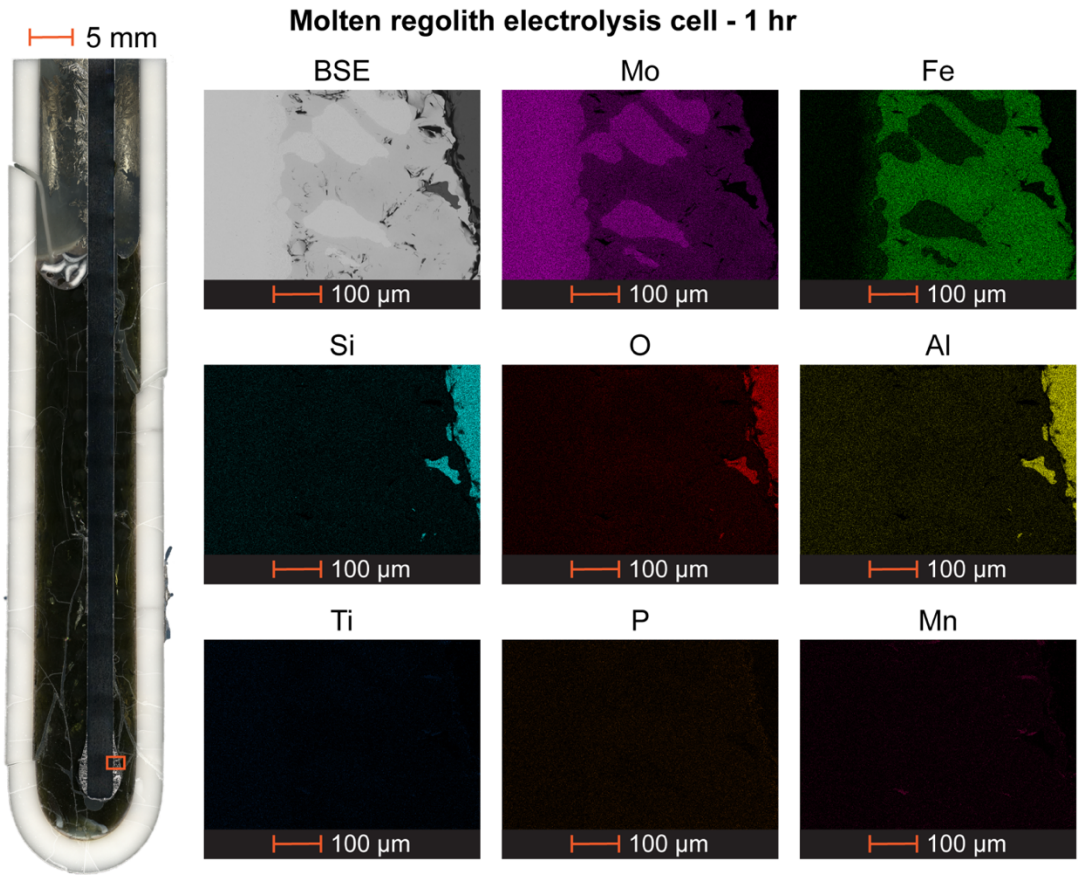

Figure 4.3. Optical microscopy of the 1-hour electrolysis cell and EDS elemental maps of the cathodic products generated. EDS analysis area is denoted with the orange box in the optical microscope image.

The EDS analysis for the 1-hour electrolysis cell indicates that Fe is the primary cathodic product. Figure 4.3 shows that there is a significant amount of Fe detected in the cathodic products, and it has alloyed with Mo from the cathode. The O EDS map in Figure 4.3 suggests that the Fe detected is Fe^0, not FeO/Fe_2O_3, since no O was detected in the cathodic products. The Fe and Mo maps also indicate that there are two different Fe-Mo alloys within the cathodic products. However, the bulb shape of the cathodic products (Figure 4.3) indicates that it is liquid at operational temperature, and likely phase separates on cooling, which is consistent with the Fe-Mo phase diagram [21]. No Si is detected within the cathodic

products, which demonstrates that SiO_2 electrolysis has not been achieved in the 1-hour electrolysis cell.

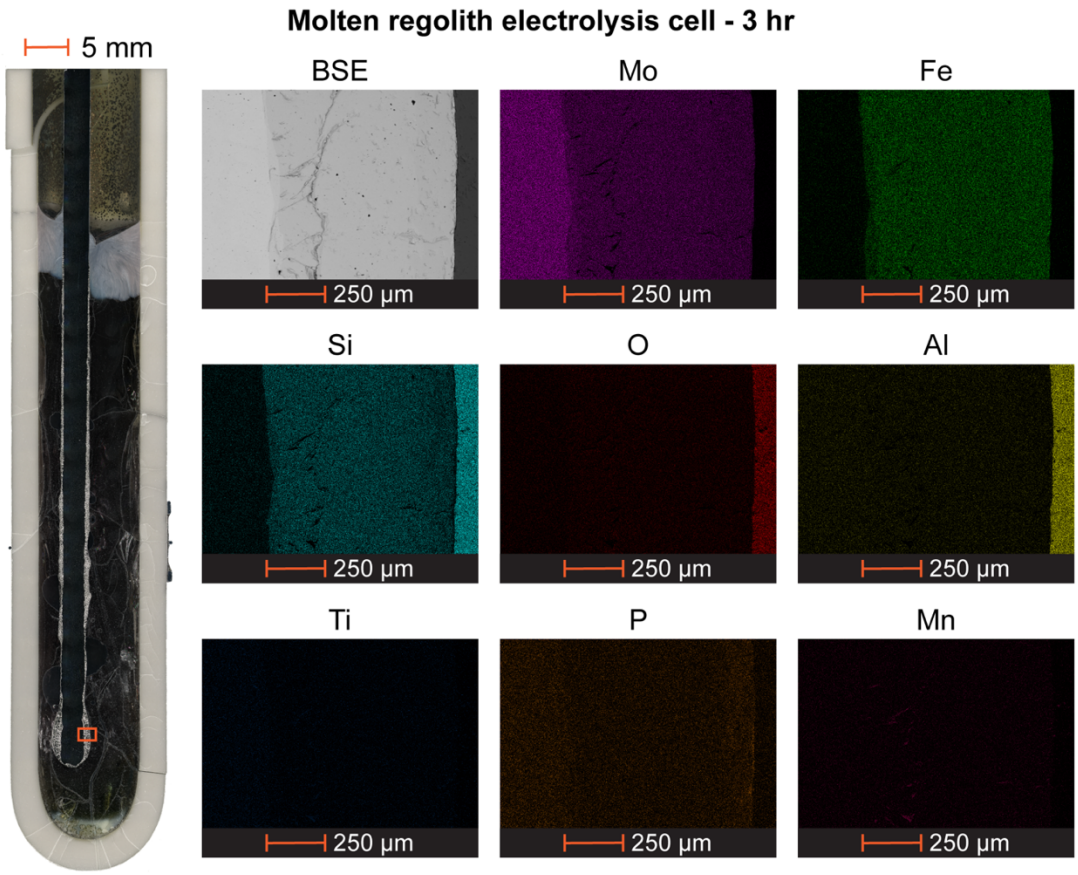

Figure 4.4. Optical microscopy of the 3-hour electrolysis cell and EDS elemental maps of the cathodic products generated. EDS analysis area is denoted with the orange box in the optical microscope image.

In contrast to the 1-hour electrolysis cell, EDS maps of the 3-hour electrolysis cell (Figure 4.4) show the presence of both Fe and Si in the cathodic products. Additionally, there is a detectable amount of P observed in the cathodic products. The Fe, Si, and P are also alloyed with Mo from the cathode. However, unlike the 1-hour cell (Figure 4.3), there does not appear to be significant phase separation in the cathodic products, indicating that the overall composition of the cathodic products is stable down to ambient temperature. The observation of Si in the cathodic products is significant since it indicates that SiO_2 electrolysis is being

performed. To the authors' awareness, this is the first reported experimental confirmation of Si production from the direct electrolysis of a molten lunar regolith simulant. Given that SiO_2 is the most abundant oxide species in LHS-1, this result provides a path for MRE with a hollow anode to achieve O_2 extraction efficiencies up to 25%.

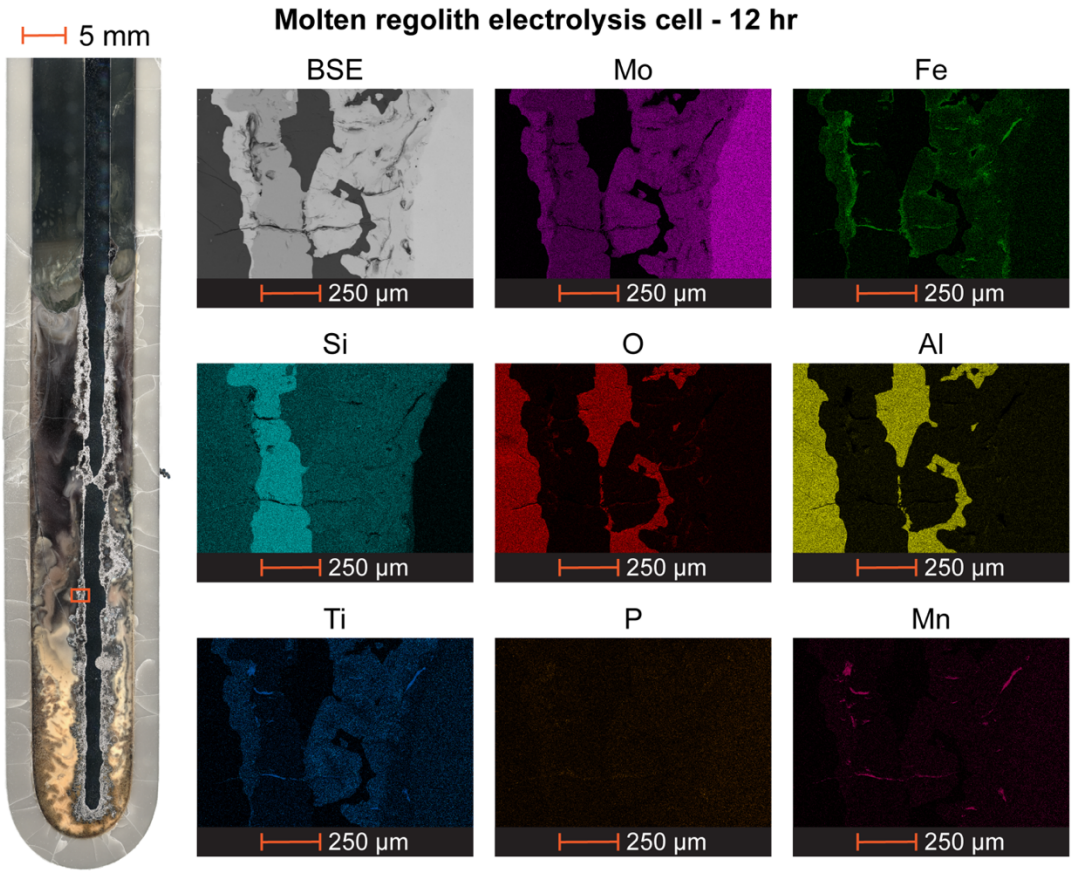

Figure 4.5. Optical microscopy of the 12-hour electrolysis cell and EDS elemental maps of the cathodic products generated. EDS analysis area is denoted with the orange box in the optical microscope image.

The cathodic products within the 12-hour electrolysis cell no longer form a dense film along the cathode surface and have begun migrating away from the cathode. Due to the cell design, there is likely a thermal gradient within the molten regolith. The top of the molten regolith is expected to be cooler since it can radiate to the cold side of the electrolysis cell. The separation of the cathodic products from the cathode is attributed to the growing size of the

liquid cathodic products layer. This results in a layer thickness that exceeds the flow boundary layer induced by convection from a thermal gradient, causing the cathodic products to be mixed with the remaining molten regolith.

Within the cathodic products, Ti and Mn are observed in addition to the previously observed Fe, Si, and P from the shorter duration electrolysis experiments. There is also now significant Si produced, such that Si in the cathodic products has a higher concentration (brighter in Si EDS map) than Si remaining in the molten regolith. A lower concentration of P is detected in the 12-hour electrolysis cell compared to the 3-hour electrolysis cell. Based on FactSage calculations (see Section 4.3.4), it is expected that P_2O_5 electrolysis occurs simultaneously with FeO reduction. Thus, by the end of the 3-hour electrolysis experiment, most of the P_2O_5 is likely already electrolyzed. The lower concentration of P in the 12-hour cell is attributed to dilution of the cathodic products with the continued production of Si.

The production of fully reduced cationic components from the molten regolith is expected for MRE. The presence of these reduced species in all three electrolysis cells provides further validation beyond O_2 production that MRE can be performed through a YSZ solid electrolyte. Though the production of these cathodic products is not the focus of the present study, it is important to confirm that the presence of YSZ at the anode does not significantly alter the expected cathodic half-reactions that balance the anodic half-reaction of O_2 production.

4.3.3 Solidified regolith analysis

Extended electrolysis of molten regolith alters the regolith composition since specific oxides in the regolith are preferentially reduced. The changing regolith (electrolyte) composition can cause both the thermophysical properties (i.e. viscosity, density, etc.) and the electrical conductivity to vary from the beginning-of-life (BOL) LHS-1 properties. The average solidified LHS-1 composition for each of the three electrolysis cells was measured using EDS. The BOL composition of the molten LHS-1 when exposed to 1600°C in a YSZ crucible from Chapter 3 is included [2]. A comparison between the BOL composition and the post-electrolysis composition for each electrolysis experiment is presented in Table 4.3.

Table 4.3. Average regolith composition after melting and electrolysis (at%)

Species	Si	Fe	Mg	Ca	Al	Ti	Na	K	Y	Zr	O
BOL [2]	18.17	1.01	1.32	5.36	11.68	0.23	1.87	0.31	0.24	0.60	59.20
1 hr	18.21	0.47	1.30	5.23	11.70	0.22	1.90	0.32	0.17	0.47	60.01
3 hr	18.06	0.04	1.45	5.87	12.41	0.22	1.87	0.31	0.24	0.63	58.91
12 hr	15.23	0.00	1.78	7.21	12.95	0.17	2.32	0.34	0.37	0.66	58.97

The composition changes detected in LHS-1 are consistent with the observed cathodic products. A clear decrease in Fe concentration is detected from BOL to 12 hours of electrolysis, which is expected since Fe is electrolyzed across all three electrolysis experiments. A minor reduction in the Si concentration is detected in the 3-hour electrolysis cell and becomes a significant reduction in the 12-hour electrolysis cell, consistent with the continued electrolysis of SiO_2. The Ti concentration is consistent with BOL across the 1-hour and 3-hour electrolysis results but begins to decrease in the 12-hour electrolysis result, also consistent with the observation of Ti in the cathodic products of the 12-hour electrolysis result. Across all electrolysis experiments and the BOL specimen, Y and Zr are detected due to the dissolution of YSZ by molten regolith. This is discussed in further detail in Section 4.3.5.1.

4.3.4 FactSage thermochemical results

The FactSage thermochemical predictions of O_2 removal from LHS-1 are presented in Figure 4.6. At 0% extraction efficiency (no O_2 removed from regolith), the only thermodynamically stable phase is the molten regolith, as expected at BOL. Figure 4.6(a) presents only the species that are major components of the regolith (Ca, Al) or are involved in electrolysis (Fe, Si, Ti). O is omitted from Figure 4.6(a) for the sake of clarity but is approximately 60 at% throughout the electrolysis. As the extraction efficiency is increased, cathodic products begin to form in low absolute mass quantities. In Figure 4.6(b), the normalized composition of cathodic products is presented. There is significant variation in the elemental composition of

the cathodic products at low O_2 extraction efficiencies that is attributed to the relatively small mass of cathodic products that initially forms compared with the regolith. The full dataset of FactSage predictions is provided in Appendix E (E.6 – E.7).

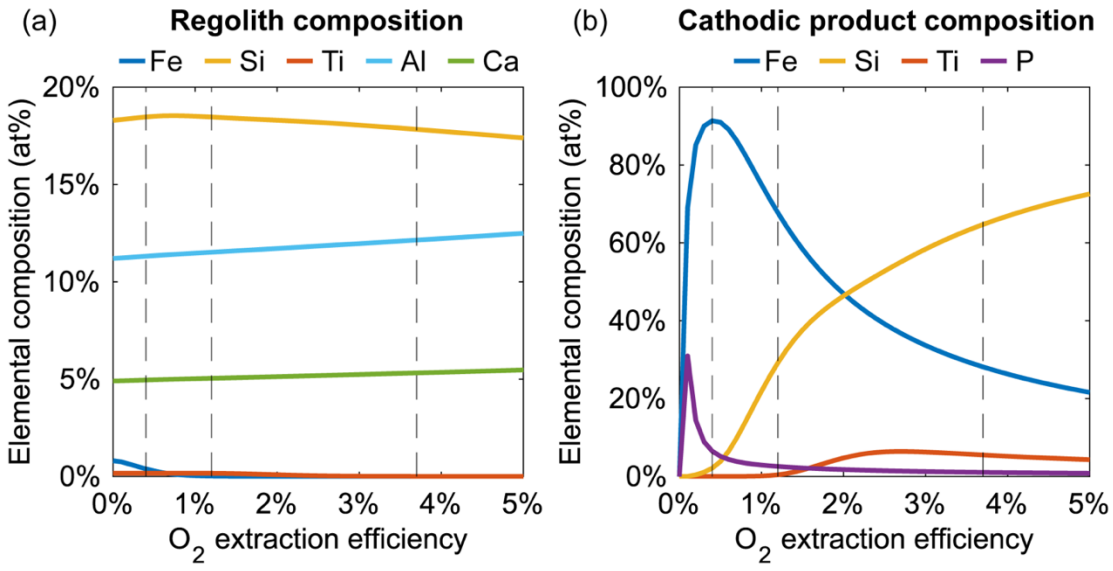

Figure 4.6. FactSage predictions of (a) the percent atomic elemental composition of the remaining regolith and (b) the cathodic products composition vs. O_2 extraction efficiency. Dashed vertical lines in (a) and (b) represent the O_2 extraction efficiency achieved in the 1-hour (0.4%), 3-hour (1.2%), and 12-hour (3.7%) electrolysis cells.

These FactSage predictions generally agree with experimental observations, even though YSZ was not included in the FactSage model. Based on the results in Figure 4.6(a), it appears that the switchover between predominantly FeO electrolysis to predominantly SiO_2 electrolysis occurs near an O_2 extraction efficiency of 1%. This is consistent with the observation that Si is not present in the cathodic products of the 1-hour electrolysis cell but is present in the cathodic products of the 3-hour electrolysis cell where the electrolysis cell achieved an O_2 extraction efficiency of 1.2%. Similarly, TiO_2 electrolysis is not predicted until an O_2 extraction efficiency of approximately 2%, which agrees with the experimental observation that Ti is not detected in cathodic products until the 12-hour electrolysis cell, which achieved an O_2 extraction efficiency of 3.7%. These results also provide further

evidence that the inclusion of YSZ as a solid electrolyte does not significantly impact which oxides are electrolyzed during MRE.

4.3.5 YSZ interactions

4.3.5.1 Thermochemically-induced interactions

The findings presented in Chapter 3 demonstrated that YSZ exhibits thermochemical interactions when in contact with molten regolith simulants, which result from two mechanisms – the dissolution of YSZ and the depletion of Y_2O_3 from YSZ [2]. It is expected that both mechanisms are occurring in the electrolysis cells and will eventually lead to YSZ failure in long-term electrolysis experiments. Thus, it is paramount to investigate the rates of dissolution to provide guidance for design lifetimes of YSZ hollow anodes in a MRE environment.

Evidence of YSZ dissolution is observed in the three electrolysis cells. Table 4.3 shows that Y and Zr are both detected in the solidified LHS-1, indicating that YSZ is dissolving into the molten LHS-1 at operational temperatures. YSZ dissolution by molten silicates is well studied and has been observed in other systems [22]. In Chapter 3, it was shown that the equilibrium solubility of Y and Zr in LHS-1 at 1600°C is approximately 1.4 at% and 1.2 at%, respectively [2]. The measured concentrations of Y and Zr in these electrolysis cells are lower than the solubility limit, which is expected. These experiments were cooled slowly and compared to the quenching experiments used to determine the equilibrium solubility of Y and Zr. As a result, the YSZ dissolved into molten LHS-1 is able to nucleate and grow within the molten regolith as the temperature is decreased. Such YSZ particles are observed at the bottom of the 1-hour and 3-hour cells in Figures 4.3 and 4.4. The tan-colored opacity observed in the bottom half of the 12-hour electrolysis cell (Figure 4.5) is also due to YSZ particles that have nucleated from the molten LHS-1 on cooling. EDS maps of YSZ particles from all electrolysis cells are provided in Appendix E (E.8 – E.10).

Furthermore, YSZ wall recession is observed in these electrolysis cells due to dissolution. The recession only occurs where YSZ is in contact with molten LHS-1. Using the portion of

YSZ that remains above the molten regolith liquid line as a baseline for the original wall thickness, wall recession is calculated for the YSZ in contact with molten LHS-1. The average wall recession is determined for each electrolysis experiment and summarized in Table 4.4. The electrolysis durations and the time spent at 1600°C are both provided in Table 4, since it is thermal exposure to molten LHS-1, and not electrolysis itself, that causes YSZ dissolution.

Table 4.4. YSZ wall recession due to dissolution by molten LHS-1

Electrolysis duration	Time at 1600°C	YSZ recession (μm)
1 hr	3 hr	22 ± 10
3 hr	5 hr	54 ± 12
12 hr	14 hr	85 ± 19

Based on the data in Table 4.4, it appears that the rate of YSZ wall recession is slowing with increasing time in contact with molten LHS-1 at 1600°C. This result suggests that there are additional effects slowing the rate of YSZ dissolution. Kowalski et al. evaluated varying YSZ grain sizes when exposed to molten silicates similar in composition to the molten LHS-1 in this study [23]. They showed that the grain size of YSZ can influence the rate of penetration and dissolution, with larger grains being preferred for minimizing silicate penetration [23]. To better understand YSZ in the current study, EBSD was performed at the YSZ/LHS-1 interface in each cell to generate a grain microstructure map. Additionally, the same EBSD analysis was applied to a piece of YSZ that was not exposed to molten LHS-1 to serve as the BOL reference. The EBSD results are summarized in a grain size histogram, provided in Figure 4.7.

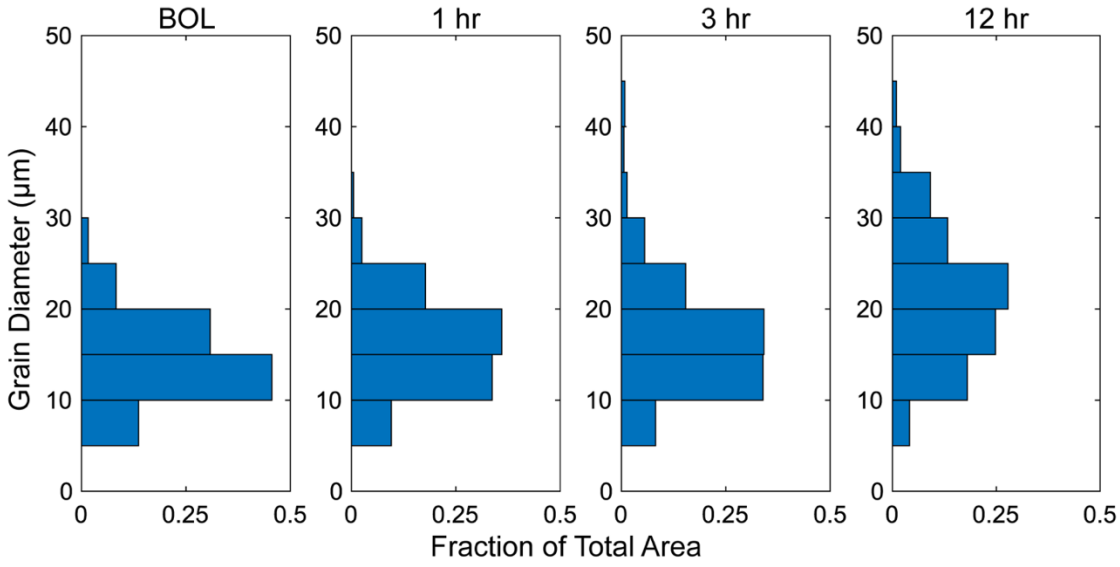

Figure 4.7. Area-weighted histogram of YSZ grain diameters (5 μm bins) at beginning-of-life (BOL), 1-hour electrolysis, 3-hour electrolysis, and 12-hour electrolysis.

From Figure 4.7, it is clear that grain coarsening is occurring. The molten LHS-1 is penetrating along YSZ grain boundaries and increasing the effective diffusivity of Y_2O_3 and ZrO_2 along grain boundaries, allowing for coarsening to occur. Increasing durations in contact with molten LHS-1 at 1600°C pushes the average grain diameter to larger values. The slowing of YSZ dissolution is attributed to the grain coarsening behavior discussed here.

It is noted that all three electrolysis cells exhibit YSZ cracking on cooling (seen in Figures 4.3, 4.4, and 4.5). The cracking was observed on the exterior of the cell prior to cross-sectioning. After cross-sectioning, optical and electron microscopy of each cell shows no evidence of regolith penetration along the cracks in the YSZ. These results suggest that the YSZ is cracking on cooling, specifically below the temperature at which LHS-1 solidifies, since cracking while LHS-1 is still liquid would cause the regolith to seep through the YSZ along cracks. This behavior is consistent with what was observed in Chapter 3 using YSZ crucibles to contain LHS-1 [2].

The cause of YSZ cracking is due to Y_2O_3 depletion from the YSZ. Pure ZrO_2 undergoes a monoclinic-to-tetragonal phase transition between 800°C – 1100°C [24]. Y_2O_3 is a common

stabilizer used to suppress this phase transition and allows YSZ to survive thermal cycling. However, exposure to molten regolith causes Y_2O_3 to diffuse out of YSZ and into the molten regolith, forming a YSZ region that is depleted of the Y_2O_3 stabilizer [2]. Due to the low stabilizer content, the YSZ in this region undergoes the tetragonal-to-monoclinic phase transition on cooling. It is this phase transition that causes the YSZ to crack on cooling.

As further evidence, Table 4.3 shows that average measured concentrations of Y and Zr in the solidified LHS-1 are 0.26 at% and 0.59 at%, resulting in a ratio of Y:Zr of approximately 0.44. In contrast, the ratio of Y:Zr in YSZ at BOL is approximately 0.1, significantly lower than what is observed in the molten regolith. To achieve the 0.44 ratio measured, Y_2O_3 must be preferentially diffusing out of the YSZ. The EBSD analysis used to determine grain sizes can also provide the crystallographic phase of YSZ and reveals that there is an approximately 100 μm thick layer of YSZ that is monoclinic at the YSZ/LHS-1 interface. EBSD phase maps of YSZ are provided in Appendix E (E.11). The presence of monoclinic YSZ at the interface provides further evidence of Y_2O_3 depletion and reveals the cause of YSZ cracking.

4.3.5.2 Potential-induced interactions

All the electrolysis cells exhibited a decrease in cell resistance after their respective electrolysis periods, with longer durations causing a larger decrease in resistance. A summary of cell resistances is presented in Table 4.5. There are three contributing factors to the changes in cell resistance: an increase in cathodic surface area, changes in regolith viscosity/conductivity, and the onset of electronic conductivity in YSZ. The cathode surface is already significantly larger than the anode (~10 cm^2 vs ~1 cm^2) at BOL, so an increase in the cathode surface area, resulting from the evolution of liquid cathodic products, is unlikely to cause the magnitude of cell resistance changes observed. The regolith viscosity is inversely related to the regolith electrical conductivity. In the 1-hour electrolysis cell, the removal of FeO/Fe_2O_3 is expected to increase the regolith viscosity, decrease the regolith conductivity, and cause the cell resistance to increase if the regolith viscosity is the dominant factor affecting the cell resistance. However, the data in Table 4.5 reveals that a resistance decrease is observed in the 1-hour electrolysis cell, indicating that regolith conductivity is not the

dominant factor in cell resistance. Thus, the resistance decrease is attributed to the onset of electronic conductivity in the YSZ.

Table 4.5. Cell resistances at 1600°C before and after electrolysis

Electrolysis duration	Initial resistance	Final resistance	% Change
1 hr	1.54 Ω	1.44 Ω	-6.5%
3 hr	1.59 Ω	1.12 Ω	-29.6%
12 hr	1.46 Ω	0.78 Ω	-46.6%

It has been reported in literature that YSZ can have a significant electronic conductivity in low pO_2 environments and/or under an applied DC bias [17–19]. The MRE cell environment exposes YSZ to both conditions, in addition to a higher temperature than typical YSZ applications require. The combination of these factors leads to a high concentration of O^{2-} vacancies forming within the YSZ crystal structure, which can interact with the electrons in the crystal structure to form *F* centers, creating a reduced YSZ structure. These *F* centers give rise to electron states within the band gap of YSZ, allowing high electronic conductivity to exist in a material that is typically an electron insulator [25]. The decrease in cell resistance is a result of this behavior. As a DC bias is applied at 1600°C, more O^{2-} vacancies are formed, allowing for more electron states to open within the band gap of the YSZ, increasing the electronic conductivity of YSZ. This behavior is exacerbated with increasing duration of applied DC potential, thereby resulting in a lower cell resistance (Table 4.5) with increasing electrolysis duration.

The formation of *F* centers in YSZ not only increases the electronic conductivity of YSZ but also manifests as a darkening in the color of YSZ [25,26]. This effect was also observed in the cells. In Figures 4.3, 4.4, and 4.5, the optical image of the electrolysis cells shows a clear darkening of YSZ from white to gray as the electrolysis duration is increased.

Hastak et al. demonstrated that Raman spectroscopy can be used to qualitatively determine the difference in O^{2-} vacancy concentration of YSZ at varying degrees of reduction [27]. Specifically, the A_{1g} Raman mode becomes broader and lower in intensity as the O^{2-} vacancy concentration increases, while the E_g Raman mode is relatively unaffected [27]. Raman spectra of the YSZ in all three electrolysis cells, as well as a BOL sample, are presented in Figure 4.8. The A_{1g} (260 cm^{-1}) and E_g (640 cm^{-1}) Raman modes are labeled in Figure 4.8. The Raman spectra are normalized to the intensity of the E_g peak, which is denoted with the horizontal dashed line for each of the spectra. The associated labels summarize the intensity of the A_{1g} peak relative to the E_g peak.

The reduction in A_{1g} peak intensity was also observed in the YSZ of the electrolysis cells. The highest intensity YSZ A_{1g} peak occurs in the BOL sample, which has not been reduced or exposed to the MRE conditions. Each electrolysis run shows a decreased A_{1g} intensity compared to the BOL sample, suggesting that more O^{2-} vacancies are present with increasing electrolysis duration. This is consistent with the observed cell resistance behavior (Table 4.5) and the YSZ color in the electrolysis cells (Figures 4.3, 4.4, 4.5). Based on these results, it is expected that YSZ will become further reduced and electronically conductive with increasing electrolysis duration.

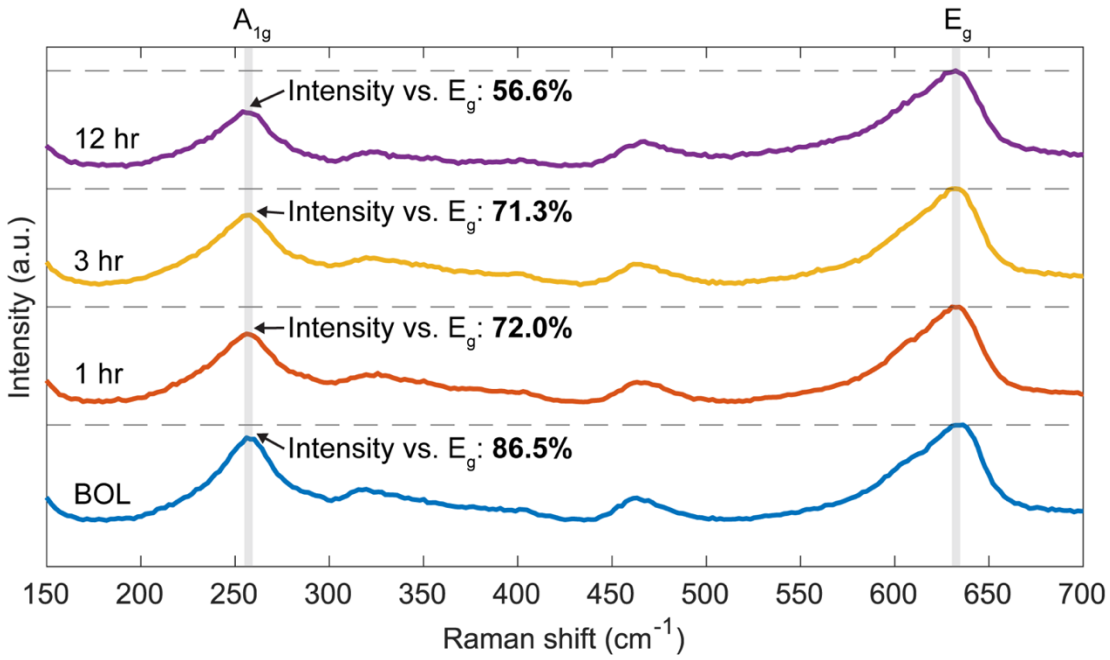

Figure 4.8. Raman spectra of YSZ from beginning-of-life (BOL), 1-hour, 3-hour, and 12-hour electrolysis cells.

4.4 Implications for hollow anode design

The results from the *inverted* hollow anode experiments conducted in this study provide insight into how a hollow anode can be incorporated into a MRE reactor. The experimental results presented indicate that MRE can be successfully performed using YSZ/Pt at the anode, without altering the metallic products that form at the cathode. For a hollow anode utilizing YSZ as the solid electrolyte, there are three primary mechanisms affecting electrolysis performance: the onset of electronic conductivity in YSZ, the thermochemical dissolution of YSZ into molten regolith, and the cracking of YSZ induced by Y_2O_3 depletion and thermal cycling. Each mechanism has been previously discussed in the context of the electrolysis experiments performed. In this section, the implications of each mechanism on YSZ hollow anodes in a prototypical MRE reactor are assessed with potential solutions. Additionally, the rate of O_2 generation is compared to the rate of YSZ dissolution to provide an estimate of the anodic mass payback ratio for YSZ hollow anodes.

4.4.1 YSZ regeneration

The increasing electronic conductivity of YSZ with increasing electrolysis duration is undesirable in a hollow anode application. If YSZ is electronically conductive, O_2 generation is not isolated to the YSZ/Pt interface and can be produced at the YSZ/regolith interface. Within the hollow anode design, this may cause O_2 to be generated as if the anode were Ir or an ideal inert anode, allowing the produced O_2 to be bubbled through the molten regolith. This would reintroduce bubble separation and reoxidation challenges, resulting in a lower O_2 production efficiency. A method of regenerating YSZ performance is important to enable consistent high O_2 production efficiencies using a hollow anode.

As discussed previously, the electronic conductivity observed in YSZ is due to the formation of reduced YSZ, with a high concentration of O^{2-} vacancies. Thus, the concentration of O^{2-} vacancies must remain low to minimize the electronic conductivity of YSZ. One proposed method of regeneration is to pause MRE after a set amount of time and allow O_2 to dissociate and reabsorb into the YSZ crystal structure (reoxidation), filling the excess O^{2-} vacancies. The reversible uptake of O_2 into YSZ and subsequent metal-to-insulator transition is well studied [28]. However, further work is necessary to determine the correct conditions (pO_2 and duration) to regenerate the performance of YSZ in a hollow anode application. Guo et al. investigated the thermochemical darkening of YSZ for oxygen sensor applications in low pO_2 environments and provided a similar suggestion that YSZ should be periodically reoxidized to prolong the performance of YSZ [26]. The same type of thermochemical reoxidation is proposed here to reduce the electronic conductivity of YSZ, increasing the O_2 production efficiency of the hollow anode. Based on Figure 4.2, it appears that regeneration should be performed approximately every 6 hours if the same current density (0.5 A/cm^2) is used. YSZ regeneration is explored further in Chapter 5.

4.4.2 Design life

YSZ undergoes dissolution in contact with molten regolith. For highlands regolith, this process appears to be relatively slow when compared to the timescale of increasing YSZ electronic conductivity. From Table 4.4, an average of 85 μm of wall recession was observed

for 12 hours of electrolysis, providing a wall recession rate of approximately 7 μm/hr. Linearly extrapolating these values suggests that a week of operation would result in approximately 1.2 mm of recession, roughly 40% of the original YSZ wall thickness. Based on these values, it appears that a YSZ hollow anode would need to be changed out every one to two weeks if used continuously in contact with highlands regolith. However, these results do not account for the decrease in the rate of YSZ wall recession that stems from grain coarsening at the interface. Thus, the conservative design life of one to two weeks is likely a lower bound on the usable life of YSZ in contact with molten highlands regolith. It is possible that grain coarsening can significantly decrease the rate of YSZ dissolution and extend the design life of YSZ hollow anodes, but further experiments are needed to quantify the expected design life of YSZ hollow anodes.

4.4.3 Thermal cycling behavior

The Y_2O_3 depletion caused by interactions between YSZ and molten regolith will cause YSZ to crack on cooling. Since no regolith penetration is detected along YSZ cracks in the inverted hollow anode, the cracks are assumed to form below the solidification temperature of LHS-1. This behavior indicates that YSZ hollow anodes are expected to survive through only a single thermal cycle. However, given the relatively long usable life of YSZ, the expectation is that MRE reactors incorporating a hollow anode would not be thermally cycled until the design life of the YSZ is reached (one to two weeks). Since the cracking would occur after the usable life of a YSZ hollow anode is reached, it would be replaced regardless. Large-scale O_2 production rates (>10 MT/year) are necessary to meet NASA's production goal for a technology demonstration [29], which will likely require an MRE reactor to operate continuously and with a high duty cycle. The continuous operation of a MRE reactor will decrease the number of thermal cycles, ideally extending high temperature operation to the full design life of a YSZ hollow anode.

4.4.4 Anode mass payback ratio

Given that YSZ hollow anodes exhibit dissolution in molten regolith, it is paramount to assess the tradeoff between oxygen production and anode material loss over time. For this

analysis, a YSZ anode with dimensions of 1 cm × 1 cm and a wall thickness of 0.3 cm is considered, consistent with the geometry of the cells utilized in this study. Based on the manufacturer-reported density of 5.92 g/cm³, this anode has a mass of approximately 1.78 g. Due to observed thermal cycling-induced cracking, it is conservatively assumed that the full mass of the anode is lost upon reaching the end of its design life. From the 12-hour electrolysis tests reported in Tables 4.2 and 4.4, the average anode wall recession rate is 7 μm/hr, while the corresponding average O_2 production rate is 0.062 g/hr. Assuming anode replacement is required upon dissolution of half the wall thickness, the projected operational lifetime is approximately 214 hours (~8.9 days). Over this duration, the anode is expected to produce approximately 13.4 g of O_2. This yields an anode mass payback ratio of approximately 7.5, defined as the mass of O_2 produced per unit mass of YSZ consumed.

It is important to note that this estimate assumes a constant rate of O_2 production and YSZ recession, both of which require further testing to validate. Additionally, this analysis excludes the mass of the MRE system and the cathode but also does not account for the mass of cathodic products generated, which has value for in situ construction/manufacturing. Overall, these results suggest that each unit mass of YSZ delivered to the lunar surface could enable the production of up to 7.5 times its own mass in O_2 under the assumed conditions.

4.4.5 Lunar maria electrolysis

As discussed previously, the primary focus of hollow anode testing in this chapter was on the lunar highlands regolith simulant (LHS-1). However, MRE should be agnostic to specific composition of regolith used, as long as FeO and SiO_2 are abundant. Thus, proof-of-principle testing was also performed on lunar maria regolith simulant (JSC-1A) to demonstrate that the hollow anode can function in both types of lunar regolith. The successful results of performing MRE on JSC-1A are provided in Appendix F.

4.5 Conclusions

Experimental results from an inverted hollow anode reactor demonstrate that MRE can be successfully performed through a YSZ solid electrolyte for up to 12 hours. Residual gas analysis indicates that O_2 is produced when a constant current is applied to the cell, confirming that anodic O_2 production is not affected by the YSZ solid electrolyte. Subsequent SEM/EDS analysis of the cross-sectioned cells reveal the compositions of both the cathodic products and solidified regolith simulant. The primary cathodic products are Fe and Si, which are consistent with previous MRE models. Furthermore, the FeO and SiO_2 content of the solidified regolith simulant decreases with increasing electrolysis duration, indicating that FeO and SiO_2 electrolysis is achieved in the inverted hollow anode reactor. To the authors' knowledge, this is the first reported experimental confirmation of SiO_2 electrolysis in a MRE reactor. This is significant since SiO_2 is the most abundant oxide species in lunar regolith. Demonstrating O_2 production from SiO_2 provides confirmation that high O_2 electrolysis efficiencies (>25%) are possible through MRE utilizing a hollow anode.

Post-electrolysis analysis of the YSZ reveals that there are three primary mechanisms affecting electrolysis performance: the onset of electronic conductivity in YSZ, the thermochemical dissolution of YSZ into molten regolith, and the cracking of YSZ, induced by Y_2O_3 depletion and thermal cycling. The rates associated with each mechanism are estimated from the inverted hollow anode cells. From these rates, preliminary design guidelines for YSZ hollow anodes in a prototypical MRE reactor are identified. Given the extreme operating environment of MRE, the observed interactions between YSZ and LHS-1 are expected. However, the overall dissolution rate of YSZ indicates that electrolysis durations longer than the 12 hours achieved in this study are possible, potentially allowing for a YSZ hollow anode to operate for up to two weeks. By comparing the measured rates of YSZ dissolution and O_2 production, it was determined that YSZ hollow anodes can produce up 7.5 times their mass in O_2.

The inverted hollow anode experiments provide a promising proof-of-principle, demonstrating that the hollow anode design can potentially address some of the key

challenges associated with MRE. Based on the observed rates for each degradation mechanism, the evolution of electronic conductivity of YSZ has the shortest timescale and is expected to negatively impact O_2 production efficiency. Chapter 5 will present an investigation of YSZ regeneration using the same experimental setup to reduce the electronic conductivity of YSZ and extend electrolysis beyond the 12-hour experiment presented in this chapter.

References

[1] K. Grossman, E. Petersen, E. Bell, J. Toro-Medina, L. Sibille, H. Williams, T. Newbold, K. Zacny, I. Bates, GaLORE (Gaseous Lunar Oxygen from Regolith Electrolysis): Successful Demonstration of a Cold-Walled Molten Regolith Electrolysis Reactor Design in a vacuum environment, (2023). https://isruinfo.com/public/docs/srr23/10-4%20Grossman-GALORE%20Demonstration%20of%20a%20Cold-Walled%20Molten%20Regolith%20Electrolysis%20Reactor%20Design%20in%20a%20Vacuum%20Environment.zip (accessed December 23, 2024).

[2] K. Yu, J. Stokes, B. Harder, L. Reidy, K.T. Faber, Thermochemical interactions between yttria-stabilized zirconia and molten lunar regolith simulants, Journal of the American Ceramic Society 107 (2024) 7119–7130. https://doi.org/10.1111/jace.19821.

[3] C.A. Krier, R.I. Jaffee, Oxidation of the platinum-group metals, Journal of the Less Common Metals 5 (1963) 411–431. https://doi.org/10.1016/0022-5088(63)90055-9.

[4] J. Guo, T. Villalon, U. Pal, S. Basu, Effect of optical basicity on the stability of yttria-stabilized zirconia in contact with molten oxy-fluoride flux, J Am Ceram Soc 101 (2018) 3605–3616. https://doi.org/10.1111/jace.15496.

[5] Y. Gao, C. Duan, Y. Yang, D. Ruan, C. Yang, C. Hong, Effect of Applied Voltage on Electroreduction with Controlled Oxygen Flow of Molten Slag Containing FeO at 1723 K, ISIJ International 55 (2015) 2273–2282. https://doi.org/10.2355/isijinternational.ISIJINT-2014-826.

[6] Y. Gao, C. Yang, C. Zhang, Q. Qin, G.Z. Chen, Magnesia-stabilised zirconia solid electrolyte assisted electrochemical investigation of iron ions in a SiO_2–CaO–MgO–Al_2O_3 molten slag at 1723 K, Phys. Chem. Chem. Phys. 19 (2017) 15876–15890. https://doi.org/10.1039/C7CP01945A.

[7] NASA, Why Artemis will focus on the Lunar South Pole region, 2022. https://www.lpi.usra.edu/lunar/artemis/resources/WhitePaper_2023_WhyLunarSouthPolarRegion.pdf.

[8] M.P. Lucas, C.R. Neal, J.M. Long-Fox, D. Britt, Simulating lunar highlands regolith profiles on Earth to inform infrastructure development and ISRU activities on the Moon, Acta Astronautica 224 (2024) 161–171. https://doi.org/10.1016/j.actaastro.2024.08.019.

[9] Space Resource Technologies, LHS-1 Lunar Highlands Simulant Fact Sheet (002-01-001-0621), (2021). https://cdn.shopify.com/s/files/1/0398/9268/0862/files/lhs-1-spec-sheet-Dec2022.pptx.pdf?v=1688051876.

[10] J.J. Papike, S.B. Simon, J.C. Laul, The lunar regolith: Chemistry, mineralogy, and petrology, Reviews of Geophysics 20 (1982) 761–826. https://doi.org/10.1029/RG020i004p00761.

[11] H.M. Sargeant, F.A.J. Abernethy, S.J. Barber, I.P. Wright, M. Anand, S. Sheridan, A. Morse, Hydrogen reduction of ilmenite: Towards an in situ resource utilization demonstration on the surface of the Moon, Planetary and Space Science 180 (2020) 104751. https://doi.org/10.1016/j.pss.2019.104751.

[12] C.A. Schneider, W.S. Rasband, K.W. Eliceiri, NIH Image to ImageJ: 25 years of image analysis, Nat Methods 9 (2012) 671–675. https://doi.org/10.1038/nmeth.2089.

[13] F. Bachmann, R. Hielscher, H. Schaeben, Grain detection from 2d and 3d EBSD data—Specification of the MTEX algorithm, Ultramicroscopy 111 (2011) 1720–1733. https://doi.org/10.1016/j.ultramic.2011.08.002.

[14] C.W. Bale, E. Bélisle, P. Chartrand, S.A. Decterov, G. Eriksson, A.E. Gheribi, K. Hack, I.-H. Jung, Y.-B. Kang, J. Melançon, A.D. Pelton, S. Petersen, C. Robelin, J. Sangster, P. Spencer, M.-A. Van Ende, FactSage thermochemical software and databases, 2010–2016, Calphad 54 (2016) 35–53. https://doi.org/10.1016/j.calphad.2016.05.002.

[15] R.I. Webster, E.J. Opila, Viscosity of $CaO–MgO–Al_2O_3–SiO_2$ (CMAS) melts: Experimental measurements and comparison to model calculations, J Non-Cryst Solids 584 (2022) 121508. https://doi.org/10.1016/j.jnoncrysol.2022.121508.

[16] M.S. Humbert, G.A. Brooks, A.R. Duffy, C. Hargrave, M.A. Rhamdhani, Thermophysical property evolution during molten regolith electrolysis, Planet Space Sci 219 (2022) 105527. https://doi.org/10.1016/j.pss.2022.105527.

[17] N. Masó, A.R. West, Electronic Conductivity in Yttria-Stabilized Zirconia under a Small *dc* Bias, Chem. Mater. 27 (2015) 1552–1558. https://doi.org/10.1021/cm503957x.

[18] R. Kirchheim, On the mixed ionic and electronic conductivity in polarized yttria stabilized zirconia, Solid State Ionics 320 (2018) 239–258. https://doi.org/10.1016/j.ssi.2018.03.014.

[19] M. Jovaní, H. Beltrán-Mir, E. Cordoncillo, A.R. West, Field-induced p-n transition in yttria-stabilized zirconia, Sci Rep 9 (2019) 18538. https://doi.org/10.1038/s41598-019-54588-y.

[20] A.H. Sirk, D.R. Sadoway, L. Sibille, Direct Electrolysis of Molten Lunar Regolith for the Production of Oxygen and Metals on the Moon, ECS Transactions 28 (2010) 367–373. https://doi.org/10.1149/1.3367929.

[21] J. Houserová, J. Vřešťál, M. Šob, Phase diagram calculations in the Co–Mo and Fe–Mo systems using first-principles results for the sigma phase, Calphad 29 (2005) 133–139. https://doi.org/10.1016/j.calphad.2005.06.002.

[22] C.S. Holgate, G.G.E. Seward, A.R. Ericks, D.L. Poerschke, C.G. Levi, Dissolution and diffusion kinetics of yttria-stabilized zirconia into molten silicates, J Eur Ceram Soc 41 (2021) 1984–1994. https://doi.org/10.1016/j.jeurceramsoc.2020.10.056.

[23] B. Kowalski, J. Stokes, P.E. Albert, P.E. Lauer, D.E. Wolfe, Effect of test parameters in the exposure of Ca–Mg–Al–silicate on yttria stabilized zirconia, J Am Ceram Soc 106 (2023) 3911–3921. https://doi.org/10.1111/jace.19025.

[24] G.M. Wolten, Diffusionless Phase Transformations in Zirconia and Hafnia, Journal of the American Ceramic Society 46 (1963) 418–422. https://doi.org/10.1111/j.1151-2916.1963.tb11768.x.

[25] V.R. PaiVerneker, A.N. Petelin, F.J. Crowne, D.C. Nagle, Color-center-induced band-gap shift in yttria-stabilized zirconia, Phys. Rev. B 40 (1989) 8555–8557. https://doi.org/10.1103/PhysRevB.40.8555.

[26] Xin Guo, Yao-Qing Sun, Kun Cui, Darkening of zirconia: a problem arising from oxygen sensors in practice, Sensors and Actuators B: Chemical 31 (1996) 139–145. https://doi.org/10.1016/0925-4005(96)80058-X.

[27] V. Hastak, E.J. Gildersleeve, S. Batna, A.S. Gandhi, S. Sampath, On the oxygen vacancy annealing in air plasma sprayed yttria-stabilized zirconia thermal barrier coatings, J Am Ceram Soc. 107 (2024) 920–932. https://doi.org/10.1111/jace.19477.

[28] A. Alvarez, Y. Dong, I.-W. Chen, DC electrical degradation of YSZ: Voltage-controlled electrical metallization of a fast ion conducting insulator, Journal of the American Ceramic Society 103 (2020) 3178–3193. https://doi.org/10.1111/jace.17004.

[29] NASA, Lunar Infrastructure Foundational Technologies-1: Request for Information, (2023). https://nspires.nasaprs.com/external/viewrepositorydocument/cmdocumentid=967421/solicitationId=%7B23D0FE0E-099D-77A8-3E06-2C516D900762%7D/viewSolicitationDocument=1/LIFT-1%20RFI%20STMD%20Amednment%201.pdf (accessed December 23, 2024).

Chapter 5

TESTING YTTRIA-STABILIZED ZIRCONIA ELECTRONIC CONDUCTIVITY SUPRESSION METHODS

Portions of experimental methodology of this chapter are also presented in "Improving molten regolith electrolysis with zirconia-based hollow anode technology" by K. Yu, W. West, J. Stokes, B. Harder, L. Reidy, J. Dominguez, and K. T. Faber, which was published in Acta Astronautica in 2025. Specifically, the inverted hollow anode electrolysis cell fabrication and experimental setup is the same as the cited manuscript. The results and discussion are not published.

K. Yu, W. West, J. Stokes, B. Harder, L. Reidy, J. Dominguez, K.T. Faber (2025). "Improving molten regolith electrolysis with zirconia-based hollow anode technology". In: *Acta Astronautica* 235, pp. 723-735. DOI: 10.1016/j.actaastro.2025.06.028

5.1 Introduction

This chapter is focused on testing different methods to regenerate yttria-stabilized zirconia (YSZ) performance or to mitigate the electrochemical degradation of YSZ. In Chapter 4, it was shown that YSZ hollow anodes are feasible for usage in molten regolith electrolysis (MRE) reactors. However, YSZ hollow anodes can become electronically conductive with an applied DC potential, which can reduce the O_2 production efficiency. The timescale of this electrochemically induced degradation is on the order of hours, while the thermochemical degradation (dissolution) is on the order of days. Thus, it is paramount to investigate methods to limit the electronic conductivity of YSZ. In the context of this thesis, regeneration refers to techniques that can eliminate or reduce the electronic conductivity of YSZ between electrolysis periods. Mitigation refers to changes in operating conditions, while performing electrolysis, that can eliminate or reduce the electronic conductivity of YSZ.

When YSZ becomes electronically conductive, the entire YSZ solid electrolyte goes from an ideal ionic conductor to a mixed ion-electron conductor. While this effect does not cause failure of the cell, it does decrease the effective Faradaic efficiency of O_2 production. Two resistor models (Figures 5.1 – 5.2) are used to describe the effect of electronic conductivity. Figure 5.1 provides a simple resistor model and electron transfer schematic to summarize the ideal hollow anode behavior. Figure 5.2 offers a modified resistor model and electron transfer schematic that includes the electronic conductivity of YSZ, resulting from an applied DC potential. Table 5.1 provides definitions of the subscripts of each resistor used in the resistor models. The molten regolith electrolyte is assumed to be only ionically conductive for both models, but the validity of this assumption is discussed later in this section.

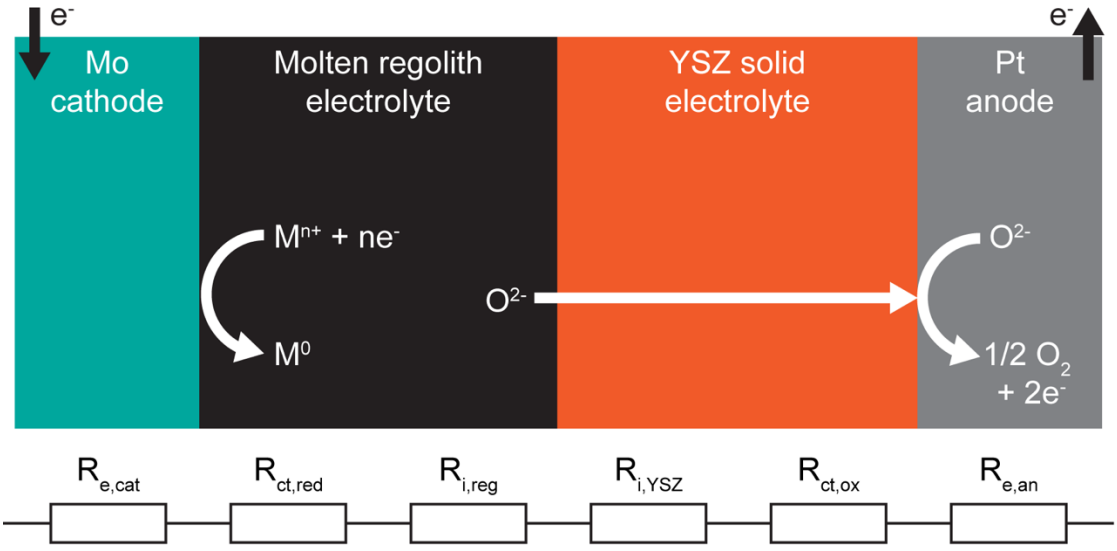

Figure 5.1. Schematic of ideal (fully ionic) YSZ hollow anode charge transport and resistor model.

In Figure 5.1, O_2 is solely generated at the YSZ/Pt interface since YSZ is an ideal ion conductor (no electron conductivity). Importantly, the O_2 does not contact the molten regolith electrolyte, which is the ideal operation of the hollow anode. In this case, the O_2 can be easily collected, since it is generated physically away from molten regolith, at a solid-solid interface. Additionally, the cathodic reaction is not impacted since metal cations (M^{n+}) can migrate to the cathode surface for reduction.

With electronic conductivity in the YSZ, the situation becomes more complicated. In Figure 5.2, the ionic conduction of YSZ still allows some O_2 to be produced at the YSZ/Pt anode. However, the increased electronic conductivity of YSZ now allows the Faradaic oxidation reaction to occur at the YSZ/regolith interface, similar to the metallic, bare anodes used in existing MRE reactors. In this case, the O_2 is produced at a solid-liquid interface, forming O_2 bubbles. Collection of O_2 after production becomes more difficult in this case, since these bubbles must migrate to the surface of the molten regolith before the gas can be collected. The YSZ hollow anode was designed to address the challenges stemming from O_2 bubble formation (Chapter 1).

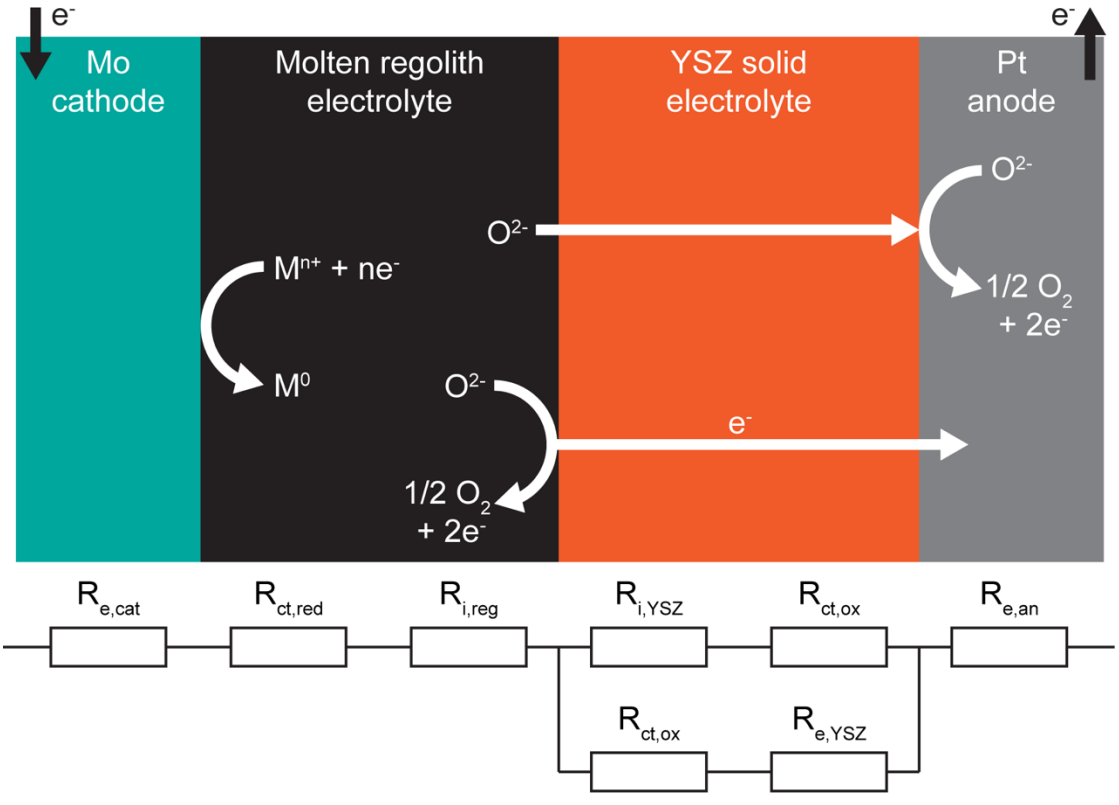

Figure 5.2. Schematic of degraded (ionic and electronic conduction) YSZ hollow anode charge transport and resistor model.

The molten regolith electrolyte possesses higher viscosity and surface tension compared to that observed in aqueous electrolysis, resulting in a larger critical buoyancy force for bubbles

to separate from the electrode surface [1]. This problem is further exacerbated by the reduced acceleration due to gravity on the lunar surface (~1/6x compared to Earth) [2]. The result is that these O_2 bubbles can cover a significant portion of the electrode surface, reducing the available active surface for electrolysis and potentially causing electrolysis to stall [3]. Additionally, the separated bubbles must migrate through the molten regolith, where the produced O_2 can be reabsorbed by the molten regolith, or even worse, oxidize the metallic products forming at the cathode. Thus, the evolution of electronic conductivity in YSZ (Figure 5.2) can reduce the effective Faradaic efficiency since the useful electrolysis products (metals and O_2) are consumed before they can be collected.

Table 5.1. Resistor subscript definitions for Figures 5.1 – 5.2

R_x	Definition
$R_{e,cat}$	Electronic resistance in the Mo cathode
$R_{ct,red}$	Charge transfer resistance for reduction half-reaction
$R_{i,reg}$	Ionic resistance in molten regolith electrolyte
$R_{i,YSZ}$	Ionic resistance in YSZ solid electrolyte
$R_{e,YSZ}$	Electronic resistance in YSZ solid electrolyte
$R_{ct,ox}$	Charge transfer resistance for oxidation half-reaction
$R_{e,an}$	Electronic resistance in the Pt anode

In these models, the molten regolith electrolyte is assumed to be only ionically conductive. A literature review indicates that oxides of multivalent cations, such as FeO/Fe_2O_3 and Ti_2O_3/TiO_2, can cause an increase in electronic conductivity of the molten oxide electrolyte [4,5]. However, the content of these oxides is low in highlands regolith (Table 5.2), so electronic conduction of the molten regolith is assumed to be negligible.

In the Chapter 4, it was hypothesized that the generated cathodic products (molten Fe and Si) could cause an electronic short in the cell. Since the YSZ is also electronically conductive, if any of the cathodic products contacts both the Mo cathode and the YSZ solid electrolyte, then a purely electronic short forms in the cell. This effect would be detrimental and cause the Faradaic efficiency to drop to 0%, since there is a direct path for electrons to pass through the cell without any redox reactions. However, this behavior is caused by the confined inverted hollow anode cell geometry and is not expected to occur in the envisioned hollow anode usage. Figure 5.3 provides a schematic of how the cathodic products are positioned in both the envisioned hollow anode design and the inverted cell configuration used in experiments presented in this work.

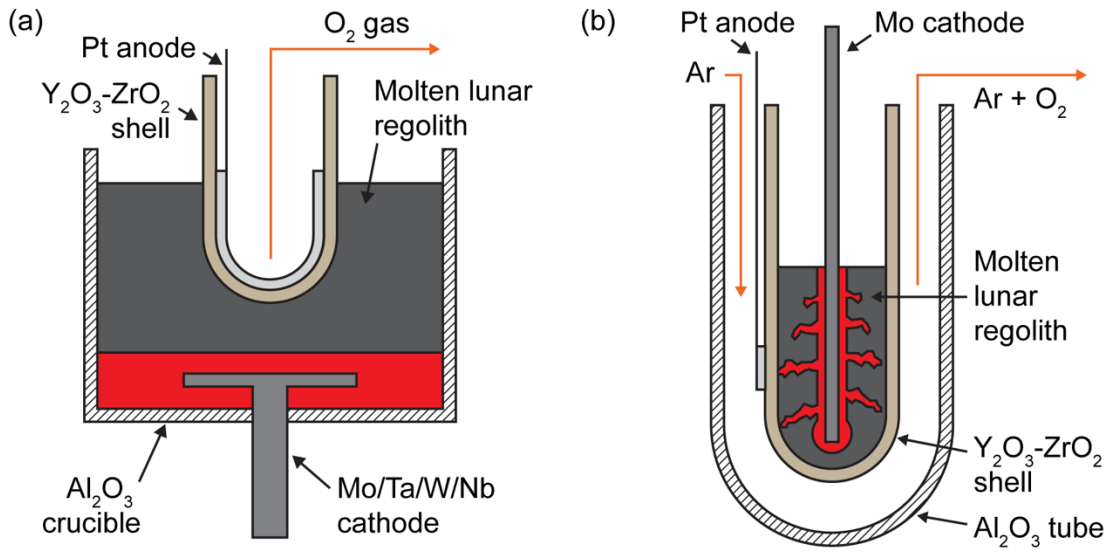

Figure 5.3. Schematic of (a) envisioned integration of hollow anode into existing MRE reactors and (b) inverted hollow anode used to perform thesis experiments. Cathodic products are highlighted in red to show their position in the MRE reactor.

In the envisioned design of the hollow anode (Figure 5.3(a)), the cathode is positioned at the bottom of the cell. The cathodic products resulting from MRE are generated at the bottom of the cell. The density of the cathodic products (~3.5 – 7.0 g/cm^3) are higher than the molten regolith (~3.0 g/cm^3), so there is no buoyancy-induced flow. In inverted hollow anode design (Figure 5.3(b)), the cathode is oriented vertically and runs down the center of the cell. The cathodic products from MRE are generated along the cathode. However, the difference in density between the cathodic products and the molten regolith causes the cathodic products to flow toward the bottom of the cell. In the inverted cell design, a thermal gradient exists due to radiative thermal losses at the top of the cell. This thermal gradient is expected to drive convective mass transfer of the hotter (lower density) molten regolith from the bottom to the top of the electrolysis cell.

If the cathodic product layer thickness becomes large enough (with increasing electrolysis duration), it can exceed the convective flow boundary layer caused by the thermal gradient in the cell. Once the flow boundary layer is exceeded, the cathodic products will separate from the cathode, mixing with the molten regolith by natural convection and forming wisps. Evidence of cathodic product separation from the cathode was observed in Chapter 4 (Figure 4.5). Any of these wisps can contact the YSZ and cause an electronic short to form. However, this effect is unlikely to occur in the envisioned operation of an MRE cell utilizing the hollow anode, since all cathodic products are generated at the bottom of the cell and thermal gradients are minimized in industrial-scale MRE reactors. Thus, it was determined that this effect is likely not present in larger-scale MRE reactors and is not investigated further since it likely stems from the geometry and configuration of the inverted hollow anode cell. It is noted that this behavior will be referenced in the remainder of this chapter.

5.2 Rationale for regeneration and mitigation

As discussed in Chapter 4 (Section 4.3.5.2), the electronic conductivity of YSZ is attributed to the generation of excess O^{2-} vacancies, caused by the applied DC potential. These vacancies can interact with electrons in the crystal structure to form *F* centers, creating a reduced YSZ structure. These *F* centers give rise to electron states within the band gap of

YSZ, allowing high electronic conductivity to exist in a material that is typically an electron insulator [6]. Thus, the objective of regeneration (performed in periods between electrolysis) and mitigation (performed during electrolysis) is to fill the excess vacancies in YSZ, thereby eliminating or decreasing the electronic conductivity of YSZ. A high pO_2 carrier gas could be used to test both regeneration and mitigation methods. For the regeneration and mitigation experiments described in this chapter, 10% O_2 in Ar was arbitrarily selected as the high pO_2 carrier gas, while Ar (from Chapter 4) was the low pO_2 carrier gas.

For the regeneration process, MRE is performed under Ar flow. Regeneration periods are established between electrolysis periods, during which the carrier gas is switched from Ar (low pO_2) to 10% O_2 (high pO_2). The cell remains in the high pO_2 environment for varying durations, which are presented in the next section. Once the regeneration period ends, the gas is switched back to Ar and MRE is restarted. In contrast, the mitigation technique applies the high pO_2 condition during electrolysis. MRE is performed under 10% O_2 flow, shifting the entire operation to high pO_2. In this case, regeneration is not considered necessary since the high pO_2 environment persists for the duration of electrolysis.

A Brouwer diagram can be used to visualize the effect of either regeneration or mitigation. The possible charge carriers in YSZ are ions (O^{2-}), electrons (e), and holes (h). In YSZ, the Y_2O_3 dopants can be treated as defects introduced into the ZrO_2 crystal structure [7]. Using Kröger-Vink notation, the defect chemistry is expressed as:

$$Y_2O_3 \rightarrow 2Y'_{Zr} + 3O_O^x + V_O^{\cdot\cdot} \tag{5.1}$$

The creation of additional vacancies occurs at low pO_2 and can be expressed as:

$$O_O^x \rightleftharpoons 2e' + V_O^{\cdot\cdot} + \frac{1}{2}O_2(g) \tag{5.2}$$

Similarly, the filling of additional vacancies occurs at high pO_2 and can be expressed as:

$$V_O^{\cdot\cdot} + \frac{1}{2}O_2(g) \rightleftharpoons 2h^{\cdot} + O_O^x \tag{5.3}$$

The law of mass action can be used for both the low and high pO_2 regimes to obtain (in order):

$$K = [V_O^{\cdot\cdot}][e']^2 pO_2^{1/2} \tag{5.4}$$

$$K = [h^{\cdot}]^2 / \left([V_O^{\cdot\cdot}] pO_2^{1/2}\right) \tag{5.5}$$

These equations can be solved for the concentration of electrons ($[e']$) and holes ($[h^{\cdot}]$):

$$[e'] = \sqrt{K / [V_O^{\cdot\cdot}]} \left(pO_2^{-1/4}\right) \tag{5.6}$$

$$[h^{\cdot}] = \sqrt{K[V_O^{\cdot\cdot}]} \left(pO_2^{1/4}\right) \tag{5.7}$$

To maintain electroneutrality, the relationship between the charged defects is:

$$2[V_O^{\cdot\cdot}] = [Y'_{Zr}] + [e'] \tag{5.8}$$

$$2[V_O^{\cdot\cdot}] = [Y'_{Zr}] - [h^{\cdot}] \tag{5.9}$$

A generally used assumption is that the concentration of Y substitutions on Zr sites is significantly larger than the concentration of electrons and holes ($[Y'_{Zr}] \gg [e']$, $[h^{\cdot}]$) [7]. For the YSZ used in this research, $[Y'_{Zr}] \sim 10^{21}$ cm^{-3}, while Park et al. showed that $[e'] \sim 10^{18}$ cm^{-3} at $pO_2 = 10^{-14}$ atm and $[h^{\cdot}] \sim 10^{18}$ cm^{-3} at $pO_2 = 1$ atm [7]. The limits of pO_2 are unlikely to be exceeded in either direction in the MRE cell. Thus, this assumption is valid and Equations 5.8 and 5.9 can be simplified to:

$$2[V_O^{\cdot\cdot}] = [Y'_{Zr}] \tag{5.10}$$

This simplified Equations 5.6 and 5.7 so that the only variable is pO_2. The conductivities associated with each charge carrier are shown below, along with their dependence on pO_2:

$$\sigma_i = [V_O^{\cdot\cdot}]\frac{q_V^2}{kT}D_v \;\rightarrow \sigma_i \neq f(pO_2) \tag{5.11}$$

$$\sigma_e = [e']|q|\,\mu_e \;\rightarrow \sigma_e \propto pO_2^{-1/4} \tag{5.12}$$

$$\sigma_h = [h^{\cdot}]\,|q|\,\mu_h \;\rightarrow \sigma_h \propto pO_2^{1/4} \tag{5.13}$$

where σ_i is the ionic conductivity, σ_e is the electronic conductivity, σ_h is the hole conductivity, q_v is the charge of the vacancy, q is the elementary charge, D_v is the diffusivity of vacancies, μ_e is the electron mobility, μ_h is the hole mobility, k is the Boltzmann constant, and T is the temperature. From Equations 5.11, 5.12, and 5.13, it is shown that the ionic conductivity does not depend on pO_2, while the electronic and hole conductivities vary with pO_2. These conductivities can be plotted against pO_2 on a log-log scale to obtain a Brouwer diagram. Park et al. obtained the following relationships for the ionic, electronic, and hole conductivities (in S/cm) in YSZ [7]:

$$\sigma_i = 1.63 \times 10^2 \times e^{\left(-\frac{0.79\ eV}{kT}\right)} \tag{5.14}$$

$$\sigma_e = 1.31 \times 10^7 \times e^{\left(-\frac{3.88\ eV}{kT}\right)} \times pO_2^{-1/4} \tag{5.15}$$

$$\sigma_h = 2.35 \times 10^2 \times e^{\left(-\frac{1.67\ eV}{kT}\right)} \times pO_2^{1/4} \tag{5.16}$$

It is noted that these relationships were obtained at a temperature range of 800°C – 1050°C. Thus, it is not clear if the exact values from Equations 5.14 – 5.16 are accurate at 1600°C. However, the dependance of the conductivities on pO_2 is expected to be the same. The total electrical conductivity (σ_T) is the sum of Equations 5.14 – 5.16. Figure 5.4 presents the Brouwer diagram at 1600°C.

In Figure 5.4, two red dashed lines are also included to illustrate the rationale behind the regeneration and mitigation techniques tested in this research. The exact effective pO_2 within the YSZ is unknown, since the applied DC potential changes the electrochemical potential of O_2 in the YSZ. However, an estimate is provided based on the work reported in Chapter

4. In Figure 4.2, the O_2 production drops to half the starting value after 12 hours of electrolysis. This suggests that the overall conductance of the electronic and ionic transport mechanisms is approximately equal, since only half the current is following the ionic path and generating O_2. Thus, the low pO_2 estimate is at the intersection of the ionic and electronic conductivity curves (low $pO_2 \sim 10^{-14}$ atm). Based on residual gas analysis measurements, the average pO_2 increases 2000x under 10% O_2 gas flow. The high pO_2 estimate is set at 2000x higher than the low pO_2 estimate (high $pO_2 \sim 10^{-11}$ atm).

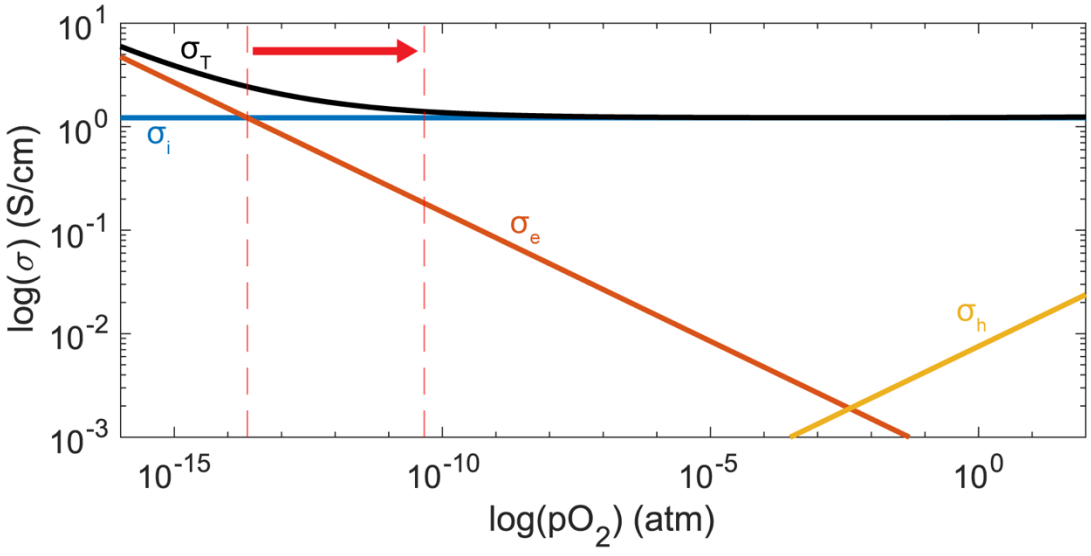

Figure 5.4. Brouwer diagram for YSZ at 1600°C. Data taken from [7]. Red dashed lines define the shift in pO_2 for the regeneration and mitigation techniques.

Figure 5.4 summarizes the effect of shifting the pO_2 of the gas in the cell. At low pO_2, which is only achieved due to the applied DC potential, the ionic and electronic conductivities are approximately equal, resulting in a parasitic current loss through electronic conduction. By shifting to high pO_2 (red arrow in Figure 5.4), the electronic conductivity should decrease significantly, while the ionic conductivity is unaffected. The result is that the total current flowing through the cell is primarily along the ionic conduction path, which results in the O_2 generation. The rationale behind introducing a 10% O_2 carrier gas, instead of the prior Ar, is to reduce the electronic conductivity of YSZ by shifting the effective pO_2 in the YSZ to higher values.

5.3 Materials and methodology

5.3.1 Lunar regolith simulant

Similar to Chapter 4, only the lunar highlands regolith simulant was used. LHS-1 (Space Resource Technologies) was selected as the highlands regolith simulant. The composition of LHS-1 [8], and a comparison to lunar highlands regolith returned from Apollo 16 [9], are presented in Table 5.2.

Table 5.2. Major abundances of LHS-1 simulant and highlands lunar regolith (wt%) [8,9]

Species	SiO_2	FeO	MgO	CaO	Al_2O_3	TiO_2	Na_2O	K_2O	MnO	P_2O_5
LHS-1 (Simulant)	51.2	2.7	1.6	12.8	26.6	0.6	2.9	0.5	0.1	0.1
Apollo 16 (#64501)	45.3	4.2	4.9	17.2	27.7	0.4	0.4	0.1	< 0.1	-

5.3.2 Molten regolith electrolysis experiments

The regeneration and mitigation techniques were performed in the inverted hollow anode configuration, shown in Figure 5.3(b). A mass flow controller (FMA series, OMEGA) was used to provide a consistent Ar (low pO_2) or 10% O_2 in Ar (high pO_2) flow to serve as the carrier gas. The gas outlet was connected to a residual gas analyzer (HPR-20, Hiden Analytical) for compositional analysis to track the production of O_2. The sealed electrolysis reactor was placed into a high-temperature box furnace (Rapid Temp Furnace, CM Furnaces) for heating to the operational temperature. The electrolysis cell was designed such that the lower ¼ portion of the cell containing LHS-1 is exposed to operational temperature, as shown in Figure 5.3(b). The upper portion of the electrolysis reactor with electrical leads, gas fittings, and tube gaskets (not shown) remained near ambient temperature. A potentiostat (VersaStat 4, Princeton Applied Research) was attached to the cathode and anode leads to perform electrolysis. Additional images and details of the electrolysis cell design, fabrication, and shakedown testing are provided in Appendix D.

5.3.2.1 Electrolysis cell fabrication

A custom stainless steel endplate was designed and machined to provide a mounting point for the interior 10.5 wt% YSZ tube and a sealing surface for the exterior alumina tube (McDanel Advanced Material Technologies). The endplate also contained feedthroughs for the cathode, anode, gas inlet tube, and gas outlet tube. To fabricate the electrolysis cell, a YSZ tube was loaded with approximately 20 grams of LHS-1 and mounted onto the endplate. The cathode was an alumina-sheathed Mo rod that was inserted into the center of the endplate and pushed down the YSZ tube through the loose regolith simulant. The anode consisted of a Pt wire mesh that was adhered to the exterior of the YSZ tube with Pt ink (Fuel Cell Store). The gas inlet and outlet tubes were then attached to the endplate. Finally, the entire assembly was lowered into the exterior alumina tube and sealed off by a Viton gasket at the endplate.

5.3.2.2 Regeneration and mitigation testing

For testing both regeneration and mitigation techniques, the electrolysis cell was heated to 1600°C using the same temperature ramp rates as shown in Appendix E (E.1). The dwell segment at 1600°C was programmed for 48 hours to allow for multiple shorter electrolysis periods, with regeneration testing between runs. All experiments were run under 100 sccm of either flowing Ar or flowing 10% O_2 in Ar. The electrolysis tests were performed with a constant current set at 0.5 A on the potentiostat. The cathode surface area is ~10 cm^2 and the anode pad surface area is ~1 cm^2, giving an anodic current density of ~0.5 A/cm^2. A total of six electrolysis tests were performed, with five segments of 6-hour electrolysis and a final segment of 10-hour electrolysis. Each electrolysis period is referred to by a number (i.e. electrolysis #1 for the first electrolysis period). The total electrolysis duration across all six electrolysis periods was 40 hours.

The first electrolysis period (electrolysis #1) was performed under Ar flow without any prior regeneration testing. Since this was the first electrolysis period, the results represent the beginning-of-life (BOL) condition of the YSZ. Chapter 4 showed that the O_2 generation for the BOL YSZ inverted hollow anode are high, indicating that electronic conductivity is likely negligible at BOL. As a result, testing regeneration prior to the first electrolysis period is

unproductive, since there is effectively no electronic conductivity in the YSZ at BOL. The objective of this first electrolysis period was to cause electronic conductivity to increase in the YSZ so that regeneration methods could be tested.

Following the first electrolysis period, three additional electrolysis periods were performed under Ar flow (electrolysis #2, 3, and 4). Each of these electrolysis periods had a regeneration method performed prior to initiating the electrolysis period. For the sake of clarity, each regeneration period is referred to by the number of the electrolysis period that followed the regeneration period (i.e. regeneration #2 was performed prior to starting electrolysis #2). It is noted that using this numbering scheme means that there is no regeneration #1 for the reasons described in the previous paragraph. Thus, the only regeneration periods are regeneration #2, 3, and 4. Regeneration #2 tested exposing the cell to 10% O_2 for 30 minutes, without an applied potential. Regeneration #3 tested exposing the cell to 10% O_2 for 60 minutes, without an applied potential. Regeneration #4 tested exposing the cell to 10% O_2 for 30 minutes, with a reverse potentiostatic held at -40 mV. The rationale for regeneration #4 was that a reversed electric field may accelerate the filling of O^{2-} vacancies. This is effectively electrochemically pumping O_2 from the carrier gas into the YSZ, which may allow O_2 to dissociate and diffuse into YSZ faster than the purely Fickian diffusion mechanisms at work in regeneration #2 and #3.

After electrolysis #4, mitigation testing was performed with electrolysis #5 and electrolysis #6 under 10% O_2 flow. Prior to beginning electrolysis #5, the gas flow was switched from Ar to 10% O_2 and allowed to equilibrate for approximately an hour. During this switchover period, the cell resistance was measured every 5 minutes to monitor the effects switching from Ar to 10% O_2 gas flow. After the cell resistance measurements, electrolysis #5 was initiated and lasted 6 hours. Following electrolysis #5, the cell and gas environment were allowed to equilibrate again for an hour prior to initiating electrolysis #6, which lasted for 10 hours. Since both electrolysis #5 and #6 were performed under 10% O_2 flow, the equilibration period was used to establish a baseline O_2 content on the outlet gas prior to initiating electrolysis. This baseline was subtracted from the O_2 content measured during electrolysis to determine the amount of O_2 produced by electrolysis.

The regeneration and mitigation testing represent several experiments exploring improving the O_2 production rate with increasing electrolysis duration. However, due to the cracking caused by Y_2O_3 depletion and thermal cycling (Chapters 3 and 4), it is not possible to cool the cell down before tests, which caused the condensed and complicated testing conditions described above. A summary table of the different electrolysis periods, regeneration tests, and mitigation experiments is presented in Table 5.3.

Table 5.3. Summary of regeneration and mitigation testing

Segment	Carrier gas	Duration	Notes
Electrolysis #1	Ar	6 hours	Produce electronic conductivity in YSZ
Regeneration #2	10% O_2	30 minutes	Anneal in high pO_2, no applied potential
Electrolysis #2	Ar	6 hours	Evaluate electrolysis after regeneration #2
Regeneration #3	10% O_2	60 minutes	Anneal in high pO_2, no applied potential
Electrolysis #3	Ar	6 hours	Evaluate electrolysis after regeneration #3
Regeneration #4	10% O_2	30 minutes	Anneal in high pO_2, applied -40 mV to pump O_2 into YSZ
Electrolysis #4	Ar	6 hours	Evaluate electrolysis after regeneration #4
Cell resistance test	Ar → 10% O_2	70 minutes	Monitor cell resistance while switching from Ar to 10% O_2
Electrolysis #5	10% O_2	6 hours	Mitigation test, perform electrolysis in high pO_2 gas
Electrolysis #6	10% O_2	10 hours	Mitigation test, perform electrolysis in high pO_2 gas

5.3.3 Characterization

The geometry of the MRE cell was designed to allow for characterization of all heated cell components, including the YSZ solid electrolyte, cathodic products, and solidified regolith simulant after the experiment. After cooling, the cell was mounted in epoxy and cross-sectioned down the middle of the cell. One half of the cell was polished to 0.05 μm to prepare for subsequent characterization to evaluate the electrochemical performance of the YSZ inverted hollow anode. Additionally, the introduction of 10% O_2 into the inverted cell configuration and pausing electrolysis several times is expected to cause oxidation of the cathode and potentially the cathodic products. Consequently, the composition of the cathodic products is no longer representative of the expected MRE cathodic products with an equivalent, continuous 40-hour electrolysis period. For these reasons, only optical microscopy was performed on the cell.

The cross-sectioned cell was optically imaged at 30x (VHX-7000, Keyence) and stitched together to capture macroscopic changes resulting from high-temperature operation and electrolysis. Further investigation of regions of interest was performed at 50x – 200x (VHX-2000, Keyence). ImageJ was used to measure YSZ wall recession from these images [10].

5.4 Results and discussion

5.4.1 Electrolysis #1 data

The volumetric percentage of O_2 in the outlet gas stream and the potential required to maintain 0.5 A of current through the cell for electrolysis #1 are presented in Figure 5.5. Elapsed time in these plots is counted from the application of constant current to the cell. The same data from the 12-hour electrolysis test, presented in Chapter 4, are also included in Figure 5.5 for comparison.

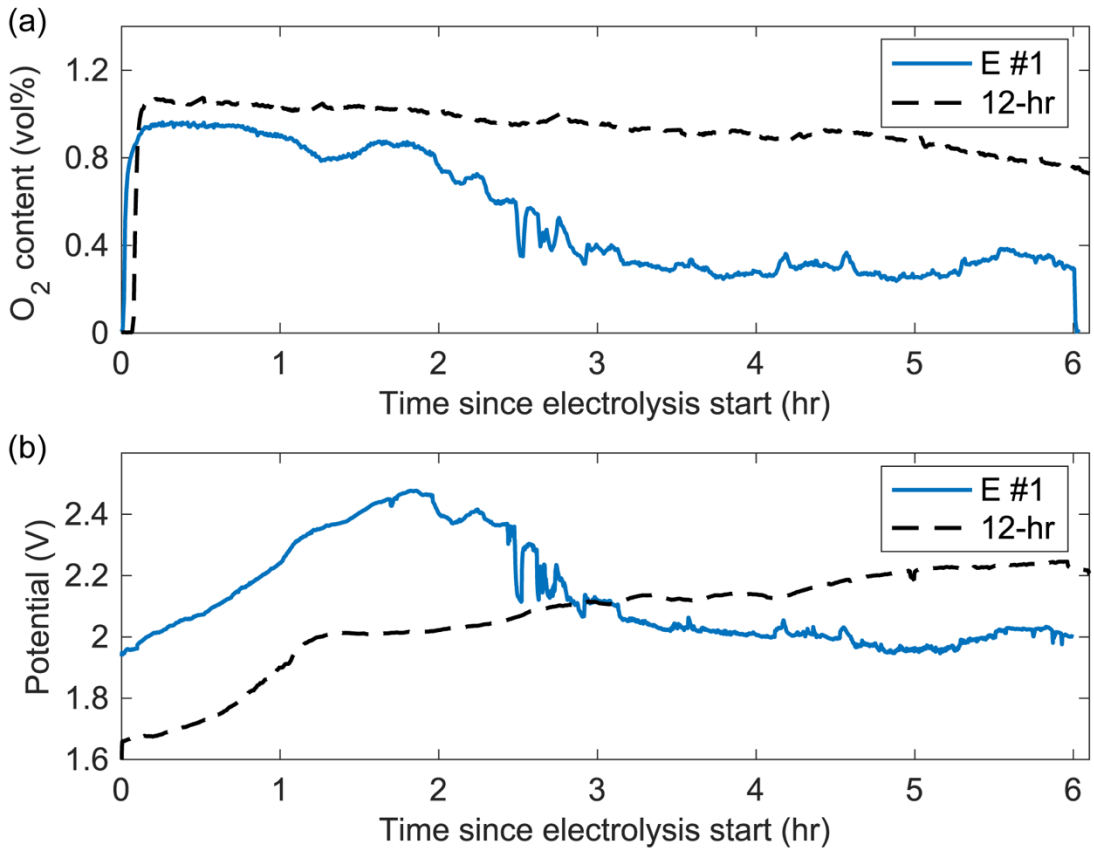

Figure 5.5. (a) O_2 content of outlet gas stream and (b) potential across electrolysis cell vs. elapsed time since electrolysis start for electrolysis #1 and the 12-hour electrolysis cell from Chapter 4 [11].

Based on Figure 5.5, the first two hours of electrolysis #1 are approximately in line with the results from Chapter 4. In the period between 2 and 3 hours since electrolysis start, there are several sharp decreases in both the O_2 content of the outlet gas and applied potential. The combination of these two factors indicates that electronic conductivity is present in the YSZ. Additionally, this behavior suggests that the cathodic products are forming an electronic short within the cell, as suggested in Figure 5.3. When the molten cathodic products temporarily bridge the cathode and YSZ, the current can pass through this electronic short, resulting in sharp decreases in the applied potential (Figure 5.5(b)). Since the electronic short also bypasses the Faradaic process of O_2 generation, there are also sharp decreases seen in the O_2 content of the outlet gas (Figure 5.5(a)).

After the series of sharp decreases between 2 and 3 hours of electrolysis, both the O_2 content and applied potential continue trending downward. As more cathodic product is generated, the short between the cathode and YSZ becomes more conductive, due to increased cross-sectional area of the short. The increased conductance of the cathodic product short allows more of the current to pass through the short instead of driving electrolysis, resulting in the gradual decrease in the O_2 content. The O_2 content of the outlet gas eventually settles at ~0.3 vol%. This is consistent with the 12-hour electrolysis cell, which settled at ~0.4 vol% O_2 (Figure 4.2). However, in the 12-hour electrolysis cell (Chapter 4), the plateau in O_2 content in the outlet gas did not occur until approximately 10 hours into the electrolysis period. In contrast, electrolysis #1 reached the plateau in O_2 content in the outlet gas after 3 – 4 hours of electrolysis.

The difference in the observed behavior of electrolysis #1 is attributed to misalignment of the cathode relative to the YSZ. Ideally, the Mo cathode should run straight down the center of the YSZ tube, resulting in a consistent distance between the cathode surface and the YSZ. Due to the high tolerances associated with ceramic parts, including the Al_2O_3 cathode sheath and the YSZ tube, it is possible that the cathode was significantly closer to the YSZ than designed. The shorter distance between the cathode and YSZ causes electronic shorts to form more easily, since the cathodic products need to bridge a smaller distance. Evidence of cathode misalignment is observed in the cross-sectioned cell (Section 5.4.5). Though this behavior is concerning, it is not expected to occur in the envisioned operation of an MRE cell incorporating the hollow anode (Figure 5.3(a)). The confined inverted cell design is likely the root cause of this issue (Figure 5.3(b)).

Though electrolysis #1 did not produce as much O_2 as the 12-hour electrolysis cell from Chapter 4, it met the objective stated in Section 5.3.2.2., specifically to get the cell to a state in which the YSZ has become electronically conductive. The data presented in Figure 5.5 indicates that this has been achieved by the end of electrolysis #1.

5.4.2 Regeneration testing

Regeneration #2 exposed the cell to 10% O_2 for 30 minutes without an applied potential, while regeneration #3 exposed the cell to 10% O_2 for 60 minutes without an applied potential, and regeneration #4 exposed the cell to 10% O_2 for 30 minutes with a reversed applied potential. Section 5.3.2.2 and Table 5.3 provide further details about each regeneration method. Each test was evaluated by performing 6 hours of electrolysis (in Ar) after regeneration to determine if there was any improvement in the electrochemical performance of the cell. These electrolysis segments are labeled electrolysis #2, #3, and #4. The volumetric percentage of O_2 in the outlet gas stream and the potential required to maintain 0.5 A of current through the cell for electrolysis #2, #3, and #4 are presented in Figure 5.6.

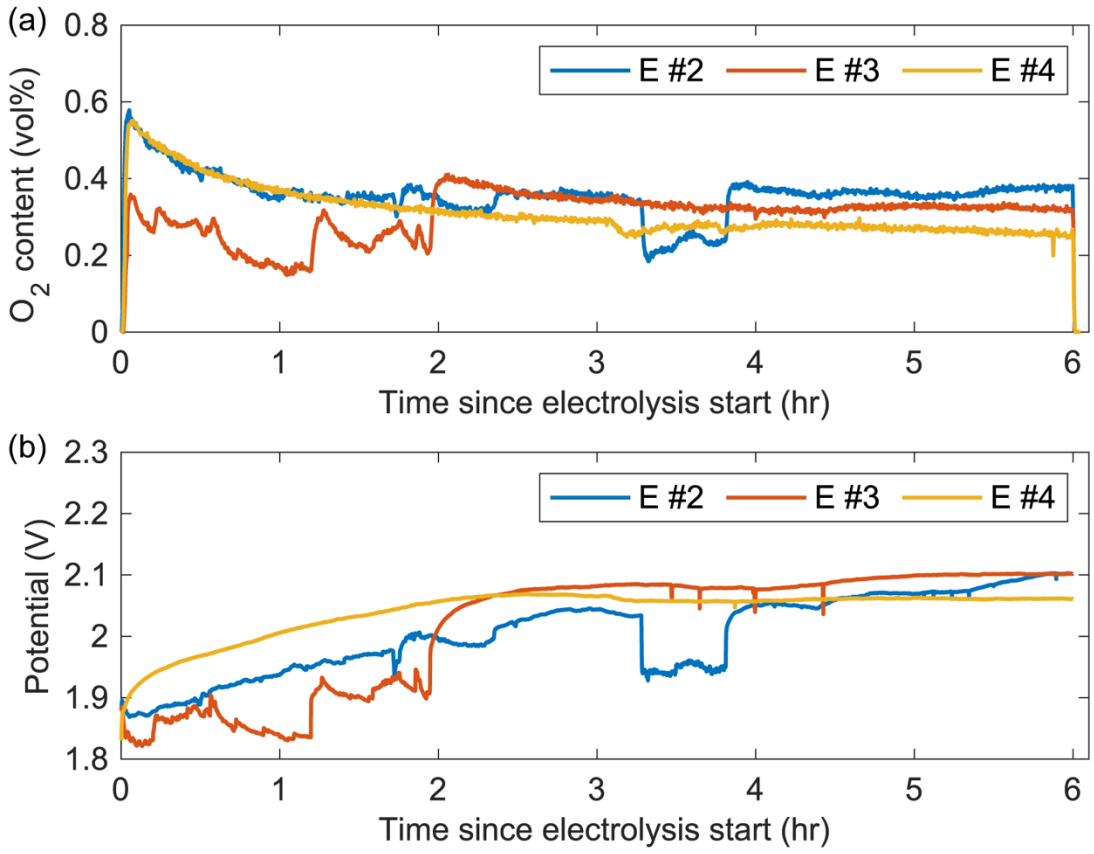

Figure 5.6. (a) O_2 content of outlet gas stream and (b) potential across electrolysis cell vs. elapsed time since electrolysis start for electrolysis #2, #3, and #4.

Based on the data in Figure 5.6, it appears that all regeneration methods result in similar electrolysis behavior after electrolysis. In electrolysis #2 and #3, there are sharp decreases in O_2 content and applied potential that suggest large electronic shorts formed from cathodic products bridging the cathode and YSZ. This behavior was also observed in electrolysis #1, providing further evidence that the cathode may be misaligned in the electrolysis cell. Electrolysis #4 has the most stable O_2 content and applied potential, but there are some comparatively smaller decreases in O_2 and applied potential at 3 – 4 hours of electrolysis.

If the effects of the cathodic product shorts are ignored, then the general trend across electrolysis #2, #3, and #4 are similar. All three of these electrolysis periods start at a relatively high O_2 content on the outlet gas that decreases with increased electrolysis duration. The applied potential needed to maintain 0.5 A in the cell starts at ~1.85 V and continues increasing with electrolysis duration up to ~2.1 V. Since the applied potential starts and ends at similar voltages across all three electrolysis segments, it is likely that the increase in potential is caused by degradation mechanisms that increase in severity with electrolysis but are reversed when current is not flowing through the cell. Some observed behaviors that could result in increased cell potential include a reduction in the cross-sectional area of the Mo cathode and the changing viscosity of LHS-1 with increasing electrolysis. However, these effects are expected to be permanent and would result in the applied potential increasing between each electrolysis segment, which is not the observed behavior in Figure 5.6(b).

It is hypothesized that increase in applied potential with increasing electrolysis, but similar starting and ending potentials across these electrolysis segments, is attributed to bubble generation at the YSZ/regolith interface. As proposed in Figure 5.2, the electronic conductivity of YSZ leads to O_2 bubble formation at the YSZ/regolith interface. The generation of bubbles reduces the active surface available for electrolysis, increasing the overpotential needed to maintain the same electrolysis rate [3]. The generated bubbles are released when electrolysis is stopped, allowing the cell to return to the same starting active area for electrolysis between each segment. Additional experiments are necessary to confirm this effect. It is noted that direct observation of bubble formation is nontrivial at 1600°C.

Examining Figure 5.6(a), it appears that the regeneration process works, but not for the entire duration of each of the 6-hour electrolysis periods. The O_2 content is high for the first hour of electrolysis but decreases to approximately half of the starting value after two hours of electrolysis. Electrolysis #4 appears to be the most stable electrolysis period of the three shown in Figure 5.6. Using the data for regeneration #4 and electrolysis #4, the ideal operation of the YSZ hollow anode should be 1 hour of electrolysis, to produce O_2 at the highest rate, followed by a regeneration period of 30 minutes with an applied reverse potential. However, the duty cycle of this concept of operation is only 67% (60 minutes of electrolysis divided by 90 minutes of total time per cycle). This is likely too low of a duty cycle to meet the O_2 production rates necessary for oxidizer resupply. Thus, from this regeneration testing data, it appears that regeneration methods may not be suitable for long-term O_2 production using a hollow anode in MRE reactors. The next section explorers whether the regeneration duration can be shortened from 30 minutes, which would improve the duty cycle of electrolysis.

5.4.3 Cell resistance testing

In the previous section, the shortest duration regeneration method tested was 30 minutes. However, it is possible that even shorter regeneration durations can reduce the electronic conductivity of YSZ. The resistance of the electrolysis cell is a useful proxy for evaluating the electronic conductivity of YSZ. From Figure 5.2, the ionic and electronic paths for the applied current can be represented as two resistors in parallel. As the electronic conductivity of YSZ is reduced, the resistance of the electronic path increases, which results in an increase in the overall cell resistance. After electrolysis #4 was completed, the cell resistance was monitored in every 5 minutes, while the carrier gas was switched from Ar to 10% O_2. These data provide guidance for how short the regeneration period can be before an increase in cell resistance is detected, which indicates that the electronic conductivity of YSZ has decreased. The cell resistances and the measured O_2 content are presented in Figure 5.7.

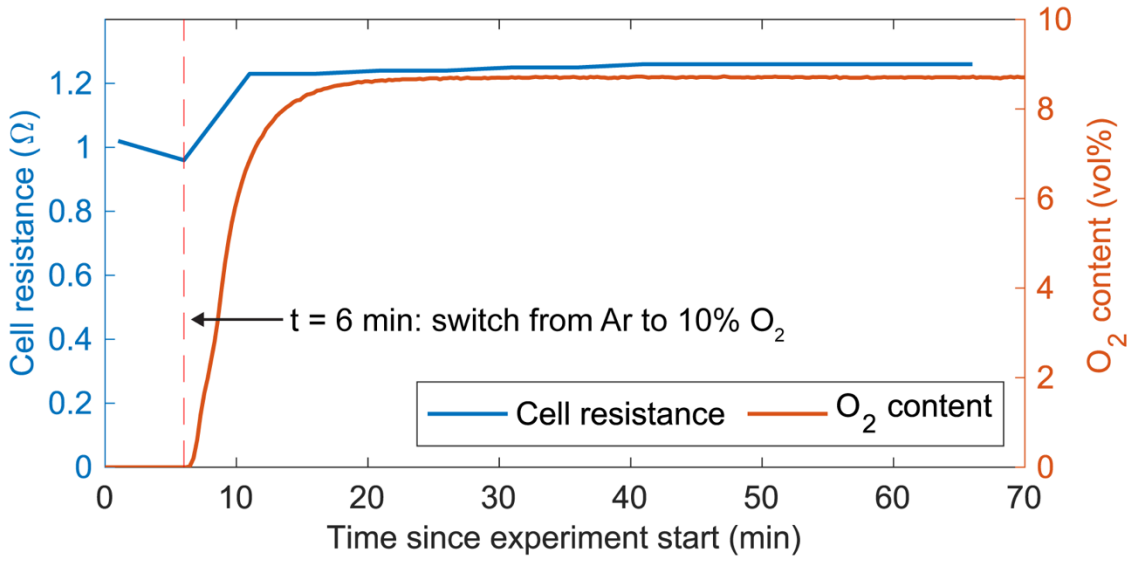

Figure 5.7. Cell resistance (left) and O_2 content of the outlet gas (right) vs. elapsed time since experiment start. Switchover from Ar to 10% O_2 flow occurs at 6 minutes.

Based on data in Figure 5.7, the cell resistance increases from ~ 1 Ω to ~1.25 Ω approximately 5 minutes after the carrier gas is switched from Ar to 10% O_2. There is a gradual increase in resistance over the next 60 minutes, but most of the cell resistance increase has occurred by 5 to 10 minutes after the gas switchover. This is direct evidence that the YSZ electronic conductivity can be reduced by exposing the cell to high pO_2 gas. Additionally, these results indicate that the previous regeneration methods are likely too long in duration. Thus, the duty cycle for a regeneration process can be revaluated using this data.

The data in Figure 5.7 suggest that a conservative estimate of 10 minutes of regeneration in 10% O_2 is enough to reduce the electronic conductivity of YSZ. If a similar electrolysis period of 60 minutes of high O_2 production is performed after regeneration, then the duty cycle increases to 86%. This higher duty cycle may be acceptable for the lunar surface, but further systems analysis is required to determine if this is the case. Ideally, an electrolysis segment under Ar should be performed after a shorter duration regeneration method to validate the notion that a shorter regeneration method can be applied. However, due to the limited time at 1600°C, this experiment was deprioritized in favor of the mitigation experiments presented in the next section.

5.4.4 Mitigation experiments

The mitigation experiments evaluated performing MRE directly in 10% O_2 (high pO_2) instead of Ar (low pO_2). Electrolysis #5 was the initial mitigation experiment whereby electrolysis was performed for 6 hours. The results of electrolysis #5 were promising, so electrolysis #6 pushed the electrolysis duration to 10 hours. The volumetric percentage of O_2 in the outlet gas stream and the potential required to maintain 0.5 A of current through the cell for electrolysis #5 and #6 are presented in Figure 5.8. The data from electrolysis #4 are also included in Figure 5.8 for comparison.

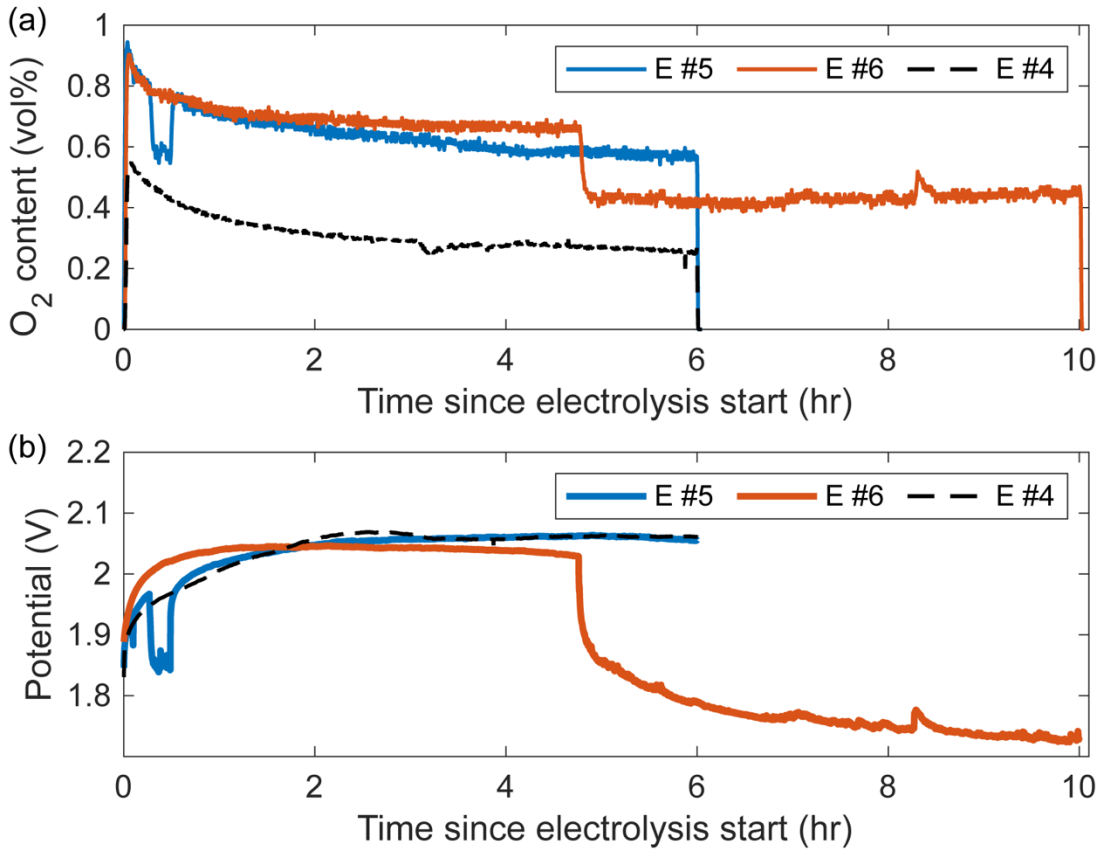

Figure 5.8. (a) O_2 content of outlet gas stream and (b) potential across electrolysis cell vs. elapsed time since electrolysis start for electrolysis #5 and #6 (10% O_2). The data from electrolysis #4 (Ar) are also shown for comparison.

In Figure 5.8(a), electrolysis #5 and #6 both achieved a higher O_2 production rate compared to electrolysis #4. On average, both the mitigation experiments achieved approximately double the O_2 production rate. These results suggest that the mitigation strategy of operating hollow anodes in a high pO_2 environment outperforms the previously discussed regeneration methods.

In both electrolysis #5 and #6, similar sharp decreases in O_2 content and applied potential are observed. This behavior is also attributed to the formation of cathodic shorts, which has been discussed in Section 5.4.1. In electrolysis #6, there is a significant drop in O_2 content and applied potential, occurring after 5 hours of electrolysis. This is likely due to a large droplet of cathodic product that has bridged the cathode and YSZ. Unlike the spikes observed in previous electrolysis segments, this decrease persists for the reminder of the electrolysis period (5 hours). However, even in this decreased O_2 production region, the average O_2 production rate is still higher than the average O_2 production rate observed in electrolysis #4. As stated previously, this type of behavior is caused by the confined cell geometry and is not expected to affect the envisioned operation of YSZ hollow anodes.

In Figure 5.8(b), the initial behavior of the applied potential is similar between electrolysis #5 and #6. Interestingly, the applied potential is also similar to electrolysis #4, which was performed in Ar. Since O_2 is one of the products of electrolysis, the Nernst equation indicates that there should be an increase in the equilibrium potential since there is now a higher pO_2 in the surrounding gas environment (Appendix C). However, this effect is not observed in Figure 5.8(b). Electrolysis #5 is nearly identical in applied potential to electrolysis #4, while electrolysis #6 has a lower applied potential than both. This behavior is attributed to a reduction in bubble formation at the YSZ/regolith interface. As discussed previously, the presence of bubbles at the YSZ/regolith interface reduces the active area available for electrolysis, requiring a larger overpotential to maintain the same current in the cell. If the electronic conductivity of YSZ is lower, then fewer bubbles will be generated at the YSZ/regolith interface, reducing the overpotential needed to maintain 0.5 A in the cell. This effect appears to offset the increased Nernst potential, resulting from producing O_2 into a high pO_2 environment.

5.4.5 Microscopy of cross-sectioned cell

Optical microscopy of the polished, cross-sectioned cell is presented in Figure 5.9. In general, the YSZ is in good condition after exposure to molten regolith at 1600°C for 48 hours. In the region near the cathode and anode, there is clear evidence of an electronic short that forms from the cathodic products. Evidence of accelerated degradation is observed on both the Mo cathode and the YSZ solid electrolyte contacting the cathodic product short. This localized, accelerated degradation is attributed to localized Joule heating due to electrons flowing through the cathodic product short, causing higher temperatures in this region.

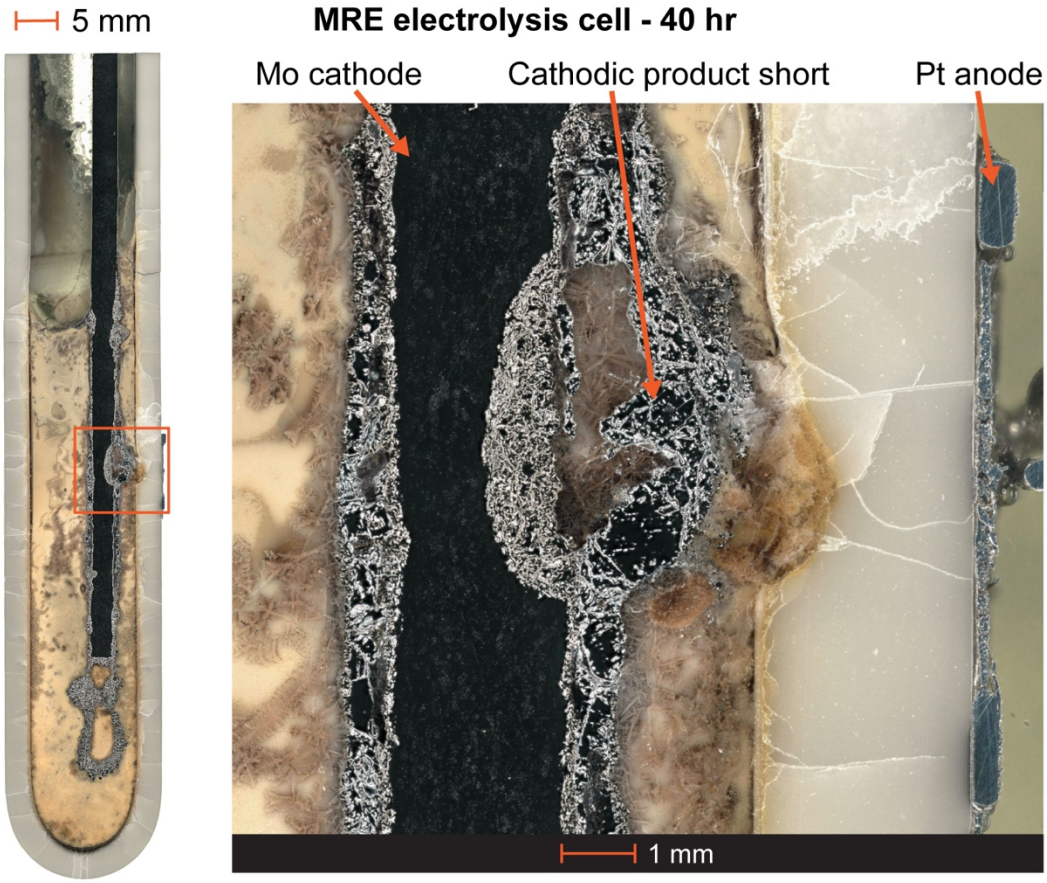

Figure 5.9. Optical microscopy of cross-sectioned YSZ inverted hollow anode used in regeneration and mitigation testing. The entire cell is shown on the left. The region near the cathode and anode with a cathodic product short is shown on the right.

Most of the cathodic products have settled toward the bottom of the cell, as expected based on their higher density. The solidified regolith has significantly more tan-colored opacity compared to the 12-hour electrolysis cell from Chapter 4 (Figure 4.5). Though compositional analysis was not performed on this cell, prior analysis from Chapter 4 indicates that this opacity is caused by nucleation of YSZ during cooling, due to the decreasing solubility of YSZ in molten LHS-1 with decreasing temperature. Beyond the localized YSZ degradation observed near the Pt anode, the majority of the YSZ appears to be in similar condition to the YSZ in the 12-hour electrolysis cell from Chapter 4. The estimate from Chapter 4 was that it would take approximately 9 days for the YSZ wall recession to reach 1.5 mm, which is half of the initial wall thickness of 3 mm. Based on Figure 5.9, it appears that estimate is likely accurate, since 48 hours of exposure to molten regolith have not caused significant YSZ wall recession. A refined design life estimate for YSZ is presented in Section 5.5.3 based on the wall recession measurements obtained from Figure 5.9.

5.5 Implications for hollow anode design

5.5.1 Regeneration vs. mitigation

Based on the results presented in Sections 5.4.2 and 5.4.4, the mitigation strategy of operating in high pO_2 environments outperforms the regeneration methods necessary for operating in low pO_2 environments. Table 5.4 presents a summary of each electrolysis segment, along with the mass of O_2 produced and the anodic Faradaic efficiency of each segment. The methodology for calculating the anodic Faradaic efficiency is the same as that reported in Chapter 4 (Section 4.3.1). Based on Table 5.4, the mitigation experiments (electrolysis #5 and #6) have the highest Faradaic efficiency, resulting from the lower electronic conductivity of YSZ from operating in a high pO_2 environment. All electrolysis periods following regeneration (#2, #3, and #4) have Faradaic efficiencies that are approximately half of the Faradaic efficiencies of the mitigation experiments. Thus, it is clear that the mitigation strategy should be employed in future testing of YSZ hollow anodes. It is noted that the mitigation experiments and Brouwer diagram (Figure 5.4) suggest that even higher pO_2 may offer improved performance.

Table 5.4. Summary of each electrolysis segment and associated Faradaic efficiencies

Electrolysis #	Duration	Carrier gas	Mass of O_2 produced	Anodic Faradaic efficiency
#1	6 hours	Ar	0.275 g	30.8%
#2	6 hours	Ar	0.184 g	20.6%
#3	6 hours	Ar	0.157 g	17.5%
#4	6 hours	Ar	0.161 g	18.0%
#5	6 hours	10% O_2	0.308 g	34.5%
#6	10 hours	10% O_2	0.480 g	32.2%
Total	40 hours	Both	1.566 g	26.3%

Implementing the mitigation strategy in MRE reactors incorporating a YSZ hollow anode should be straightforward. Since O_2 is already produced by electrolysis, two methods are proposed. The first method is to control the gas flow rate sent to collection such that the headspace (empty volume above the molten regolith) of the reactor remains at high pO_2 due to the produced O_2. The second method is to split the flow of the generated O_2 so that a certain percentage of the generated O_2 is recirculated into the headspace of the reactor. Both methods can be accomplished with a mass flow controller to control O_2 flow and a pressure transducer measuring the headspace pressure of a MRE reactor. The only concerns that this mitigation strategy presents are oxidation of the pressure vessel containing the MRE reactor. However, it is likely that the reactor will be lined with refractory oxide materials to reduce thermal losses from the heated region of the reactor, in which case, oxidation is not a concern.

If a low pO_2 environment is preferred, then regeneration may still be viable. Section 5.4.3 provided evidence that a shorter regeneration duration (5 – 10 minutes) may achieve the same results as the 30 minute and 60 minute regenerations tests that were performed. Further testing is required to provide validation that this method can work.

5.5.2 YSZ wall recession

The cross-sectioned cell provides another data point at longer exposure durations for YSZ wall recession, which is caused by YSZ dissolution by molten lunar regolith. The method of measuring YSZ wall recession is the same as that reported in Chapter 4 (Section 4.3.5.1). The YSZ wall recessions from this chapter and from Chapter 4 are plotted against the exposure duration and presented in Figure 5.10. Since YSZ dissolution is a thermochemical degradation mechanism, the exposure duration is used instead of the electrolysis duration. In this context, the exposure duration is the amount of time that the cell was held at 1600°C in contact with molten LHS-1. The data were fit with both a single linear fit and a piecewise linear fit, both shown in Figure 5.10. A piecewise fit was selected since the recession data between 0 and 5 hours of exposure have a higher recession rate than later exposure durations.

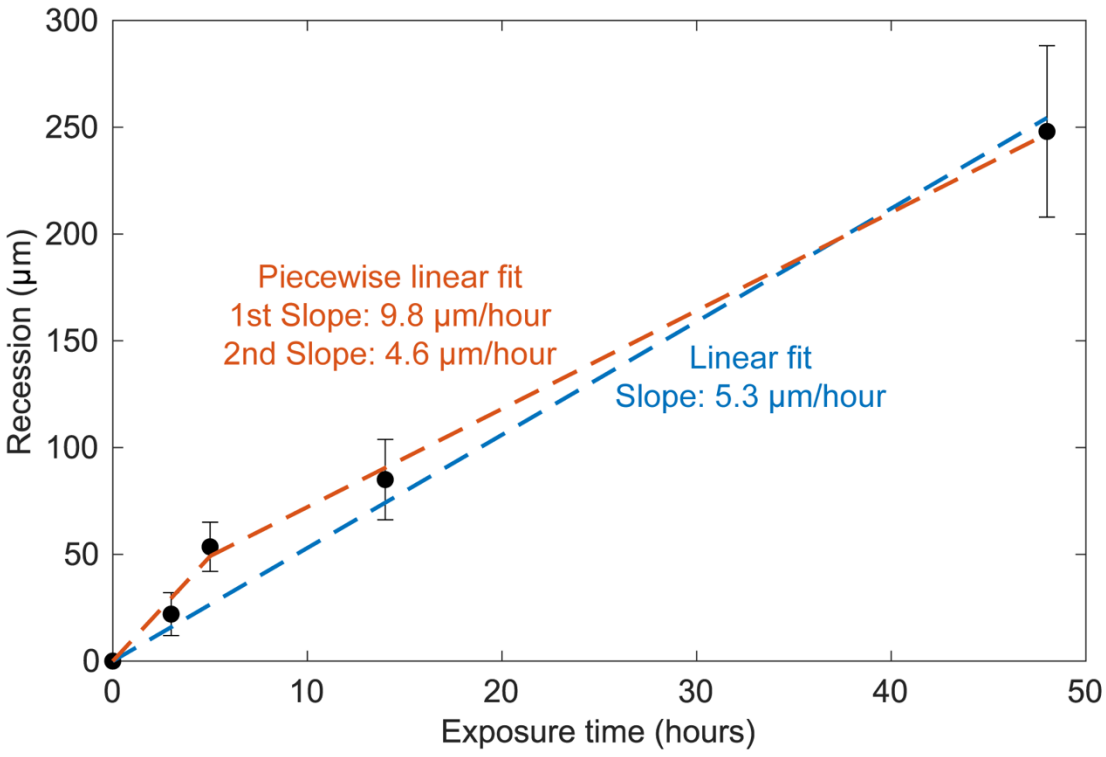

Figure 5.10. YSZ wall recession vs. exposure time. Error bars representing the standard deviation of recession measurements are shown. Linear fit shown as blue dashed line. Piecewise fit shown as orange dashed line.

5.5.3 Refined anode mass payback ratio

A metric for assessing the tradeoff between O_2 production and anode material loss over time was presented in Chapter 4 (Section 4.4.4). The same analysis is refined using the data presented in this chapter. For this analysis, a YSZ anode with dimensions of 1 cm × 1 cm and a wall thickness of 0.3 cm is considered, consistent with the geometry of the cells utilized in Chapter 4 and this chapter. Based on the manufacturer-reported density of 5.92 g/cm³, this anode has a mass of approximately 1.78 g. Due to observed thermal cycling-induced cracking, it is conservatively assumed that the full mass of the anode is lost upon reaching the end of its design life. The recession rate is obtained from Figure 5.10, with both fits evaluated. The average O_2 production rate is obtained from the results of the mitigation experiments (Table 5.4). The design life of the anode is assumed to be when the wall recession reaches half of the wall thickness (1.5 mm). The O_2 produced is calculated by multiplying the design life by the O_2 production rate. Finally, the mass payback ratio is calculated by dividing the mass of O_2 produced by the mass of YSZ consumed. These calculations are summarized in Table 5.5. The original calculation from Chapter 4 is also included for comparison.

Table 5.5. Summary of anode mass payback ratio calculations. Previous data is from Chapter 4 [11].

Description	Design life	O_2 production rate	Mass of O_2 produced	**Anode mass payback ratio**
Previous data	214 hours (8.9 days)	0.062 g/hour	13.4 g	**7.5x**
Linear fit	283 hours (11.8 days)	0.050 g/hour	14.2 g	**7.9x**
Piecewise fit	321 hours (13.4 days)	0.050 g/hour	16.1 g	**9.0x**

As discussed in Chapter 4, this estimate assumes a constant rate of O_2 production and YSZ recession, both of which require further testing to validate. Additionally, this analysis excludes the mass of the MRE system and the cathode but also does not account for the mass of cathodic products generated, which has value for in situ construction/manufacturing. Overall, the refined calculations suggest that each unit mass of YSZ delivered to the lunar surface could enable the production of up to 7.9x – 9.0x its own mass in O_2 under the assumed conditions, depending on the fit used for YSZ wall recession.

It is important to note that the average O_2 production rate has decreased from the original estimate presented in Chapter 4. In the previous estimate, the average production rate was taken from the 12-hour electrolysis cell. However, Figure 4.2 indicates that the O_2 production rate decreases with continuing electrolysis, thereby driving the evaluation of regeneration and mitigation methods in this chapter. The higher average O_2 production rate from the previous data (12-hour electrolysis cell from Chapter 4) is likely unsustainable for longer electrolysis durations. The average O_2 rate obtained from the experiments performed in this chapter represent a more accurate and sustainable rate, since O_2 production remained relatively steady in both mitigation experiments.

Despite the lower O_2 production rate, the anode mass payback ratio has increased compared to previous data. The lower O_2 production rate is offset by the lower rate of YSZ recession obtained in this chapter. This effect was hypothesized in Chapter 4 but appears to be accurate. If the YSZ recession rate continues to decrease, then the anode mass payback ratio will continue to increase. This would represent an ideal scenario for YSZ hollow anodes but will require a significant experimental campaign to confirm.

5.6 Conclusion

Based on the experimental data collected from the regeneration and mitigation experiments, it was determined that the mitigation strategy of operating the electrolysis in a high pO_2 environment outperforms the regeneration methods. Though the regeneration methods were not as successful as the mitigation strategy, it is feasible that shorter duration regeneration periods may offer some improvement in electrolysis efficiency, at the cost of decreasing the duty cycle for electrolysis. The mitigation experiments demonstrated a nearly 2x improvement in Faradaic efficiency, compared to the post-regeneration electrolysis. As a result, future YSZ hollow anode testing should be performed in a high pO_2 environment to maintain a high Faradaic efficiency while performing MRE.

The experimental data collected from the electrolysis testing and post-mortem analysis of the inverted YSZ hollow anode were used to provide average O_2 production and YSZ wall recession rates. These rates were used to refine the anode mass payback ratio, resulting in incremental improvement compared to the value presented in Chapter 4. More importantly, it is believed that the newly obtained O_2 production rate is more sustainable for longer electrolysis periods compared to the previously obtained rate. Additionally, the newly obtained YSZ wall recession rates support the hypothesis that the rate of YSZ dissolution slows with increasing exposure duration.

The 40-hour electrolysis duration achieved here represent a significant increase over the 12-hour electrolysis duration achieved in Chapter 4. However, it is noted that several examples of cathodic product shorts forming during electrolysis were observed in the experiments presented here. These shorts have been attributed to the confined, vertical geometry of the inverted hollow anode cell design. Ultimately, there is no replacement for extended duration testing of YSZ hollow anodes in MRE reactors to enable their usage in a flight-ready MRE system. However, it does not appear that extended electrolysis testing can be performed with the inverted hollow anode cell design used here. Further testing should be performed in larger-scale MRE reactors with the envisioned configuration to remove the limitations of the inverted hollow anode cell.

References

[1] M.S. Humbert, G.A. Brooks, A.R. Duffy, C. Hargrave, M.A. Rhamdhani, Thermophysical property evolution during molten regolith electrolysis, Planet Space Sci 219 (2022) 105527. https://doi.org/10.1016/j.pss.2022.105527.

[2] P.A. Burke, M.E. Nord, C.A. Hibbitts, J.R. Berdis, Modeling electrolysis in reduced gravity: producing oxygen from in-situ resources at the moon and beyond, Front. Space Technol. 5 (2024). https://doi.org/10.3389/frspt.2024.1304579.

[3] B.A. Lomax, G.H. Just, P.J. McHugh, P.K. Broadley, G.C. Hutchings, P.A. Burke, M.J. Roy, K.L. Smith, M.D. Symes, Predicting the efficiency of oxygen-evolving electrolysis on the Moon and Mars, Nat Commun 13 (2022) 583. https://doi.org/10.1038/s41467-022-28147-5.

[4] M. Barati, K.S. Coley, Electrical and electronic conductivity of CaO-SiO_2-FeO_x slags at various oxygen potentials: Part II. Mechanism and a model of electronic conduction, Metall Mater Trans B 37 (2006) 51–60. https://doi.org/10.1007/s11663-006-0085-9.

[5] M. Wang, H. Jiao, Z. Pu, B. Hong, J. Ge, W. Xiao, S. Jiao, Ultra-High Temperature Molten Oxide Electrochemistry, Angew Chem Int Ed 61 (2022). https://doi.org/10.1002/anie.202206482.

[6] V.R. PaiVerneker, A.N. Petelin, F.J. Crowne, D.C. Nagle, Color-center-induced band-gap shift in yttria-stabilized zirconia, Phys. Rev. B 40 (1989) 8555–8557. https://doi.org/10.1103/PhysRevB.40.8555.

[7] J. Park, R.N. Blumenthal, Electronic Transport in 8 Mole Percent Y_2O_3-ZrO_2, J. Electrochem. Soc. 136 (1989) 2867–2876. https://doi.org/10.1149/1.2096302.

[8] Space Resource Technologies, LHS-1 Lunar Highlands Simulant Fact Sheet (002-01-001-0621), (2021). https://cdn.shopify.com/s/files/1/0398/9268/0862/files/lhs-1-spec-sheet-Dec2022.pptx.pdf?v=1688051876.

[9] J.J. Papike, S.B. Simon, J.C. Laul, The lunar regolith: Chemistry, mineralogy, and petrology, Reviews of Geophysics 20 (1982) 761–826. https://doi.org/10.1029/RG020i004p00761.

[10] C.A. Schneider, W.S. Rasband, K.W. Eliceiri, NIH Image to ImageJ: 25 years of image analysis, Nat Methods 9 (2012) 671–675. https://doi.org/10.1038/nmeth.2089.

[11] K. Yu, W. West, J. Stokes, B. Harder, L. Reidy, J. Dominguez, K.T. Faber, Improving molten regolith electrolysis with zirconia-based hollow anode technology, Acta Astronautica 235 (2025) 723–735. https://doi.org/10.1016/j.actaastro.2025.06.028.

Chapter 6

DISCOVERY AND CHARACTERIZATION OF A SILICON ALUMINUM SCANDATE (SAS) MATERIAL

The contents of this chapter are also presented in "Discovery and characterization of a silicon aluminum scandate (SAS) material" by K. Yu, J. Stokes, K. K. Jha, B. Harder, H. M. Nelson, and K. T. Faber, which is under review. K. Yu led the experimental portion of this work and wrote the original draft of the manuscript. J. Stokes and B. Harder provided resources and subject matter expertise to design the experiments and assist in analyzing the results. K. K. Jha performed the microcrystal electron diffraction to solve the SAS crystal structure. H. M. Nelson provided the microcrystal electron diffraction instrument and subject matter expertise. K. T. Faber supervised the work. All authors were involved in editing the manuscript.

K. Yu, J. Stokes, K.K. Jha, B. Harder, H.M. Nelson, K.T. Faber (n.d.). "Discovery and characterization of a silicon aluminum scandate (SAS) material". In: *under review*.

6.1 Introduction

Chapter 6 focuses on the synthesis, structure determination, and characterization of a newly discovered silicon aluminum scandate (SAS) material, with the nominal formula of $Si_2Al_2Sc_{14}O_{28}$. The SAS phase was first discovered in this work through reaction experiments between pure Sc_2O_3 and molten regolith simulants (Chapter 2). A phase-pure SAS material was subsequently synthesized based on the composition of the initial reaction product. This material, with minority oxide dopants of MgO, CaO, TiO_2, and Fe_2O_3, is herein referred to as doped SAS. Preliminary phase identification did not match any crystal structure in existing databases, suggesting that the doped SAS material possesses a previously unreported structure.

Sc_2O_3-based materials have garnered interest for applications such as solid state electrolytes, refractory oxide materials, and thermionic converters [1,2]. As a solid state electrolyte, Sc_2O_3 has been used to improve ionic conductivity in the oxygen conductor Sc_2O_3-ZrO_2 system [3] and in the proton conductor Sc_2O_3-$SrCeO_3$ system [4]. As a refractory material, Sc_2O_3 exhibits low creep rates compared to Al_2O_3, MgO, and ZrO_2, enabling its usage in load-supporting applications at elevated temperatures [5]. For thermionic converters, the Sc_2O_3-Y_2O_3 system can decrease converter degradation rates by leveraging the material's resistance to radiation and alkali metal plasmas [1]. Research on Sc_2O_3-based materials have typically focused on its usage with other rare earth elements (Y, Ce) or heavier transition metals (Zr).

Sc_2O_3 compounds with more common oxides, such as SiO_2, Al_2O_3, and CaO, are comparatively underexplored. Zhi et al. investigated both the CaO-Al_2O_3-Sc_2O_3 and Al_2O_3-SiO_2-Sc_2O_3 systems to evaluate the formation of reaction products [6,7]. For the CaO-Al_2O_3-Sc_2O_3 system, a single ternary oxide phase was observed, with the formula $Ca_2Sc_6Al_6O_{20}$ [6]. The $Ca_2Sc_6Al_6O_{20}$ structure, first identified from mineralogical samples as Warkite, has a low symmetry (triclinic) and a relatively large unit cell volume (739.41 $Å^3$) compared to the other phases observed in this system [8]. For the Al_2O_3-SiO_2-Sc_2O_3 system, several binary oxide phases were observed, including mullite ($Al_{4+2x}Si_{2-2x}O_{10-x}$), Sc_2SiO_5, $Sc_2Si_2O_7$, and $Sc_2Al_2O_6$ [7]. Despite the many binary reaction products observed, no ternary oxide phases were detected in their experiments. However, the authors were focused on the SiO_2-rich and Al_2O_3-rich regions of the Al_2O_3-SiO_2-Sc_2O_3 phase diagram, with the highest Sc_2O_3 composition evaluated being 50 wt% [7]. It was hypothesized that a ternary oxide phase (similar to $Ca_2Sc_6Al_6O_{20}$) may also be present in the Al_2O_3-SiO_2-Sc_2O_3 system.

Due to the small crystallite size of doped SAS, the material was not suitable for structure determination using conventional single-crystal X-ray diffraction. The unknown crystal structure of the doped SAS phase was solved using microcrystal electron diffraction since electrons interact more strongly with atoms than X-rays [9,10]. The resulting structure was then validated with powder X-ray diffraction and Rietveld refinement. Given the multiple dopants present in the material, ^{27}Al, ^{29}Si, and ^{45}Sc solid-state nuclear magnetic resonance was employed to probe the local coordination of Al, Si, and Sc and to provide guidance for

minority dopant substitutions. These results collectively elucidate the atomic structure of the doped SAS phase and enable further materials characterization techniques to be used.

Due to the refractory nature of Sc_2O_3, it is hypothesized that the doped SAS material may also have high-temperature applications. The remainder of this study investigates properties relevant to its use as a refractory material, including thermal expansion, maximum usage temperature, reaction pathway, and thermal conductivity. High-temperature, in situ X-ray diffraction was employed to assess the thermal expansion of the doped SAS structure. Differential thermal analysis established the temperature limit of thermal stability, providing a maximum usage temperature. A combination of high-temperature X-ray diffraction and annealing experiments provided insight into how the doped SAS material forms from oxide precursors. Laser flash analysis was employed to characterize the thermal conductivity of doped SAS. Finally, implications of the doped SAS phase are discussed based on these material characterization results. The measured material properties suggest that the doped SAS phase has applications as a thermally insulating, refractory material.

6.2 Materials and methods

6.2.1 Experimental methods

6.2.1.1 Powder synthesis

The doped silicon aluminum scandate (SAS) material was produced through a conventional solid-state reaction using oxide precursors. Sc_2O_3 (99.999%, HEFA Rare Earth Canada Co. Ltd.), Al_2O_3 (>99.0%, Almatis Inc.), SiO_2 (99.5% Alfa Aesar), $CaCO_3$ (>99.0% Alfa Aesar), MgO (99.95%, Cerac Inc.), Fe_2O_3 (99%, Alfa Aesar), and TiO_2 (99.99%, MTI Corp.) were added to a ball-milling vial in amounts shown in Table 6.1 to produce a 100 g batch. The precursor powders were mixed in ethanol using 10 mm cylindrical yttria-stabilized zirconia media on a ball mill for 16 hours. The powders were then dried at 200°C in a bake-out furnace prior to heat treatment to produce the precursor mixture. To convert this mixture into the doped SAS phase, the powder was heat-treated in a platinum crucible at 2°C/min to 950°C and held for 10 hours to decompose the $CaCO_3$ into CaO and CO_2. Following decomposition,

the powders were heated at 10°C/min to 1600°C and held for 10 hours to form the doped SAS phase. Figure 6.1 shows the color change from the precursor mixture (pink) to the converted, doped SAS phase (tan).

Table 6.1. Binary oxide loading amount (grams) for producing doped SAS phase.

Sc_2O_3	Al_2O_3	SiO_2	$CaCO_3$	MgO	Fe_2O_3	TiO_2
74.794	9.117	12.263	1.284	0.752	0.900	0.807

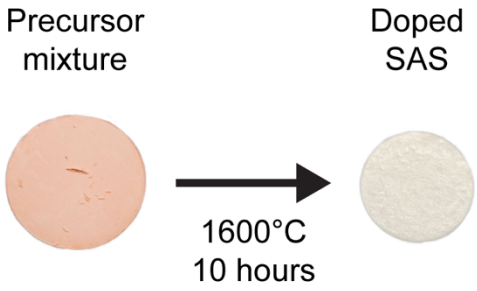

Figure 6.1. Image showing the pink color of the precursor mixture and the tan color of the converted doped SAS phase.

6.2.1.2 Pellet experiments

Sintered, polycrystalline pellets of the doped SAS material were produced to evaluate the composition over large (~10 mm) length scales. Approximately 0.5 g of the precursor mixture was uniaxially pressed in a 12.7 mm diameter die. The resulting pellet was heat-treated using the same thermal profile as the powders to convert the precursor mixture into the doped SAS phase. The resulting fully converted pellet was mounted in epoxy and polished for compositional and microstructural analysis.

Additionally, pellets pressed from the mixed precursor powder were also used to perform a heat-treatment study to determine the extent of reaction as a function of temperature. In these experiments, a precursor pellet was heated at 2°C/min to 950°C for 10 hours (to decompose

$CaCO_3$) and then heated at 10°C/min to 1300°C, 1400°C, 1500°C, or 1600°C and held at the target temperature for 10 hours. The resulting pellets were then divided in half, with one half being ground up using a mortar and pestle for X-ray diffraction (XRD) and the other half mounted in epoxy and polished for scanning electron microscopy (SEM).

6.2.2 Microcrystal electron diffraction

Microcrystal electron diffraction (MicroED) was used to solve the crystal structure of the doped SAS phase. The powder was loaded on a 3 mm copper grid with 200 mesh and Formvar/carbon support by shaking the grid in the powder. The specimen grid was tapped to knock off excess powder and to avoid overloading the grid. The diffraction dataset was collected on a ThermoFisher Talos Arctica transmission electron microscope equipped with a CetaD camera and an autoloader, operating with an accelerating voltage of 200 keV at 80 K, and an electron wavelength of 0.0251 Å. Data were amassed in a continuous diffraction mode by rotating crystallites at a rate of 0.3° per second with the detector distance set to 960 mm and the tilt range typically from −65° to +65°. Crystals chosen for data collection were isolated by a selected area aperture of 100 μm to reduce the background noise contributions and calibrated to eucentric height to stay in the aperture over the entire tilt range. All diffraction data were processed using the XDS suite of programs [11–13]. Datasets from four crystallites were merged. The structure was solved *ab initio* by direct methods in SHELXT [14]. The preliminary structure solution was refined with olex2.refine using the Olex2 program and incorporating electron scattering factors [15,16]. Thermal parameters were refined as anisotropic.

6.2.3 X-ray diffraction

6.2.3.1 Ambient X-ray diffraction

XRD (Bruker D8, Cu Kα radiation) was performed at room temperature on the fully converted, doped SAS phase. Data were collected from 10° to 80° 2θ. Initial phase identification was performed with the Powder Diffraction File database (International Center for Diffraction Data PDF-4+) and did not reveal any crystalline phases that matched the

acquired data. The solved structure obtained from MicroED was then used to perform whole pattern fitting (Rietveld refinement) for the doped SAS using JADE analysis software (International Center for Diffraction Data).

Additionally, the same procedure was used on the powders obtained from the pellet experiments (Section 6.2.1.2). The doped SAS structure was imported from the MicroED analysis, while other crystalline phases were obtained from the PDF-4+ database. Whole pattern fitting was employed to determine the weight percent of each phase after annealing at 1300°C, 1400°C, 1500°C, or 1600°C.

6.2.3.2 High-temperature in situ X-ray diffraction

In situ XRD (Panalytical Empyrean, Co Kα) was performed using a platinum heating strip (Anton Paar HTK 2000N), which allowed for XRD to be performed up to 1500°C in air. It is noted that the high-temperature XRD measurements were performed with a Co Kα source instead of a Cu Kα source used in the ambient temperature diffractometer. National Institutes of Standards and Technology (NIST) standard reference material (SRM) 676a aluminum oxide (Al_2O_3) powder was used as a calibrant to determine temperature set points for the platinum heating strip. Two experiments were performed on the hot-stage XRD. The first experiment was used to determine the crystallographic coefficients of thermal expansion (CTE) as a function of temperature. For this experiment, fully reacted SAS powder was dispersed on the platinum strip heater with isopropanol. Once dried, XRD scans were taken with a large 2θ range of 10° to 100° at 200°C increments from room temperature to 1000°C and then in 100°C increments from 1000°C to 1500°C. The lattice parameters (a, b, c, α, β, γ) were determined from each scan using a Le Bail refinement in TOPAS (Bruker) [17]. The lattice parameters and Bragg peaks were processed using the coefficient of thermal expansion analysis suite (CTEAS) to obtain a thermal expansion tensor, along with the eigenvalues and eigenvectors of the tensor [18].

The second experiment was to monitor the phases that form during the SAS reaction by placing the precursor mixture powder on the platinum strip heater. For these scans, a small

2θ range of 24° to 42° was used to minimize the scan time (6 minutes) and to cover the maximum intensity diffraction peaks of the major precursors (Sc_2O_3, SiO_2, and Al_2O_3) and the doped SAS phase. Due to the reaction between the precursors, it was important to minimize the scan time so that the material did not change significantly during the scan. Scans were performed at 200°C increments from room temperature to 1000°C and then in 100°C increments from 1000°C to 1500°C. Scans were also taken every 6 minutes once the heater reached 1500°C for 1 hour. Whole pattern fitting was performed in JADE to determine the weight percent of each crystalline phase for each scan.

6.2.4 Electron-probe microanalysis

The composition of a pellet of doped SAS was obtained using electron-probe microanalysis (EPMA) (JEOL JXA-iHP200F). Standards were used for Sc, Al, Si, Ca, Mg, Fe, and Ti. Oxygen content was obtained based on stoichiometry, assuming all species were fully oxidized. Since Ti^{4+} (TiO_2) and Fe^{3+} (Fe_2O_3) were used in the precursors and the heat treatment was performed in air, it is expected that Ti and Fe remain in their fully oxidized states. Compositional analysis was performed on 51 sites, spread evenly over a ~11 mm diameter pellet to determine if there were any compositional variations across the doped SAS material.

6.2.5 Scanning electron microscopy

The microstructure of doped SAS pellets was evaluated using SEM (ZEISS 1550VP FESEM) with a backscattered electron (BSE) detector. Specifically, a portion of each of the precursor pellets that were heated to 1300°C, 1400°C, 1500°C, or 1600°C (Section 6.2.1.2) were evaluated to qualitatively determine porosity and SAS reaction conversion.

Electron backscatter diffraction (EBSD) (Oxford Instruments HKL EBSD) was used to assess the microstructure of doped SAS grains in a fully reacted, sintered pellet (1600°C). EBSD point analysis was employed to determine grain orientations relative to cracking observed in the specimen. The EBSD pattern was collected using 2x2 binning, with an 87 millisecond frame acquisition time and 8 frame averaging. Pattern indexing was performed

using Aztec (Oxford Instruments) with 8 bands used for solutions to account for the large number of reflectors present in the doped SAS crystal structure.

6.2.6 Solid-state nuclear magnetic resonance

Solid-state nuclear magnetic resonance (NMR) experiments were performed on the fully reacted, doped SAS powder. ^{45}Sc, ^{27}Al, and ^{29}Si magic angle spinning (MAS) NMR spectra were collected using a Bruker DSX-500 spectrometer equipped with a 2 mm probe (Ago Samoson) and a 4 mm probe (Bruker). The minority dopants (Ca, Mg, Fe, Ti) were too low in concentration to obtain NMR spectra. For ^{45}Sc, a 2 mm diameter rotor was spun at 32,000 Hz and the chemical shift was referenced with a 1M $Sc(NO_3)_3$ aqueous solution. For ^{27}Al, a 2 mm diameter rotor was spun at 32,400 Hz and the chemical shift was externally referenced with a 1M $Al(NO_3)_3$ aqueous solution. For ^{29}Si, a 4 mm diameter rotor was spun at 8,000 Hz with $Si(CH_3)_4$ (tetramethylsilane) as the chemical shift reference. Peak fitting was performed using DMFit to determine the relative occupancy of sites by integrating the simulated peak intensities [19]. The Monte Carlo procedure in DMFit was used to obtain the standard deviations of relative occupancy using 250 iterations for each NMR spectra [19].

6.2.7 Differential thermal analysis

Differential thermal analysis (DTA) and thermogravimetric analysis (TGA) (Setaram Themys TG-DTA) were performed on both the precursor mixture and the reacted, doped SAS powder. For the precursor mixture, DTA was performed up to 1600°C with a 5°C/min heating rate in a platinum crucible and under flowing air. The primary goal of the precursor mixture experiment was to determine the temperature at which the SAS reaction occurs and whether the heat of reaction is endothermic or exothermic. For the reacted SAS powder, DTA was performed up to 2400°C with a 10°C/min heating rate in a tungsten crucible and under flowing argon. The objective of the reacted SAS experiment was to determine the maximum usage temperature of the doped SAS material.

6.2.8 Laser flash analysis

Laser flash analysis (Netzsch LFA 457) was performed on a sintered, doped SAS pellet in vacuum, from ambient temperature to 1000°C. The pellet geometry was approximately 11 mm in diameter and 1.5 mm thick. The sample density was 3.405 g/cm^3 (~90% dense). A PyroCeram 9606 standard was used to obtain the specific heat capacity, which was used to calculate the thermal conductivity of the doped SAS sample.

6.3 Results

6.3.1 Structure determination

6.3.1.1 Microcrystal electron diffraction solution

MicroED was performed on four micro-/nano-sized, doped SAS crystallites to obtain continuous diffraction patterns. Figure 6.2 presents the doped SAS crystallites (a) and a still frame of the continuous diffraction patterns (b) of the doped SAS crystallites. Full continuous diffraction datasets are accessible on Zenodo (10.5281/zenodo.15992324). Through merging the datasets collected from the four crystallites, a completeness of 97.2% is obtained at 0.8 Å resolution. The final reliability factor ($\#R_1$) obtained from this fit is 12.98%. A Crystallographic Information File (CIF) produced from this structure solution and deposited into the Cambridge Structural Database (CCDC: 2473395). This CIF is used as the basis for XRD and EBSD experiments, enabling further characterization of the doped SAS phase. The refinement process of the structure did not include dopant substitutions since it is unclear which specific sites within the doped SAS crystal structure contain partial occupancy. The lattice parameters and unit cell volume are presented in Table 6.2 (Section 6.3.1.3).

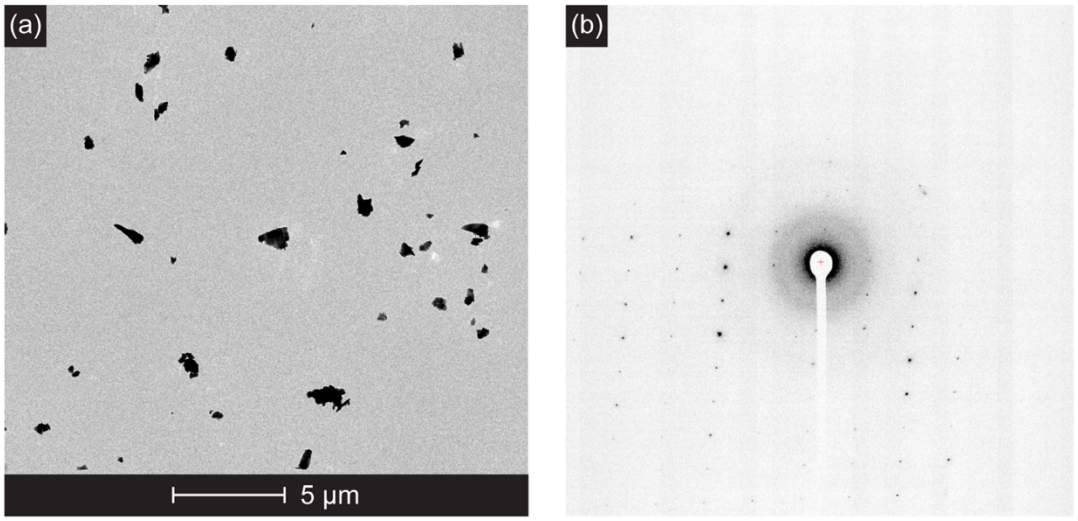

Figure 6.2. (a) Transmission electron microscope image of doped SAS crystallites and (b) selected area diffraction still frame (from continuous diffraction dataset) of doped SAS crystallite, both from MicroED.

6.3.1.2 Powder XRD refinement

Rietveld refinement was performed on the ambient temperature, powder XRD pattern collected from the doped SAS powder. The structure from MicroED was imported to provide a baseline for the doped SAS phase. The XRD data are presented in Figure 6.3. The doped SAS phase is the only crystalline phase that was detected. The major precursor oxides (Sc_2O_3, Al_2O_3, and SiO_2) and possible reaction products (Sc_2SiO_5 and $Sc_2Si_2O_7$) were included in the analysis and are presented in Appendix G (G.1). No additional peaks from these precursors and possible reaction phases are observed. This suggests that the reaction is completed following the heat treatment of the precursor powder mixture and that the primary reaction product is the doped SAS phase. The final reliability factor (R_{wp}) obtained from Rietveld refinement is 9.35%.

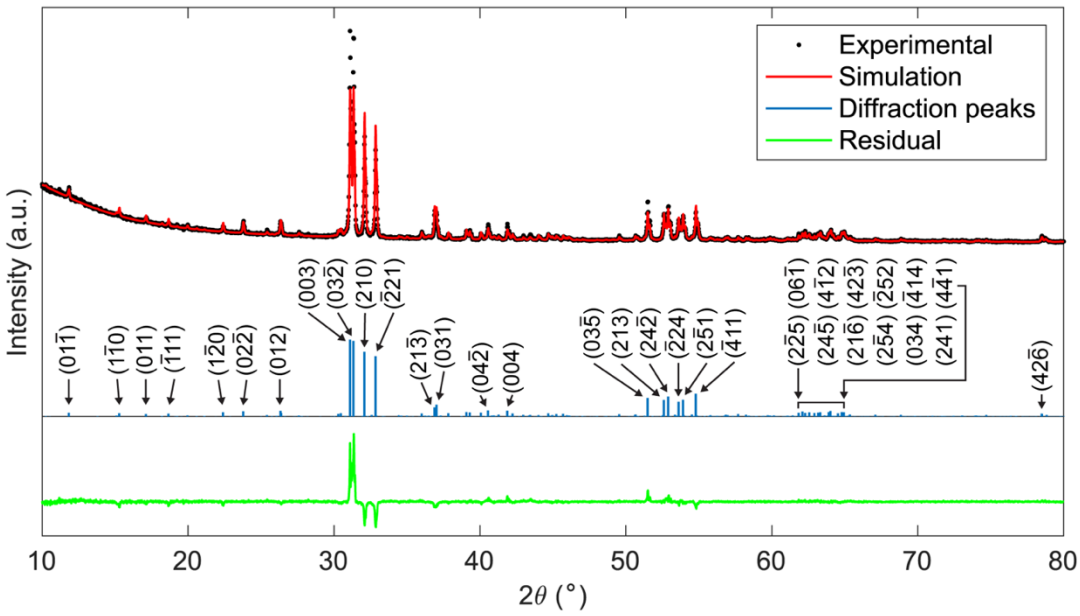

Figure 6.3. XRD (Cu Kα) of doped SAS powder with simulated pattern after Rietveld refinement (red), calculated diffraction peaks (blue), and residual error (green).

From this analysis, the lattice parameters and volume of the unit cell were obtained at room temperature. These data are summarized in Table 6.2 (Section 6.3.1.3). It is noted that site substitution by the dopant cations was not included in the refinement process. The largest residual error occurs at the highest intensity Bragg peaks between a 2θ of 30° and 33°. The data suggest that the relative intensity of these peaks, as calculated from the crystal structure, are not consistent with experimentally measured intensities. However, including the dopant substitutions equally on each Sc site results in a larger refinement error, which is provided in Appendix G (G.2). This larger refinement error suggests the substitution of each dopant species on specific Sc sites and the formation of defects due to aliovalent dopant substitution. These effects can alter the relative intensities of diffraction peaks due to differences in the X-ray scattering cross-sections of specific Sc sites [20]. However, the peak locations are consistent with the solved crystal structure obtained from MicroED, signifying that the atomic positions and lattice parameters derived from MicroED are accurate.

6.3.1.3 Crystal structure

The crystal structure of the SAS phase derived from MicroED, without the dopant cations (Ca, Mg, Fe, Ti) or site substitutions, is presented in Figure 6.4. The unit cell is in the triclinic crystal system, with a space group of $P\bar{1}$. The stoichiometric unit cell formula is $Si_2Al_2Sc_{14}O_{28}$, with one unique Si site, one unique Al site, and seven unique Sc sites. Based on MicroED analysis, the Si site has near-ideal tetrahedral coordination with O^{2-} and the Al site has a distorted tetrahedral coordination, bordering on a trigonal bipyramidal, 5-folded coordination with O^{2-}. Of the seven unique Sc sites, four have octahedral coordination (Sc01, Sc02, Sc06, Sc07 in Figure 6.4) and three have 7-fold coordination (Sc03, Sc04, Sc05 in Figure 6.4) with O^{2-}. Additional analysis on the coordination of each Sc site is presented in Appendix G (G.3).

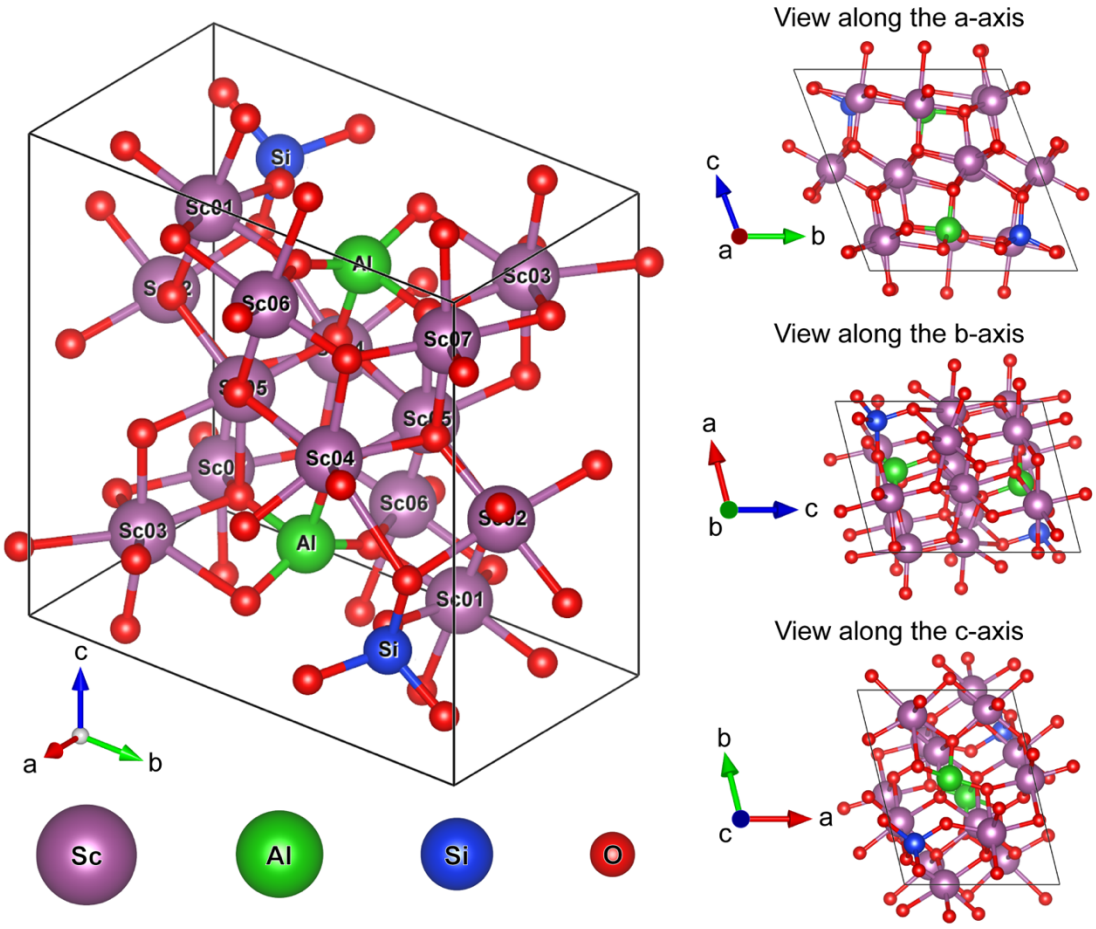

Figure 6.4. Isometric view of $Si_2Al_2Sc_{14}O_{28}$ unit cell with views along the a-, b-, and c-axes.

A comparison of the lattice parameters and unit cell volumes obtained from MicroED and XRD is presented in Table 6.2. The results are consistent between the two techniques, indicating that the solved structure is correct. There are small differences (~1%) between the two results. These discrepancies are mostly attributed to the sampling differences between MicroED and XRD. In the MicroED data, only four crystallites were analyzed at 80 K under vacuum to obtain the structure. In contrast, the XRD data were obtained from doped SAS powder, consisting of significantly more crystallites at ambient temperature and pressure. Thus, the XRD data represent an average unit cell of the powder, whereas the MicroED result is specific to the crystallites analyzed. It is possible that there are minor variations of unit cell lattice parameters between crystallites that result in the differences observed between the two techniques.

Table 6.2. Unit cell lattice parameters obtained from MicroED and powder XRD. Standard deviations are presented in parentheses.

Lattice Parameter	MicroED	XRD
a [Å]	6.800(1)	6.6988(7)
b [Å]	9.090(2)	9.1084(6)
c [Å]	9.420(4)	9.3517(6)
α [°]	108.306(8)	108.273(4)
β [°]	100.173(9)	99.951(4)
γ [°]	99.518(8)	99.467(3)
V [Å^3]	528.7(3)	518.88(7)

6.3.1.4 Solid-state NMR

Solid-state NMR with MAS was performed to evaluate the local structure of Si, Al, and Sc. It is likely that there are substitutions in the structure, both between the majority Sc^{3+}, Si^{4+}, and Al^{3+} cations, as well as the dopant cations. The NMR spectra and simulated lineshapes for Si, Al, and Sc are presented in Figure 6.5. The ^{27}Al and ^{29}Si NMR spectra have lower signal-to-noise ratios compared to ^{45}Sc. This is attributed to the lower concentrations of Si and Al in doped SAS relative to Sc. Additionally, for ^{27}Al, a faster spinning frequency was necessary to avoid spinning side bands from overlapping. This resulted in the usage of a smaller rotor that also limited the amount of sample loading in comparison to ^{29}Si. The rotor contained Al impurities, which are labeled in Figure 6.5. This impurity peak was fit and then deconvoluted from the integrated intensity for ^{27}Al. The partial occupancy of each coordination for Sc, Al, and Si is presented later in this work in Table 6.4 (Section 6.3.2.1).

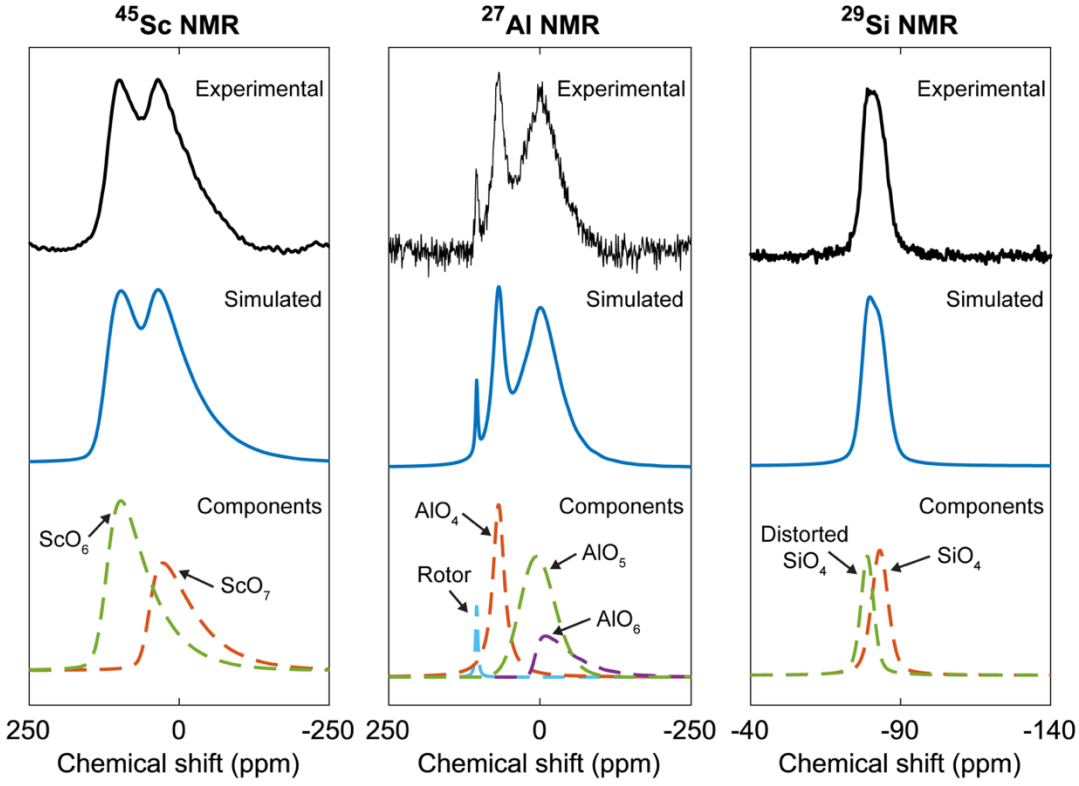

Figure 6.5. MAS NMR spectra for ^{45}Sc, ^{27}Al, and ^{29}Si. Simulated lineshapes and component curves, obtained from DMFit, are also presented.

The ^{45}Sc NMR spectra contain two asymmetric peaks. The asymmetry of these peaks is attributed to second-order quadrupolar interactions, similar to other reports of ^{45}Sc [21,22]. Due to the number of Sc sites available in the crystal structure (four for ScO_6 and three for ScO_7), the Czjzek distribution was used by approximating the different sites as disorder around 6-fold and 7-fold coordinated Sc atoms [23]. Literature reports of ^{45}Sc NMR give an account of a trend of decreasing chemical shift with increasing Sc coordination number [24–26]. Thus, the left peak (higher chemical shift) is attributed to 6-fold coordinated Sc and the right peak (lower chemical shift) is attributed to 7-fold coordinated Sc. Qualitatively, the relative areas under each component curve are consistent with the doped SAS structure obtained from MicroED: there are more Sc atoms in 6-fold coordination (four sites) than in 7-fold coordination (three sites).

The ^{27}Al NMR spectra also contain two peaks other than the rotor impurity peak. However, the broader peak at lower chemical shift was not able to be fit by a single Gaussian/Lorentzian curve. Thus, the broader peak was fit with two components. Al in oxides with 4-fold and 6-fold coordination are common. Al in oxides with 5-fold coordination is rare, but has been observed in the andalusite [27,28] and strontium/calcium hexaluminate structures [29,30]. Similar to Sc, Al also exhibits a trend of decreasing chemical shifts with increasing coordination number [31,32]. The AlO_4 peak (tetrahedral) is attributed to Al substitution on the Si site in the doped SAS structure. The AlO_5 peak is ascribed to the single Al site in the doped SAS structure and the AlO_6 peak (octahedral) is attributed to Al substitution on one or more of the four octahedral Sc sites. Since there is only a single Si site and Al site in the doped SAS structure, these peaks were fit with a Gaussian/Lorentzian curve. However, there are multiple octahedral Sc sites, which required the Czjzek model to fit the AlO_6 component. The relative areas under each component are also consistent with the doped SAS crystal structure, indicating that Al atoms predominantly occupy the Al site, with a smaller fraction substituting for either Si or Sc in the crystal structure.

The ^{29}Si NMR spectra contain a single peak that could not be accurately fit with a single Gaussian/Lorentzian curve due to asymmetry. Two Gaussian/Lorentzian curves were used

to account for this asymmetry. Given that the ^{27}Al NMR indicated that Al may be substituting for Si on the Si site, it is likely that Si is also substituting on the Al site in the doped SAS structure. Due to the smaller ionic radii of Si compared to Al in 4-fold coordination (0.26 Å vs 0.39 Å) [33], it is hypothesized that Si substitution on the Al site causes the site to become closer to a distorted tetrahedron, rather than the near trigonal bipyramidal coordination that Al exhibits. This behavior is likely caused by the tendency of the smaller Si atom to be closer to the centroid of the tetrahedron. Hansen et al. has shown that higher distortion in the SiO_4 tetrahedron is correlated to increasing (toward positive) chemical shifts in the ^{29}Si NMR spectra [34]. The authors also proposed the following parameter to estimate the degree of distortion, *D*:

$$D = \frac{1}{6}\sum_{i=1}^{6}|\theta_i - \theta_T| \tag{6.1}$$

which quantifies the average deviation of the O-Si-O bond angles (θ_i) from the O-Si-O bond angles in a perfect tetrahedron (θ_T = 109.47°) [34]. Using the doped SAS structure, *D* is calculated to be 2.58° for the Si site and 14.11° for the Al site, indicating that the Al site is more distorted compared to the Si site. Thus, it is probable that the component peak at higher chemical shift is caused by Si substitution on the Al site (distorted tetrahedron), while the component peak at lower chemical shift is attributed to Si occupancy on the Si site (closer to a perfect tetrahedron). Literature reports of ^{29}Si NMR have demonstrated that the chemical shift can vary depending on the first cation neighbors [35]. In the doped SAS material, the first cation neighbors of the Si and Al sites are predominantly Sc. The peak observed in Figure 6.5 occurs at ~80 ppm, which is consistent with literature-reported values for ^{29}Si NMR of Sc_2SiO_5, which also contains predominantly Sc as the first cation neighbors of the Si site [36].

6.3.2 Composition

The average composition of the doped SAS phase is presented in Table 6.3 using the unit cell basis. The full EPMA dataset is provided in Appendix G (G.4). The standard deviations

demonstrate that the doped SAS composition was uniform over the 11 mm diameter pellet, indicating that the heat treatment duration was long enough to allow all cations to be well-mixed. In comparison to the unit cell formula ($Si_2Al_2Sc_{14}O_{28}$), there is an excess of both Al and Si and a deficiency in Sc. The measured composition also suggests that the excess Al and Si, as well as the dopants (Ca, Mg, Fe, Ti), must substitute for Sc across the entire doped SAS structure. The sum of all cations is 17.929 is in close agreement with the 18 cations in unit cell formula, indicating that nearly all the cations are accounted for with EPMA.

Table 6.3. Average electron-probe microanalysis of doped SAS from 51 sites. Standard deviations are presented in parentheses.

Sc	Al	Si	Ca	Mg	Fe	Ti	O
12.783 (0.022)	2.097 (0.021)	2.357 (0.012)	0.144 (0.005)	0.209 (0.005)	0.131 (0.003)	0.209 (0.003)	28.000

6.3.2.1 Dopant site assignment

The NMR data (Section 6.3.1.4) indicate that there is likely to be cross-substitution between Si and Al on the Si and Al site. Octahedrally coordinated Si was not observed, suggesting that Si does not substitute for Sc on any of the seven Sc sites. In contrast, octahedrally coordinated Al was observed with NMR and reveal that Al substitutes for Sc in one or more of the 4 octahedrally coordinated Sc sites. The ionic radii of octahedrally coordinated Mg (0.72 Å), Fe (0.645 Å), and Ti (0.605 Å) are similar or smaller compared to octahedrally coordinated Sc (0.745 Å) [33]. Thus, it is assumed that Mg, Fe, and Ti occupy one or more of the four octahedrally coordinated Sc sites. The ionic radius of Ca (1.0-1.2 Å) is significantly larger than Sc, so it was assigned to the 7-fold coordinated Sc sites [33].

The unit cell formula can be written as (Si_2) (Al_2) (Sc_8) (Sc_6) O_{28} to separate the sites by coordination, where (Si_2) is tetrahedral, (Al_2) is distorted tetrahedral or trigonal bipyramidal,

(Sc_8) is octahedral, and (Sc_6) is 7-fold coordinated. Using this convention and combining it with the compositional and NMR analysis, the doped SAS material can be represented as:

$$(Si_{1.367}Al_{0.633})\ (Si_{0.990}Al_{1.010})\ (Sc_{6.998}Al_{0.454}Ti_{0.209}Mg_{0.209}Fe_{0.131})\ (Sc_{5.785}Ca_{0.144})\ O_{28}$$

This convention enables the direct calculation of Sc, Al, and Si occupancy for each different type of coordination. Given the aforementioned assumptions of cation substitution, the formula presented is the best fit with the integrated intensities from the NMR data. Table 6.4 presents the occupancy percentage obtained from NMR and the formula above.

Table 6.4. Fractional occupancy of Sc, Al, and Si coordination.
Standard deviations for NMR coordination are presented in paratheses.

Method	Sc		Al			Si	
	ScO_6	ScO_7	AlO_4	AlO_5	AlO_6	SiO_4	d-SiO_4
Site assignment	55%	45%	30%	48%	22%	58%	42%
NMR	59% (3%)	41% (3%)	32% (1%)	49% (5%)	19% (5%)	58% (2%)	42% (2%)

It is noted that though this analysis relies on the NMR data presented, it does not assign the dopant cations or Al to specific Sc sites. This is due in part to the usage of the Czjzek distribution to approximate the effect of four unique octahedral sites and 3 unique 7-fold coordinated Sc sites. The ScO_6 and ScO_7 peaks shown in Figure 6.5 are likely to have four and three overlapping peaks, respectively. This is further complicated since each component can have a potentially complex lineshape due to the quadrupolar ^{45}Sc nuclei. Higher fidelity techniques may enable the accurate determination of cations onto specific Sc sites, but these are beyond the scope of this work.

6.3.3 Material characterization

6.3.3.1 Theoretical density

The theoretical density for the doped SAS phase can be determined from the composition (previously presented in Table 6.3) and lattice parameters of the unit cell obtained from the Rietveld refinement of the ambient-temperature XRD data (Table 6.2). By converting the atomic composition to mass and dividing by the unit cell volume, the theoretical density of the doped SAS phase is determined to be 3.756 g/cm^3.

6.3.3.2 Thermal expansion behavior

High-temperature XRD data for the doped SAS phase are presented in Figure 6.6. As the temperature is increased, there is a general shift of diffraction peaks to lower 2θ angles indicating an increase in d-spacing and positive expansion of the unit cell. By expanding the region of the highest intensity peaks (Figure 6.6(b)), there is also evidence of anisotropic thermal expansion occurring. The $(03\bar{2})$ peak initially starts at higher 2θ (lower d-spacing) than the (003) peak at room temperature. By 1100°C, the $(03\bar{2})$ peak has shifted more than the (003) peak, such that they overlap. At 1500°C, the $(03\bar{2})$ peak has now shifted to the left of the (003) peak. These results indicate that the d-spacing of the $(03\bar{2})$ planes initially starts at a lower value than (003), but expands more with increasing temperature than (003), eventually having a larger d-spacing than (003) at 1500°C. This is a direct observation of anisotropic thermal expansion since this behavior implies that certain crystallographic directions have larger coefficients of thermal expansion.

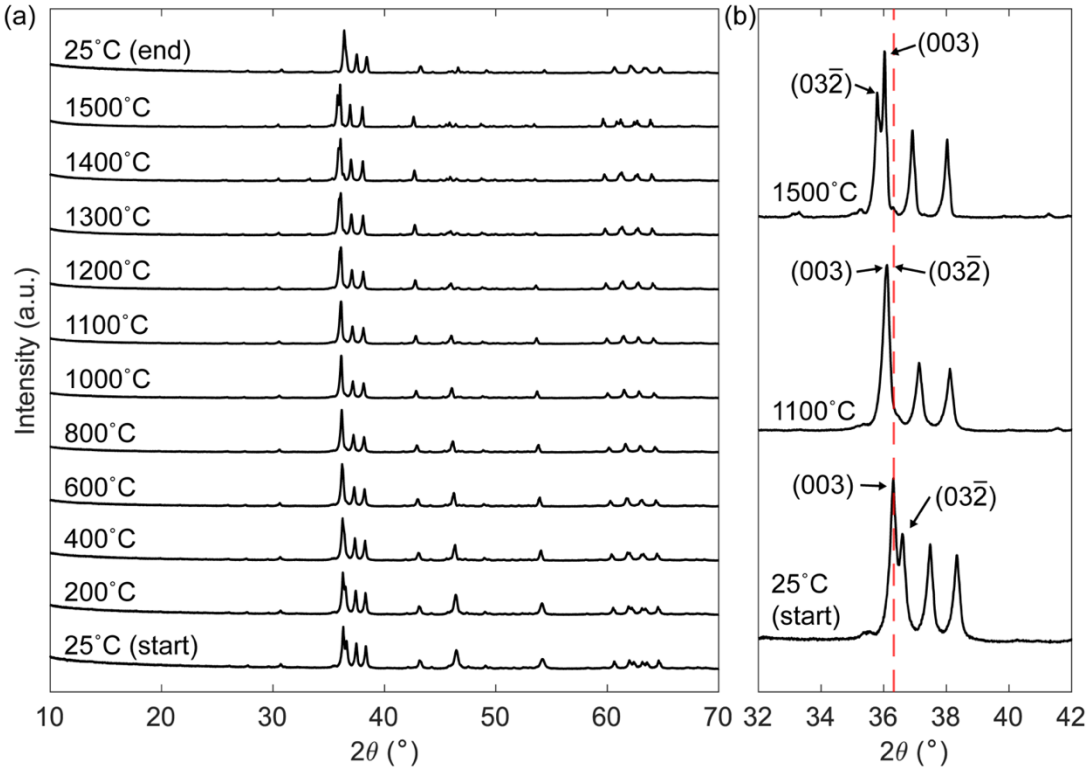

Figure 6.6. Room-temperature and high-temperature XRD (Co Kα) patterns of doped SAS of (a) the full 2θ range and temperatures between 25°C and 1500°C, and (b) an expanded view of (003) and (03$\bar{2}$) at 25°C, 1100°C, and 1500°C.

Through a Le Bail refinement of each XRD pattern, it was possible to obtain the changes in the unit cell lattice parameters as a function of temperature [37]. These data are presented in Figure 6.7(a). The data show that the unit cell lengths and the α angle increases with temperature, while the β and γ angles generally decrease with temperature. The normalized change in the unit cell lengths is presented in Figure 6.7(b), highlighting that the thermal expansion along the b-axis is approximately double the expansion along the a-axis and c-axis. Due to the anisotropy of thermal expansion, the thermal expansion is best expressed using a volumetric basis. The change in the unit cell volume is presented in Figure 6.7(c). By fitting these data with a polynomial, it is possible to obtain the volumetric coefficient of thermal expansion, which is shown in Figure 6.7(d). The polynomial fit is provided in Appendix G (G.5).

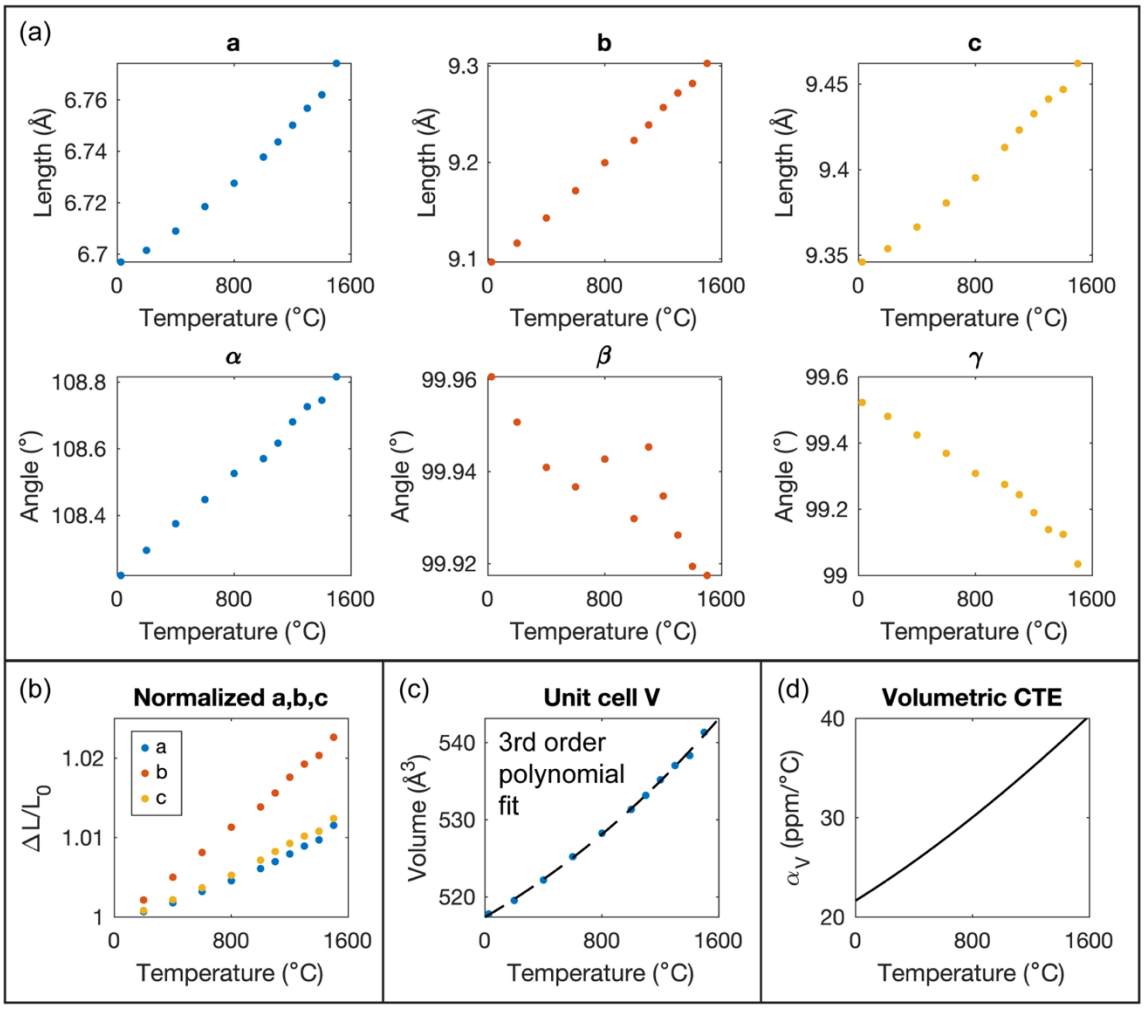

Figure 6.7. (a) Lattice parameters (a, b, c, α, β, γ), (b) normalized unit cell lengths, (c) unit cell volume, and (d) calculated volumetric coefficient of thermal expansion obtained from high-temperature XRD as a function of temperature.

Evidence of anisotropic thermal expansion is also observed in the microstructure of sintered, doped SAS pellets. Microstructural analysis reveals several sets of aligned parallel cracks within grains. A representative SEM image of these cracks is provided in Figure 6.8, with the aligned cracks highlighted using orange arrows. EBSD spot analysis of similar parallel cracks within a grain is presented in Figure 6.9. Three EBSD patterns were collected within the regions between the observed cracks. The grain orientations are overlayed in this image. The EBSD patterns indicate that all three sites are within a single grain, since the EBSD patterns are nearly identical. The black vectors shown in the unit cell denote the eigenvector with the largest eigenvalue from the thermal expansion tensor, obtained using CTEAS [18]. Thus, this vector represents the direction with the largest thermal expansion. The full CTEAS results, including the thermal expansion tensor, eigenvalues, and eigenvectors are provided in Appendix G (G.6 – G.7). This direction does not fall directly on crystallographic axes of the unit cell, which is expected for a triclinic unit cell. However, this eigenvector has the highest component along the b-axis, consistent with data from Figure 6.7(b) showing that the b-axis has the largest thermal expansion of the three crystallographic axes.

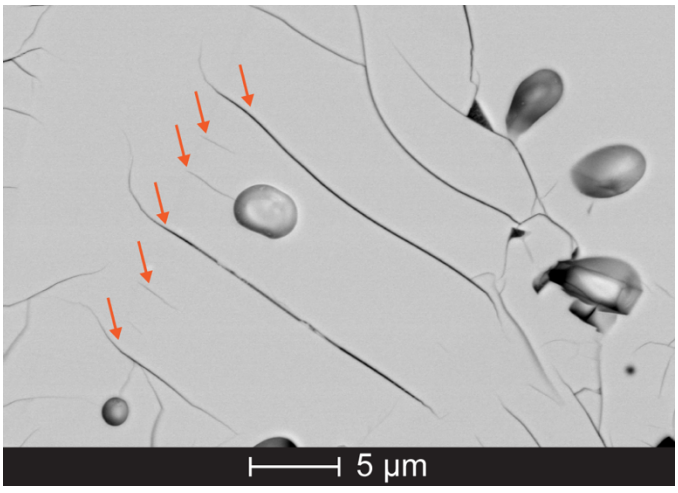

Figure 6.8. SEM image of aligned parallel cracks observed in doped SAS pellet. Orange arrows mark the locations of the parallel cracks.

In Figure 6.9, grain orientations indicate that the cracks run perpendicular to the direction of the largest thermal expansion/contraction. The black vector represents the direction of largest thermal expansion, so the opposite direction of this vector represents the direction of largest thermal contraction. This orientation suggests that these parallel cracks likely form on cooling, The cracks form due to the tensile stress of larger thermal contraction along this direction. Thus, the anisotropic thermal expansion of the doped SAS material causes this parallel fracture pattern to occur within grains. This effect likely dominates in the interior of large grains. It is noted that cracking is a three-dimensional phenomenon, while the EBSD analysis was performed on a two-dimensional surface. Most cracks are not aligned with the surface normal vector, in which case, the eigenvector would not be in the plane of the specimen surface. Additionally, it is likely that this behavior does not account for all cracks observed in the sample since the influence of grain boundaries, grain sizes, and porosity all contribute to the fracture behavior of a material.

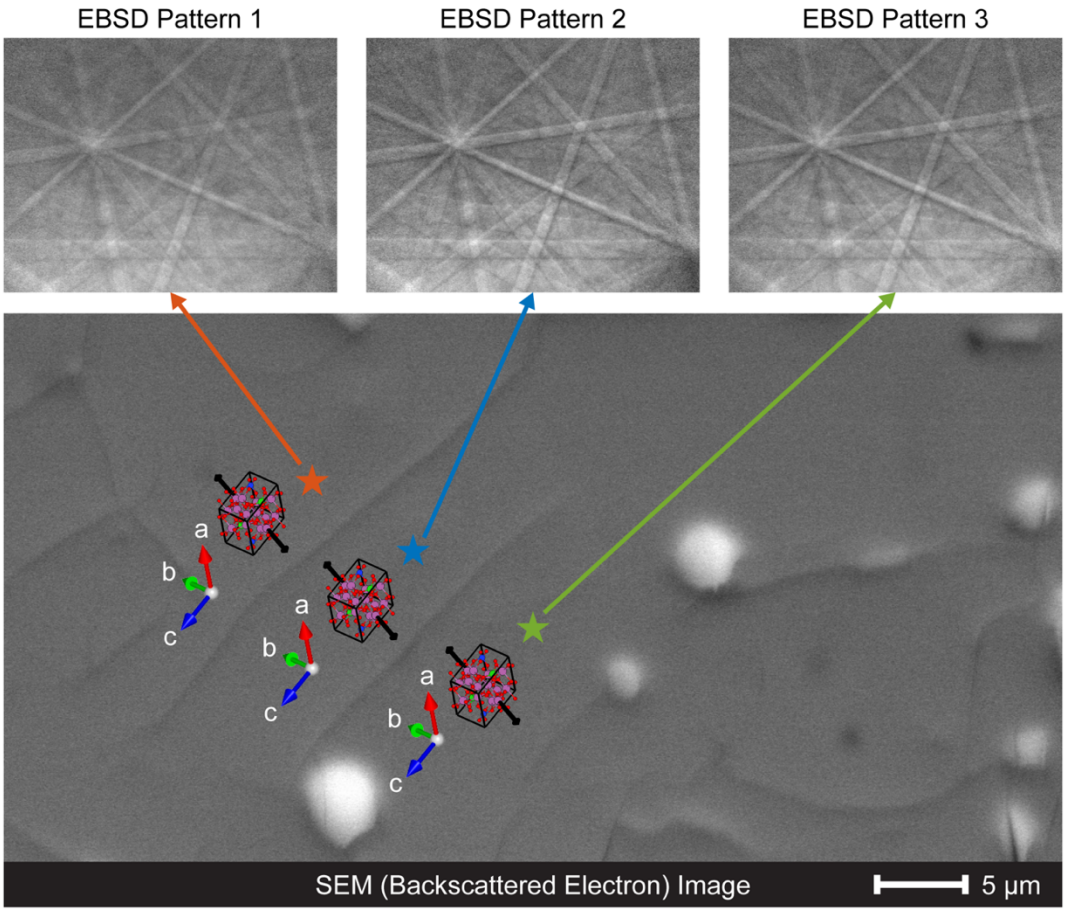

Figure 6.9. EBSD spot analysis and grain orientation of doped SAS in a region exhibiting parallel cracks. Black vector in the unit cell represents the eigenvector of the thermal expansion tensor with the largest eigenvalue. The opposite direction of the black vector (not shown) represents the direction of largest thermal contraction due to cooling. The white regions are pores within the doped SAS material.

6.3.3.3 Thermal analysis

The DTA/TGA results of both the precursor mixture and the doped SAS material are presented in Figure 6.10. Examining the DTA data for the precursor mixture in Figure 6.10(a), there is an endothermic peak observed at ~700°C, paired with a mass loss event. This peak is attributed to the decomposition of $CaCO_3$, which releases gaseous CO_2 that causes the mass loss event. The temperature of $CaCO_3$ decomposition is consistent with

values reported in literature [38]. As the temperature increases to nearly 1200°C, the TGA data are constant, indicating that there is no volatility of the remaining precursor mixture. At approximately 1200°C, there is a broad endothermic peak that extends to 1600°C. This endothermic behavior is attributed to the reaction of the precursor mixture to form the doped SAS phase. This broad endothermic peak is likely comprised of several peaks associated with the different oxides in the precursor mixture reacting over the 1200°C-1600°C temperature range. It is noted that these reactions likely include any transient phases that form before eventually converting to the doped SAS phase. Based on this DTA data, the doped SAS reaction initiates at approximately 1200°C and continues reacting until 1550°C, where the endothermic signal begins to decrease.

Figure 6.10(b) provides an expanded view of the doped SAS DTA/TGA from 1900°C to 2400°C. The full dataset is provided in Appendix G (G.8). Since the material was reacted prior to DTA/TGA, both signals are stable until the temperature reaches 1900°C. Based on Figure 6.10(b), there are two smaller exothermic peaks occurring around 2020°C and 2120°C that do not cause mass loss. These exothermic peaks are attributed to reactions between the doped SAS and the W crucible used in this experiment. At approximately 2150°C, there is a sharp endothermic peak, followed by a broader endothermic peak, both of which are associated with a significant mass loss event of ~12%. This behavior is ascribed to either the thermal decomposition or sublimation of doped SAS. It is possible that melting also occurred, but this cannot be verified since the sharp endothermic peak is also associated with a mass loss event, which melting alone would not cause. At 2300°C, the thermocouple used in the DTA measurement failed, likely due to the volatile oxide species produced from the thermal decomposition or sublimation of doped SAS. The TGA data have a plateau in this region, before continuing to measure another mass loss event above 2300°C. This indicates that the decomposition or sublimation occurs in two steps, first at 2150°C and again at 2300°C. Based on these results, it was determined that the maximum usage temperature of the doped SAS is ~2000°C to avoid any reactions and decomposition that occurs.

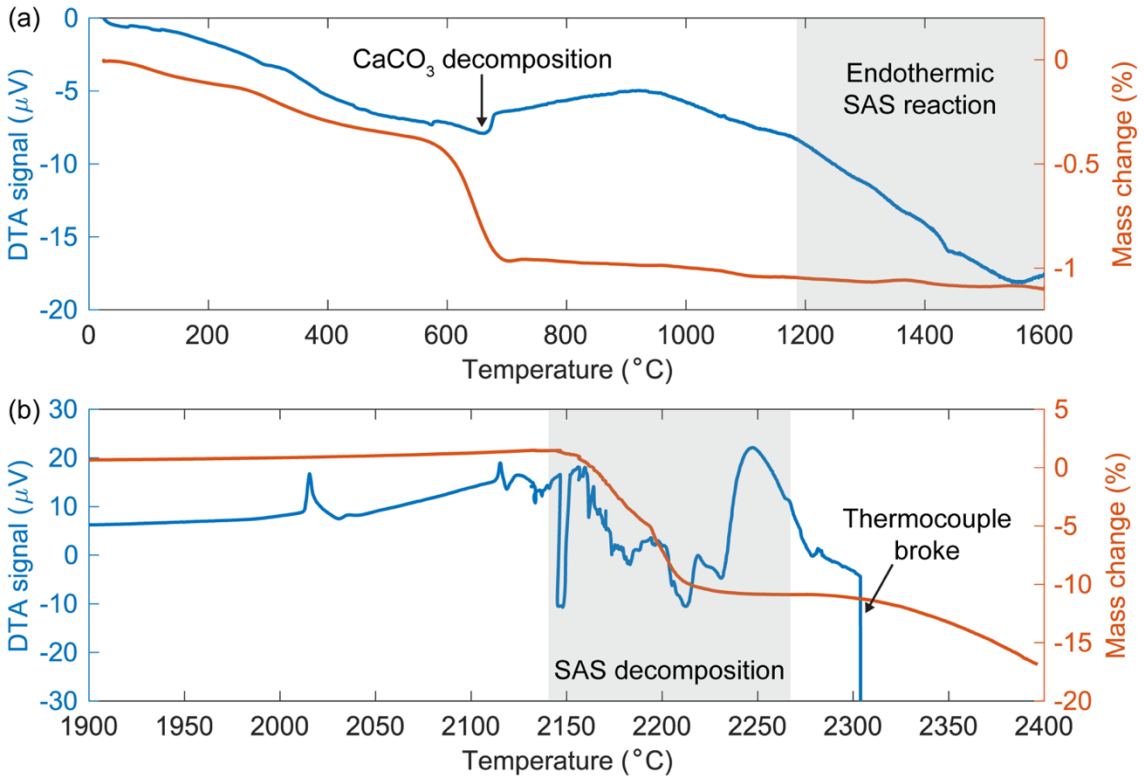

Figure 6.10. Differential thermal analysis of (a) precursor mixture to 1600°C and (b) reacted, doped SAS to 2400°C.

6.3.4 Reaction pathway

The reaction of the precursor mixture to doped SAS was monitored using high-temperature XRD. Whole pattern fitting of each XRD scan enabled the relative concentration of each crystalline phase to be determined and tracked as a function of temperature. These data are presented in Figure 6.11. Based on this analysis, there are no significant reactions occurring until 1200°C, since the weight fractions of Sc_2O_3, SiO_2 (quartz), and Al_2O_3 are relatively constant from room temperature until 1200°C. At 1200°C, $Sc_2Si_2O_7$ begins to form. At 1300°C, $Sc_2Si_2O_7$ and the doped SAS phase are both ~15 wt%, while the weight fractions of Sc_2O_3, SiO_2 (quartz), and Al_2O_3 begin to decrease, indicating that the reaction of the precursor mixture has begun. The cristobalite polymorph of SiO_2 also appears at 1300°C, which is consistent with cristobalite formation reported in literature [39]. Revisiting the previously discussed DTA results, it is believed that the onset of the endothermic peak

observed in Figure 6.10(a) is associated with both doped SAS and $Sc_2Si_2O_7$ formation. The onset of the endothermic peak occurred ~1200°C, while $Sc_2Si_2O_7$ is first observed at 1200°C and doped SAS at 1300°C. Thus, the reaction observed in situ using high-temperature XRD is consistent with the DTA results discussed earlier.

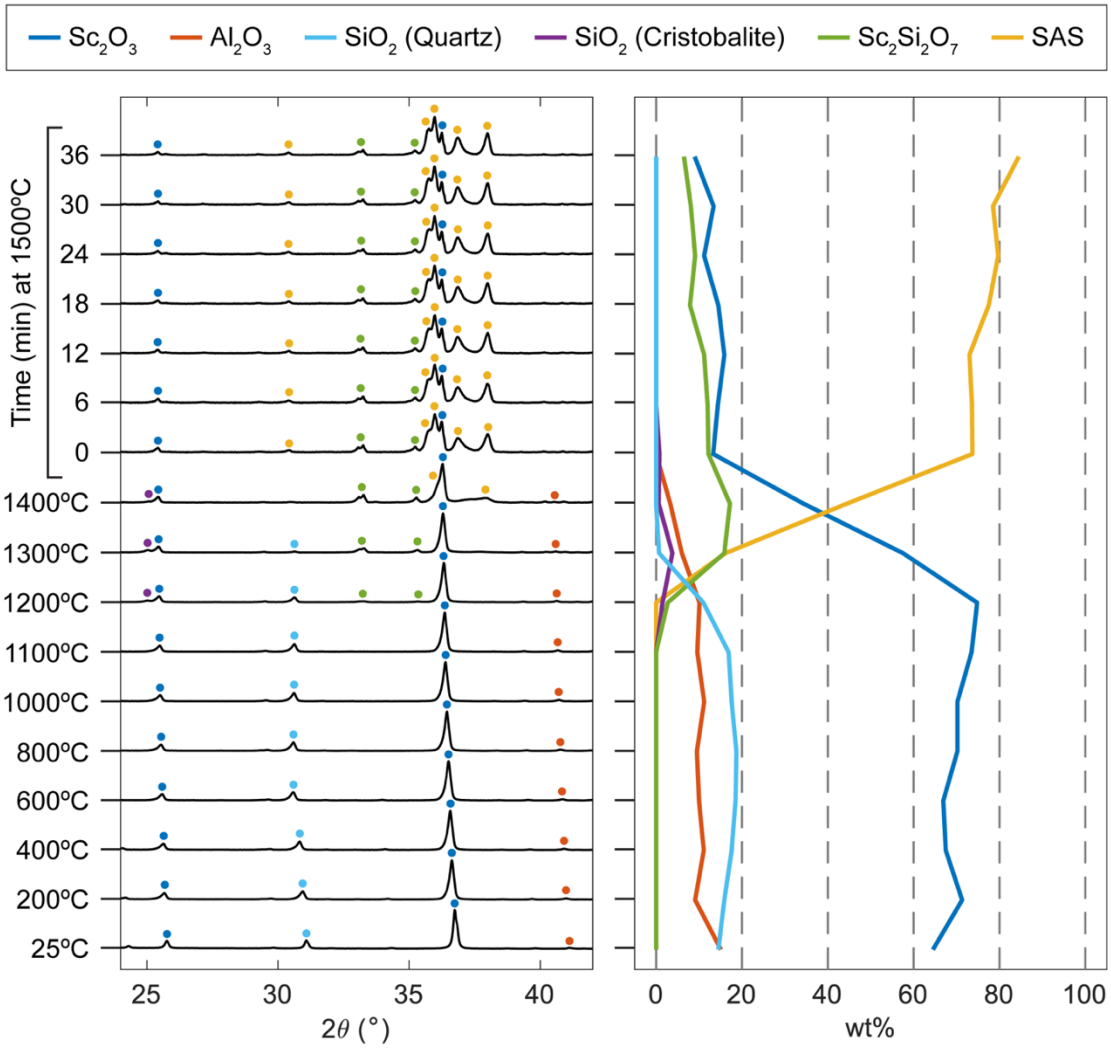

Figure 6.11. High-temperature XRD (Co Kα) scans of the precursor mixture (left) and weight percent of major crystalline phases at each temperature (right).

Based on Figure 6.11, the maximum weight fraction of $Sc_2Si_2O_7$ is observed at 1400°C, which then decreases at 1500°C and continues decreasing with increasing time spent at 1500°C. In contrast, the doped SAS material continues to increase in weight fraction until the end of the experiment after annealing at 1500°C. This result suggests that $Sc_2Si_2O_7$ forms

as a transient species, which then further reacts to finally form the doped SAS. Additionally, these results indicate that there is no pure SiO_2 (either quartz or cristobalite) available for the doped SAS reaction. Any SiO_2 that is not already reacted to form the doped SAS is locked in the $Sc_2Si_2O_7$ structure. This effect could impede the kinetics of doped SAS formation since the SiO_2 must come from the dissociation of $Sc_2Si_2O_7$ for the reaction to occur. Due to kinetic limitations, it is possible that the doped SAS phase may form in higher weight fractions at temperatures lower than 1500°C. This is explored in a set of annealing experiments presented in the Appendix G (G.9).

6.3.5 Thermal conductivity

The thermal conductivity of sintered, doped SAS is presented in Figure 6.12. Y_2O_3-stabilized ZrO_2 (YSZ) is a commonly used thermal insulator at elevated temperatures, due to its low thermal conductivity [40]. The thermal conductivity of 3 mol% YSZ (3YSZ) is also included for comparison [40]. Both the materials were approximately 90% dense, enabling a direct comparison of their thermal conductivities. From Figure 6.12, the thermal conductivity of doped SAS is lower than 3YSZ from 25°C to 900°C. The average thermal conductivity from 25°C to 1000°C is 1.6 W m^{-1} K^{-1} for doped SAS and 2.2 W m^{-1} K^{-1} for 3YSZ. Thus, the thermal conductivity data indicates that doped SAS may outperform 3YSZ in thermal insulation applications at temperatures up to 1000°C.

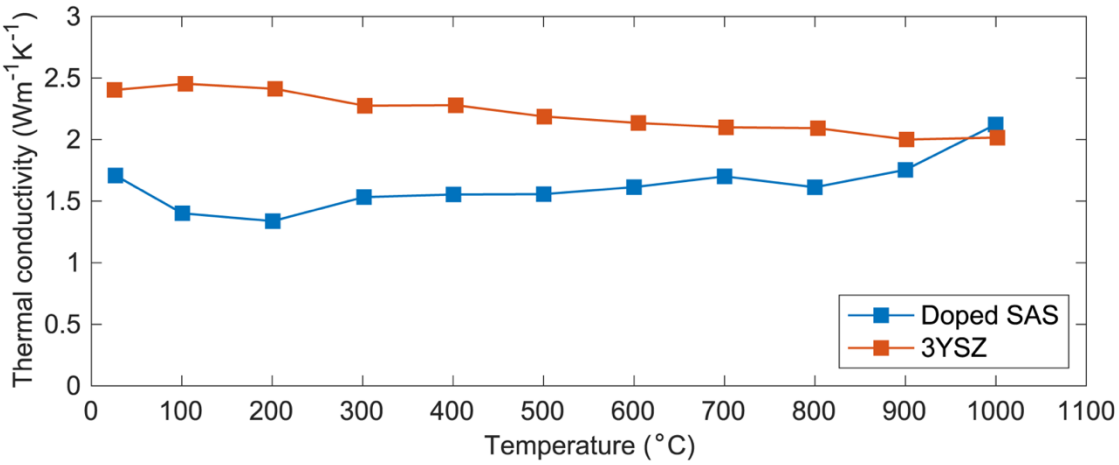

Figure 6.12. Thermal conductivity of doped SAS measured by laser flash analysis. Thermal conductivity of 3YSZ included for comparison [40].

6.4 Discussion

6.4.1 Implications of crystal structure

The doped SAS phase discovered in this work possesses a new crystal structure. Based on literature reports of the CaO-Al_2O_3-Sc_2O_3 and Al_2O_3-SiO_2-Sc_2O_3 systems, it does not appear that this phase has been previously observed [6,7]. Pattern matching with the PDF4+ database for powder XRD also did not yield any matches to existing structures. To the authors' knowledge, this work is the first to report and characterize the crystal structure of the doped SAS phase.

The doped SAS phase was synthesized using typical solid-state reaction methods, without the need for rapid quenching to preserve the crystal structure. Additionally, the synthesis procedure demonstrated that relatively large batches (~100 grams) of doped SAS can be produced without significant synthesis complexity. These results indicate that the reaction to form doped SAS is likely spontaneous ($\Delta G = \Delta H - T\Delta S < 0$), specifically starting at 1200°C-1300°C based on high-temperature XRD data (Figure 6.11). However, DTA of the precursor mixture (Figure 6.10(a)) reveals that the enthalpy of reaction is endothermic ($\Delta H > 0$), suggesting that the entropic term of the Gibbs free energy change ($-T\Delta S$) must dominate at high temperature and causes the overall reaction to be exergonic. This analysis implies that the entropy change (ΔS) must be positive, or that the entropy of the system increases going from the oxide precursors to the doped SAS phase. Given the four minority dopants (Ca, Mg, Fe, Ti), as well as cross-substitution of the majority cations (Si, Al, Sc), it is believed that the entropy increase is mostly due to an increase in configurational entropy, though vibrational and electronic contributions may also have an effect. Thus, based on the characterization presented in this work, the doped SAS phase is likely entropically stabilized at high temperature (>1200°C). This also suggests that, though the decomposition of the doped SAS may be thermodynamically favorable at lower temperatures (<1200°C), the kinetics of decomposition are slow, allowing the phase to be preserved without rapid quenching during the synthesis step.

Despite being an entropy-stabilized material, it is hypothesized that the doped SAS phase is not a high-entropy oxide. For high-entropy oxides containing multiple atomic sublattices, the ideal configurational entropy can be estimated using a model that is normalized to the number of atoms in a unit cell. The ideal configurational entropy of complex crystal structures can be estimated using this sublattice model:

$$S_{config} = \frac{-R \sum_{x=1}^{x} a^x \sum_{i=1}^{N} f_i^x \ln(f_i^x)}{\sum_{x=1}^{x} a^x} \tag{6.2}$$

where a^x is the number of sites on the x sublattice, f_i^x is the fractional occupancy of element species i distributed on the x sublattice, and N is the total number of element species [41]. By applying this method and assuming that all substitutions on 6-fold and 7-fold Sc sites are distributed equally, the configurational entropy per mol of atoms is calculated to be 0.17R.

High-entropy ceramics (including oxides) typically possess highly symmetric crystal structures [42]. The high entropy of these materials is achieved through the use of multiple cations in equimolar ratios, thereby increasing the configurational entropy of the structure [42]. For comparison, one of the simplest high-entropy oxides is (MgNiCuZnCo)O, possessing the rocksalt crystal structure [43]. Applying the sublattice model for this material results in 0.8R, significantly higher than the result for the doped SAS material. For low symmetry structures, Stenzel et al. discovered that high-entropy, triclinic molybdate, (MgNiCuZnFe)MoO_4 with equimolar amounts of metals besides Mo, can be synthesized and is phase pure [44]. Applying the sublattice model to the molybdate results in 0.27R, which is still higher than the doped SAS material. Thus, the doped SAS material is not likely to be a high-entropy oxide. Though there are many metal cations in the doped SAS phase, Sc is by far the most prevalent cation, resulting in a lower configurational entropy compared to oxides employing equimolar ratios of multiple metal cations.

6.4.2 MicroED on inorganic materials

Beyond the newly discovered doped SAS material, this work also highlights the value of MicroED for inorganic materials. For bulk, inorganic materials, single-crystal XRD has been

traditionally used for structure determination [45]. However, the doped SAS material in this work presents a unique challenge for single-crystal XRD. Due to the ball-milling step used during synthesis, the resulting doped SAS crystallite sizes (~ 1 – 30 μm) were significantly smaller than the size required for single-crystal XRD (>100 μm). The doped SAS material is also a refractory oxide, with high thermal stability as observed in the DTA data (Figure 6.10(b)). Coarsening the doped SAS crystallites to the size required for single-crystal XRD and subsequent isolation of appropriately sized grains was determined to be too difficult.

The challenges posed by the doped SAS material for single-crystal XRD do not apply to MicroED. Since electrons interact more strongly with atoms than X-rays, electron diffraction can be applied to crystallites ranging from 1 - 10^{-4} μm^3, several orders-of-magnitude smaller than required for X-ray diffraction techniques [9,10]. Crystallites of the correct size for MicroED are already produced through the ball-milling step during the synthesis procedure, eliminating the need for extensive sample preparation. Additionally, the doped SAS is not beam-sensitive since it is a refractory oxide material. Solving the crystal structure with MicroED enabled several of the characterization techniques employed in this work, including the thermal expansion and reaction pathway analysis. MicroED has been applied successfully to a variety of inorganic systems, including identifying oxides produced through new processing methods [46] and determining structures for minerals that were previously unsolved [47]. This work provides another demonstration that MicroED is a powerful tool for solving structures of newly discovered inorganic materials and minerals.

6.4.3 Potential applications

The clearest application for doped SAS is as a thermal insulator at intermediate temperatures, between 25°C and 1000°C. The thermal conductivity data (Figure 6.12) shows that doped SAS possesses a lower thermal conductivity than 3YSZ, a commonly used thermal insulator. The low thermal conductivity of doped SAS is attributed to the structural disorder found in entropy-stabilized oxides [48]. Additionally, the density of doped SAS (3.756 g/cm^3) is approximately 35% lower than the density of YSZ (5.9 - 6.0 g/cm^3) [40]. The combination of lower density and thermal conductivity suggests that doped SAS may be well-suited as a

thermal insulator for aerospace applications that require lightweight materials, such as thermal barrier coatings and thermal protection systems. Other material properties, including electrical, magnetic, and optical properties, require more investigation to determine if the unique crystal structure of doped SAS offers any improvements over existing materials for those applications.

6.5 Conclusion

The discovery and characterization of a novel doped SAS phase, synthesized from majority oxides of Sc_2O_3, Al_2O_3, and SiO_2 and minority oxides of CaO, MgO, Fe_2O_3, and TiO_2. The crystal structure of the doped SAS phase was solved using MicroED, resulting in a triclinic ($P\bar{1}$) unit cell. The nominal formula for the solved unit cell is $Si_2Al_2Sc_{14}O_{28}$ with unit cell lattice parameters determined by MicroED and confirmed with powder XRD and Rietveld refinement. EPMA results revealed that the full composition of the SAS material is $Si_{2.357}Al_{2.097}Ca_{0.144}Mg_{0.209}Fe_{0.131}Ti_{0.209}Sc_{12.783}O_{28}$. Solid-state NMR on ^{27}Al, ^{29}Si, and ^{45}Sc provided guidance for assigning partial occupancy on cation sites (by site coordination) in the doped SAS crystal structure. These results implied that there is substitution of Si on the Al site and Al on the Si and octahedral Sc sites within the doped SAS structure.

Additional characterization of the doped SAS material, enabled by solving the crystal structure, was also performed. The thermal expansion of doped SAS was evaluated using high-temperature XRD and was determined to be highly anisotropic. The microstructure of sintered, doped SAS specimens revealed cracking that was caused in part by the anisotropic thermal expansion. High-temperature XRD was also used to evaluate the reaction pathway of doped SAS formation. This reaction pathway analysis indicated that the doped SAS reaction begins at 1200°C-1300°C, with $Sc_2Si_2O_7$ also forming as an intermediate phase. This result was also validated with DTA experiments. DTA on the precursor mixture indicated that the reaction begins at ~1200°C (consistent with high-temperature XRD) and the enthalpy of reaction is endothermic. DTA on the doped SAS material revealed that

decomposition occurs around 2150°C, indicating that the doped SAS phase possesses high thermal stability.

Ultimately, these results establish a baseline set of material properties for the newly discovered doped SAS phase. The endothermic enthalpy of reaction indicates that this phase is entropy-stabilized, likely due to substantial configurational entropy from extensive cation site substitutions. Additionally, this study also demonstrates the power of MicroED in resolving inorganic crystal structures of refractory materials that are unsuitable for conventional single-crystal XRD. The lower thermal conductivity and density of doped SAS suggest its potential for thermal insulation applications up to 1000°C, especially in applications that require lightweight materials. Further investigation into its functional properties may uncover other relevant applications for this material.

References

[1] E.S. Lukin, Modern high-density oxide-based ceramics with a controlled microstructure. Part V. Chemical-resistant high-density yttrium-, scandium-, and alumina-based ceramics, Refractories and Industrial Ceramics 38 (1997) 47–51. https://doi.org/10.1007/BF02767832.

[2] C. Wang, Scandium and Its Materials Applications, in: Theory and Application of Rare Earth Materials, Springer Nature Singapore, Singapore, 2023: pp. 333–350. https://doi.org/10.1007/978-981-19-4178-8_19.

[3] Y. Mizutani, M. Tamura, M. Kawai, O. Yamamoto, Development of high-performance electrolyte in SOFC, Solid State Ionics 72 (1994) 271–275. https://doi.org/10.1016/0167-2738(94)90158-9.

[4] H. Iwahara, T. Esaka, H. Uchida, N. Maeda, Proton conduction in sintered oxides and its application to steam electrolysis for hydrogen production, Solid State Ionics 3–4 (1981) 359–363. https://doi.org/10.1016/0167-2738(81)90113-2.

[5] V.A. Smirnov, R.Ya. Popil'skii, Creep and recrystallization of sintered scandium oxide at high temperatures, Refractories 14 (1973) 305–308. https://doi.org/10.1007/BF01285735.

[6] W. Zhi, F. Wang, B. Yang, T. Qu, Y. Deng, Y. Tian, J. Zhao, Phase relations of CaO-Al_2O_3-Sc_2O_3 ternary system, J Am Ceram Soc 102 (2019) 2863–2870. https://doi.org/10.1111/jace.16104.

[7] W. Zhi, F. Wang, X. Chen, Y. Tian, B. Yang, Phase equilibria and thermodynamic assessment of the Al_2O_3-SiO_2-Sc_2O_3 system, Ceramics International 49 (2023) 9735–9747. https://doi.org/10.1016/j.ceramint.2022.11.147.

[8] C. Ma, A.N. Krot, J.R. Beckett, K. Nagashima, O. Tschauner, G.R. Rossman, S.B. Simon, A. Bischoff, Warkite, $Ca_2Sc_6Al_6O_{20}$, a new mineral in carbonaceous chondrites and a key-stone phase in ultrarefractory inclusions from the solar nebula, Geochimica et Cosmochimica Acta 277 (2020) 52–86. https://doi.org/10.1016/j.gca.2020.03.002.

[9] C.G. Jones, M.W. Martynowycz, J. Hattne, T.J. Fulton, B.M. Stoltz, J.A. Rodriguez, H.M. Nelson, T. Gonen, The CryoEM Method MicroED as a Powerful Tool for

Small Molecule Structure Determination, ACS Cent. Sci. 4 (2018) 1587–1592. https://doi.org/10.1021/acscentsci.8b00760.

[10] M. Gemmi, E. Mugnaioli, T.E. Gorelik, U. Kolb, L. Palatinus, P. Boullay, S. Hovmöller, J.P. Abrahams, 3D Electron Diffraction: The Nanocrystallography Revolution, ACS Cent. Sci. 5 (2019) 1315–1329. https://doi.org/10.1021/acscentsci.9b00394.

[11] W. Kabsch, *XDS*, Acta Crystallogr D Biol Crystallogr 66 (2010) 125–132. https://doi.org/10.1107/S0907444909047337.

[12] W. Kabsch, Integration, scaling, space-group assignment and post-refinement, Acta Crystallogr D Biol Crystallogr 66 (2010) 133–144. https://doi.org/10.1107/S0907444909047374.

[13] J. Hattne, F.E. Reyes, B.L. Nannenga, D. Shi, M.J. De La Cruz, A.G.W. Leslie, T. Gonen, MicroED data collection and processing, Acta Crystallogr A Found Adv 71 (2015) 353–360. https://doi.org/10.1107/S2053273315010669.

[14] G.M. Sheldrick, Crystal structure refinement with *SHELXL*, Acta Crystallogr C Struct Chem 71 (2015) 3–8. https://doi.org/10.1107/S2053229614024218.

[15] O.V. Dolomanov, L.J. Bourhis, R.J. Gildea, J.A.K. Howard, H. Puschmann, *OLEX2* : a complete structure solution, refinement and analysis program, J Appl Crystallogr 42 (2009) 339–341. https://doi.org/10.1107/S0021889808042726.

[16] L.-M. Peng, Electron atomic scattering factors and scattering potentials of crystals, Micron 30 (1999) 625–648. https://doi.org/10.1016/S0968-4328(99)00033-5.

[17] A. Le Bail, H. Duroy, J.L. Fourquet, Ab-initio structure determination of $LiSbWO_6$ by X-ray powder diffraction, Materials Research Bulletin 23 (1988) 447–452. https://doi.org/10.1016/0025-5408(88)90019-0.

[18] Z.A. Jones, P. Sarin, R.P. Haggerty, W.M. Kriven, *CTEAS* : a graphical-user-interface-based program to determine thermal expansion from high-temperature X-ray diffraction, J Appl Crystallogr 46 (2013) 550–553. https://doi.org/10.1107/S0021889813002938.

[19] D. Massiot, F. Fayon, M. Capron, I. King, S. Le Calvé, B. Alonso, J. Durand, B. Bujoli, Z. Gan, G. Hoatson, Modelling one- and two-dimensional solid-state NMR

spectra, Magnetic Reson in Chemistry 40 (2002) 70–76. https://doi.org/10.1002/mrc.984.

[20] B. Fultz, J. Howe, Transmission Electron Microscopy and Diffractometry of Materials, Springer Berlin Heidelberg, Berlin, Heidelberg, 2013. https://doi.org/10.1007/978-3-642-29761-8.

[21] B. Pahari, S. Iftekhar, A. Jaworski, K. Okhotnikov, K. Jansson, B. Stevensson, J. Grins, M. Edén, Composition-Property-Structure Correlations of Scandium Aluminosilicate Glasses Revealed by Multinuclear ^{45}Sc, ^{27}Al, and ^{29}Si Solid-State NMR, J. Am. Ceram. Soc. 95 (2012) 2545–2553. https://doi.org/10.1111/j.1551-2916.2012.05288.x.

[22] A. Jaworski, T. Charpentier, B. Stevensson, M. Edén, Scandium and Yttrium Environments in Aluminosilicate Glasses Unveiled by ^{45}Sc/^{89}Y NMR Spectroscopy and DFT Calculations: What Structural Factors Dictate the Chemical Shifts?, J. Phys. Chem. C 121 (2017) 18815–18829. https://doi.org/10.1021/acs.jpcc.7b05471.

[23] D.R. Neuville, L. Cormier, D. Massiot, Al environment in tectosilicate and peraluminous glasses: A ^{27}Al MQ-MAS NMR, Raman, and XANES investigation, Geochimica et Cosmochimica Acta 68 (2004) 5071–5079. https://doi.org/10.1016/j.gca.2004.05.048.

[24] N. Kim, C.-H. Hsieh, J.F. Stebbins, Scandium Coordination in Solid Oxides and Stabilized Zirconia: ^{45}Sc NMR, Chem. Mater. 18 (2006) 3855–3859. https://doi.org/10.1021/cm060590l.

[25] M.D. Alba, P. Chain, P. Florian, D. Massiot, ^{45}Sc Spectroscopy of Solids: Interpretation of Quadrupole Interaction Parameters and Chemical Shifts, J. Phys. Chem. C 114 (2010) 12125–12132. https://doi.org/10.1021/jp1036525.

[26] T. Bräuniger, A.J. Hofmann, I.L. Moudrakovski, C. Hoch, W. Schnick, A ^{45}Sc-NMR and DFT calculation study of crystalline scandium compounds, Solid State Sciences 51 (2016) 1–7. https://doi.org/10.1016/j.solidstatesciences.2015.11.002.

[27] S.F. Dec, J.J. Fitzgerald, J.S. Frye, M.P. Shatlock, G.E. Maciel, Observation of six-coordinate aluminum in andalusite by solid-state ^{27}Al MAS NMR, Journal of

Magnetic Resonance (1969) 93 (1991) 403–406. https://doi.org/10.1016/0022-2364(91)90015-L.

[28] P.L. Bryant, C.R. Harwell, K. Wu, F.R. Fronczek, R.W. Hall, L.G. Butler, Single-Crystal ^{27}Al NMR of Andalusite and Calculated Electric Field Gradients: the First Complete NMR Assignment for a 5-Coordinate Aluminum Site, J. Phys. Chem. A 103 (1999) 5246–5252. https://doi.org/10.1021/jp990374i.

[29] L.-S. Du, J.F. Stebbins, Calcium and Strontium Hexaluminates: NMR Evidence that "Pentacoordinate" Cation Sites Are Four-Coordinated, J. Phys. Chem. B 108 (2004) 3681–3685. https://doi.org/10.1021/jp037615d.

[30] K. Harindranath, K. Anusree Viswanath, C. Vinod Chandran, T. Bräuniger, P.K. Madhu, T.G. Ajithkumar, P.A. Joy, Evidence for the co-existence of distorted tetrahedral and trigonal bipyramidal aluminium sites in $SrAl_{12}O_{19}$ from ^{27}Al NMR studies, Solid State Communications 150 (2010) 262–266. https://doi.org/10.1016/j.ssc.2009.11.008.

[31] B. Walkley, J.L. Provis, Solid-state nuclear magnetic resonance spectroscopy of cements, Materials Today Advances 1 (2019) 100007. https://doi.org/10.1016/j.mtadv.2019.100007.

[32] S. Xu, N.R. Jaegers, W. Hu, J.H. Kwak, X. Bao, J. Sun, Y. Wang, J.Z. Hu, High-Field One-Dimensional and Two-Dimensional ^{27}Al Magic-Angle Spinning Nuclear Magnetic Resonance Study of θ-, δ-, and γ-Al_2O_3 Dominated Aluminum Oxides: Toward Understanding the Al Sites in γ-Al_2O_3, ACS Omega 6 (2021) 4090–4099. https://doi.org/10.1021/acsomega.0c06163.

[33] R.D. Shannon, Revised effective ionic radii and systematic studies of interatomic distances in halides and chalcogenides, Acta Cryst A 32 (1976) 751–767. https://doi.org/10.1107/S0567739476001551.

[34] M.R. Hansen, H.J. Jakobsen, J. Skibsted, ^{29}Si Chemical Shift Anisotropies in Calcium Silicates from High-Field ^{29}Si MAS NMR Spectroscopy, Inorg. Chem. 42 (2003) 2368–2377. https://doi.org/10.1021/ic020647f.

[35] P. Duxson, J.L. Provis, G.C. Lukey, F. Separovic, J.S.J. Van Deventer, ^{29}Si NMR Study of Structural Ordering in Aluminosilicate Geopolymer Gels, Langmuir 21 (2005) 3028–3036. https://doi.org/10.1021/la047336x.

[36] M.D. Alba, P. Chain, T. González-Carrascosa, Synthesis, Rietveld Analysis, and Solid State Nuclear Magnetic Resonance of X_2-Sc_2SiO_5, Journal of the American Ceramic Society 92 (2009) 487–490. https://doi.org/10.1111/j.1551-2916.2008.02877.x.

[37] J.L. Stokes, β-Cristobalite thermal expansion and stability in environmental barrier coating systems, J Am Ceram Soc. 108 (2025) e20214. https://doi.org/10.1111/jace.20214.

[38] I. Galan, F.P. Glasser, C. Andrade, Calcium carbonate decomposition, J Therm Anal Calorim 111 (2013) 1197–1202. https://doi.org/10.1007/s10973-012-2290-x.

[39] L. Pagliari, M. Dapiaggi, A. Pavese, F. Francescon, A kinetic study of the quartz–cristobalite phase transition, Journal of the European Ceramic Society 33 (2013) 3403–3410. https://doi.org/10.1016/j.jeurceramsoc.2013.06.014.

[40] K.W. Schlichting, N.P. Padture, P.G. Klemens, Thermal conductivity of dense and porous yttria-stabilized zirconia, Journal of Materials Science 36 (2001) 3003–3010. https://doi.org/10.1023/a:1017970924312.

[41] D.B. Miracle, O.N. Senkov, A critical review of high entropy alloys and related concepts, Acta Materialia 122 (2017) 448–511. https://doi.org/10.1016/j.actamat.2016.08.081.

[42] C. Oses, C. Toher, S. Curtarolo, High-entropy ceramics, Nat Rev Mater 5 (2020) 295–309. https://doi.org/10.1038/s41578-019-0170-8.

[43] C.M. Rost, E. Sachet, T. Borman, A. Moballegh, E.C. Dickey, D. Hou, J.L. Jones, S. Curtarolo, J.-P. Maria, Entropy-stabilized oxides, Nat Commun 6 (2015) 8485. https://doi.org/10.1038/ncomms9485.

[44] D. Stenzel, I. Issac, K. Wang, R. Azmi, R. Singh, J. Jeong, S. Najib, S.S. Bhattacharya, H. Hahn, T. Brezesinski, S. Schweidler, B. Breitung, High Entropy and Low Symmetry: Triclinic High-Entropy Molybdates, Inorg. Chem. 60 (2021) 115–123. https://doi.org/10.1021/acs.inorgchem.0c02501.

[45] J. Li, J. Sun, Application of X-ray Diffraction and Electron Crystallography for Solving Complex Structure Problems, Acc. Chem. Res. 50 (2017) 2737–2745. https://doi.org/10.1021/acs.accounts.7b00366.

[46] A. Baraldi, E. Buffagni, R. Capelletti, M. Mazzera, M. Fasoli, A. Lauria, F. Moretti, A. Vedda, M. Gemmi, Eu Incorporation into Sol–Gel Silica for Photonic Applications: Spectroscopic and TEM Evidences of α-Quartz and Eu Pyrosilicate Nanocrystal Growth, J. Phys. Chem. C 117 (2013) 26831–26848. https://doi.org/10.1021/jp4101174.

[47] B. Rondeau, B. Devouard, D. Jacob, P. Roussel, N. Stephant, C. Boulet, V. Mollé, M. Corre, E. Fritsch, C. Ferraris, G.C. Parodi, Lasnierite, $(Ca,Sr)(Mg,Fe)_2Al(PO_4)_3$, a new phosphate accompanying lazulite from Mt. Ibity, Madagascar: an example of structural characterization from dynamical refinement of precession electron diffraction data on submicrometre sample, Ejm 31 (2019) 379–388. https://doi.org/10.1127/ejm/2019/0031-2817.

[48] G.N. Kotsonis, S.S.I. Almishal, F. Marques Dos Santos Vieira, V.H. Crespi, I. Dabo, C.M. Rost, J. Maria, High-entropy oxides: Harnessing crystalline disorder for emergent functionality, J Am Ceram Soc. 106 (2023) 5587–5611. https://doi.org/10.1111/jace.19252.

Chapter 7

CONCLUSIONS AND FUTURE WORK

7.1 Conclusions

The objective of this thesis was to demonstrate that oxide ceramics can be used in a hollow anode design for performing molten regolith electrolysis (MRE), while also investigating degradation mechanisms of oxide ceramics exposed to the MRE environment. The degradation of Sc_2O_3, Y_2O_3, ZrO_2, and HfO_2 unary oxides by molten regolith simulants were evaluated through powder experiments. Quenching these specimens locked in the equilibrium behavior of these oxides at 1600°C and enabled characterization at ambient temperature. Sc_2O_3 and Y_2O_3 exhibited reactive crystallization in contact with molten lunar regolith, while ZrO_2 and HfO_2 exhibited dissolution into the molten lunar regolith. Based on the analysis of ZrO_2 and HfO_2, it was determined that their solubilities are similar in LHS-1 (lunar highlands simulant) while HfO_2 has a marginally lower solubility in JSC-1A (lunar maria simulant) than ZrO_2. Since the focus of this thesis was on MRE of lunar highlands regolith, ZrO_2 was selected as the preferred solid electrolyte system since HfO_2 did not appear to offer any advantages, while also being more difficult to source and more expensive. However, both ZrO_2 and HfO_2 require dopants to stabilize the tetragonal/cubic phase and to increase the ionic conductivity. Sc_2O_3 and Y_2O_3 are both commonly used dopants for ZrO_2 for solid electrolyte applications. Both formed complex oxide phases, but Y_2O_3 was selected as the dopant since there was more data available on its thermochemical properties and reaction phases. From these experiments, Y_2O_3-stabilized ZrO_2 (YSZ) was determined to be the most suitable solid electrolyte material for the hollow anode design.

With YSZ selected as the solid electrolyte, a series of both powder and crucible experiments were performed to provide the equilibrium state of YSZ in contact with lunar regolith simulants and to assess how degradation affects bulk YSZ. The powder experiment revealed that YSZ also undergoes dissolution, similar to ZrO_2, but also degrades by Y_2O_3 depletion from YSZ. The Y_2O_3 dopants in YSZ preferentially diffuse out of YSZ and dissolve into the

molten regolith. This behavior is not an issue for powders, but presents challenges for bulk YSZ parts, including crucibles. The YSZ crucible experiments demonstrated that YSZ can contain molten regolith for at least 3 hours, but the crucible will crack on cooldown, due to the loss of Y_2O_3 as a stabilizer for the tetragonal/cubic phase. However, it was also determined that the crucible cracking does not occur until after the molten regolith has solidified. Thus, YSZ can be used both as a containment material for molten regolith and as the solid electrolyte but will need to be replaced after one thermal cycle to a temperature above the liquidus temperature of the molten regolith. Additionally, YSZ grain coarsening, caused by exposure to molten regolith, was also observed, which can slow the rate of YSZ dissolution with increased exposure duration.

A laboratory-scale MRE cell was designed and fabricated, incorporating an inverted hollow anode design. In this design, the YSZ functions as both the solid electrolyte and primary containment vessel for molten regolith. Several electrolysis experiments were performed with LHS-1, successfully demonstrating that O_2 production with a YSZ hollow anode is possible for up to 12 hours. Analysis of the cathodic products indicates that FeO is electrolyzed first, followed by SiO_2. Additionally, P, Ti, and Mn were observed in the cathodic products, suggesting that these oxides are coelectrolyzed with FeO and SiO_2. Post-electrolysis analysis of the MRE cell reveals a new degradation mechanism caused by the applied DC potential for electrolysis. YSZ develops electronic conductivity with increasing electrolysis duration. Evidence of thermochemical degradation mechanisms (YSZ dissolution and Y_2O_3 depletion from YSZ) were also observed. From the electrolysis experiments, rates of all three degradation mechanisms were estimated to provide guidelines for the integration of YSZ hollow anodes into industrial-scale MRE reactors.

Of the observed degradation mechanisms, the evolution of electronic conductivity in YSZ is the most concerning since it has the shortest timescale and causes reduced O_2 production. An additional electrolysis experiment, with multiple electrolysis segments, was performed to test regeneration and mitigation techniques to reduce the electronic conductivity of YSZ. Both regeneration and mitigation methods introduced a high pO_2 environment to decrease the electronic conductivity of YSZ. Through this electrolysis experiment, it was determined that

MRE operation in a high pO_2 environment can provide an increase in O_2 production, resulting in approximately double the O_2 production rate compared to operating in a low pO_2 environment. Additionally, this electrolysis experiment exposed the YSZ to molten regolith for 48 hours and produced O_2 for 40 total hours, which is a significant increase over the previous longest electrolysis experiment of 12 hours. Post-electrolysis analysis of the cell provided another data point at longer exposure durations for YSZ dissolution, allowing for a refined design life estimate for YSZ hollow anodes. Recommendations for maintaining a high pO_2 operating environment in MRE reactors were provided. Using the refined degradation and O_2 production rates obtained from this electrolysis experiment, it was determined that each unit mass of YSZ delivered to the lunar surface could enable the production of up to 7.9x – 9.0x its own mass in O_2.

The previously described powder testing of Sc_2O_3 and molten lunar regolith simulants produced a Sc_2O_3-rich phase that has not been observed before. Compositional analysis of this phase indicates that the major oxide components are Sc_2O_3, SiO_2, and Al_2O_3. This phase is referred to as silicon aluminum scandate (SAS). Based on the measured composition of SAS, a synthesis procedure was developed to produce phase-pure SAS material and successfully scaled up to 100 gram batches. Microcrystal electron diffraction was performed on the phase pure material to solve the unknown structure, enabling several other material characterization techniques to be used. Several materials properties were characterized, with a focus on material properties relevant to both MRE and refractory oxides in general, such as thermal decomposition behavior and thermal expansion. Ultimately, these results establish a baseline set of material properties for the newly discovered doped SAS phase. The endothermic enthalpy of reaction, obtained through differential thermal analysis, indicated that this phase is entropy-stabilized, likely due to substantial configurational entropy from extensive cation site substitutions. Initial thermal conductivity measurements suggest that SAS may be used as a thermally insulating, refractory material in in high-temperature (>1000°C) environments.

7.2 Suggestions for future work

7.2.1 YSZ hollow anodes

While investigating electrical transport in MRE, it appears that there is still a knowledge gap for how the electrical conductivity of molten regolith evolves with increasing electrolysis. Both computational and experimental methods have been used for evaluating the changing molten regolith viscosity with increasing O_2 removal from the electrolyte. Though viscosity is a proxy for ionic conductivity, it may not trend directly with the total electrical conductivity if electronic transport exists in the molten regolith. The presence of multivalent cation species, such as Fe^{2+}/Fe^{3+} and Ti^{3+}/Ti^{4+}, has been shown to increase the electronic conductivity of molten regolith. It is recommended that a comprehensive study evaluating both the ionic and electronic contributions to molten regolith electrical conductivity be performed.

It was observed in several electrolysis experiments that cathodic products formed electronic shorts in the inverted cell design used in this thesis, especially with increased electrolysis duration. This behavior has resulted in sharp decreases in the applied cell potential and measured O_2 production rate, making it difficult to compare electrolysis results. It is expected that a shift to industrial-scale MRE reactors would eliminate this behavior. At this point, it appears that further testing in the inverted cell is unlikely to provide useful O_2 production data. Additionally, the larger geometry of industrial-scale MRE reactors may enable quasi-reference electrodes to be used. No quasi-reference electrodes were used in this thesis due to the confined, inverted cell geometry. The inclusion of these quasi-reference electrodes provides a method to separate the effects of degradation and charge transfer resistance at the cathode and anode. Thus, it is recommended that future YSZ hollow anode testing be performed in the envisioned configuration, rather than the inverted cell design used in this thesis.

The clearest extension of the YSZ hollow anode testing presented in this research is direct integration of YSZ hollow anodes into existing MRE reactors. Based on available literature, it appears that existing MRE reactors use an Ir or Ir-coated anode. By substituting the Ir-

based anode for YSZ hollow anodes, a direct comparison between the two anode technologies can be made. Current estimates of Ir anode dissolution rates are ~8 mm/year, while the YSZ dissolution rates measured in this research are ~5 μm/hr, equating to ~44 mm/year. Though this represents a significant increase in the volume of YSZ needed, compared to Ir, it is generally the mass that is the largest constraint for resupply launches. Ir has a higher density than YSZ (22.56 g/cm^3 vs 5.92 g/cm^3). The area-normalized, mass corrosion rate for Ir is ~18 $g/(cm^2*year)$ and for YSZ is ~26 $g/(cm^2*year)$. These corrosion rates indicate that YSZ hollow anodes would require a ~44% increase in resupply mass compared to Ir, resulting in an increased launch cost. However, Ir is also significantly more expensive than YSZ, which can offset the increase in launch cost. Ultimately, a full system and cost analysis is recommended as future work to determine if YSZ hollow anodes can provide a reduction in long-term MRE operational costs.

Beyond a comparison of bare Ir anodes and YSZ hollow anodes, integration and testing of hollow anodes in full-scale MRE reactors enable testing of downstream processing and collection methods. After O_2 is generated through MRE, it must be collected, liquefied, and stored until it is used for refueling launch vehicles on the lunar surface. For YSZ hollow anodes, the resulting gas stream is already high purity O_2, due to the selective diffusion and oxidation of O^{2-} through using YSZ as a solid electrolyte. To obtain liquid O_2, which is used as the oxidizer in liquid rocket propellants, the O_2 gas must been cooled to below its boiling point (-183°C). The cryocooler is likely required to obtain this temperature, though the low ambient temperatures on the lunar surface may provide partial cooling to get below the boiling point of O_2. It is suggested that a cryogenic processing unit is tested downstream of the MRE reactor in a relevant thermal environment to the lunar surface.

The metals and metalloids produced as cathodic products must also be processed downstream of the MRE reactor to provide useful resources. As discussed in this thesis (Chapter 4), the cathodic products will be predominantly molten Fe and Si, with smaller amounts of P, Ti, and Mn. These cathodic products will settle to the bottom of the MRE reactor due to their higher density compared to molten regolith. A tapping mechanism is required to periodically empty the MRE reactor of these cathodic products. Methods for

tapping can be adapted from the terrestrial steel and aluminum refining industries. However, it is noted that the reduced acceleration due to gravity on the lunar surface may require modifications to existing tapping processes so that the cathodic products are withdrawn from the MRE reactor quickly. Testing in reduced gravity environments is difficult on Earth. It is suggested that this the downstream tapping process for collecting molten cathodic products use computational fluid dynamics for the initial design, which can be iterated and improved through direct testing on the lunar surface.

Finally, it is recommended that advanced multiphysics models are developed for simulating MRE reactor operation. COMSOL and ANSYS are two examples of multiphysics simulation software that can be used to accomplish this. In the MRE reactor, there are many physical and chemical interactions occurring that should be modeled. These interactions include heat transfer, melting and solidification, electrical conduction, electrochemistry, liquid phase separation (between the molten regolith and cathodic products), and gas evolution. A successful initial model of an MRE reactor has been developed in COMSOL (see Introduction references [30], [31]). However, these models do not include the specific composition changes to the molten regolith and cathodic products that result from continuing electrolysis. Instead, the material properties, such as thermal/electrical conductivity, density, surface tension, are fed into the model as temperature-dependent properties for the initial regolith composition. The work presented in this thesis demonstrate that FactSage can be used to estimate the composition trajectories of both the molten regolith and cathodic products that form. It is suggested that the evolving composition be directly integrated into a multiphysics model to account for the differences in material properties and mass transfer that occurs from molten regolith and cathodic products that have spatially dependent compositions. If a unified model for MRE reactors can be developed and validated, that includes the compositional variation at the electrodes and composition dependent material properties, then a digital twin can be produced for a specific MRE reactor design, enabling iteration and optimization through simulation rather than experimental testing. However, it is noted that additional characterization experiments are necessary to obtain the material properties that are used in multiphysics simulations of MRE reactors.

7.2.2 SAS material

Since the SAS phase is a new material, there are significant remaining questions about the properties of this material. Initial thermochemical data for the enthalpy of reaction has been provided here. However, due to reactions between the W crucibles used in differential thermal analysis of the SAS material, it was only determined that the enthalpy of reaction is endothermic. Several techniques are recommended to evaluate the thermochemistry of the SAS system. Laser-based drop-and-catch colorimetry can be used to determine the enthalpy of fusion and melting point, while avoiding container reactivity challenges. High-temperature oxide solution calorimetry can be used to determine the enthalpy of reaction by comparing the difference in enthalpy of solution between the SAS material and the unreacted oxide constituents. High-temperature differential scanning calorimetry can provide the heat capacity of the SAS material, but it is noted that Pt or Ir crucibles should be used since other refractory metals may react with the doped SAS material. The measurement of these thermodynamic properties enables CALPHAD models to be developed for the SAS material.

The only functional material property of SAS characterized in this research is the thermal conductivity, which was comparable to the thermal conductivity of YSZ up to 1000°C. Given the thermal stability of SAS, thermal conductivity measurements to even higher temperatures are recommended. Additionally, the high-temperature ionic/electronic conductivity should be evaluated given the high probability of defects in the SAS crystal structure. Thermomechanical testing should also be performed including, the compressive strength and creep rate with increasing temperature for refractory oxide applications.

Finally, testing of coating methods on SAS microstructure is recommended. Given the relatively high cost of Sc_2O_3, it is unlikely that bulk SAS parts will be used unless the SAS material offers a significant increase in some aspect of material performance. However, it can be applied as a coating to reduce the amount of Sc_2O_3 needed. Due to the thermal stability of SAS and the lack of phase transitions up to 1600°C, it appears that SAS is well-suited for thermal spray coating methods. Since thermal spray processes generally cause large thermal gradients during growth, it is recommended that the thermally sprayed SAS coating be

investigated to determine the relationship between as-sprayed microstructure and processing conditions. It is noted that the cracking induced by thermal expansion anisotropy, presented in this research, may reduce the effective strength and/or toughness of SAS coatings. However, the presence of cracks will also increase porosity, potentially lowering the effective thermal conductivity of SAS coatings. Ultimately, the material requirements of specific applications will determine the suitability of SAS coatings, but an initial understanding of thermally sprayed SAS can provide insight on which applications may benefit from SAS over other thermally insulating oxides, such as YSZ.

Appendix A

ANALYSIS OF LUNAR OXYGEN PRODUCTION AND REFUELING FOR STARSHIP HUMAN LANDING SYSTEM

An estimate of the cost savings is presented using approximate values for SpaceX's Starship Human Landing System (HLS), which is the planned lunar lander for Artemis 3 and 4 [1]. It is noted that the specific values for Starship HLS are not publicly available and are likely changing with further development of the spacecraft. However, public information from SpaceX's website and press releases indicate that Starship HLS will be able to deliver a 100 mt payload to the lunar surface, with a dry mass of 85 mt and a propellant mass of 1500 mt [2]. Of the 1500 mt of propellant, 1170 mt are liquid O_2 and 330 mt are liquid CH_4 [3]. These values can be used in the Tsiolkovsky rocket equation to estimate the effective exhaust velocity ratio necessary for a round trip journey to the lunar surface:

$$m_0 = m_f e^{\Delta v / v_e} \qquad (A.1)$$

where m_0 is the initial total mass, m_f is the final total mass, and $\Delta v/v_e$ is the effective exhaust velocity ratio. Using the numbers from Starship HLS, m_0 = 1685 mt (85 mt + 100 mt + 1500 mt) and m_f = 185 mt, Equation 1.1 can be solved to obtain that $\Delta v/v_e$ = 2.209. Since this effective exhaust velocity ratio represents the round trip journey, it is divided in half to obtain the effective exhaust velocity ratio required for a one-way trip to the lunar surface, which results in $\Delta v/v_e$ = 1.105. From here, O_2 refueling on the lunar surface can be incorporated to determine the new final mass that can be sent to the Moon, assuming that the initial total mass is unchanged. This uses $\Delta v/v_e$ = 1.105 and m_0 = 1685 mt in Equation A.1, which can be solved to obtain m_f = 558 mt.

Consequently, the total final mass that can be transported to the lunar surface, if lunar-derived O_2 refueling on the lunar surface is possible, is 558 mt. However, this final mass still contains the dry mass of Starship HLS and mass of liquid CH_4 for the return trip since it is not refueled on the lunar surface. The dry mass is unchanged (85 mt). The mass of liquid CH_4 for the

return trip can be calculated by determining the amount of CH_4 that was already burned. Using the values above and assuming that the propellant burn ratio is the same as the propellant mass ratio, the amount of CH_4 remaining is 82 mt. Subtracting the dry mass (85 mt) and remaining CH_4 mass (82 mt) from the calculated final mass (558 mt), the payload mass, using lunar O_2 refueling, is 391 mt. Thus, the payload capacity was 100 mt without O_2 refueling and increases to 391 mt with O_2 refueling on the lunar surface. Assuming the same launch cost in both cases, this analysis indicates that the cost per unit mass delivered to the lunar surface can decrease by 74% by utilizing lunar-derived O_2 refueling on the lunar surface. This represents a significant reduction in the cost associated with either human or cargo transport to the lunar surface, which decreases the cost of a sustained human presence on the Moon.

References

[1] NASA, Artemis III: NASA's First Human Mission to Lunar South Pole, NASA.Gov (2023). https://www.nasa.gov/missions/artemis/artemis-iii/ (accessed August 30, 2025).

[2] SpaceX, Starship, SpaceX (n.d.). http://www.spacex.com/vehicles/starship (accessed August 30, 2025).

[3] E. Musk, Starbase Tour and Interview with Elon Musk, (2021). https://everydayastronaut.com/starbase-tour-and-interview-with-elon-musk/ (accessed August 30, 2025).

Appendix B

COMPARISON OF ENERGY-DISPERSIVE X-RAY SPECTROSCOPY VS. ELECTRON PROBE MICROANALYSIS FOR OXIDES

The samples of unary and binary oxides/simulants presented in Chapters 2 and 3 offer an opportunity to compare energy-dispersive X-ray spectroscopy (EDS) and electron probe microanalysis (EPMA). A total of 26 phases were analyzed by EDS and EPMA, covering amorphous oxide glasses, reaction products containing multiple oxide species, and nearly pure unary/binary oxides with impurities. Observations and error analysis are presented in the next paragraphs, while the tabulated data from these phases are provided at the end of this appendix. It is noted that this comparison is specific to the EPMA and EDS systems in Caltech's Geology and Planetary Sciences Division Analytical Facility.

EDS and EPMA are both non-destructive spectroscopic techniques that can be used to determine the composition of relatively small (~1 μm) solid phases [1]. Both techniques rely on a focused electron beam to produce characteristic X-rays from atoms in the solid [1]. Generally, the main difference between EDS and EPMA is how these techniques measure the emitted characteristic X-ray spectrum. Modern EDS systems use a silicon drift detector that functions as an energy dispersive spectrometer to obtain the X-ray spectra [2]. EPMA relies on a wavelength dispersive spectrometer (WDS), using several crystals of known lattice parameters to effectively filter X-rays based on wavelength [1]. The crystals are rotated and only X-rays with wavelengths satisfying Bragg's law are transmitted into a proportional counter detector for quantification [1]. Due to these differences, WDS offers improved energy resolution in the obtained X-ray spectrum compared to EDS [1]. This allows EPMA, using a WDS, to resolve X-ray peaks that would be overlapping in EDS. EDS relies on peak deconvolution in order to extract X-ray intensities of elements that have similar characteristic X-rays [1].

Due to the devolution method used in EDS, it is paramount that the user has prior information on the elements present and checks each collected spectrum to ensure that there are no

misidentified or missing elements. Modern EDS analysis software includes auto-identification, which works well for elements with high concentration (>1 at%) and for X-ray spectrums with limited overlapping elements. However, it has been observed in the samples analyzed and reported in this appendix that low concentration (<1 at%) elements can be misidentified or not indexed at all, leading to incorrect peak deconvolution.

In addition to the difference in X-ray spectrometers, EPMA generally have a more stable and confined electron beam, offering better control of both the interaction volume and drift of the electron beam compared to the scanning electron microscope (SEM) that provides the focused electron beam for EDS [1]. In the context of the data collected here, another major difference between the two datasets is standard calibration. All the EPMA data presented in this appendix were collected after performing calibration on standards. EDS systems can also be calibrated on standards but are more commonly used in standardless analysis [2]. Usually, EDS is calibrated by the manufacturer but not calibrated prior to each analysis session. The EDS data in this appendix were obtained using standardless analysis.

EPMA was performed using a JEOL JXA-iHP200F system, with calibration performed on standards for Si, Al, Ti, Ca, K, Na, Mg, Fe, Mn, Sc, Hf, Zr, Sc, and Y. Since these are oxide samples, heat-treated in air at 1600°C, all cationic species were assumed to be in their highest oxidation state. O content was calculated based on the cation composition measured by EPMA, which is the standard for analyzing oxide materials. EDS was performed in a ZEISS 1550VP FESEM, with an Oxford Instruments X-Max EDS detector without standards used. Two methods of analysis are included for the EDS data. In the first analysis method, O content is determined from peak deconvolution. It is expected that this method is less accurate since O is a light element with a low-energy characteristic X-ray ($K_\alpha \approx 0.525$ keV) [3]. The low-energy X-rays of O will be more strongly absorbed (by the X-ray detector window or sample) compared to the higher energy X-rays of the other metal and semi-metal species in these samples [3]. As such, it is expected that the O content obtained from peak deconvolution will underestimate the O content. The second analysis method for determining O content is the same as EPMA. It is calculated assuming that all metal and semi-metal species are in their highest oxidation state.

The composition and standard deviation of each phase are presented in Tables B.1 – B.26. The number of sites analyzed are included the table captions. The EPMA-measured composition is assumed to be the most accurate. Both methods of obtaining the O content from EDS are included. O content obtained from the EDS measurement through peak deconvolution is labeled EDS-M. O content obtained through a charge balance calculation is denoted EDS-C. Relative error is also included as the difference between the EDS-measured composition and the EPMA-measured composition for a certain species in at%, with +/- denoting the direction of deviation from the EPMA-measured composition. A dash (-) is used in the EDS data to indicate that an element was detected by EPMA but not by EDS.

The first comparison to be made between EPMA and EDS is examining the average and maximum error. The average error reported here is of the absolute value of the relative errors, to avoid having positive and negative errors being averaged out. For EDS-M (O content obtained through peak deconvolution), the average error relative to EPMA is 0.48 at% and the maximum error is -5.97 at%. For EDS-C (O content obtained through charge balance calculation), the average error relative to EPMA is 0.07 at% and the maximum error is +1.41 at%. Thus, it appears that EDS-C provides a more accurate composition compared to EDS-M. The average error of EDS-C is extremely low (0.07 at%) and EDS-C generally produced accurate results compared to EPMA, when elemental species were correctly identified for analysis.

However, there are some limitations to EDS-C compared to EPMA. Specifically, there are several elemental species that were not included for analysis by EDS-C but were within the limits of detection by EPMA. The average concentration of all EDS-missed elements is 0.07 at% and the maximum concentration of an EDS-missed element is 0.50 at%. These values indicate that only trace elements (<1.00 at%) are missed by EDS analysis. Of the elements that were not detected by EDS, the majority are within the nearly pure oxide phases. A total of 59 elements were missed across all phases. Splitting by phase type, 34 elements in nearly pure oxides, 18 elements in glasses, and 8 elements in mixed oxide phases were missed. It is not surprising that the majority of elements not detected by EDS were in the nearly pure

unary/binary oxides since these phases possess the highest concentration of Sc, Y, Zr, or Hf, which cause the characteristic X-ray peaks of these elements to have significantly higher counts than any remaining trace elements. Additionally, this analysis indicates that EDS is not suited for trace element analysis and that EPMA should be used in for these cases, especially if the trace elements are in an otherwise nearly pure unary/binary oxide phase.

Finally, a comparison of EDS-M and EDS-C for the concentration of O is presented. For EDS-M, the average error of O is -2.96 at% and the maximum error is -5.97 at%. For EDS-C, the average error of O is +0.17 at% and the maximum error is +0.86 at%. Thus, EDS-C provides the more accurate determination of O content, with EDS-M underestimating the O content by an average of nearly 3 at%. This is consistent with the expected result discussed above. EDS-M is not accurate for O concentration and likely underestimates the O concentration, since it relies on deconvoluting the low-energy O characteristic X-ray peak. EDS-C and EPMA obtain O content in the same way, so the O content between these two techniques is expected to be close to each other. It is noted that this method of O content determination is only for oxide materials, with fully oxidized cationic species.

Despite the limitations discussed above, this analysis shows that EDS-C can produce accurate results compared to EPMA for oxide materials. The main limitation of EDS is that trace elements are undetected. Oxide materials possessing trace elements of interest should be evaluated with EPMA. It is noted that many EDS manufacturers have often advertised their systems as offering point-and-click elemental identification and quantification [2]. Though EDS can be quite accurate, this statement by manufacturers is somewhat misleading. Ultimately, the accuracy of EDS relies on user intervention and nuance when performing compositional analysis. If automated analysis is used, each spectrum should be examined to ensure that the results do not include elements that were erroneously added.

References

[1] V. De Oliveira Campos, F.F. Barbosa, E.K.L. De Morais, D.M.A. Melo, J. De Jesus Santana, G.S. Patience, Experimental methods in chemical engineering: Electron probe micro-analysis—EPMA, Can J Chem Eng 103 (2025) 3000–3011. https://doi.org/10.1002/cjce.25712.

[2] D.E. Newbury, N.W.M. Ritchie, Is Scanning Electron Microscopy/Energy Dispersive X-ray Spectrometry (SEM/EDS) Quantitative?, Scanning 35 (2013) 141–168. https://doi.org/10.1002/sca.21041.

[3] M. Malac, R.F. Egerton, Calibration Specimens for Determining Energy-Dispersive X-ray k-Factors of Boron, Nitrogen, Oxygen, and Fluorine, Microsc. Microanal. 5 (1999) 29–38. https://doi.org/10.1017/s1431927699000021.

Table B.1. EPMA and EDS composition of bright phase in 50:50 JSC-1A/ZrO_2 samples. EPMA used 3 sites. EDS used 9 sites.

50:50 JSC-1A/ZrO_2 - Bright phase (ZrO_2)							
		Ti	**Ca**	**Fe**	**Zr**	**Hf**	**O**
EPMA	Average	0.10	0.04	0.33	32.6	0.39	66.54
	Std Dev	0.01	0.01	0.04	0.03	0.01	0.02
EDS-M	Average	-	-	0.40	37.49	0.43	61.67
	Std Dev	-	-	0.08	0.31	0.01	0.39
	Error (at%)	-	-	+0.07	+4.89	+0.04	-4.87
EDS-C	Average	-	-	0.35	32.66	0.38	66.61
	Std Dev	-	-	0.07	0.06	0.01	0.01
	Error (at%)	-	-	+0.02	+0.06	-0.01	+0.07

Table B.2. EPMA and EDS composition of regolith in 50:50 JSC-1A/ZrO_2 samples. EPMA used 10 sites. EDS used 31 sites.

50:50 JSC-1A/ZrO_2 - Solidified regolith													
		Si	**Al**	**Ti**	**Ca**	**K**	**Na**	**Mg**	**Fe**	**Mn**	**Zr**	**Hf**	**O**
EPMA	Average	17.11	6.41	0.33	4.18	0.29	1.92	4.85	3.09	0.05	1.30	0.02	60.43
	Std Dev	0.11	0.05	0.01	0.03	0.01	0.05	0.04	0.03	0.01	0.13	0.00	0.03
EDS-M	Average	17.96	6.90	0.38	4.32	0.33	1.82	4.97	3.23	-	1.48	-	58.61
	Std Dev	0.24	0.10	0.02	0.05	0.02	0.05	0.06	0.06	-	0.30	-	0.25
	Error (at%)	+0.85	+0.49	+0.05	+0.14	+0.04	-0.10	+0.12	+0.14	-	+0.18	-	-1.82
EDS-C	Average	16.85	6.47	0.36	4.06	0.31	1.71	4.66	3.03	-	1.39	-	61.17
	Std Dev	0.20	0.09	0.02	0.05	0.02	0.05	0.06	0.06	-	0.28	-	0.04
	Error (at%)	-0.26	+0.06	+0.03	-0.12	+0.02	-0.21	-0.19	-0.06	-	+0.09	-	+0.74

Table B.3. EPMA and EDS composition of bright phase in 50:50 LHS-1/ZrO_2 samples. EPMA used 3 sites. EDS used 10 sites.

50:50 LHS-1/ZrO_2 - Bright phase (ZrO_2)							
		Ti	**Ca**	**Fe**	**Zr**	**Hf**	**O**
EPMA	Average	0.05	0.03	0.09	32.81	0.38	66.63
	Std Dev	0.02	0.00	0.04	0.06	0.02	0.01
EDS-M	Average	-	-	0.11	37.44	0.42	62.03
	Std Dev	-	-	0.12	0.44	0.02	0.42
	Error (at%)	-	-	+0.02	+4.63	+0.04	-4.60
EDS-C	Average	-	-	0.10	32.88	0.37	66.65
	Std Dev	-	-	0.10	0.09	0.01	0.02
	Error (at%)	-	-	+0.01	+0.07	-0.01	+0.02

Table B.4. EPMA and EDS composition of regolith in 50:50 LHS-1/ZrO_2 samples. EPMA used 10 sites. EDS used 30 sites.

50:50 LHS-1/ZrO_2 - Solidified regolith													
		Si	**Al**	**Ti**	**Ca**	**K**	**Na**	**Mg**	**Fe**	**Mn**	**Zr**	**Hf**	**O**
EPMA	Average	17.36	11.00	0.13	5.14	0.23	1.7	1.1	0.71	0.01	1.07	0.02	61.55
	Std Dev	0.11	0.06	0.01	0.06	0.01	0.03	0.02	0.01	0.00	0.18	0.00	0.03
EDS-M	Average	18.48	11.97	0.14	5.35	0.26	1.69	1.17	0.76	-	1.06	-	59.13
	Std Dev	0.20	0.08	0.02	0.06	0.01	0.04	0.01	0.03	-	0.16	-	0.35
	Error (at%)	+1.12	+0.97	+0.01	+0.21	+0.03	-0.01	+0.07	+0.05	-	-0.01	-	-2.42
EDS-C	Average	17.30	11.21	0.13	5.01	0.24	1.58	1.09	0.71	-	0.99	-	61.73
	Std Dev	0.09	0.07	0.01	0.03	0.01	0.04	0.02	0.02	-	0.14	-	0.03
	Error (at%)	-0.06	+0.21	+0.00	-0.13	+0.01	-0.12	-0.01	-0.00	-	-0.08	-	+0.18

Table B.5. EPMA and EDS composition of bright phase in 50:50 JSC-1A/HfO_2 samples. EPMA used 3 sites. EDS used 7 sites.

50:50 JSC-1A/HfO_2 - Bright phase (HfO_2)					
		Ti	**Mn**	**Hf**	**O**
EPMA	Average	0.20	0.06	33.09	66.65
	Std Dev	0.07	0.01	0.06	0.00
EDS-M	Average	-	-	37.94	62.06
	Std Dev	-	-	0.27	0.27
	Error (at%)	-	-	+4.85	-4.59
EDS-C	Average	-	-	33.33	66.67
	Std Dev	-	-	0.00	0.00
	Error (at%)	-	-	+0.24	+0.02

Table B.6. EPMA and EDS composition of regolith in 50:50 JSC-1A/HfO_2 samples. EPMA used 10 sites. EDS used 16 sites.

50:50 JSC-1A/HfO_2 - Solidified regolith													
		Si	**Al**	**Ti**	**Ca**	**K**	**Na**	**Mg**	**Fe**	**Mn**	**Zr**	**Hf**	**O**
EPMA	Average	17.58	6.32	0.33	4.11	0.25	1.84	4.84	3.09	0.05	0.02	1.03	60.54
	Std Dev	0.07	0.07	0.01	0.02	0.01	0.04	0.04	0.04	0.00	0.00	0.12	0.03
EDS-M	Average	18.86	6.77	0.39	4.31	0.27	1.74	4.89	3.30	-	0.08	1.56	57.84
	Std Dev	0.07	0.13	0.02	0.04	0.02	0.05	0.08	0.07	-	0.06	0.34	0.10
	Error (at%)	+1.28	+0.45	+0.06	+0.20	+0.02	-0.10	+0.05	+0.21	-	+0.06	+0.53	-2.70
EDS-C	Average	17.27	6.20	0.36	3.94	0.25	1.59	4.48	3.02	-	0.07	1.42	61.40
	Std Dev	0.11	0.14	0.01	0.05	0.02	0.05	0.09	0.06	-	0.06	0.31	0.09
	Error (at%)	-0.31	-0.12	+0.03	-0.17	-0.00	-0.25	-0.36	-0.07	-	+0.05	+0.39	+0.86

Table B.7. EPMA and EDS composition of bright phase in 50:50 LHS-1/HfO_2 samples. EPMA used 3 sites. EDS used 6 sites.

50:50 LHS-1/HfO_2 - Bright phase (HfO_2)					
		Ti	**Mn**	**Hf**	**O**
EPMA	Average	0.15	0.06	33.14	66.65
	Std Dev	0.01	0.02	0.00	0.01
EDS-M	Average	-	-	37.61	62.34
	Std Dev	-	-	0.24	0.33
	Error (at%)	-	-	+4.47	-4.31
EDS-C	Average	-	-	33.33	66.67
	Std Dev	-	-	0.00	0.00
	Error (at%)	-	-	+0.19	+0.02

Table B.8. EPMA and EDS composition of regolith in 50:50 LHS-1/HfO_2 samples. EPMA used 10 sites. EDS used 13 sites.

50:50 LHS-1/HfO_2 - Solidified regolith													
		Si	**Al**	**Ti**	**Ca**	**K**	**Na**	**Mg**	**Fe**	**Mn**	**Zr**	**Hf**	**O**
EPMA	Average	17.61	10.77	0.12	5.06	0.20	1.72	1.11	0.75	0.01	0.02	1.03	61.6
	Std Dev	0.04	0.06	0.01	0.04	0.01	0.02	0.01	0.02	0.00	0.00	0.11	0.03
EDS-M	Average	19.06	11.61	0.16	5.42	0.23	1.67	1.18	0.85	-	0.06	1.35	58.39
	Std Dev	0.20	0.13	0.01	0.02	0.01	0.04	0.01	0.03	-	0.06	0.23	0.14
	Error (at%)	+1.45	+0.84	+0.04	+0.36	+0.03	-0.05	+0.07	+0.10	-	+0.04	+0.32	-3.21
EDS-C	Average	17.47	10.64	0.14	4.97	0.21	1.53	1.08	0.78	-	0.06	1.24	61.87
	Std Dev	0.15	0.12	0.01	0.03	0.01	0.04	0.02	0.03	-	0.05	0.21	0.04
	Error (at%)	-0.14	-0.13	+0.02	-0.09	+0.01	-0.19	-0.03	+0.03	-	+0.04	+0.21	+0.27

Table B.9. EPMA and EDS composition of bright phase in 50:50 JSC-1A/Y_2O_3 samples. EPMA used 3 sites. EDS used 7 sites.

50:50 JSC-1A/Y_2O_3 - Bright phase (Y_2O_3)						
		Ti	**Ca**	**Fe**	**Y**	**O**
EPMA	Average	0.01	0.03	0.02	39.94	59.99
	Std Dev	0.01	0.00	0.01	0.02	0.00
EDS-M	Average	-	-	-	44.79	55.21
	Std Dev	-	-	-	0.42	0.42
	Error (at%)	-	-	-	+4.85	-4.78
EDS-C	Average	-	-	-	40.00	60.00
	Std Dev	-	-	-	0.00	0.00
	Error (at%)	-	-	-	+0.06	+0.01

Table B.10. EPMA and EDS composition of reaction phase in 50:50 JSC-1A/Y_2O_3 samples. EPMA used 5 sites. EDS used 7 sites.

50:50 JSC-1A/Y_2O_3 - Reaction phase										
		Si	**Al**	**Ti**	**Ca**	**Na**	**Mg**	**Fe**	**Y**	**O**
EPMA	Average	7.29	2.86	0.16	1.73	0.24	1.89	1.35	24.07	60.4
	Std Dev	0.06	0.04	0.01	0.01	0.09	0.05	0.03	0.07	0.04
EDS-M	Average	7.41	3.00	0.20	1.78	-	2.04	1.42	27.25	56.89
	Std Dev	0.07	0.05	0.02	0.03	-	0.04	0.04	0.26	0.38
	Error (at%)	+0.12	+0.14	+0.04	+0.05	-	+0.15	+0.07	+3.18	-3.51
EDS-C	Average	6.76	2.74	0.18	1.62	-	1.86	1.29	24.85	60.69
	Std Dev	0.03	0.04	0.02	0.02	-	0.05	0.03	0.08	0.01
	Error (at%)	-0.53	-0.12	+0.02	-0.11	-	-0.03	-0.06	+0.78	+0.29

Table B.11. EPMA and EDS composition of bright phase in 50:50 LHS-1/Y_2O_3 samples. EPMA used 3 sites. EDS used 6 sites.

50:50 LHS-1/Y_2O_3 - Bright phase (Y_2O_3)								
		Si	**Al**	**Ti**	**Ca**	**Mn**	**Y**	**O**
EPMA	Average	0.09	0.01	0.01	0.05	0.01	39.82	60.01
	Std Dev	0.07	0.01	0.01	0.01	0.01	0.09	0.01
EDS-M	Average	-	-	-	-	-	44.77	55.23
	Std Dev	-	-	-	-	-	0.58	0.58
	Error (at%)	-	-	-	-	-	+4.95	-4.78
EDS-C	Average	-	-	-	-	-	40.00	60.00
	Std Dev	-	-	-	-	-	0.00	0.00
	Error (at%)	-	-	-	-	-	+0.18	-0.01

Table B.12. EPMA and EDS composition of reaction phase in 50:50 LHS-1/Y_2O_3 samples. EPMA used 5 sites. EDS used 7 sites.

50:50 LHS-1/Y_2O_3 – Reaction phase										
		Si	**Al**	**Ti**	**Ca**	**Na**	**Mg**	**Fe**	**Y**	**O**
EPMA	Average	7.03	5.15	0.08	2.17	0.02	0.43	0.32	23.98	60.83
	Std Dev	0.13	0.18	0.02	0.08	0.02	0.04	0.06	0.12	0.02
EDS-M	Average	7.24	4.80	-	2.14	0.18	0.49	0.32	27.76	57.14
	Std Dev	0.17	1.11	-	0.40	0.31	0.11	0.08	1.46	0.88
	Error (at%)	+0.21	-0.35	-	-0.03	+0.16	+0.06	0.00	+3.78	-3.69
EDS-C	Average	6.62	4.39	-	1.95	0.10	0.45	0.29	25.39	60.81
	Std Dev	0.04	1.01	-	0.36	0.22	0.10	0.07	1.28	0.02
	Error (at%)	-0.41	-0.76	-	-0.22	+0.08	+0.02	-0.03	+1.41	-0.02

Table B.13. EPMA and EDS composition of reaction phase in 50:50 JSC-1A/Sc_2O_3 samples. EPMA used 5 sites. EDS used 4 sites.

50:50 JSC-1A/Sc_2O_3 - Reaction phase											
		Si	**Al**	**Ti**	**Ca**	**Na**	**Mg**	**Fe**	**Mn**	**Sc**	**O**
EPMA	Average	6.99	2.15	0.26	0.27	0.01	2.14	0.94	0.01	26.44	60.77
	Std Dev	0.05	0.03	0.01	0.04	0.00	0.03	0.00	0.00	0.09	0.01
EDS-M	Average	6.98	2.21	-	0.38	-	2.16	1.04	-	27.78	59.46
	Std Dev	0.17	0.11	-	0.04	-	0.06	0.03	-	0.16	0.12
	Error (at%)	-0.01	+0.06	-	+0.11	-	+0.02	+0.10	-	+1.34	-1.31
EDS-C	Average	6.73	2.13	-	0.37	-	2.09	1.00	-	26.82	60.86
	Std Dev	0.15	0.10	-	0.04	-	0.06	0.03	-	0.24	0.04
	Error (at%)	-0.26	-0.02	-	+0.10	-	-0.05	+0.06	-	+0.38	+0.09

Table B.14. EPMA and EDS composition of regolith in 50:50 JSC-1A/Sc_2O_3 samples. EPMA used 3 sites. EDS used 2 sites.

50:50 JSC-1A/Sc_2O_3 - Solidified regolith												
		Si	**Al**	**Ti**	**Ca**	**K**	**Na**	**Mg**	**Fe**	**Mn**	**Sc**	**O**
EPMA	Average	16.29	6.52	0.14	6.50	0.37	2.80	3.54	1.08	0.04	2.92	59.79
	Std Dev	0.04	0.08	0.01	0.10	0.02	0.08	0.05	0.02	0.01	0.15	0.03
EDS-M	Average	16.93	6.79	0.16	6.54	0.37	2.66	3.70	1.11	-	3.75	58.01
	Std Dev	0.03	0.03	0.01	0.04	0.05	0.01	0.06	0.03	-	0.14	0.05
	Error (at%)	+0.64	+0.27	+0.02	+0.04	0.00	-0.14	+0.16	+0.03	-	+0.83	-1.78
EDS-C	Average	16.06	6.44	0.15	6.20	0.35	2.52	3.51	1.05	-	3.56	60.15
	Std Dev	0.04	0.03	0.01	0.04	0.05	0.01	0.06	0.03	-	0.13	0.01
	Error (at%)	-0.23	-0.08	+0.01	-0.30	-0.02	-0.28	-0.03	-0.03	-	+0.64	+0.36

Table B.15. EPMA and EDS composition of reaction phase in 50:50 LHS-1/Sc_2O_3 samples. EPMA used 5 sites. EDS used 4 sites.

50:50 LHS-1/Sc_2O_3 - Reaction phase											
		Si	**Al**	**Ti**	**Ca**	**Na**	**Mg**	**Fe**	**Mn**	**Sc**	**O**
EPMA	Average	5.25	4.60	0.26	0.33	0.01	0.48	0.29	0.01	27.90	60.88
	Std Dev	0.03	0.02	0.00	0.02	0.00	0.01	0.01	0.01	0.03	0.01
EDS-M	Average	5.26	4.72	-	0.42	-	0.51	0.29	-	28.55	60.25
	Std Dev	0.04	0.02	-	0.01	-	0.04	0.04	-	0.06	0.11
	Error (at%)	+0.01	+0.12	-	+0.09	-	+0.03	0.00	-	+0.65	-0.63
EDS-C	Avg	5.18	4.65	-	0.41	-	0.50	0.29	-	28.12	60.85
	Std Dev	0.03	0.02	-	0.01	-	0.04	0.03	-	0.04	0.01
	Error (at%)	-0.07	+0.05	-	+0.08	-	+0.02	-0.00	-	+0.22	-0.03

Table B.16. EPMA and EDS composition of regolith in 50:50 LHS-1/Sc_2O_3 samples. EPMA used 3 sites. EDS used 2 sites.

50:50 LHS-1/Sc_2O_3 - Solidified regolith												
		Si	**Al**	**Ti**	**Ca**	**K**	**Na**	**Mg**	**Fe**	**Mn**	**Sc**	**O**
EPMA	Average	16.45	8.59	0.10	6.72	0.20	1.80	0.69	0.26	0.01	4.20	60.97
	Std Dev	0.09	0.04	0.00	0.01	0.01	0.04	0.01	0.01	0.00	0.12	0.03
EDS-M	Average	16.84	8.95	-	6.95	0.21	1.84	0.70	0.24	-	4.35	59.94
	Std Dev	0.40	0.15	-	0.18	0.01	0.00	0.01	0.01	-	0.45	0.33
	Error (at%)	+0.39	+0.36	-	+0.23	+0.01	+0.04	+0.01	-0.02	-	+0.15	-1.03
EDS-C	Average	16.39	8.71	-	6.77	0.20	1.79	0.68	0.23	-	4.23	60.99
	Std Dev	0.25	0.07	-	0.12	0.01	0.02	0.01	0.01	-	0.47	0.03
	Error (at%)	-0.06	+0.12	-	+0.05	+0.00	-0.01	-0.01	-0.03	-	+0.03	+0.02

Table B.17. EPMA and EDS composition of bright phase in 50:50 JSC-1A/Sc_2O_3 samples. EPMA used 3 sites. EDS used 2 sites.

50:50 JSC-1A/Sc_2O_3 - Bright phase (Sc_2O_3)											
		Si	**Al**	**Ti**	**Ca**	**K**	**Mg**	**Fe**	**Mn**	**Sc**	**O**
EPMA	Average	0.04	0.36	0.50	0.18	0.01	0.21	1.14	0.01	37.75	59.79
	Std Dev	0.00	0.01	0.02	0.03	0.00	0.02	0.10	0.00	0.14	0.03
EDS-M	Average	-	0.35	-	0.14	-	-	1.03	-	39.36	59.14
	Std Dev	-	0.02	-	0.19	-	-	0.08	-	0.3	0.21
	Error (at%)	-	-0.01	-	-0.04	-	-	-0.11	-	+1.61	-0.65
EDS-C	Avg	-	0.34	-	0.13	-	-	1.01	-	38.55	59.97
	Std Dev	-	0.02	-	0.19	-	-	0.08	-	0.05	0.04
	Error (at%)	-	-0.02	-	-0.05	-	-	-0.13	-	+0.80	+0.18

Table B.18. EPMA and EDS composition of bright phase in 50:50 LHS-1/Sc_2O_3 samples. EPMA used 3 sites. EDS used 2 sites.

50:50 LHS-1/Sc_2O_3 - Bright phase (Sc_2O_3)										
		Si	**Al**	**Ti**	**Ca**	**K**	**Mg**	**Fe**	**Sc**	**O**
EPMA	Average	0.04	0.51	0.40	0.24	0.01	0.07	0.27	38.49	59.97
	Std Dev	0.01	0.04	0.01	0.01	0.00	0.00	0.03	0.02	0.00
EDS-M	Average	0.24	0.57	-	0.38	-	-	0.25	38.72	59.85
	Std Dev	0.33	0.17	-	0.14	-	-	0.00	0.17	0.47
	Error (at%)	+0.20	+0.06	-	+0.14	-	-	-0.02	+0.23	-0.12
EDS-C	Average	0.23	0.57	-	0.38	-	-	0.25	38.60	59.97
	Std Dev	0.33	0.16	-	0.14	-	-	0.00	0.66	0.04
	Error (at%)	+0.19	+0.06	-	+0.14	-	-	-0.02	+0.11	+0.00

Table B.19. EPMA and EDS composition of bright phase in 50:50 JSC-1A/YSZ samples. EPMA used 5 sites. EDS used 5 sites.

50:50 JSC-1A/YSZ - Bright phase (YSZ)									
		Ti	**Ca**	**Mg**	**Fe**	**Zr**	**Hf**	**Y**	**O**
EPMA	Average	0.12	0.19	0.32	0.56	29.34	0.33	3.39	65.74
	Std Dev	0.01	0.04	0.08	0.07	0.20	0.02	0.33	0.03
EDS-M	Average	-	0.22	0.43	0.68	33.6	0.36	3.63	61.12
	Std Dev	-	0.03	0.04	0.07	0.04	0.01	0.08	0.17
	Error (at%)	-	+0.03	+0.11	+0.12	+4.26	+0.03	+0.24	-4.62
EDS-C	Average	-	0.15	0.38	0.60	29.51	0.32	3.18	65.86
	Std Dev	-	0.09	0.03	0.06	0.09	0.01	0.07	0.04
	Error (at%)	-	-0.04	+0.06	+0.04	+0.17	-0.01	-0.21	+0.12

Table B.20. EPMA and EDS composition of regolith in 50:50 JSC-1A/YSZ samples. EPMA used 10 sites. EDS used 40 sites.

50:50 JSC-1A/YSZ - Solidified regolith														
		Si	**Al**	**Ti**	**Ca**	**K**	**Na**	**Mg**	**Fe**	**Mn**	**Zr**	**Hf**	**Y**	**O**
EPMA	Average	16.80	6.27	0.35	3.78	0.25	1.78	4.24	2.60	0.05	1.65	0.02	1.38	60.82
	Std Dev	0.29	0.11	0.01	0.06	0.01	0.05	0.06	0.05	0.00	0.44	0.00	0.04	0.07
EDS-M	Average	17.07	6.59	0.39	3.89	0.31	1.83	4.41	2.71	-	2.04	-	1.68	59.07
	Std Dev	0.38	0.15	0.02	0.06	0.03	0.09	0.07	0.07	-	0.52	-	0.07	0.30
	Error (at%)	+0.27	+0.32	+0.04	+0.11	+0.06	+0.05	+0.17	+0.11	-	+0.39	-	+0.30	-1.75
EDS-C	Average	16.14	6.23	0.37	3.68	0.29	1.73	4.17	2.57	-	1.93	-	1.58	61.31
	Std Dev	0.33	0.14	0.02	0.05	0.03	0.09	0.07	0.06	-	0.50	-	0.06	0.08
	Error (at%)	-0.66	-0.04	+0.02	-0.10	+0.04	-0.05	-0.07	-0.03	-	+0.28	-	+0.20	+0.49

Table B.21. EPMA and EDS composition of bright phase in 50:50 LHS-1/YSZ samples. EPMA used 5 sites. EDS used 6 sites.

50:50 LHS-1/YSZ - Bright phase (YSZ)										
		Al	**Ti**	**Ca**	**Mg**	**Fe**	**Zr**	**Hf**	**Y**	**O**
EPMA	Average	0.04	0.07	0.18	0.03	0.13	29.72	0.34	3.53	65.96
	Std Dev	0.01	0.01	0.06	0.02	0.02	0.15	0.01	0.18	0.04
EDS-M	Average	-	-	0.26	-	0.28	35.17	0.37	4.07	59.99
	Std Dev	-	-	0.03	-	0.02	0.32	0.01	0.29	0.24
	Error (at%)	-	-	+0.08	-	+0.15	+5.45	+0.03	+0.54	-5.97
EDS-C	Average	-	-	0.22	-	0.12	29.89	0.31	3.46	66.00
	Std Dev	-	-	0.03	-	0.13	0.26	0.01	0.24	0.05
	Error (at%)	-	-	+0.04	-	-0.01	+0.17	-0.03	-0.07	+0.04

Table B.22. EPMA and EDS composition of regolith in 50:50 LHS-1/YSZ samples. EPMA used 10 sites. EDS used 36 sites.

50:50 LHS-1/YSZ - Solidified regolith														
		Si	**Al**	**Ti**	**Ca**	**K**	**Na**	**Mg**	**Fe**	**Mn**	**Zr**	**Hf**	**Y**	**O**
EPMA	Average	16.76	10.42	0.16	4.78	0.22	1.62	1.07	0.67	0.01	1.38	0.02	1.27	61.62
	Std Dev	0.08	0.08	0.01	0.04	0.01	0.03	0.02	0.02	0.00	0.18	0.01	0.02	0.03
EDS-M	Average	17.86	11.41	0.20	5.12	0.26	1.63	1.16	0.74	-	1.63	-	1.58	58.42
	Std Dev	0.24	0.15	0.02	0.06	0.02	0.06	0.02	0.03	-	0.28	-	0.05	0.31
	Error (at%)	+1.10	+0.99	+0.04	+0.34	+0.04	+0.01	+0.09	+0.07	-	+0.25	-	+0.31	-3.20
EDS-C	Average	16.42	10.49	0.18	4.71	0.23	1.50	1.06	0.68	-	1.50	-	1.46	61.77
	Std Dev	0.18	0.11	0.01	0.04	0.02	0.05	0.02	0.03	-	0.26	-	0.04	0.04
	Error (at%)	-0.34	+0.07	+0.02	-0.07	+0.01	-0.12	-0.01	+0.01	-	+0.12	-	+0.19	+0.15

Table B.23. EPMA and EDS composition of bright phase in 25:75 JSC-1A/YSZ samples. EPMA used 3 sites. EDS used 6 sites.

25:75 JSC-1A/YSZ - Bright phase (YSZ)									
		Ti	**Ca**	**Mg**	**Fe**	**Zr**	**Hf**	**Y**	**O**
EPMA	Average	0.09	0.13	0.20	0.33	29.24	0.34	3.86	65.8
	Std Dev	0.02	0.04	0.08	0.00	0.09	0.01	0.02	0.04
EDS-M	Average	-	0.16	0.37	0.44	32.06	0.32	4.45	62.21
	Std Dev	-	0.06	0.03	0.05	0.31	0.02	0.29	0.22
	Error (at%)	-	+0.03	+0.17	+0.11	+2.82	-0.02	+0.59	-3.59
EDS-C	Average	-	0.15	0.34	0.40	29.04	0.29	4.03	65.77
	Std Dev	-	0.05	0.03	0.05	0.22	0.02	0.27	0.04
	Error (at%)	-	+0.02	+0.14	+0.07	-0.20	-0.05	+0.17	-0.03

Table B.24. EPMA and EDS composition of regolith in 25:75 JSC-1A/YSZ samples. EPMA used 10 sites. EDS used 13 sites.

25:75 JSC-1A/YSZ - Solidified regolith														
		Si	**Al**	**Ti**	**Ca**	**K**	**Na**	**Mg**	**Fe**	**Mn**	**Zr**	**Hf**	**Y**	**O**
EPMA	Average	17.63	6.45	0.27	3.67	0.24	1.71	3.78	1.98	0.04	1.27	0.02	1.78	61.16
	Std Dev	0.12	0.06	0.01	0.04	0.01	0.07	0.02	0.04	0.00	0.16	0.01	0.03	0.04
EDS-M	Average	17.95	6.84	0.30	3.75	0.27	1.76	3.90	2.07	-	1.25	-	2.10	59.81
	Std Dev	0.19	0.10	0.02	0.04	0.03	0.05	0.04	0.05	-	0.15	-	0.06	0.15
	Error (at%)	+0.32	+0.39	+0.03	+0.08	+0.03	+0.05	+0.12	+0.09	-	-0.02	-	+0.32	-1.35
EDS-C	Average	17.20	6.55	0.28	3.59	0.25	1.69	3.74	1.99	-	1.19	-	2.01	61.49
	Std Dev	0.15	0.08	0.02	0.04	0.02	0.05	0.03	0.05	-	0.15	-	0.05	0.03
	Error (at%)	-0.43	+0.10	0.00	-0.08	+0.01	-0.02	-0.04	+0.01	-	-0.08	-	+0.23	+0.33

Table B.25. EPMA and EDS composition of bright phase in 25:75 LHS-1/YSZ samples. EPMA used 3 sites. EDS used 6 sites.

25:75 LHS-1/YSZ - Bright phase (YSZ)										
		Al	**Ti**	**Ca**	**Mg**	**Fe**	**Zr**	**Hf**	**Y**	**O**
EPMA	Average	0.03	0.05	0.14	0.01	0.07	29.36	0.35	4.09	65.91
	Std Dev	0.00	0.01	0.03	0.01	0.02	0.25	0.01	0.35	0.04
EDS-M	Average	-	-	0.14	-	-	32.74	0.32	4.62	62.19
	Std Dev	-	-	0.04	-	-	0.25	0.02	0.22	0.18
	Error (at%)	-	-	0.00	-	-	+3.38	-0.03	+0.53	-3.72
EDS-C	Average	-	-	0.12	-	-	29.50	0.28	4.16	65.93
	Std Dev	-	-	0.04	-	-	0.16	0.02	0.20	0.04
	Error (at%)	-	-	-0.02	-	-	+0.14	-0.07	+0.07	+0.02

Table B.26. EPMA and EDS composition of regolith in 25:75 LHS-1/YSZ samples. EPMA used 10 sites. EDS used 13 sites.

25:75 LHS-1/YSZ - Solidified regolith														
		Si	**Al**	**Ti**	**Ca**	**K**	**Na**	**Mg**	**Fe**	**Mn**	**Zr**	**Hf**	**Y**	**O**
EPMA	Average	17.11	10.63	0.14	4.63	0.19	1.57	0.84	0.48	0.01	1.09	0.02	1.5	61.77
	Std Dev	0.06	0.04	0.01	0.04	0.01	0.02	0.01	0.02	0.00	0.06	0.01	0.04	0.01
EDS-M	Average	17.84	11.46	0.16	4.82	0.22	1.5	0.88	0.53	-	1.06	-	1.82	59.71
	Std Dev	0.10	0.07	0.02	0.03	0.02	0.05	0.01	0.05	-	0.13	-	0.04	0.14
	Error (at%)	+0.73	+0.83	+0.02	+0.19	+0.03	-0.07	+0.04	+0.05	-	-0.03	-	+0.32	-2.06
EDS-C	Average	16.88	10.84	0.15	4.56	0.21	1.42	0.83	0.50	-	1.00	-	1.72	61.87
	Std Dev	0.10	0.06	0.02	0.04	0.02	0.05	0.01	0.04	-	0.12	-	0.04	0.03
	Error (at%)	-0.23	+0.21	+0.01	-0.07	+0.02	-0.15	-0.01	+0.02	-	-0.09	-	+0.22	+0.10

Appendix C

ESTIMATING ORDER OF OXIDE ELECTROLYSIS

The Nernst potential can be used to determine the applied potential at which certain oxides can be electrolyzed [1]. It is defined as:

$$E = E^0 + \frac{RT}{nF}\ln Q \qquad (C.1)$$

where E is the Nernst potential, E^0 is the standard potential, R is the molar gas constant, T is the temperature, n is the number of electrons transferred in the reaction, F is Faraday's constant, and Q is the reaction quotient [1]. The standard potential, E^0, can also be defined as:

$$E^0 = -\frac{\Delta G^0}{nF} \qquad (C.2)$$

where ΔG^0 is the standard Gibbs free energy change for a reaction [1]. By combining these equations, the Nernst potential can be expressed as:

$$E = \frac{-\Delta G^0 + RT\ln Q}{nF} \qquad (C.3)$$

This expression shows that the Nernst potential is dependent on ΔG^0, Q, and n, since the temperature is assumed to be fixed at 1873 K (1600°C) and R, F are constants. Since molten regolith electrolysis is a direct electrolysis of oxides, the reaction is simply decomposition of the oxide. The reaction and Q are shown for SiO_2:

$$SiO_2 \rightarrow Si + O_2 \qquad (C.4)$$

$$Q = \frac{(a_{Si})(pO_2)}{a_{SiO2}} \qquad (C.5)$$

By using some typical values from literature, it can be shown that the $RT\ln Q$ term is typically much smaller than ΔG^0 in Equation C.3. The term pO_2 can be measured experimentally, but is assumed to be 1 atm based on existing reactor designs [2], and a_{Si} is typically assumed to be 1, since the metals produced are typically considered pure. Determination of a_{SiO2} is not trivial. This is the activity of SiO_2 in the multicomponent molten regolith. Oxide species generally are not ideal, especially at low concentrations with significant number of other oxide species [3]. As an estimate, the nominal concentration of SiO_2 in the LHS-1 regolith simulant of 0.58 is used. Combining these values, Q ≈ 1.72 and $RT\ln Q \approx 8.5$ kJ. ΔG^0 for the SiO_2 decomposition reaction is pulled from the FToxid database in FactSage 8.3, resulting in $\Delta G^0 \approx 576$ kJ [4]. Thus, it appears that the Nernst potential of oxide electrolysis is mostly dominated by ΔG^0. This enables a comparison of the expected order of oxide electrolyzed by comparing their ΔG^0.

Ellingham has tabulated and plotted ΔG^0 for the reverse reaction (metals oxidation), producing the commonly used Ellingham diagrams [5]. The order of oxide electrolysis is estimated to be the same as oxide stability, obtained from an Ellingham diagram.

References

[1] A.J. Bard, L.R. Faulkner, Electrochemical methods: fundamentals and applications, 2nd ed, Wiley, New York, 2001.

[2] S.S. Schreiner, L. Sibille, J.A. Dominguez, J.A. Hoffman, A parametric sizing model for Molten Regolith Electrolysis reactors to produce oxygen on the Moon, Advances in Space Research 57 (2016) 1585–1603. https://doi.org/10.1016/j.asr.2016.01.006.

[3] M. Humbert, Electrolysis of Silicate Minerals in Reduced Gravity for Metal and Oxygen Production, (2024) 12445858 Bytes. https://doi.org/10.25916/SUT.28031294.V1.

[4] C.W. Bale, E. Bélisle, P. Chartrand, S.A. Decterov, G. Eriksson, A.E. Gheribi, K. Hack, I.-H. Jung, Y.-B. Kang, J. Melançon, A.D. Pelton, S. Petersen, C. Robelin, J. Sangster, P. Spencer, M.-A. Van Ende, FactSage thermochemical software and databases, 2010–2016, Calphad 54 (2016) 35–53. https://doi.org/10.1016/j.calphad.2016.05.002.

[5] H. Ellingham, Transactions and Communications, J. Soc. Chem. Ind. 63 (1944) 125–160. https://doi.org/10.1002/jctb.5000630501.

Appendix D

DESIGN, FABRICATION, AND TESTING OF INVERTED MOLTEN REGOLITH ELECTROLYSIS CELL

The molten regolith electrolysis (MRE) cell used in this research incorporated an inverted hollow anode design. This appendix will focus on the rationale and constraints of the inverted hollow anode cell. Shakedown testing results will also be presented to validate the thermal design of the cell and the gas handling/analysis system.

The largest constraint for testing an MRE cell at Caltech was furnace geometry. The Faber group possesses a high-temperature furnace (Rapid Temp Furnace, CM Furnaces) that can reach the 1600°C operational temperature required for MRE. The high-temperature furnace was custom-designed to allow for Instron mechanical testing at elevated temperatures and has a bore hole through the top of the furnace measuring 2.25" in diameter. The length of the heated zone is approximately 6". Thus, the cell was designed around these geometric constraints so that the heated region of the cell is 2.25" in diameter and not exceeding 6" in height. These constraints resulted in the inverted hollow anode design presented in Chapter 4 (Figure 4.1).

The non-inverted, or regular, cell configuration required 3 separate containment vessels – one for containing the gas environment, one for containing the molten lunar regolith, and the hollow anode. Switching to an inverted cell design eliminates one of these containment vessels by combining the molten regolith containment with the hollow anode and switching the O_2 production from the interior of the hollow anode to the exterior of the hollow anode. Due to the diameter constraint of the furnace, it was determined that the regular cell configuration would be too large to fit, so the inverted cell design was selected. A SolidWorks CAD model of the final inverted cell design is presented in Figure D.1. The major components of the electrolysis cell and the heated region of the cell are also labeled in Figure D.1.

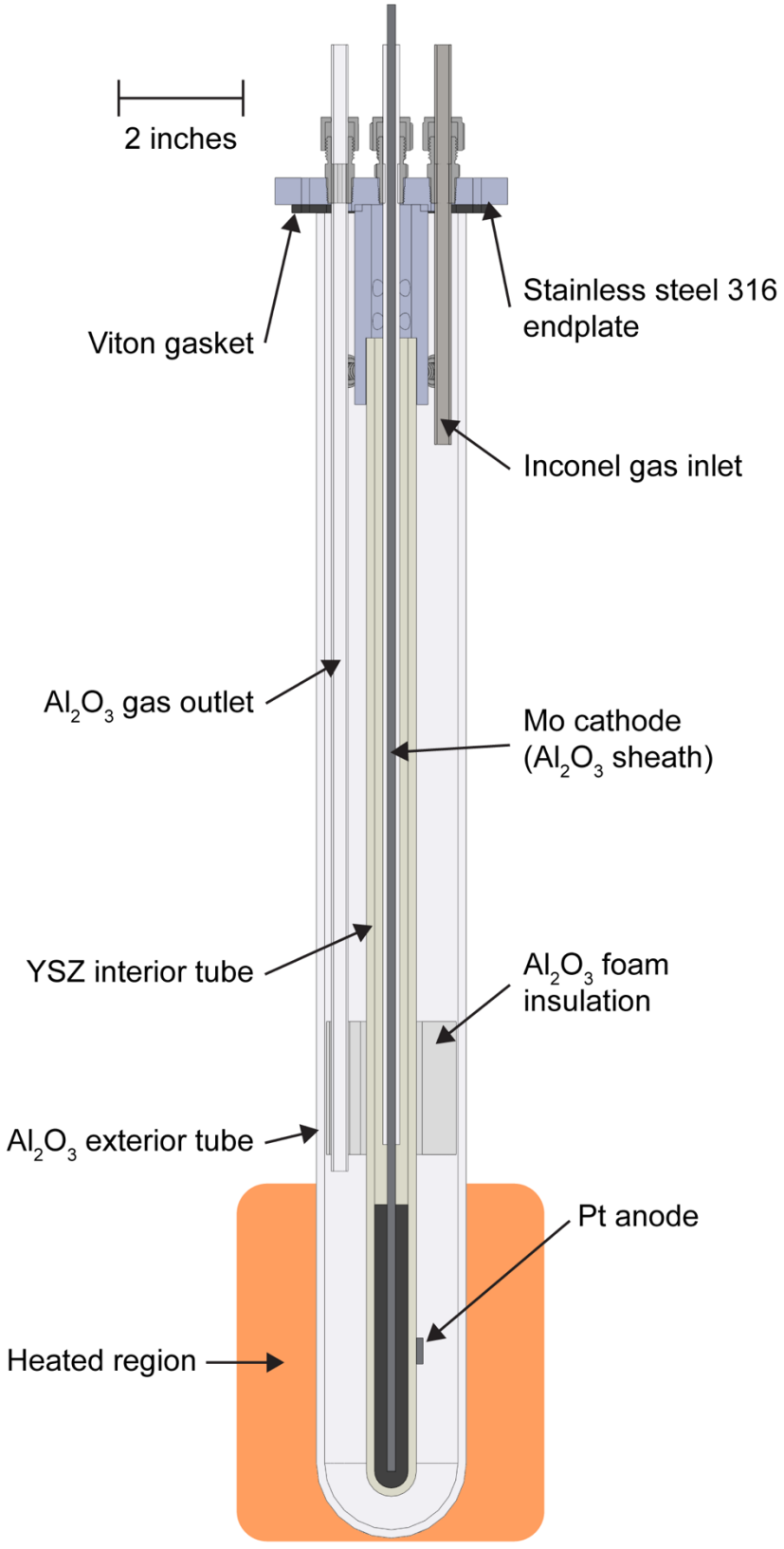

Figure D.1. CAD model of inverted electrolysis cell. Major components are labeled.

The next challenge was the thermal design of the cell. In the current design, the endplate providing gas and electrical feedthroughs is physically located above the heating elements of the furnace. Water cooling can be used to avoid overheating the endplate but adds a new safety concern that a cooling water leak can cause the heating elements to electrically short. Due to the power (~ 2 kW) necessary to reach 1600°C, it was determined that an electrical short of the heating elements would pose a significant fire and operator safety risk. Thus, the cell was designed so that passive cooling of the endplate would be sufficient to prevent overheating. This was accomplished by extended the length of the cell to allow the endplate to be approximately 16" from the edge of the heated region of the cell. A SolidWorks thermal model indicated that this was enough distance to allow the endplate to remain near ambient temperature. Ultimately, this analysis set the lengths of the two major ceramic components, the Al_2O_3 exterior tube (gas containment vessel) and the yttria-stabilized zirconia (YSZ) interior tube (the molten regolith containment vessel and inverted hollow anode).

The Al_2O_3 exterior tube diameter was set by the furnace bore hole diameter, resulting in an outer diameter of 2.25" and an inner diameter of 2". The space between the Al_2O_3 exterior tube and YSZ interior needed to accommodate the gas inlet and outlet tubes, as well as the sheathed Pt wire used to electrically connect the anode to the potentiostat. Each of these tubes has a nominal outer diameter of 0.25". The outer diameter of the YSZ tube was set at 0.75" to allow for some margin for both the inlet/outlet and anode tubes, as well as the fitting (0.125" NPT) used as the feedthroughs.

The gas inlet and outlet tube lengths are shown in Figure D.1. The anode sheath/tube is not visible in Figure D.1 but is approximately the same length as the gas outlet tube. The gas outlet tube and anode sheath both run to the edge of the heated region. This design was selected to allow the gas outlet tube to sample the gas near the Pt anode and to allow the anode tube to protect and electrically insulate the Pt wire. Al_2O_3 was selected for both the anode sheath and gas outlet tube since it is thermally stable near 1600°C in an oxidizing environment and electrically insulating. The gas inlet tube runs only a few inches into a cell, far from the heated region. Thus, Al_2O_3 is not necessary, and Inconel 600 was selected for its resistance to oxidation up to 1000°C.

Mo was selected as the cathode material since Mo possesses a high melting point (~2600°C) and is relatively easy to machine, compared to other refractory metals such as W. However, Mo rapidly oxidizes at high temperatures. Most of the Mo cathode is sheathed in Al_2O_3 (Figure D.1) and sealed using Al_2O_3 paste (Cotronics Corp.) to protect the Mo from oxidation when O_2 is being produced by MRE. The Al_2O_3 sheath only runs until the edge of the heated region so that bare Mo is contacting the molten regolith to act as the cathode. The anode was made from Pt wire that was woven into a mesh. It was then attached to the exterior of the YSZ tube using Pt ink (Fuel Cell Store).

With all these component geometries set, an endplate was designed to fix the position of each component and to provide a mounting point for all components. Stainless steel 316 (SS316) was selected for the endplate material since it is resistant to oxidation up to 800°C and is relatively easy to machine. The YSZ interior tube is fixed to a tube support on the endplate using SS316 set screws. The four total gas and electrical feedthroughs were made from 0.25” compression to 0.125” NPT fittings, which required a central bore for a 0.25” tube. Four 0.125” NPT holes were machined into the endplate to accommodate these fittings. Finally, the Al_2O_3 exterior tube was mounted using a worm clamp with four bolts and wingnuts that secured it to endplate. Four slots were cut into the edge of the endplate to allow the bolts to clamp down on the endplate. A Viton gasket was custom designed to securely fit on the endplate and provides the gas seal against the edge of the Al_2O_3 exterior tube. All fabrication work was done at either the Caltech or Jet Propulsion Laboratory (JPL) machine shops.

An Al_2O_3 foam insulation block (Figure D.1) was also included in the design to provide additional thermal insulation between the heated region of the cell and the endplate. Without this block, there is direct line-of-sight for radiative heat transfer from the heated region to the endplate. Additional quartz wool insulation (not shown in Figure D.1) was added above the Al_2O_3 foam insulation and at the endplate to further limit thermal parasitic losses. Figure D.2 shows the location of the quartz insulation used in the cell.

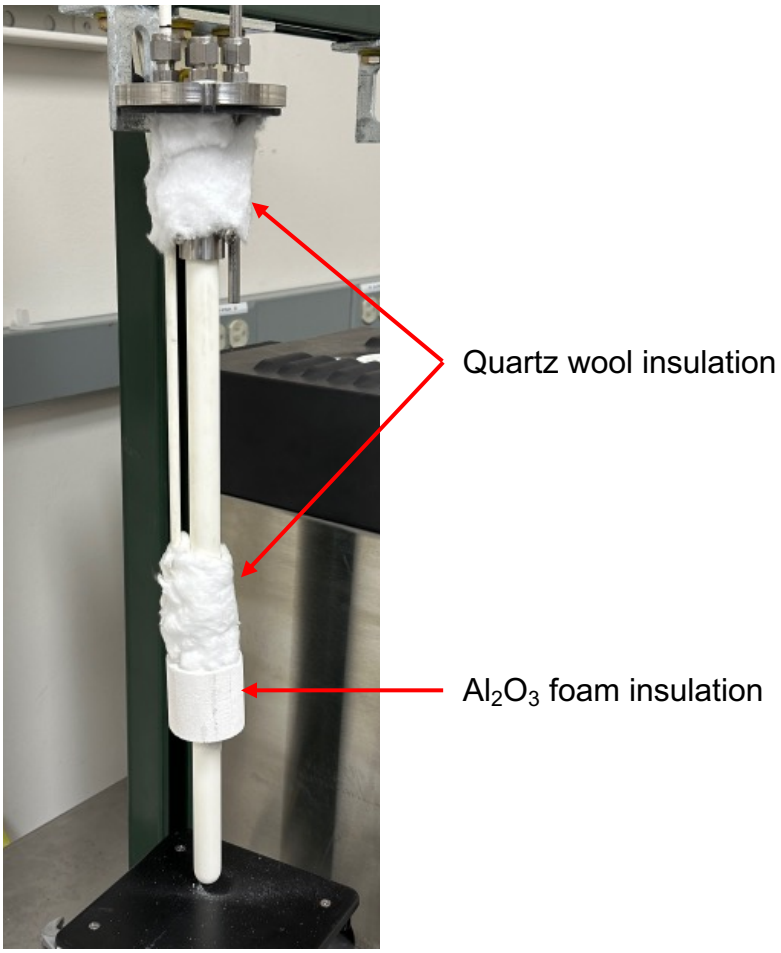

Figure D.2. Quartz wool insulation locations in electrolysis cell design.

There are several pieces of equipment used to support electrolysis testing beyond the cell. A VersaStat 4 potentiostat (Princeton Applied Research) was provided by the Fultz group at Caltech and used to provide the voltage/current to perform MRE. An HPR-20 residual gas analysis system (Hiden Analytical) was provided by the Thermal Energy Conversion group at JPL and used to measure the gas composition of the outlet gas stream. A mass flow controller (FMA series, OMEGA) was placed upstream of the electrolysis cell to control the carrier gas flow rate. A logging thermocouple (Type S) was attached to an OMEGA data logger and used to record the temperature inside the furnace. A mounting support beam for the assembled electrolysis cell was fabricated from Unistruts to hold the weight of the cell and prevent it from resting on the bottom of the furnace. Images of the assembled cell and support equipment are provided in Figure D.3.

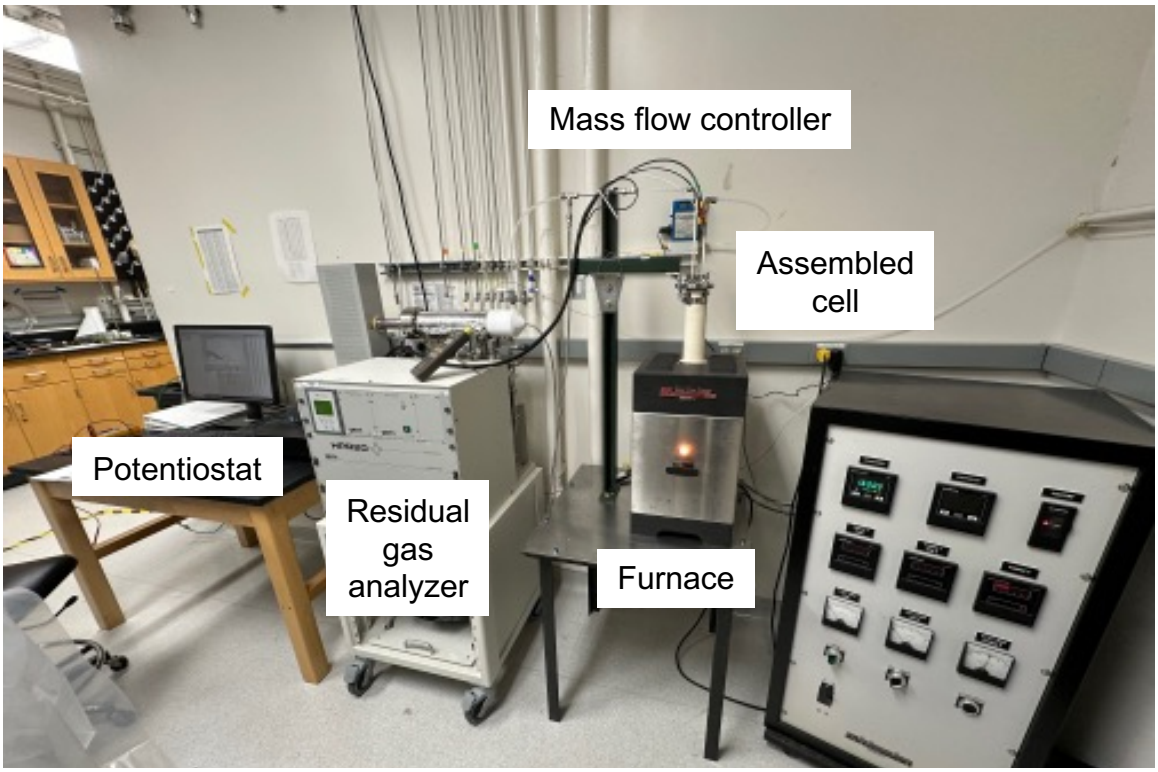

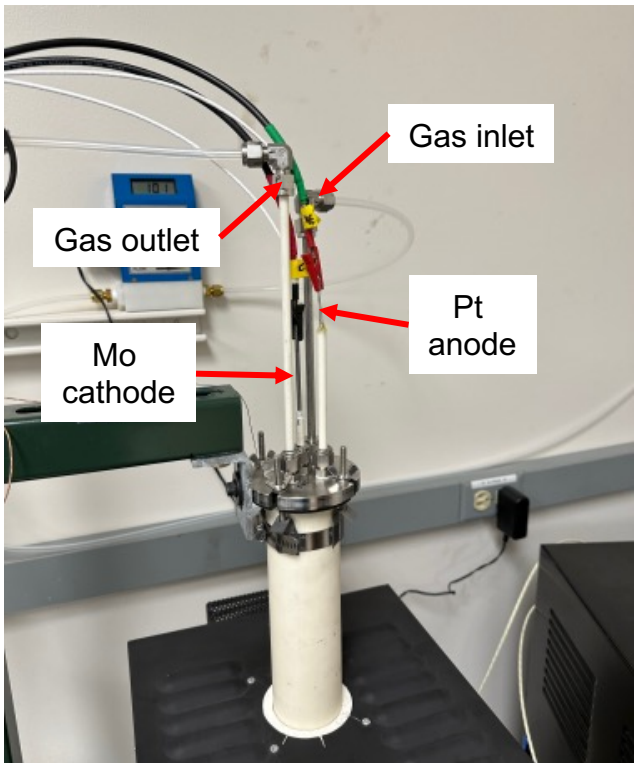

Figure D.3. Labeled images of assembled electrolysis cell, gas/electrical feedthroughs, and supporting equipment during molten regolith electrolysis testing.

After fabrication of the electrolysis cell and setup of the supporting equipment, a shakedown test was performed. The objective of the shakedown test was to validate that the interior of the YSZ tube reached 1600°C and to determine the endplate temperature while the cell was at 1600°C. To meet the first objective, a long Type B thermocouple, sheathed in Al_2O_3, was placed where the cathode is (shown in Figure D.1). This enabled temperature logging of the interior of the YSZ tube. For the second objective, a Type K thermocouple was placed on the backside of the endplate to monitor the endplate temperature. A plot of the temperature measured at the center of the YSZ tube is provided in Figure D.4.

Based on Figure D.4, the temperature of the interior of the YSZ tube is approximately the same as the furnace temperature. The temperature log shows that the interior of the YSZ tube is at 1608°C, on average, when the furnace control thermocouple is at 1600°C. This confirms that the interior of the YSZ tube is reaching the operational temperature of MRE. Thus, no adjustment or offset is necessary to ensure that the interior of the YSZ gets to 1600°C.

During the shakedown test, the maximum temperature recorded from the backside of the endplate is approximately 35°C. This temperature is slightly higher than ambient but does not pose any concerns for the materials used at the endplate. The Viton gasket is the component with the lowest maximum usage temperature of 200 – 250°C, which is significantly higher than the measured temperature of the endplate. The Type K thermocouple is kept on the endplate for all the electrolysis runs presented in this research. The highest temperature observed at the endplate was approximately 41°C. Thus, the thermal design of the electrolysis cell meets the design requirement, and the endplate temperature is not a concern, even for longer electrolysis experiments up to 48 hours.

With a successful shakedown test completed, the electrolysis cell design described in this appendix was used to perform MRE testing with an inverted hollow anode. The results of this testing are presented in Chapters 4 and 5 of the thesis.

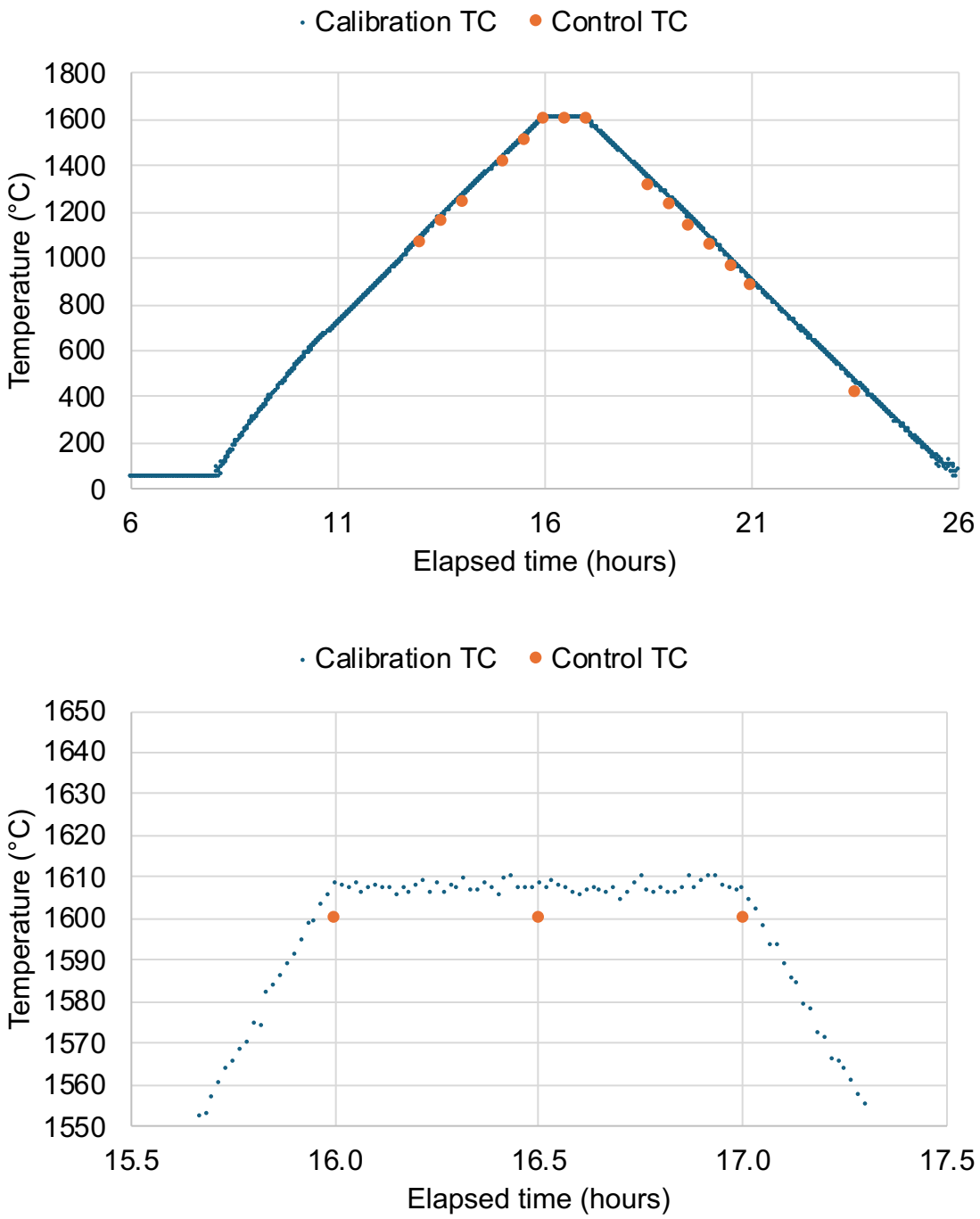

Figure D.4. Temperature calibration of interior of YSZ tube (Calibration TC) and temperature of furnace (Control TC). Top graph shows the entirety of the heating and cooling profiles. Bottom graph provides a detailed view of the dwell segment at 1600°C.

Appendix E

SUPPORTING MATERIAL FOR CHAPTER 4

The contents of this appendix are adapted from the Supplementary Material included with "Improving molten regolith electrolysis with zirconia-based hollow anode technology" by K. Yu, W. West, J. Stokes, B. Harder, L. Reidy, J. Dominguez, and K. T. Faber, which was published in Acta Astronautica in 2025. The data presented in this appendix supports the results presented in Chapter 4.

K. Yu, W. West, J. Stokes, B. Harder, L. Reidy, J. Dominguez, K.T. Faber (2025). "Improving molten regolith electrolysis with zirconia-based hollow anode technology". In: *Acta Astronautica* 235, pp. 723-735. DOI: 10.1016/j.actaastro.2025.06.028

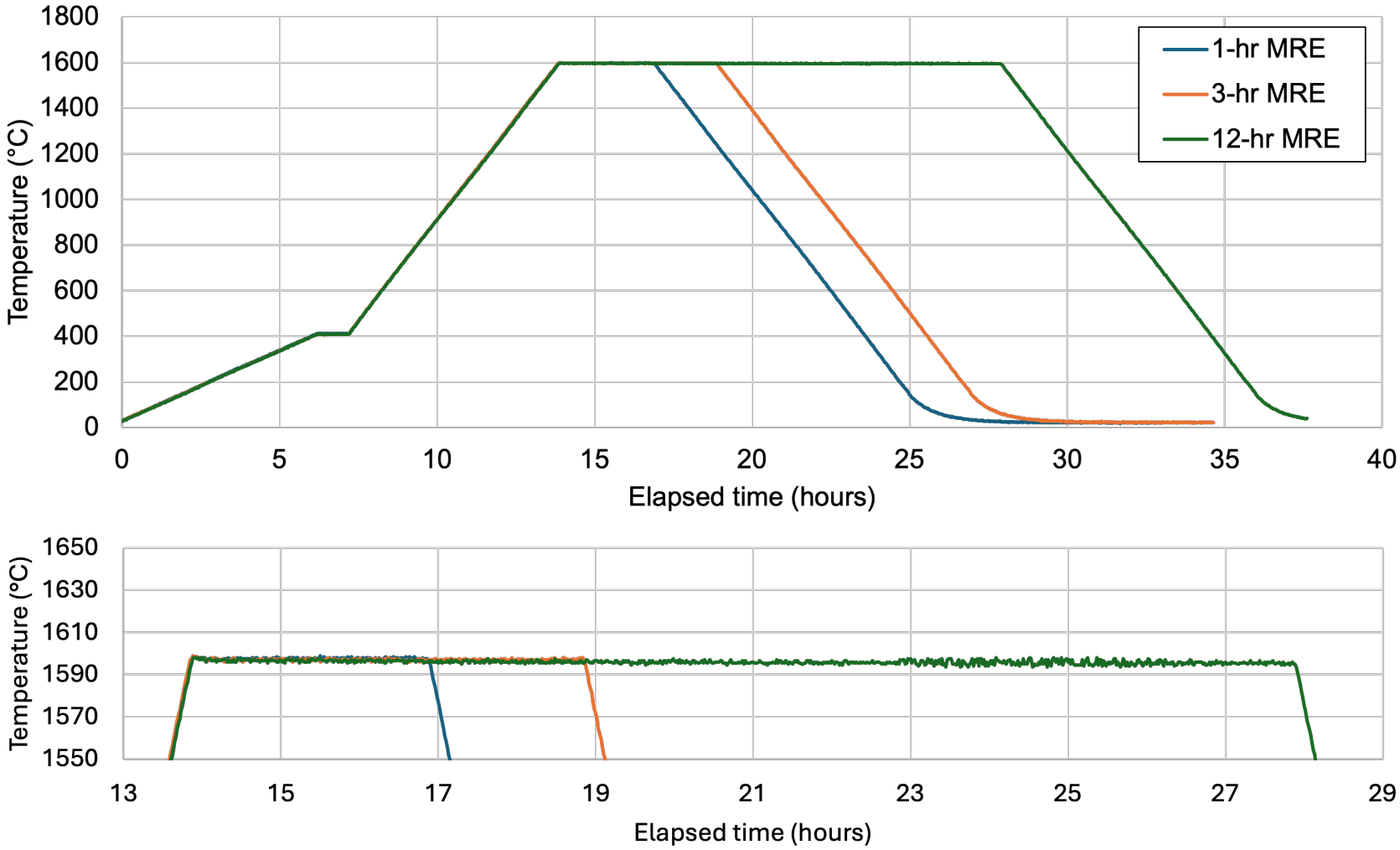

Figure E.1. Thermal profile of all three electrolysis experiments from monitoring thermocouple in furnace. Top graph shows the entirety of the heating and cooling profiles. Bottom graph provides a detailed view of the dwell segment during which electrolysis is performed.

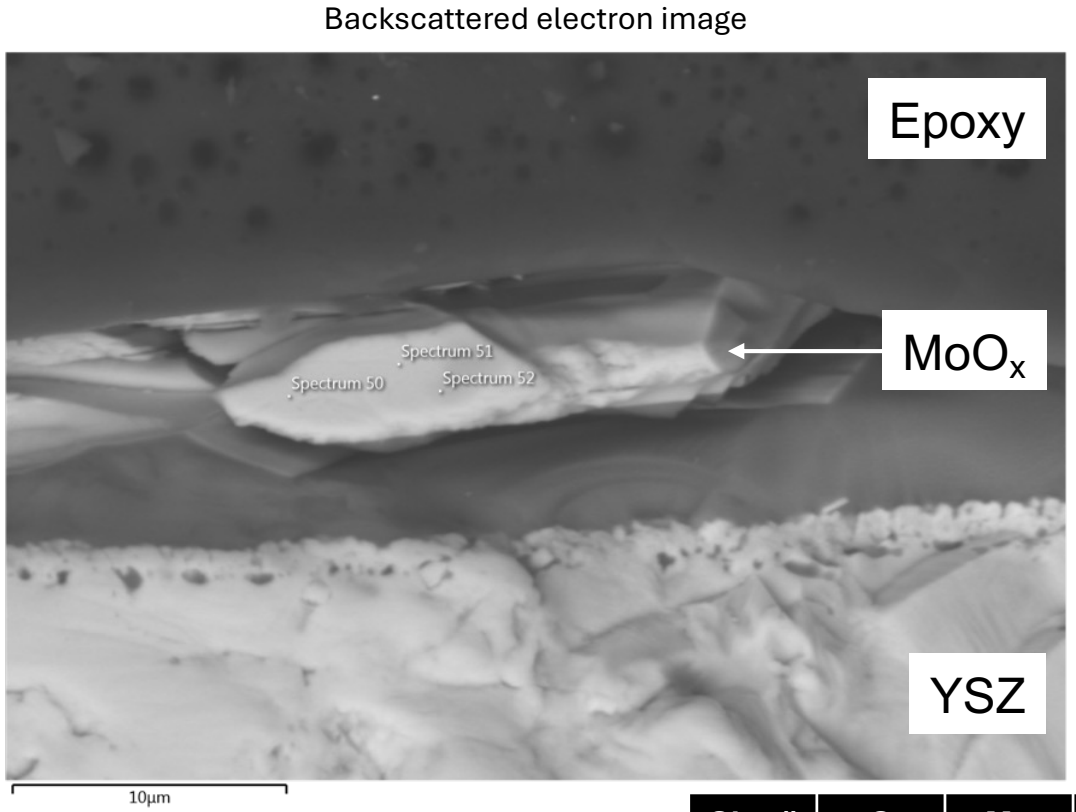

Site #	O	Mg	Al	Si	Ca	Fe	Mo
50	66.06	6.00	0.56	0.30	0.14	6.70	20.24
51	65.54	6.15	0.51	0.23	0.07	6.76	20.74
52	69.83	4.97	1.48	2.72	0.61	5.13	15.25

Figure E.2. Quantitative EDS summary of Mo oxides observed on interior of YSZ after electrolysis experiments. Data taken from 3-hour electrolysis cell. All values are in at%.

Backscattered electron image

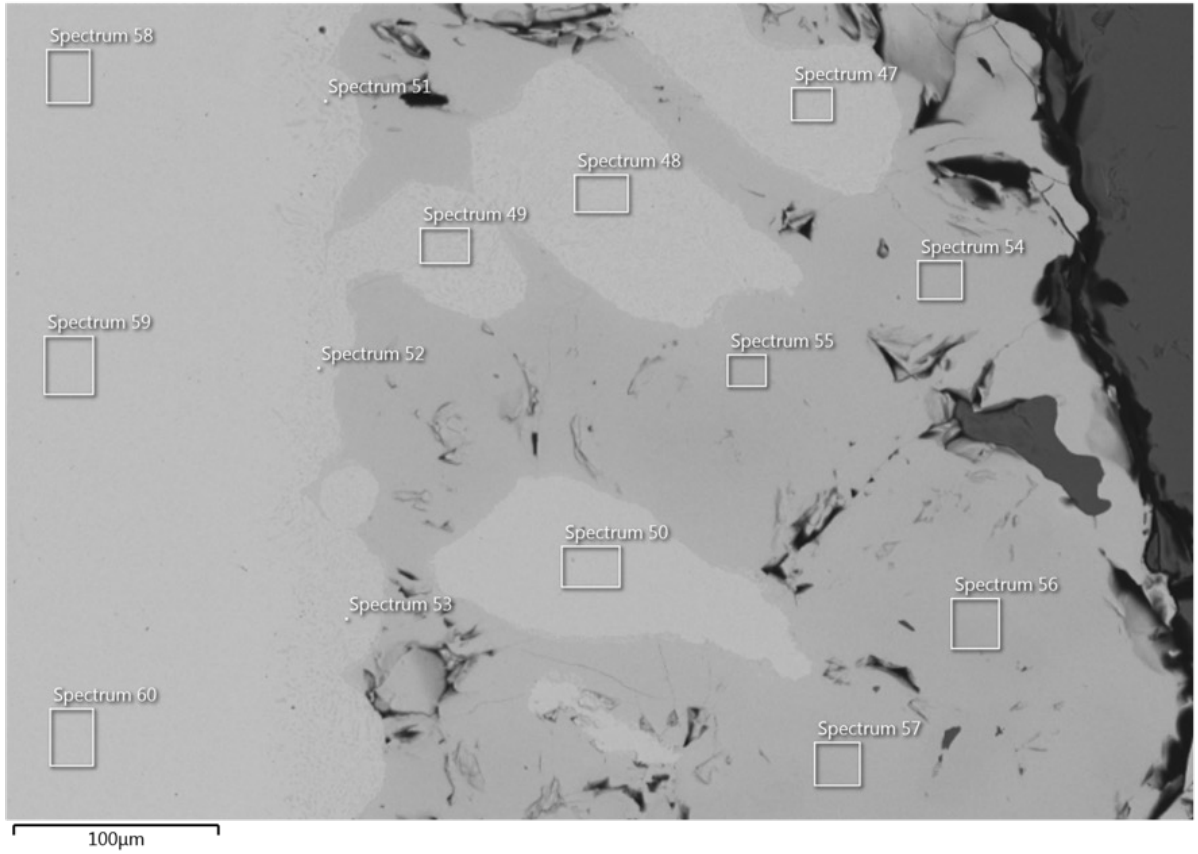

All values are in atomic %

Site #	Fe	Mo
47	19.11	80.89
48	17.57	82.43
49	17.81	82.19
50	18.09	81.91
51	8.52	91.48
52	8.79	91.21
53	36.47	63.53
54	58.07	41.93
55	57.63	42.37
56	62.95	37.05
57	58.85	41.15
58	0.00	100
59	0.07	99.93
60	0.01	99.99

Figure E.3. Quantitative EDS summary of cathodic product region in 1-hour electrolysis cell (Figure 4.3). All values are in at%.

Backscattered electron image

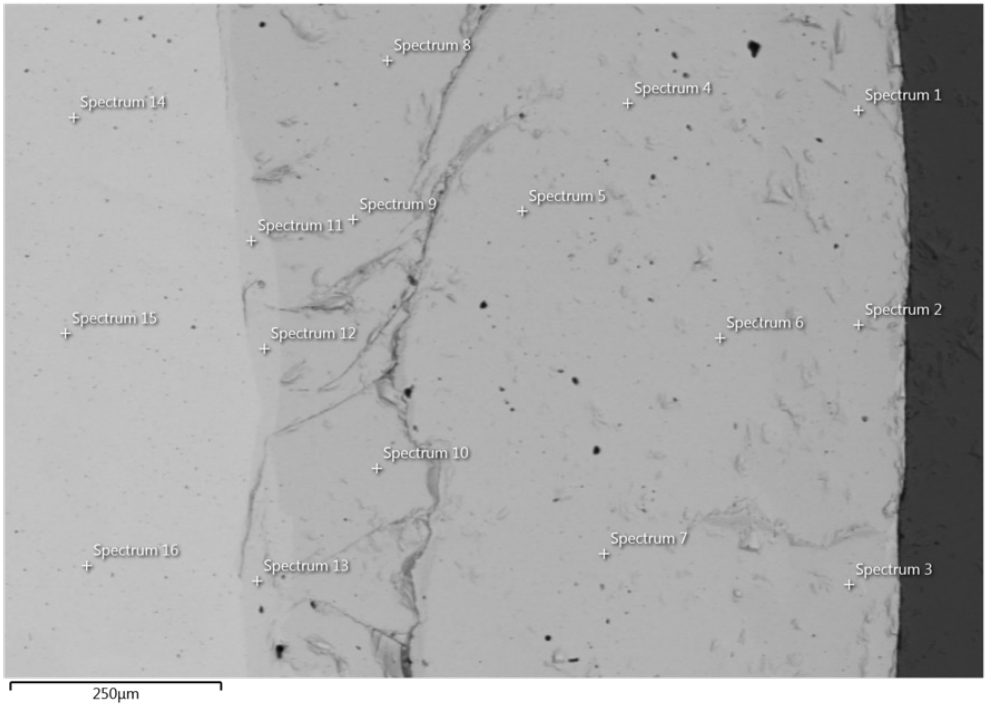

All values are in atomic %

Site #	Si	P	Fe	Mo
1	11.92	5.55	38.86	43.34
2	13.79	1.31	39.31	44.69
3	14.39	3.78	47.29	33.66
4	16.40	0.18	34.75	48.25
5	16.81	0.05	34.62	48.00
6	16.15	0.11	35.30	48.13
7	16.92	0.10	34.69	48.02
8	16.53	0.24	34.55	47.99
9	16.37	0.03	35.16	47.79
10	16.16	0.17	35.63	47.68
11	12.38	0.58	25.11	61.23
12	12.64	0.53	25.19	61.18
13	12.91	0.86	24.96	60.97
14	0.37	0.00	0.17	98.45
15	0.54	0.00	0.26	98.24
16	0.36	0.00	0.00	98.98

Figure E.4. Quantitative EDS summary of cathodic product region in 3-hour electrolysis cell (Figure 4.4). All values are in at%.

Backscattered electron image

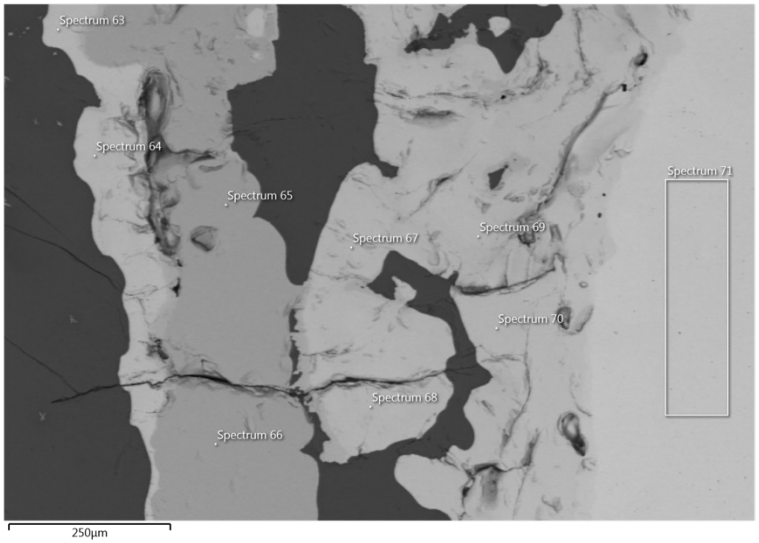

Site #	Si	P	Ti	Mn	Fe	Mo
63	37.16	0.13	4.87	0.36	6.61	50.87
64	36.29	0.29	4.42	0.49	13.36	45.15
65	65.34	0.00	0.07	0.03	0.00	34.56
66	65.24	0.00	0.05	0.08	0.11	34.52
67	37.75	0.00	4.09	0.29	5.24	52.64
68	37.45	0.04	6.48	0.37	4.91	50.75
69	37.34	0.00	2.74	0.40	6.08	53.45
70	37.23	0.12	4.92	0.32	5.52	51.90
71	0.36	-	-	-	-	99.64

All values are in atomic %

Figure E.5. Quantitative EDS summary of cathodic product region in 12-hour electrolysis cell (Figure 4.5). All values are in at%.

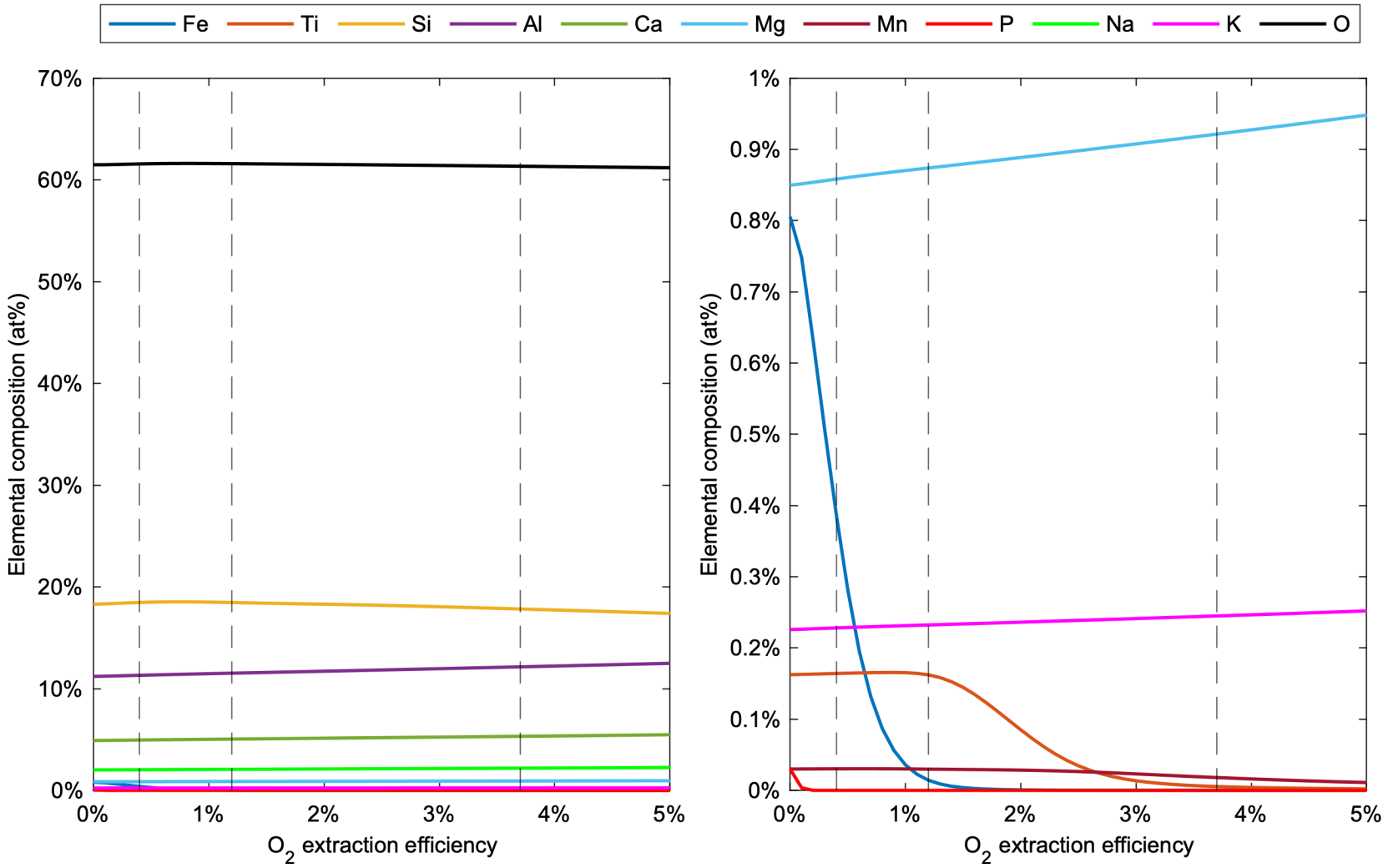

Figure E.6. FactSage predictions of the remaining regolith composition (full (left) and expanded (right)) vs. O_2 extraction efficiency. Dashed vertical lines represent the O_2 extraction efficiency achieved in the 1-hour (0.4%), 3-hour (1.2%), and 12-hour (3.7%) electrolysis cells.

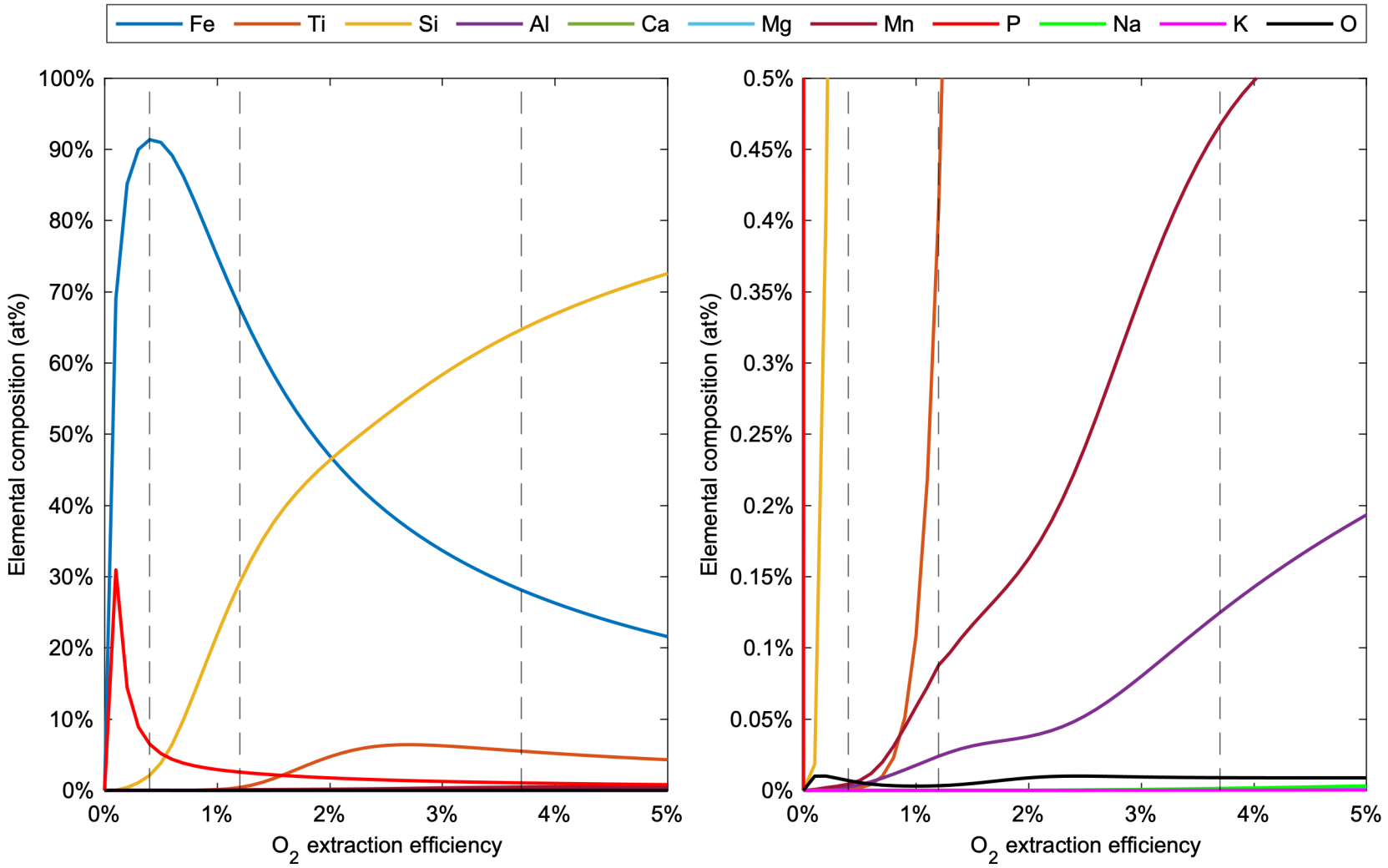

Figure E.7. FactSage predictions of the cathodic product composition (full (left) and expanded (right)) vs. O_2 extraction efficiency. Dashed vertical lines represent the O_2 extraction efficiency achieved in the 1-hour (0.4%), 3-hour (1.2%), and 12-hour (3.7%) electrolysis cells.

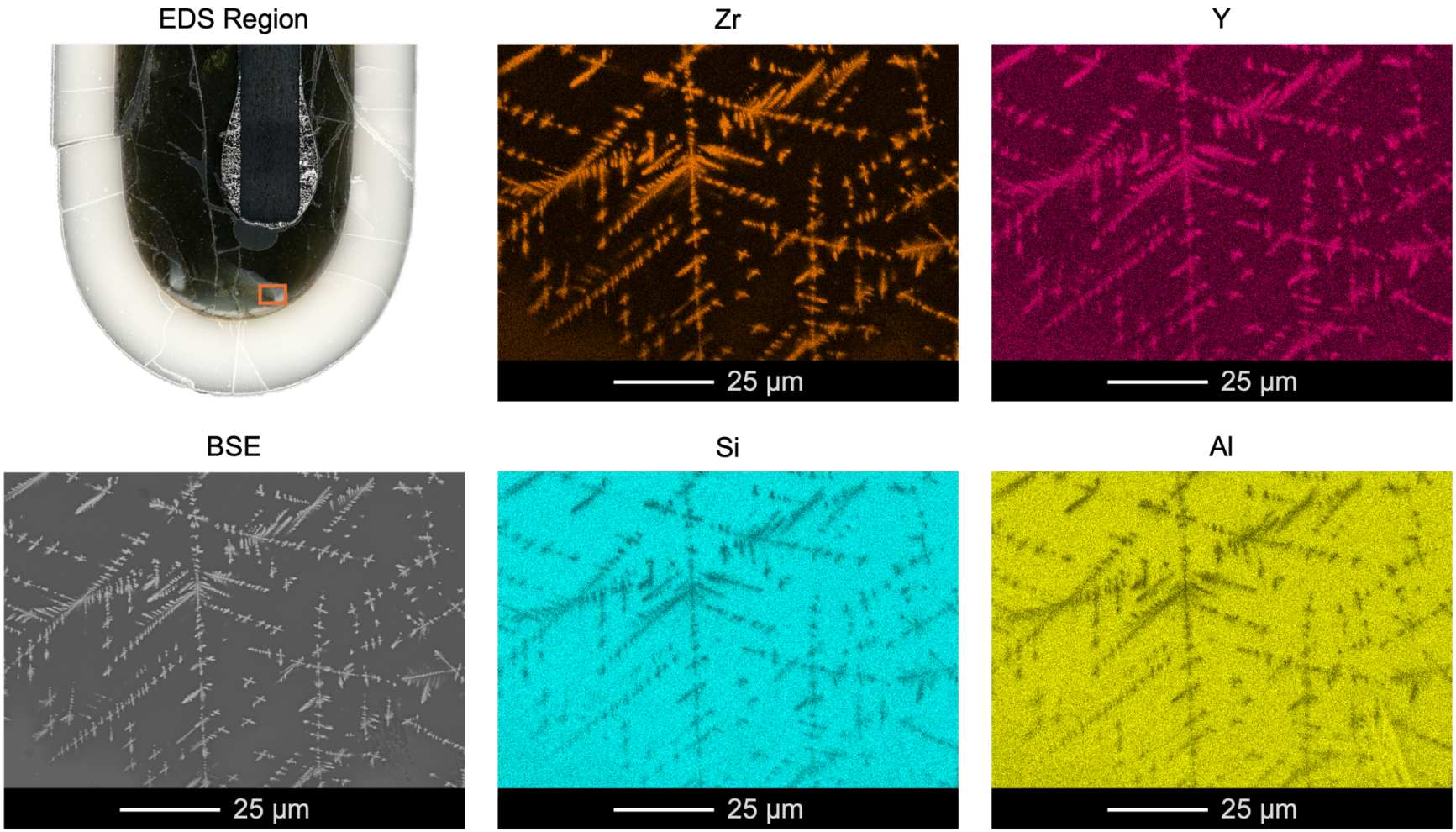

Figure E.8. Backscattered electron (BSE) image and energy-dispersive X-ray spectroscopy (EDS) maps of YSZ particles at bottom of 1-hour electrolysis cell. EDS analysis area is denoted with the orange box in the optical microscope image.

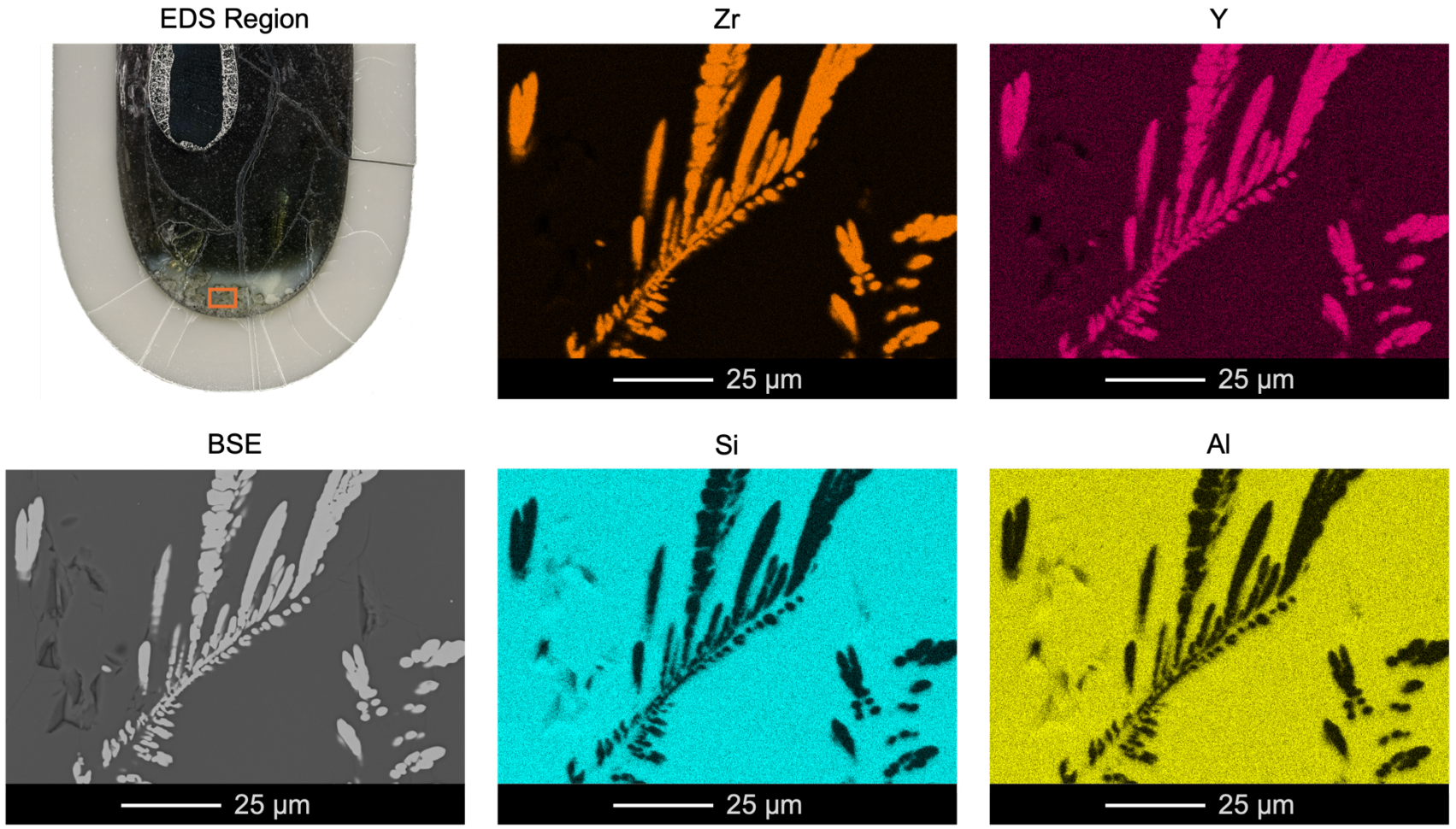

Figure E.9. Backscattered electron (BSE) image and energy-dispersive X-ray spectroscopy (EDS) maps of YSZ particles at bottom of 3-hour electrolysis cell. EDS analysis area is denoted with the orange box in the optical microscope image.

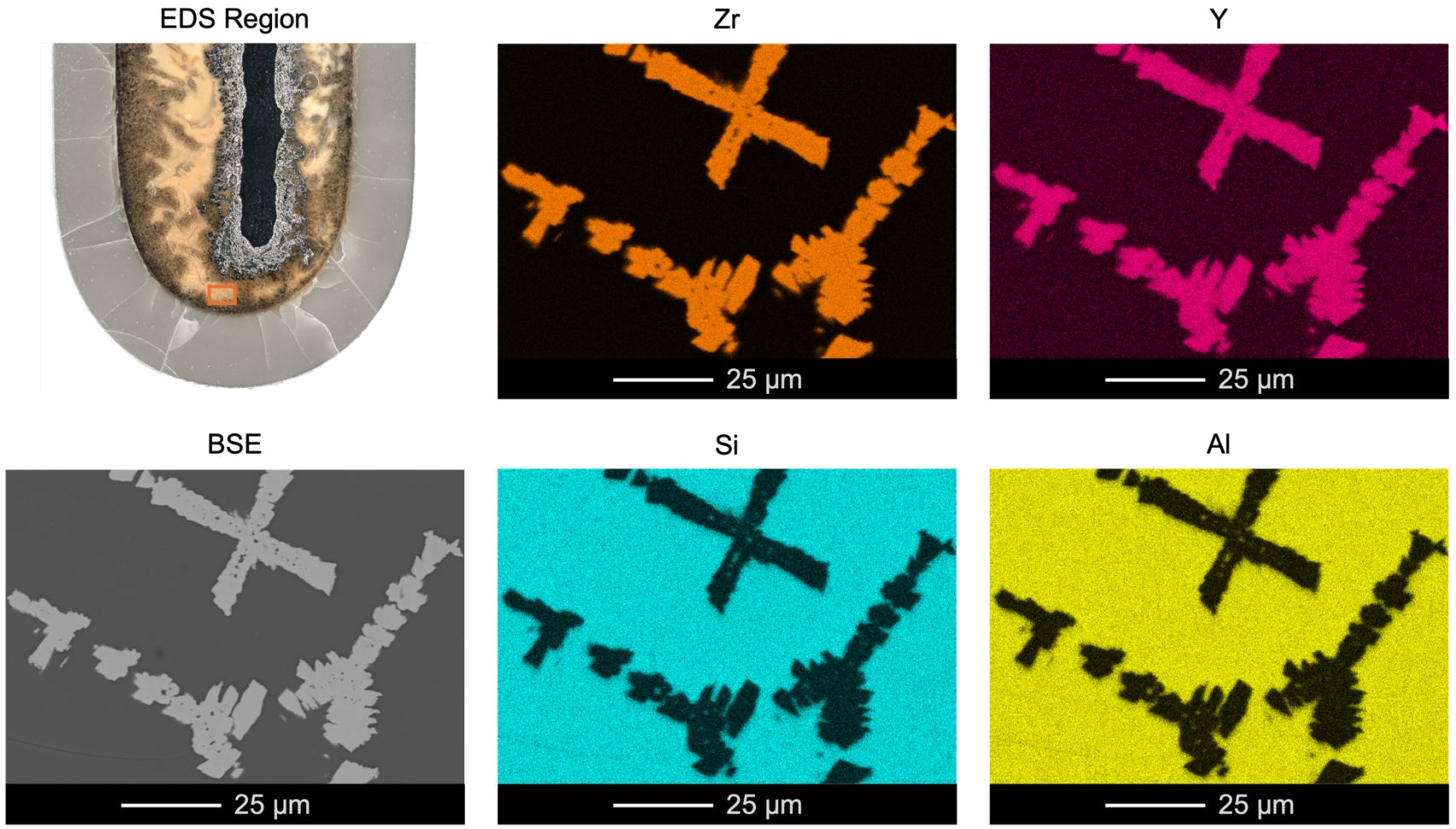

Figure E.10. Backscattered electron (BSE) image and energy-dispersive X-ray spectroscopy (EDS) maps of YSZ particles at bottom of 12-hour electrolysis cell. EDS analysis area is denoted with the orange box in the optical microscope image.

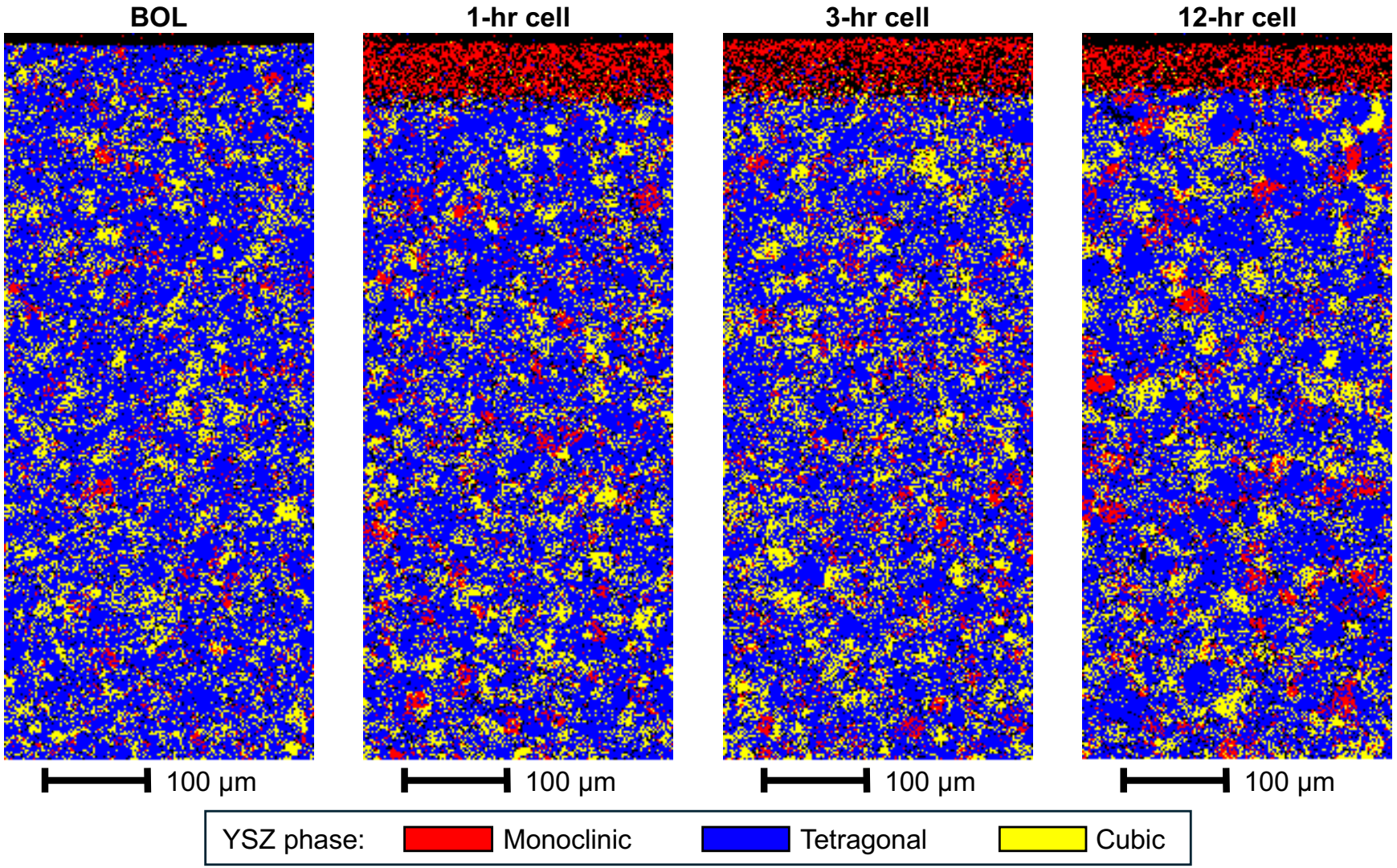

Figure E.11. EBSD phase maps of beginning-of-life (BOL) YSZ and YSZ at regolith interface for the 1-hr, 3-hr and 12-hr cells.

Appendix F

PROOF-OF-PRINCIPLE ELECTROLYSIS OF LUNAR MARIA REGOLITH USING ZIRCONIA-BASED HOLLOW ANODES

In Chapter 4 of this thesis, electrolysis testing results of lunar highlands regolith simulant (LHS-1) are presented. This appendix focuses on a single electrolysis test performed on lunar maria regolith simulant (JSC-1A). Though electrolysis was successfully performed on JSC-1A, the lunar south pole is currently the most promising site for a sustained human presence. Thus, the electrolysis of lunar highlands regolith was prioritized. The electrolysis cell and characterization methods are the same as those presented in Chapter 4 (Section 4.2), except for the regolith simulant used.

JSC-1A (NASA) was selected as the lunar maria regolith simulant for electrolysis testing. Chapters 2 and 3 discuss the main difference between the two types of regolith. Table F.1 summarizes the compositional differences between LHS-1 (highlands) and JSC-1A (maria). The lunar maria regolith generally contains more FeO, MgO, and TiO_2 compared to lunar highlands regolith. The difference in FeO content is significant, since it is the first oxide species to be electrolyzed. Thus, having more FeO means that electrolysis of JSC-1A will need to run for longer to reach the switchover to predominantly SiO_2 electrolysis. Additionally, the higher content of FeO, MgO, and TiO_2 results in a lower viscosity and higher electrical conductivity for JSC-1A.

Table F.1. Manufacturer-provided compositions of lunar regolith simulants in wt%. [1,2]

Species	SiO_2	FeO	MgO	CaO	Al_2O_3	TiO_2	Na_2O	K_2O
JSC-1A (Maria)	48.7	11.0	9.2	10.6	15.3	1.6	2.8	0.8
LHS-1 (Highlands)	51.8	2.7	1.6	12.9	26.9	0.6	2.9	0.8

JSC-1A was electrolyzed in the inverted hollow anode cell for 1 hour, matching the first electrolysis duration of the first LHS-1 test. The O_2 content of the outlet gas stream and potential required to maintain 0.5 A across the cell are presented in Figure F.1. The results of the 1-hour electrolysis run with LHS-1 are also included for comparison.

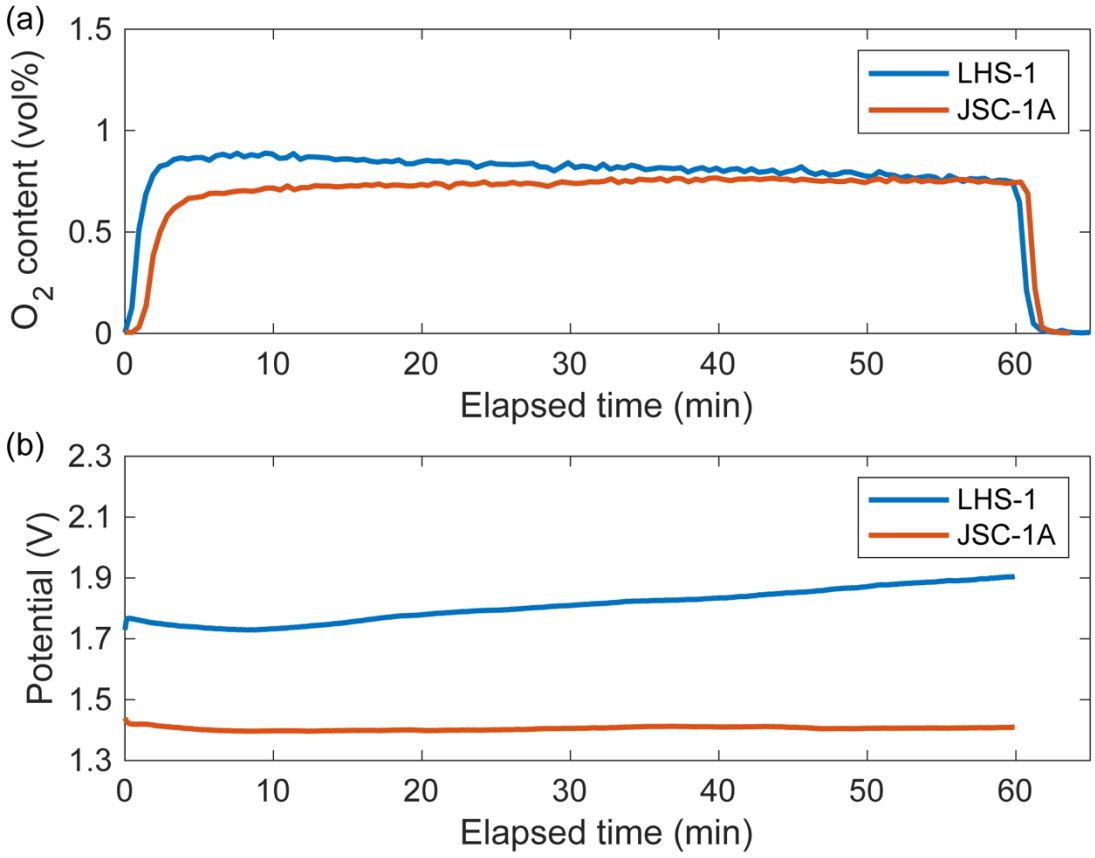

Figure F.1. (a) O_2 content of outlet gas stream and (b) potential across electrolysis cell vs. elapsed time since electrolysis start for 1-hr electrolysis of LHS-1 and JSC-1A.

In Figure F.1(a), the O_2 production rate from JSC-1A is lower than LHS-1. Given that the applied current in both cells is 0.5 A, the lower O_2 production rate of JSC-1A suggests that the Faradaic efficiency of the electrolyzing JSC-1A is lower than for LHS-1. This lower Faradaic efficiency is attributed to the higher FeO content of JSC-1A relative to LHS-1. Sirk et al. performed MRE with a Mo cathode and Ir anode, reporting Faradaic efficiencies of approximately 30-60% when electrolyzing an FeO-containing molten regolith [3]. They

attributed the lower Faradaic efficiencies to a parasitic redox cycling of Fe^{2+}/Fe^{3+} ions in the molten regolith, which is exacerbated in JSC-1A due to the higher FeO content.

In addition to Fe^{2+}/Fe^{3+} redox cycling, the presence of multivalent transition metal oxides, such as FeO and TiO_2, can significantly increase the electronic conductivity of the molten oxide electrolyte [4]. The higher FeO content of JSC-1A likely results in increased electronic conductivity of the electrolyte compared to LHS-1. The ideal molten oxide electrolyte should have no electronic conductivity, which corresponds to a 100% Faradaic efficiency, since all applied current must drive electrolysis. Introducing electronic conductivity causes the Faradaic efficiency to drop, since the current has a parasitic path through the molten regolith electrolyte. The lower O_2 production observed in the JSC-1A electrolysis experiment is attributed to the higher electronic conductivity of JSC-1A, caused by the higher FeO content compared to LHS-1.

In Figure F.1(b), the potential required to maintain 0.5 A in the JSC-1A cell (~1.4 V) is significantly lower than the LHS-1 cell (~1.8 V). The Mo cathode and Pt anode have the same geometry between both tests. The decrease in applied potential going from LHS-1 to JSC-1A is primarily attributed to a decrease in solution (molten regolith electrolyte) resistance. The decrease in solution resistance is likely caused by a combination of the higher electronic conductivity of JSC-1A, as discussed above, and the difference in viscosities between JSC-1A and LHS-1. Chapter 3 of this thesis provides a more in-depth description of the difference in viscosity between highlands (LHS-1) and maria (JSC-1A) regolith. In brief, JSC-1A is expected to have an order-of-magnitude lower viscosity, due to the higher concentration of network modifiers such as FeO and MgO.

The thesis author has also shown that diffusivity of ions (D_i) in the molten regolith is approximately inversely proportional to the viscosity (η) of molten regolith [5]. The Nernst-Einstein relation can be used to express ionic conductivity as a function of diffusivity which shows that ionic conductivity (σ_i) is directly proportional to the ion diffusivity [6]. This relation can be expressed as:

$$\sigma_i \propto D_i \qquad (F.1)$$

By substituting in the modified Stokes-Einstein relation for glass-forming melts (Equation 3.4 in Chapter 3), it is shown that:

$$\sigma_i \propto \left(\frac{1}{\eta}\right)^{\frac{1}{m}} \qquad (F.2)$$

where *m* is a positive coefficient and is the ratio of the activation energies of viscous flow and diffusion. The ideal Stokes-Einstein relation occurs when *m* = 1. Thus, from Equation F.2, it is shown that a lower viscosity will result in higher ionic conductivity. Since JSC-1A is expected to have an order-of-magnitude lower viscosity than LHS-1, this relationship supports the observation that JSC-1A has a higher ionic conductivity than LHS-1, resulting in a lower applied potential to maintain 0.5 A in the electrolysis cell.

There is also a difference in the applied potential behavior with increasing electrolysis time. In Figure F.1(b), the LHS-1 electrolysis exhibits an increase in the applied potential necessary to maintain 0.5 A in the cell. In contrast, the JSC-1A electrolysis has a stable applied potential. The increase observed in the LHS-1 electrolysis is attributed to mass transport limitations of FeO/Fe_2O_3 and the increased viscosity resulting from FeO/Fe_2O_3 removal. This behavior is described in more detail in Chapter 4 (Section 4.3.1). The higher FeO content of JSC-1A mitigates the increase in applied potential, causing the applied potential to be relatively stable in the 1-hour electrolysis period. The presence of approximately 4x FeO, compared to LHS-1, reduces the mass transport limitations and stabilizes the viscosity since more FeO is available at the cathode for electrolysis and as network modifiers for the molten regolith. It is noted that a similar increase in applied potential is likely to occur near the end of FeO electrolysis in JSC-1A. Based on the FactSage analysis done for LHS-1 (Section 4.3.4) and accounting for the 4x increase in FeO content in JSC-1A, the end of FeO electrolysis in JSC-1A is expected to occur after 4-6 hours of electrolysis.

An optical microscope image and energy dispersive X-ray spectroscopy (EDS) elemental maps of the cathodic products generated in the JSC-1A electrolysis cell are presented in Figure F.2. Based on the EDS analysis, Fe and P are the primary cathodic products generated. There is a significant amount of Fe detected in the cathodic products and it has alloyed with Mo from the cathode. Within the cathodic products, there are also regions that have a high concentration of P, indicating that P is also a cathodic product. Fe as a cathodic product is consistent with the 1-hour LHS-1 electrolysis cell. However, P was not detected in the 1-hour LHS-1 electrolysis cell. Si and O are only visible in the regions with solidified JSC-1A and not in the cathodic products.

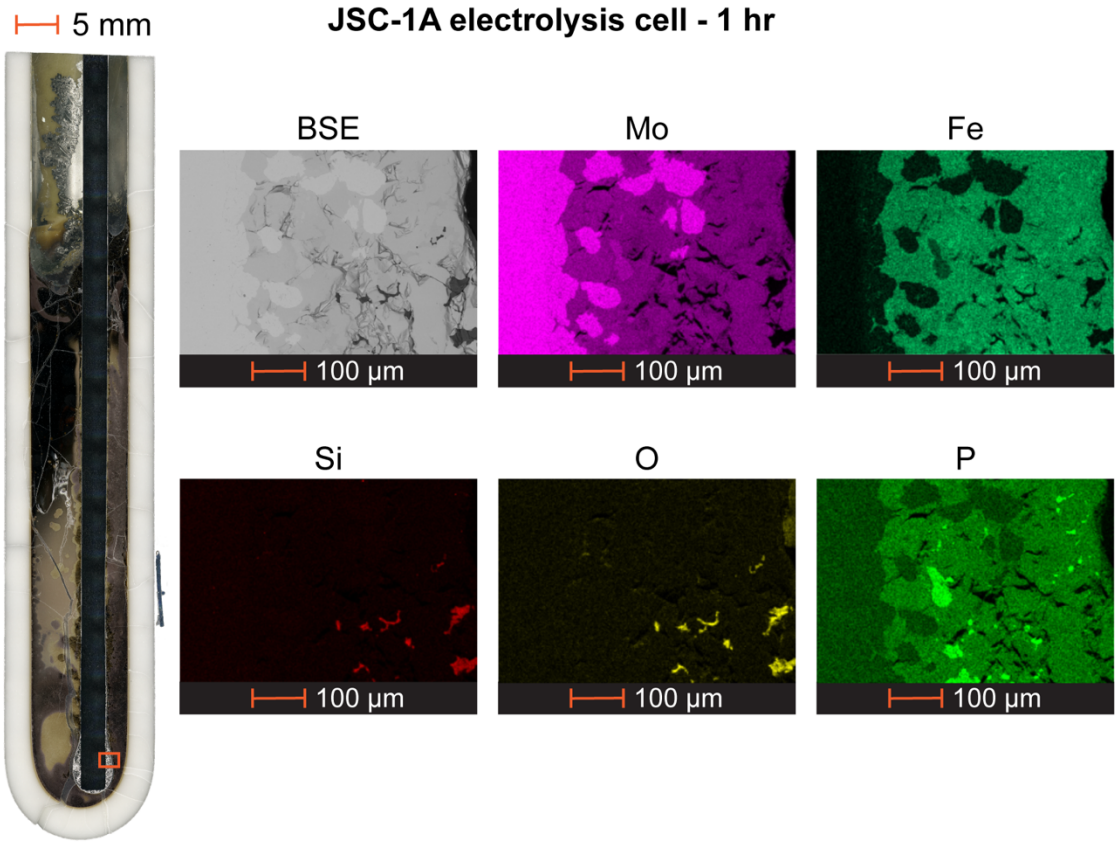

Figure F.2. Optical microscopy of the 1-hour JSC-1A electrolysis cell and EDS elemental maps of the cathodic products generated. EDS analysis area is denoted with the orange box in the optical microscope image.

The observation of P in the cathodic products is surprising. P was detected in the 3-hour and 12-hour LHS-1 electrolysis cells, but not the 1-hour LHS-1 electrolysis cell. The presence of P indicates that P_2O_5 is being coelectrolyzed with FeO in JSC-1A. Since oxides are generally electrolyzed following the order of their oxide stability, the observation of P in the cathodic products suggests that P_2O_5 is less thermodynamically stable in molten JSC-1A than in molten LHS-1. Further thermochemical experiments are needed to confirm this effect.

A comparison of the cathodic products and regolith electrolysis efficiencies for the 1-hour JSC-1A and LHS-1 electrolysis experiments is presented in Table F.2. The methodology for these calculations is presented in Chapter 4 (Section 4.3.1). As discussed previously, the main difference between JSC-1A and LHS-1 is that the Faradaic efficiency associated with electrolyzing JSC-1A is lower than LHS-1. This also results in a 10% reduction of the mass of O_2 produced during the 1-hour electrolysis period.

Table F.2. Comparison of 1-hour JSC-1A and LHS-1 cathodic products and regolith electrolysis efficiencies

Regolith simulant	Cathodic products observed	Anodic Faradaic efficiency	Mass of O_2 produced	Extraction efficiency
LHS-1	Fe	47%	0.070 g	0.4%
JSC-1A	Fe, P	42%	0.063 g	0.3%

In Chapter 3, degradation of YSZ crucibles containing either JSC-1A or LHS-1 was evaluated. The results indicated that JSC-1A causes faster YSZ dissolution than LHS-1, primarily attributed to the lower viscosity of JSC-1A. The 1-hour electrolysis cells discussed in this appendix can provide further insight into the recession rate of YSZ in JSC-1A or LHS-1 while performing MRE. Using the same methodology presented in Chapter 4 (Section 4.3.5.1), the YSZ wall recession was obtained for the 1-hour JSC-1A electrolysis cell. The results are presented in Table F.3, along with the 1-hour LHS-1 results for comparison.

Table F.3. Comparison of YSZ wall recession by molten JSC-1A or LHS-1

Simulant	Electrolysis duration	Time at 1600°C	YSZ recession (μm)
LHS-1	1 hr	3 hr	22 ± 10
JSC-1A	1 hr	3 hr	130 ± 25

Based on Table F.3, JSC-1A is causing YSZ dissolution at a faster rate than LHS-1. Specifically, the recession rate appears to be approximately 6x faster in JSC-1A than in LHS-1. This result is consistent with the findings presented in Chapter 3. These results suggest that YSZ may not be suitable for use in a hollow anode for extended duration MRE. However, it is noted that grain coarsening is expected to slow the rate of YSZ dissolution in both types of regolith, as presented in Chapter 4. The results from Chapter 3 indicate that grain coarsening is occurring significantly faster in JSC-1A than in LHS-1 (Section 3.3.2.2). It is possible that the accelerated grain coarsening, caused by contact with molten JSC-1A, can offset the higher YSZ dissolution rate for longer periods of exposure. Further experiments are necessary to evaluate this effect and to define an appropriate design life for YSZ hollow anodes performing electrolysis on lunar maria regolith.

Ultimately, the data presented in this appendix provide a proof-of-principle that YSZ hollow anodes can be used to electrolyze lunar maria regolith. Though there are some differences in the applied potential and cathodic products, electrolysis does not appear to be significantly different than the results presented in Chapter 4 for LHS-1. However, the YSZ dissolution rate in JSC-1A is concerning. If grain coarsening does not appreciably slow the dissolution rate observed in 3 hours at 1600°C, then the design life of YSZ hollow anode in lunar maria regolith will be significantly shorter than in lunar highlands regolith. Since the lunar highlands are prioritized for a sustained human presence on the lunar surface, no further experiments were performed with JSC-1A.

References

[1] Exolith Lab, LHS-1 Lunar Highlands Simulant Fact Sheet (002-01-001-0621), (2021). https://cdn.shopify.com/s/files/1/0398/9268/0862/files/lhs-1-spec-sheet-Dec2022.pptx.pdf?v=1688051876.

[2] D.S. McKay, J.L. Carter, W.W. Boles, C.C. Allen, J.H. Allton, JSC-1: A New Lunar Soil Simulant, in: Engineering, Construction, and Operations in Space IV, American Society of Civil Engineers, Albuquerque, NM, 1994: pp. 857–866. https://www.lpi.usra.edu/lunar/strategies/jsc_lunar_simulant.pdf.

[3] A.H. Sirk, D.R. Sadoway, L. Sibille, Direct Electrolysis of Molten Lunar Regolith for the Production of Oxygen and Metals on the Moon, ECS Transactions 28 (2010) 367–373. https://doi.org/10.1149/1.3367929.

[4] M. Wang, H. Jiao, Z. Pu, B. Hong, J. Ge, W. Xiao, S. Jiao, Ultra-High Temperature Molten Oxide Electrochemistry, Angew Chem Int Ed 61 (2022). https://doi.org/10.1002/anie.202206482.

[5] K. Yu, J. Stokes, B. Harder, L. Reidy, K.T. Faber, Thermochemical interactions between yttria-stabilized zirconia and molten lunar regolith simulants, Journal of the American Ceramic Society 107 (2024) 7119–7130. https://doi.org/10.1111/jace.19821.

[6] Y. Shao, K. Shigenobu, M. Watanabe, C. Zhang, Role of Viscosity in Deviations from the Nernst–Einstein Relation, J. Phys. Chem. B 124 (2020) 4774–4780. https://doi.org/10.1021/acs.jpcb.0c02544.

Appendix G

SUPPORTING MATERIAL FOR CHAPTER 6

The contents of this appendix are also presented in "Discovery and characterization of a silicon aluminum scandate (SAS) material" by K. Yu, J. Stokes, K. K. Jha, B. Harder, H. M. Nelson, and K. T. Faber, which is under review. The data presented in this appendix supports the results presented in Chapter 6.

K. Yu, J. Stokes, K.K. Jha, B. Harder, H.M. Nelson, K.T. Faber (n.d.). "Discovery and characterization of a silicon aluminum scandate (SAS) material". In: *under review*.

Appendix G.1

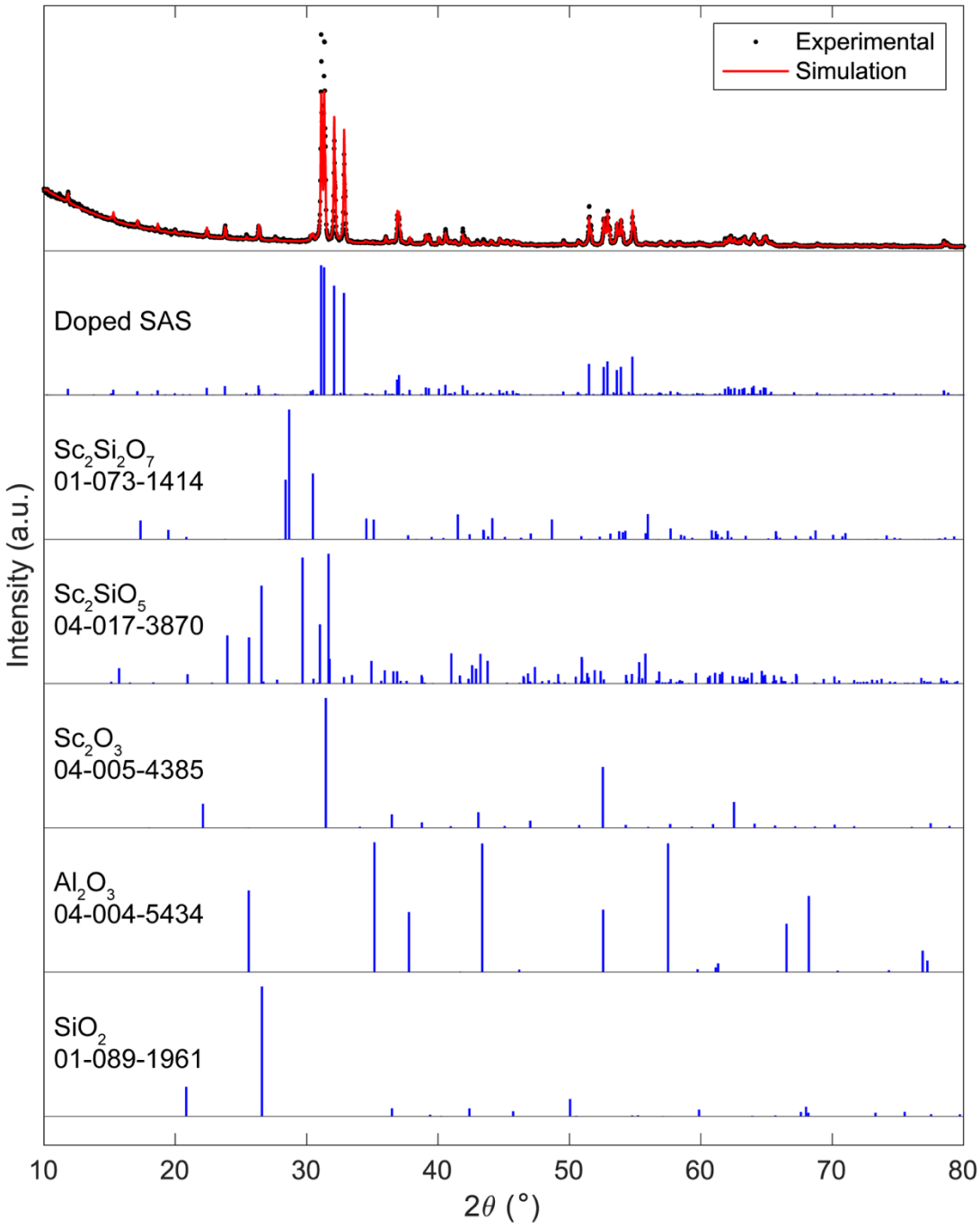

Figure G.1. XRD (Cu Kα) of doped SAS powder with simulated pattern after Rietveld refinement (red) and calculated diffraction peaks (blue) of possible impurity phases.

Appendix G.2

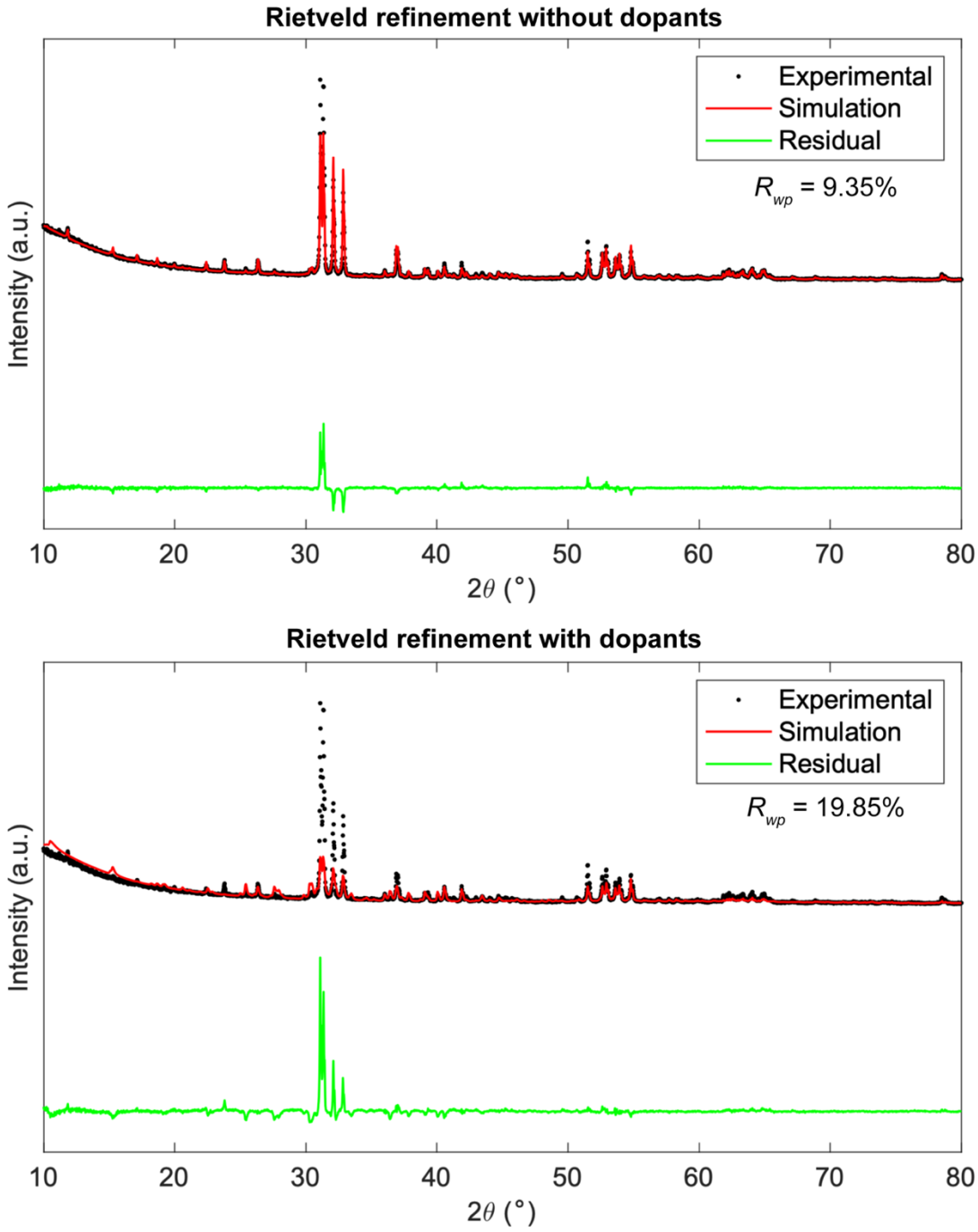

Figure G.2. XRD (Cu Kα) of doped SAS powder with simulated pattern after Rietveld refinement without dopants (top) and with equally distributed dopants (bottom).

Appendix G.3

Topological analysis using Bader's Quantum Theory of Atoms in Molecules (QTAIM) is a powerful tool for studying chemical bonding and the nature of intermolecular interactions [1]. Recently, topological analysis was performed on geometries obtained from microED data to determine the hydride position in Stryker's reagent [2].

To verify the coordination state of the seven Sc sites, topological analysis was carried out on the SAS structure obtained from the MicroED experiment. The electron density was generated theoretically using quantum-mechanical (QM) calculations based on the experimental geometry. The wavefunction file from the finite-point calculation was used. Wavefunction calculations were performed using the ORCA 4.2.1 suite [3]. Density functional theory (B3LYP) with the 6-31G(d,p) basis set was employed. The Multiwfn program suite was used for topological analysis and Laplacian map generation [4].

The topological analysis revealed that three Sc sites exhibit 7-fold coordination with O2- (Sc03, Sc04, Sc05 in Figure 6.4), whereas the remaining four Sc sites exhibit 6-fold (octahedral) coordination with O2- (Sc01, Sc02, Sc06, Sc07 in Figure 6.4). Contour maps of the Laplacian of electron density are shown below in Figures G.3.1 – G.3.7.

References

[1] R.F.W. Bader, Atoms in molecules, Acc. Chem. Res. 18 (1985) 9–15. https://doi.org/10.1021/ar00109a003.
[2] K.K. Jha, J.O. Rothbaum, V.C. Bhethanabotla, C.B. Musgrave, C.G. Jones, S.I. Morozov, W.A. Goddard, H.M. Nelson, Comparative Study of Solvatomorphs of Stryker's Reagent Using MicroED and Quantum Mechanics, Angew Chem Int Ed 64 (2025) e202502524. https://doi.org/10.1002/anie.202502524.
[3] F. Neese, F. Wennmohs, U. Becker, C. Riplinger, The ORCA quantum chemistry program package, The Journal of Chemical Physics 152 (2020) 224108. https://doi.org/10.1063/5.0004608.
[4] T. Lu, F. Chen, Multiwfn: A multifunctional wavefunction analyzer, J Comput Chem 33 (2012) 580–592. https://doi.org/10.1002/jcc.22885.

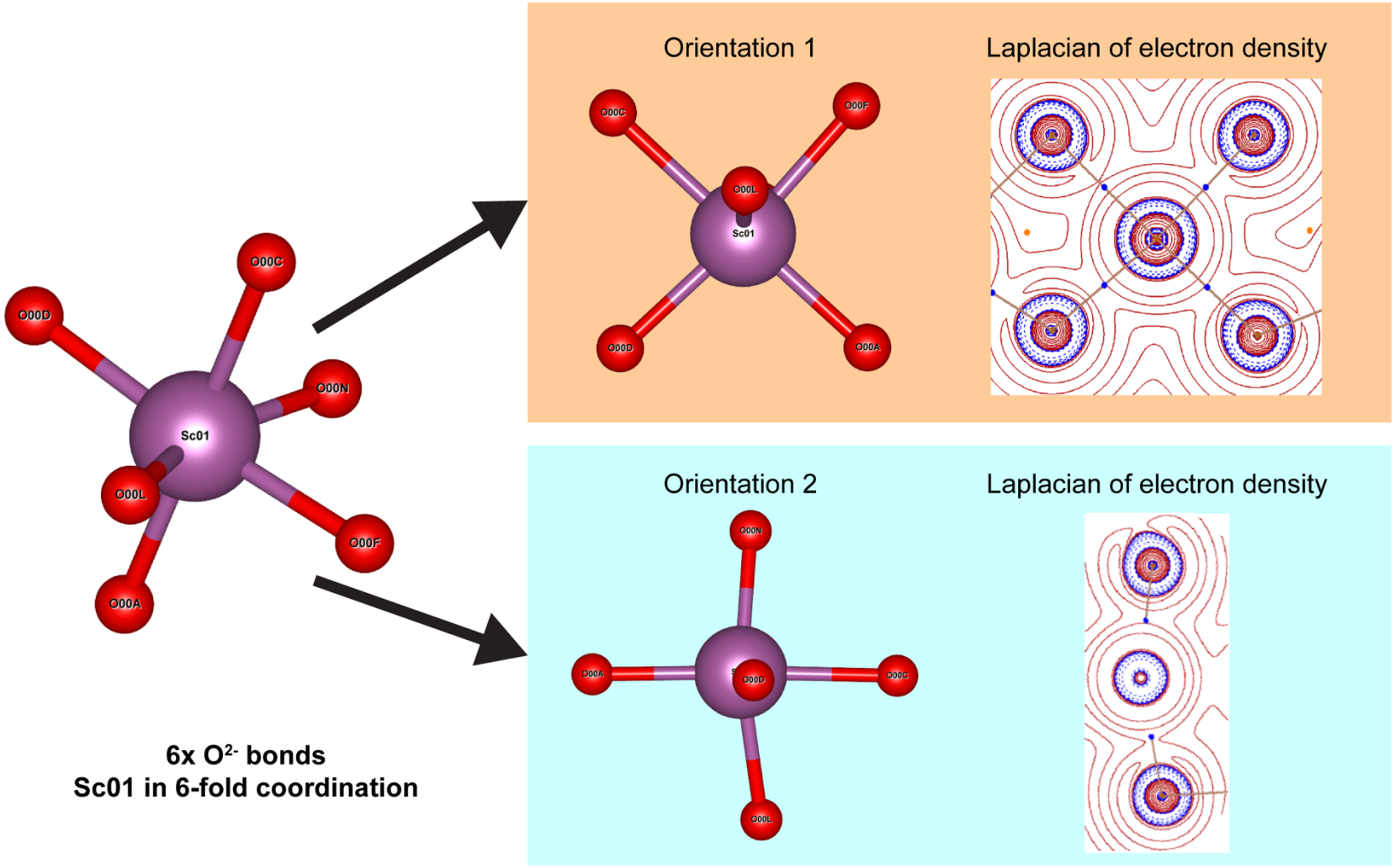

Figure G.3.1. Laplacian $\nabla^2\rho(r)$ overlayed with bond path (brown solid line) and bond critical point (blue dot) obtained on Sc01 using experimental geometry of SAS. Logarithmic scale in the form of $\pm 1,2,4,8\cdot10^n$ ($-3 \leq n \geq 8$) $eÅ^{-5}$ was adopted for drawing the contour map; blue and red colors correspond to positive and negative function values, respectively.

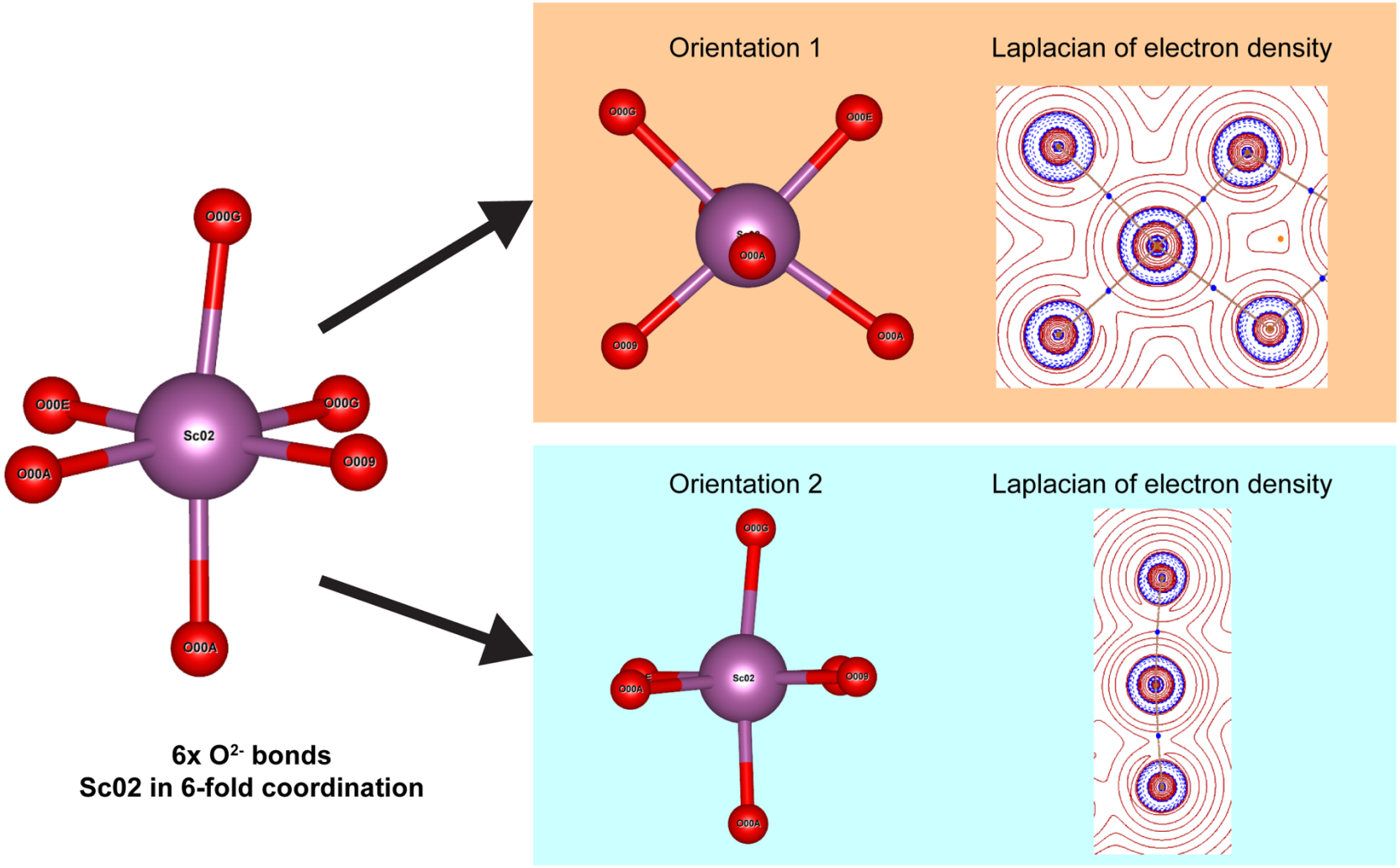

Figure G.3.2. Laplacian $\nabla^2\rho(r)$ overlayed with bond path (brown solid line) and bond critical point (blue dot) obtained on Sc02 using experimental geometry of SAS. Logarithmic scale in the form of $\pm 1,2,4,8\cdot10^n$ $(-3 \leq n \geq 8)$ $eÅ^{-5}$ was adopted for drawing the contour map; blue and red colors correspond to positive and negative function values, respectively.

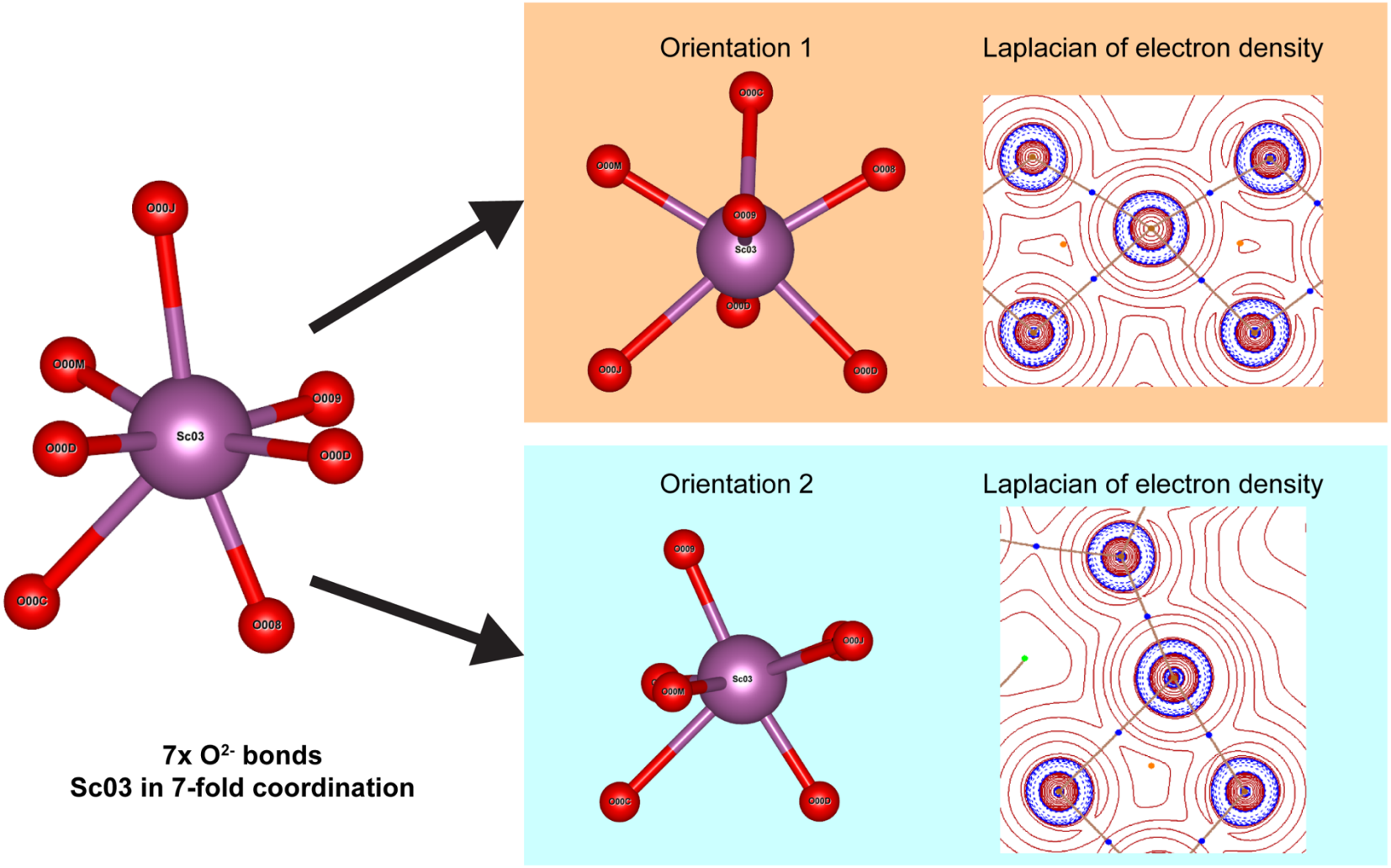

Figure G.3.3. Laplacian $\nabla^2\rho(r)$ overlayed with bond path (brown solid line) and bond critical point (blue dot) obtained on Sc03 using experimental geometry of SAS. Logarithmic scale in the form of $\pm 1,2,4,8\cdot10^n$ $(-3 \leq n \geq 8)$ $eÅ^{-5}$ was adopted for drawing the contour map; blue and red colors correspond to positive and negative function values, respectively.

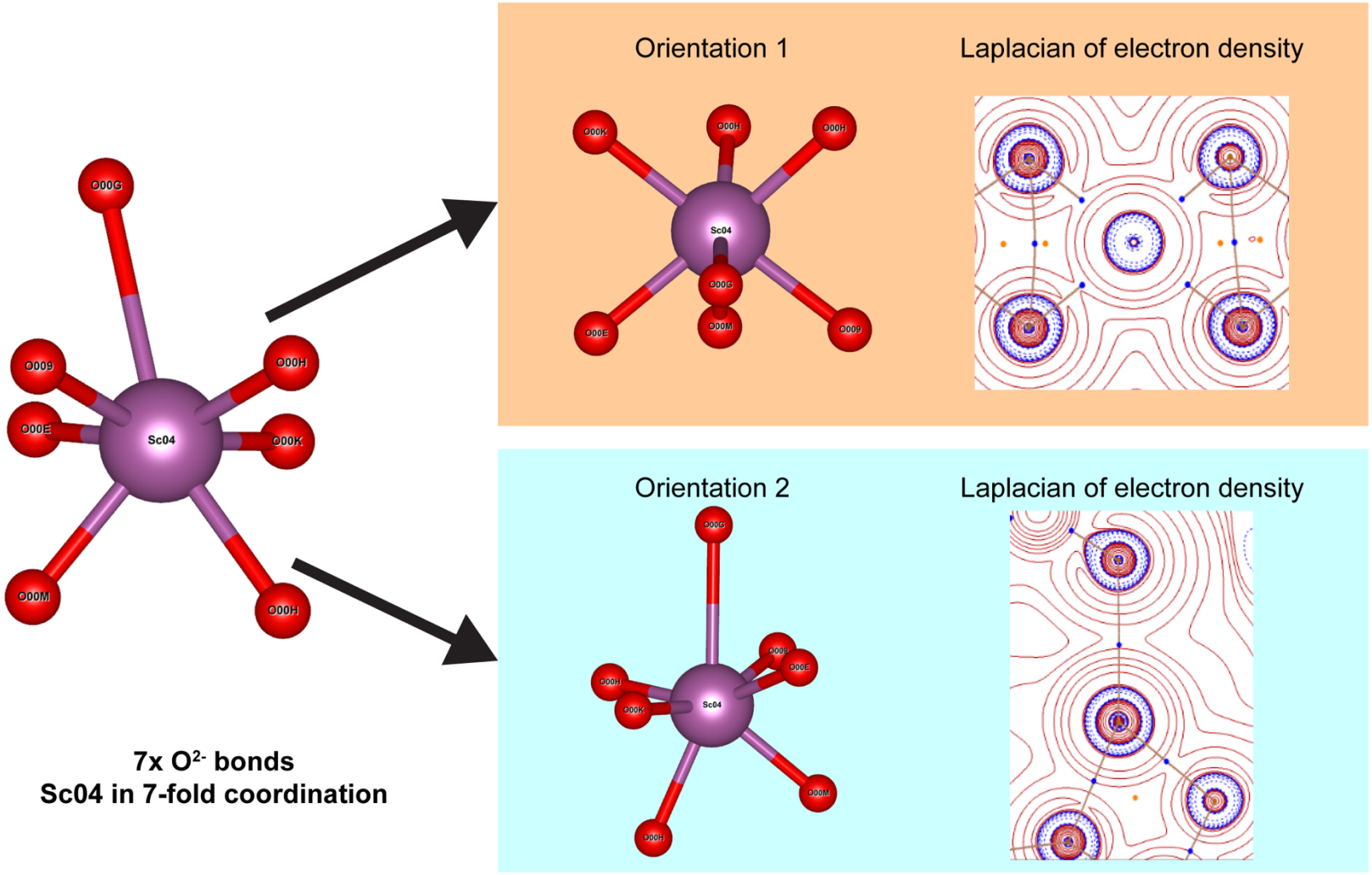

Figure G.3.4. Laplacian $\nabla^2\rho(r)$ overlayed with bond path (brown solid line) and bond critical point (blue dot) obtained on Sc04 using experimental geometry of SAS. Logarithmic scale in the form of $\pm 1,2,4,8\cdot10^n$ $(-3 \leq n \geq 8)$ $eÅ^{-5}$ was adopted for drawing the contour map; blue and red colors correspond to positive and negative function values, respectively.

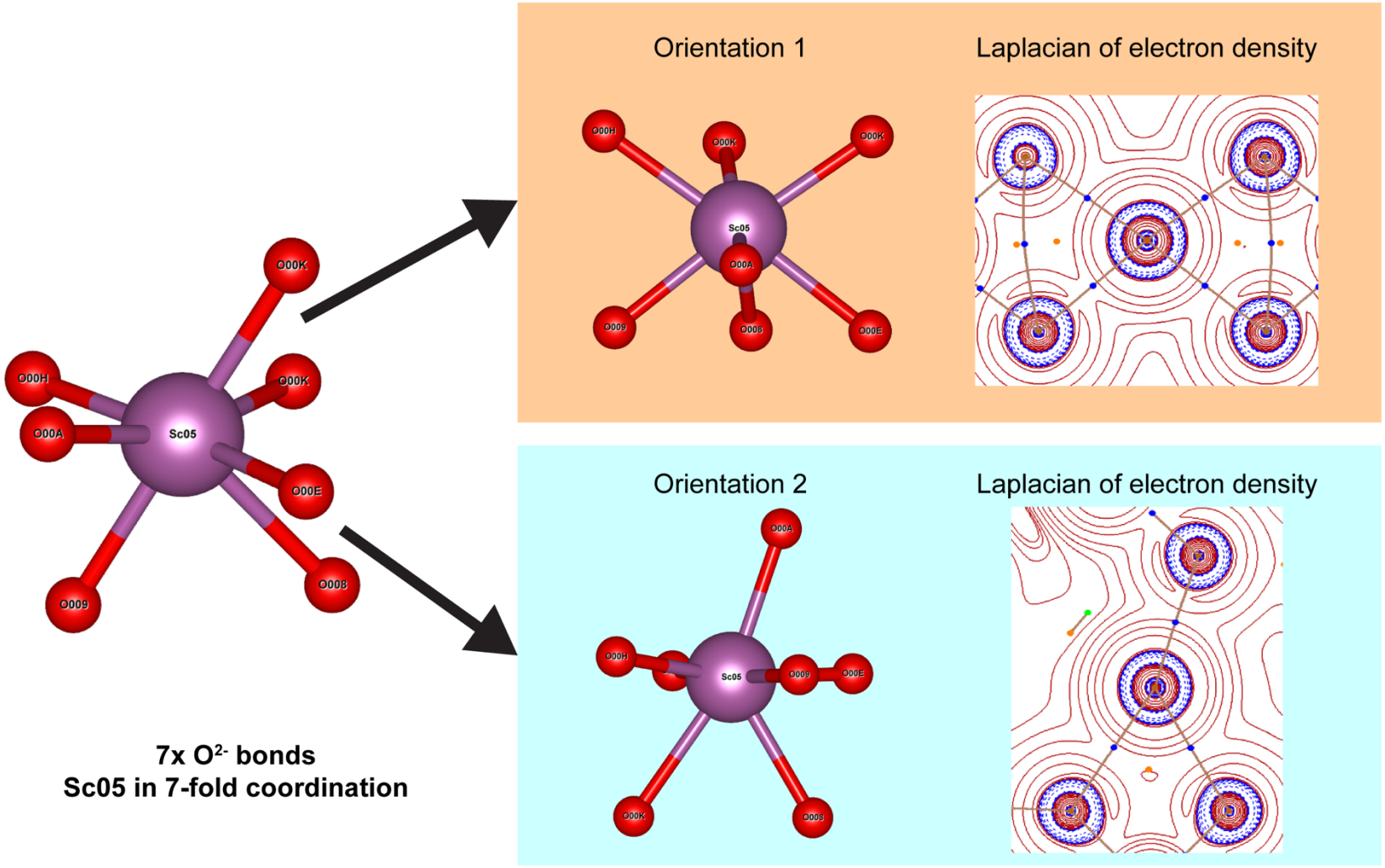

Figure G.3.5. Laplacian $\nabla^2\rho(r)$ overlayed with bond path (brown solid line) and bond critical point (blue dot) obtained on Sc05 using experimental geometry of SAS. Logarithmic scale in the form of $\pm 1,2,4,8\cdot10^n$ $(-3 \leq n \geq 8)$ $eÅ^{-5}$ was adopted for drawing the contour map; blue and red colors correspond to positive and negative function values, respectively.

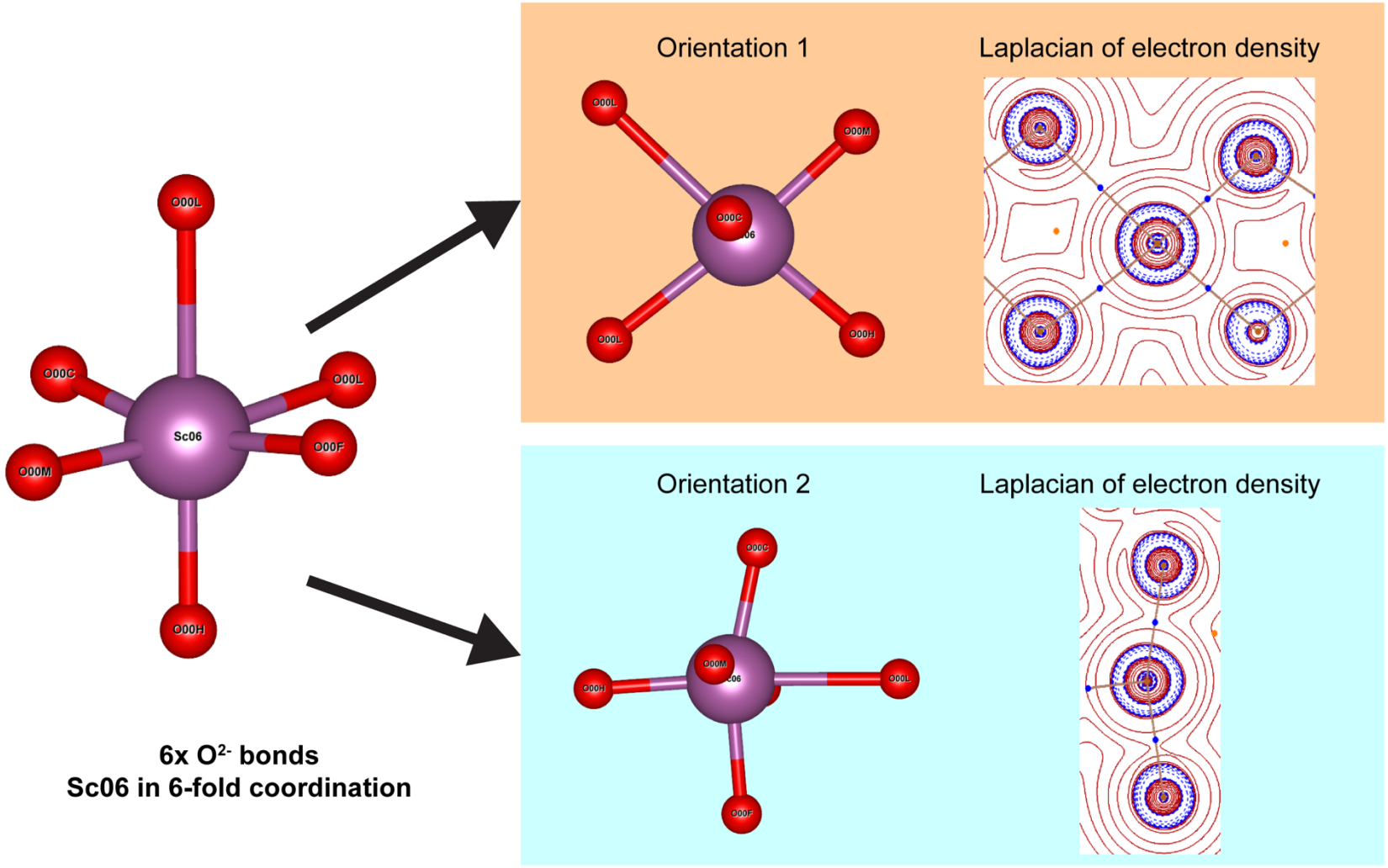

Figure G.3.6. Laplacian $\nabla^2\rho(r)$ overlayed with bond path (brown solid line) and bond critical point (blue dot) obtained on Sc06 using experimental geometry of SAS. Logarithmic scale in the form of $\pm 1,2,4,8\cdot10^n$ ($-3 \leq n \geq 8$) $eÅ^{-5}$ was adopted for drawing the contour map; blue and red colors correspond to positive and negative function values, respectively.

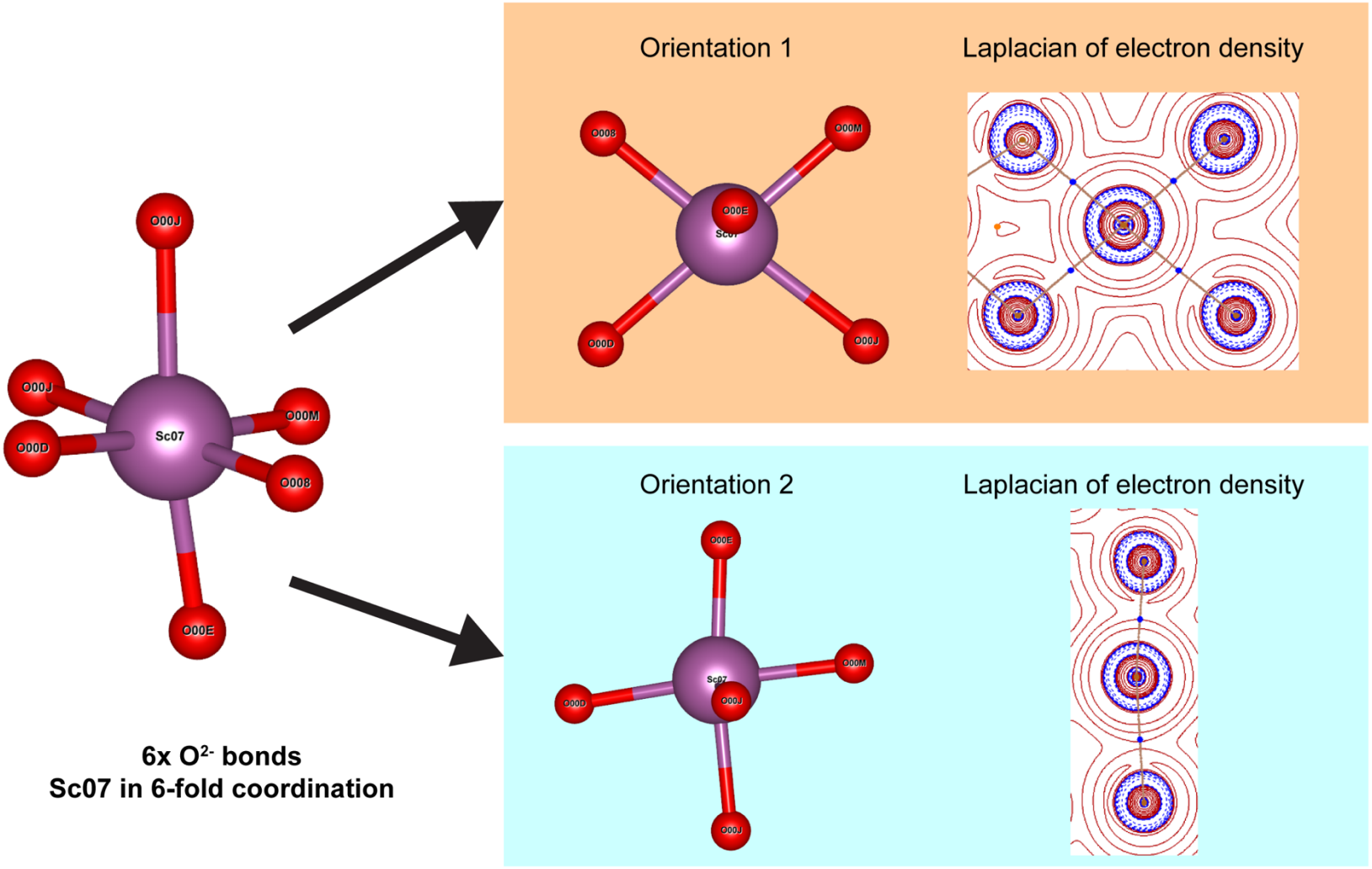

Figure G.3.7. Laplacian $\nabla^2\rho(r)$ overlayed with bond path (brown solid line) and bond critical point (blue dot) obtained on Sc07 using experimental geometry of SAS. Logarithmic scale in the form of $\pm 1,2,4,8\cdot10^n$ ($-3 \leq n \geq 8$) $eÅ^{-5}$ was adopted for drawing the contour map; blue and red colors correspond to positive and negative function values, respectively.

Appendix G.4

Table G.4. Full electron-probe microanalysis results for doped SAS. Results are presented using the unit cell formula basis.

Site #	Sc	Si	Al	Ti	Ca	Mg	Fe	O	Total ions
1	12.777	2.350	2.105	0.207	0.149	0.215	0.133	28.000	45.936
2	12.752	2.366	2.103	0.212	0.146	0.211	0.136	28.000	45.926
3	12.814	2.323	2.114	0.208	0.147	0.198	0.135	28.000	45.938
4	12.798	2.356	2.083	0.211	0.144	0.203	0.132	28.000	45.927
5	12.763	2.327	2.155	0.208	0.146	0.205	0.135	28.000	45.939
6	12.771	2.356	2.103	0.214	0.143	0.211	0.129	28.000	45.928
7	12.762	2.367	2.095	0.212	0.148	0.212	0.132	28.000	45.927
8	12.776	2.365	2.099	0.205	0.147	0.211	0.126	28.000	45.930
9	12.821	2.365	2.044	0.205	0.159	0.209	0.129	28.000	45.932
10	12.790	2.347	2.109	0.206	0.144	0.209	0.127	28.000	45.933
11	12.788	2.360	2.085	0.212	0.147	0.204	0.130	28.000	45.927
12	12.751	2.362	2.117	0.214	0.147	0.206	0.130	28.000	45.926
13	12.753	2.347	2.134	0.213	0.140	0.216	0.129	28.000	45.932
14	12.738	2.374	2.135	0.207	0.136	0.198	0.129	28.000	45.918
15	12.774	2.350	2.117	0.212	0.143	0.208	0.126	28.000	45.930
16	12.819	2.345	2.080	0.212	0.142	0.201	0.130	28.000	45.929
17	12.784	2.346	2.118	0.205	0.141	0.209	0.130	28.000	45.933
18	12.815	2.345	2.078	0.208	0.144	0.219	0.127	28.000	45.937
19	12.757	2.352	2.134	0.211	0.135	0.203	0.133	28.000	45.925
20	12.740	2.374	2.106	0.207	0.142	0.218	0.140	28.000	45.926
21	12.783	2.343	2.107	0.213	0.139	0.215	0.133	28.000	45.933
22	12.787	2.345	2.103	0.210	0.142	0.210	0.135	28.000	45.932
23	12.795	2.348	2.096	0.211	0.141	0.206	0.132	28.000	45.929
24	12.788	2.358	2.094	0.206	0.142	0.207	0.133	28.000	45.928

25	12.819	2.360	2.058	0.205	0.151	0.206	0.131	28.000	45.931
26	12.783	2.354	2.109	0.211	0.142	0.199	0.127	28.000	45.925
27	12.786	2.365	2.084	0.206	0.145	0.213	0.130	28.000	45.929
28	12.805	2.364	2.067	0.208	0.140	0.210	0.131	28.000	45.926
29	12.821	2.344	2.093	0.204	0.138	0.204	0.127	28.000	45.932
30	12.784	2.371	2.077	0.212	0.136	0.208	0.132	28.000	45.920
31	12.750	2.374	2.113	0.207	0.141	0.209	0.128	28.000	45.923
32	12.798	2.349	2.095	0.204	0.142	0.215	0.132	28.000	45.935
33	12.776	2.357	2.101	0.206	0.147	0.214	0.131	28.000	45.932
34	12.793	2.345	2.102	0.208	0.147	0.205	0.133	28.000	45.933
35	12.783	2.361	2.091	0.207	0.145	0.211	0.131	28.000	45.929
36	12.752	2.376	2.103	0.211	0.142	0.205	0.131	28.000	45.920
37	12.783	2.369	2.083	0.205	0.147	0.211	0.129	28.000	45.928
38	12.794	2.356	2.091	0.205	0.148	0.208	0.129	28.000	45.932
39	12.775	2.373	2.079	0.208	0.147	0.216	0.130	28.000	45.927
40	12.795	2.365	2.078	0.210	0.147	0.209	0.124	28.000	45.927
41	12.773	2.361	2.099	0.211	0.142	0.211	0.129	28.000	45.927
42	12.786	2.355	2.102	0.203	0.142	0.214	0.130	28.000	45.932
43	12.794	2.367	2.071	0.207	0.147	0.211	0.131	28.000	45.928
44	12.753	2.381	2.095	0.211	0.143	0.205	0.130	28.000	45.919
45	12.769	2.358	2.118	0.207	0.137	0.207	0.130	28.000	45.926
46	12.797	2.357	2.071	0.209	0.154	0.214	0.131	28.000	45.934
47	12.805	2.351	2.074	0.212	0.151	0.209	0.131	28.000	45.932
48	12.817	2.357	2.059	0.205	0.149	0.215	0.132	28.000	45.934
49	12.784	2.359	2.080	0.213	0.144	0.213	0.134	28.000	45.928
50	12.767	2.358	2.120	0.203	0.142	0.210	0.131	28.000	45.931
51	12.771	2.351	2.121	0.214	0.139	0.204	0.126	28.000	45.926
Average	**12.783**	**2.357**	**2.097**	**0.209**	**0.144**	**0.209**	**0.131**	**28.000**	**45.929**
Std Dev	**0.022**	**0.012**	**0.021**	**0.003**	**0.005**	**0.005**	**0.003**	**0.000**	**0.005**

Appendix G.5

A 3rd order polynomial was used to fit the unit cell volume (in units of $Å^3$) as a function of temperature (in units of °C).

The polynomial function is:

$$V(T) = (3.5052 * 10^{-10}) * T^3 + (2.4936 * 10^{-6}) * T^2 + (0.0112) * T + 517.3821$$

The volumetric thermal expansion coefficient is defined as:

$$\alpha_V = \frac{1}{V(T)} \frac{dV}{dT}$$

The function *V(T)* and its derivative can be used to obtain α_V.

These values are multiplied by 10^6 to convert from 1/°C to ppm/°C in Figure 6.7(d).

Appendix G.6

The Coefficient of Thermal Expansion Analysis Suite (CTEAS) results are provided below. A 3rd order polynomial was used to fit the lattice parameters. The thermal expansion tensor was calculated for the temperature range of 25°C to 1500°C, in 25°C increments.

Table G.6. Thermal expansion tensor values from CTEAS.

T (°C)	CTE(11)	CTE(12)	CTE(13)	CTE(21)	CTE(22)	CTE(23)	CTE(31)	CTE(32)	CTE(33)	CTEErr
25	5.45E-06	2.09E-06	9.69E-07	2.09E-06	1.20E-05	-5.52E-06	9.69E-07	-5.52E-06	4.63E-06	9.18E-01
50	5.44E-06	1.96E-06	9.20E-07	1.96E-06	1.21E-05	-5.42E-06	9.20E-07	-5.42E-06	4.81E-06	9.01E-01
75	5.44E-06	1.85E-06	8.73E-07	1.85E-06	1.21E-05	-5.33E-06	8.73E-07	-5.33E-06	4.98E-06	8.84E-01
100	5.45E-06	1.73E-06	8.27E-07	1.73E-06	1.22E-05	-5.24E-06	8.27E-07	-5.24E-06	5.15E-06	8.67E-01
125	5.45E-06	1.63E-06	7.83E-07	1.63E-06	1.22E-05	-5.16E-06	7.83E-07	-5.16E-06	5.32E-06	8.50E-01
150	5.47E-06	1.53E-06	7.40E-07	1.53E-06	1.23E-05	-5.07E-06	7.40E-07	-5.07E-06	5.49E-06	8.34E-01
175	5.48E-06	1.43E-06	6.99E-07	1.43E-06	1.24E-05	-5.00E-06	6.99E-07	-5.00E-06	5.65E-06	8.17E-01
200	5.51E-06	1.34E-06	6.60E-07	1.34E-06	1.24E-05	-4.92E-06	6.60E-07	-4.92E-06	5.81E-06	8.00E-01
225	5.53E-06	1.26E-06	6.22E-07	1.26E-06	1.25E-05	-4.85E-06	6.22E-07	-4.85E-06	5.96E-06	7.84E-01
250	5.56E-06	1.18E-06	5.85E-07	1.18E-06	1.25E-05	-4.78E-06	5.85E-07	-4.78E-06	6.12E-06	7.68E-01
275	5.60E-06	1.11E-06	5.50E-07	1.11E-06	1.26E-05	-4.72E-06	5.50E-07	-4.72E-06	6.27E-06	7.52E-01
300	5.63E-06	1.04E-06	5.17E-07	1.04E-06	1.26E-05	-4.66E-06	5.17E-07	-4.66E-06	6.41E-06	7.36E-01
325	5.68E-06	9.81E-07	4.85E-07	9.81E-07	1.27E-05	-4.60E-06	4.85E-07	-4.60E-06	6.56E-06	7.20E-01

350	5.73E-06	9.26E-07	4.54E-07	9.26E-07	1.28E-05	-4.54E-06	4.54E-07	-4.54E-06	6.70E-06	7.05E-01
375	5.78E-06	8.77E-07	4.25E-07	8.77E-07	1.28E-05	-4.49E-06	4.25E-07	-4.49E-06	6.84E-06	6.90E-01
400	5.83E-06	8.34E-07	3.98E-07	8.34E-07	1.29E-05	-4.45E-06	3.98E-07	-4.45E-06	6.98E-06	6.76E-01
425	5.89E-06	7.96E-07	3.72E-07	7.96E-07	1.29E-05	-4.40E-06	3.72E-07	-4.40E-06	7.11E-06	6.61E-01
450	5.96E-06	7.65E-07	3.47E-07	7.65E-07	1.30E-05	-4.36E-06	3.47E-07	-4.36E-06	7.24E-06	6.48E-01
475	6.03E-06	7.39E-07	3.24E-07	7.39E-07	1.31E-05	-4.33E-06	3.24E-07	-4.33E-06	7.37E-06	6.34E-01
500	6.10E-06	7.20E-07	3.02E-07	7.20E-07	1.31E-05	-4.30E-06	3.02E-07	-4.30E-06	7.49E-06	6.21E-01
525	6.18E-06	7.06E-07	2.82E-07	7.06E-07	1.32E-05	-4.27E-06	2.82E-07	-4.27E-06	7.62E-06	6.09E-01
550	6.26E-06	6.98E-07	2.63E-07	6.98E-07	1.32E-05	-4.24E-06	2.63E-07	-4.24E-06	7.73E-06	5.97E-01
575	6.35E-06	6.95E-07	2.46E-07	6.95E-07	1.33E-05	-4.22E-06	2.46E-07	-4.22E-06	7.85E-06	5.85E-01
600	6.44E-06	6.99E-07	2.30E-07	6.99E-07	1.34E-05	-4.20E-06	2.30E-07	-4.20E-06	7.97E-06	5.74E-01
625	6.54E-06	7.09E-07	2.16E-07	7.09E-07	1.34E-05	-4.19E-06	2.16E-07	-4.19E-06	8.08E-06	5.64E-01
650	6.64E-06	7.24E-07	2.03E-07	7.24E-07	1.35E-05	-4.18E-06	2.03E-07	-4.18E-06	8.18E-06	5.54E-01
675	6.74E-06	7.45E-07	1.92E-07	7.45E-07	1.36E-05	-4.17E-06	1.92E-07	-4.17E-06	8.29E-06	5.45E-01
700	6.85E-06	7.72E-07	1.81E-07	7.72E-07	1.36E-05	-4.17E-06	1.81E-07	-4.17E-06	8.39E-06	5.37E-01
725	6.96E-06	8.05E-07	1.73E-07	8.05E-07	1.37E-05	-4.17E-06	1.73E-07	-4.17E-06	8.49E-06	5.29E-01
750	7.08E-06	8.44E-07	1.65E-07	8.44E-07	1.38E-05	-4.17E-06	1.65E-07	-4.17E-06	8.59E-06	5.22E-01
775	7.20E-06	8.89E-07	1.60E-07	8.89E-07	1.38E-05	-4.18E-06	1.60E-07	-4.18E-06	8.68E-06	5.16E-01
800	7.33E-06	9.40E-07	1.55E-07	9.40E-07	1.39E-05	-4.19E-06	1.55E-07	-4.19E-06	8.78E-06	5.10E-01

825	7.46E-06	9.97E-07	1.52E-07	9.97E-07	1.40E-05	-4.21E-06	1.52E-07	-4.21E-06	8.86E-06	5.06E-01
850	7.59E-06	1.06E-06	1.50E-07	1.06E-06	1.40E-05	-4.23E-06	1.50E-07	-4.23E-06	8.95E-06	5.02E-01
875	7.73E-06	1.13E-06	1.50E-07	1.13E-06	1.41E-05	-4.25E-06	1.50E-07	-4.25E-06	9.03E-06	4.99E-01
900	7.88E-06	1.20E-06	1.51E-07	1.20E-06	1.42E-05	-4.28E-06	1.51E-07	-4.28E-06	9.12E-06	4.97E-01
925	8.02E-06	1.28E-06	1.54E-07	1.28E-06	1.42E-05	-4.31E-06	1.54E-07	-4.31E-06	9.19E-06	4.96E-01
950	8.18E-06	1.37E-06	1.58E-07	1.37E-06	1.43E-05	-4.34E-06	1.58E-07	-4.34E-06	9.27E-06	4.95E-01
975	8.33E-06	1.46E-06	1.63E-07	1.46E-06	1.44E-05	-4.38E-06	1.63E-07	-4.38E-06	9.34E-06	4.96E-01
1000	8.50E-06	1.56E-06	1.70E-07	1.56E-06	1.45E-05	-4.42E-06	1.70E-07	-4.42E-06	9.41E-06	4.98E-01
1025	8.66E-06	1.66E-06	1.78E-07	1.66E-06	1.45E-05	-4.46E-06	1.78E-07	-4.46E-06	9.48E-06	5.01E-01
1050	8.83E-06	1.77E-06	1.87E-07	1.77E-06	1.46E-05	-4.51E-06	1.87E-07	-4.51E-06	9.54E-06	5.04E-01
1075	9.01E-06	1.89E-06	1.98E-07	1.89E-06	1.47E-05	-4.56E-06	1.98E-07	-4.56E-06	9.60E-06	5.09E-01
1100	9.19E-06	2.01E-06	2.10E-07	2.01E-06	1.47E-05	-4.62E-06	2.10E-07	-4.62E-06	9.66E-06	5.15E-01
1125	9.37E-06	2.14E-06	2.23E-07	2.14E-06	1.48E-05	-4.67E-06	2.23E-07	-4.67E-06	9.72E-06	5.22E-01
1150	9.56E-06	2.27E-06	2.38E-07	2.27E-06	1.49E-05	-4.74E-06	2.38E-07	-4.74E-06	9.77E-06	5.30E-01
1175	9.75E-06	2.41E-06	2.54E-07	2.41E-06	1.50E-05	-4.80E-06	2.54E-07	-4.80E-06	9.82E-06	5.40E-01
1200	9.95E-06	2.56E-06	2.71E-07	2.56E-06	1.50E-05	-4.87E-06	2.71E-07	-4.87E-06	9.87E-06	5.51E-01
1225	1.01E-05	2.71E-06	2.90E-07	2.71E-06	1.51E-05	-4.95E-06	2.90E-07	-4.95E-06	9.92E-06	5.62E-01
1250	1.04E-05	2.86E-06	3.10E-07	2.86E-06	1.52E-05	-5.03E-06	3.10E-07	-5.03E-06	9.96E-06	5.76E-01
1275	1.06E-05	3.03E-06	3.31E-07	3.03E-06	1.53E-05	-5.11E-06	3.31E-07	-5.11E-06	1.00E-05	5.90E-01

1300	1.08E-05	3.20E-06	3.54E-07	3.20E-06	1.54E-05	-5.19E-06	3.54E-07	-5.19E-06	1.00E-05	6.06E-01
1325	1.10E-05	3.37E-06	3.77E-07	3.37E-06	1.54E-05	-5.28E-06	3.77E-07	-5.28E-06	1.01E-05	6.23E-01
1350	1.12E-05	3.55E-06	4.02E-07	3.55E-06	1.55E-05	-5.37E-06	4.02E-07	-5.37E-06	1.01E-05	6.41E-01
1375	1.15E-05	3.74E-06	4.29E-07	3.74E-06	1.56E-05	-5.47E-06	4.29E-07	-5.47E-06	1.01E-05	6.61E-01
1400	1.17E-05	3.93E-06	4.56E-07	3.93E-06	1.57E-05	-5.57E-06	4.56E-07	-5.57E-06	1.02E-05	6.83E-01
1425	1.19E-05	4.13E-06	4.85E-07	4.13E-06	1.58E-05	-5.67E-06	4.85E-07	-5.67E-06	1.02E-05	7.05E-01
1450	1.22E-05	4.34E-06	5.15E-07	4.34E-06	1.58E-05	-5.78E-06	5.15E-07	-5.78E-06	1.02E-05	7.30E-01
1475	1.24E-05	4.55E-06	5.47E-07	4.55E-06	1.59E-05	-5.89E-06	5.47E-07	-5.89E-06	1.02E-05	7.55E-01
1500	1.27E-05	4.77E-06	5.79E-07	4.77E-06	1.60E-05	-6.01E-06	5.79E-07	-6.01E-06	1.02E-05	7.83E-01

Appendix G.7

Table G.7. Eigenvalues (Eig) and eigenvectors (Ev1-Ev3) of the thermal expansion tensor from CTEAS. See Appendix G.6 for details.

T (°C)	Eig1	Eig2	Eig3	Ev1(1)	Ev1(2)	Ev1(3)	Ev2(1)	Ev2(2)	Ev2(3)	Ev3(1)	Ev3(2)	Ev3(3)
25	1.52E-05	6.01E-06	9.20E-07	-1.45E-01	-8.82E-01	4.48E-01	-9.11E-01	-5.79E-02	-4.08E-01	-3.86E-01	4.67E-01	7.96E-01
50	1.52E-05	5.99E-06	1.19E-06	-1.36E-01	-8.83E-01	4.50E-01	-9.12E-01	-6.62E-02	-4.05E-01	-3.87E-01	4.66E-01	7.96E-01
75	1.51E-05	5.98E-06	1.45E-06	-1.27E-01	-8.83E-01	4.52E-01	-9.13E-01	-7.43E-02	-4.02E-01	-3.89E-01	4.64E-01	7.96E-01
100	1.51E-05	5.96E-06	1.70E-06	-1.19E-01	-8.83E-01	4.54E-01	-9.13E-01	-8.21E-02	-4.00E-01	-3.90E-01	4.62E-01	7.96E-01
125	1.51E-05	5.96E-06	1.95E-06	-1.12E-01	-8.83E-01	4.56E-01	-9.13E-01	-8.97E-02	-3.98E-01	-3.92E-01	4.61E-01	7.96E-01
150	1.51E-05	5.95E-06	2.19E-06	-1.05E-01	-8.83E-01	4.57E-01	-9.13E-01	-9.69E-02	-3.96E-01	-3.94E-01	4.59E-01	7.96E-01
175	1.51E-05	5.95E-06	2.43E-06	-9.79E-02	-8.83E-01	4.59E-01	-9.13E-01	-1.04E-01	-3.95E-01	-3.96E-01	4.57E-01	7.96E-01
200	1.51E-05	5.95E-06	2.66E-06	-9.17E-02	-8.83E-01	4.60E-01	-9.12E-01	-1.11E-01	-3.94E-01	-3.99E-01	4.56E-01	7.96E-01
225	1.51E-05	5.96E-06	2.88E-06	-8.59E-02	-8.83E-01	4.61E-01	-9.12E-01	-1.17E-01	-3.94E-01	-4.02E-01	4.55E-01	7.95E-01
250	1.51E-05	5.97E-06	3.09E-06	-8.05E-02	-8.83E-01	4.63E-01	-9.11E-01	-1.23E-01	-3.94E-01	-4.05E-01	4.53E-01	7.94E-01
275	1.52E-05	5.99E-06	3.30E-06	-7.56E-02	-8.83E-01	4.64E-01	-9.10E-01	-1.29E-01	-3.94E-01	-4.08E-01	4.52E-01	7.93E-01
300	1.52E-05	6.01E-06	3.50E-06	-7.11E-02	-8.83E-01	4.65E-01	-9.09E-01	-1.35E-01	-3.95E-01	-4.11E-01	4.50E-01	7.92E-01
325	1.52E-05	6.04E-06	3.69E-06	-6.72E-02	-8.82E-01	4.66E-01	-9.07E-01	-1.40E-01	-3.97E-01	-4.15E-01	4.49E-01	7.91E-01
350	1.52E-05	6.07E-06	3.88E-06	-6.36E-02	-8.82E-01	4.67E-01	-9.06E-01	-1.46E-01	-3.99E-01	-4.19E-01	4.48E-01	7.90E-01
375	1.53E-05	6.11E-06	4.06E-06	-6.06E-02	-8.82E-01	4.68E-01	-9.04E-01	-1.51E-01	-4.01E-01	-4.24E-01	4.47E-01	7.88E-01
400	1.53E-05	6.15E-06	4.24E-06	-5.80E-02	-8.82E-01	4.69E-01	-9.02E-01	-1.55E-01	-4.04E-01	-4.28E-01	4.46E-01	7.86E-01
425	1.53E-05	6.20E-06	4.40E-06	-5.59E-02	-8.81E-01	4.70E-01	-9.00E-01	-1.60E-01	-4.07E-01	-4.33E-01	4.45E-01	7.84E-01
450	1.54E-05	6.26E-06	4.56E-06	-5.42E-02	-8.81E-01	4.70E-01	-8.97E-01	-1.64E-01	-4.10E-01	-4.38E-01	4.44E-01	7.81E-01

475	1.54E-05	6.32E-06	4.72E-06	-5.30E-02	-8.80E-01	4.71E-01	-8.95E-01	-1.68E-01	-4.14E-01	-4.43E-01	4.44E-01	7.79E-01
500	1.55E-05	6.38E-06	4.87E-06	-5.24E-02	-8.80E-01	4.72E-01	-8.93E-01	-1.71E-01	-4.17E-01	-4.48E-01	4.43E-01	7.76E-01
525	1.55E-05	6.45E-06	5.01E-06	-5.22E-02	-8.79E-01	4.73E-01	-8.90E-01	-1.74E-01	-4.21E-01	-4.52E-01	4.43E-01	7.74E-01
550	1.56E-05	6.53E-06	5.14E-06	-5.24E-02	-8.79E-01	4.74E-01	-8.88E-01	-1.76E-01	-4.25E-01	-4.57E-01	4.43E-01	7.71E-01
575	1.56E-05	6.61E-06	5.27E-06	-5.32E-02	-8.78E-01	4.75E-01	-8.86E-01	-1.78E-01	-4.28E-01	-4.60E-01	4.44E-01	7.69E-01
600	1.57E-05	6.69E-06	5.39E-06	-5.45E-02	-8.78E-01	4.76E-01	-8.85E-01	-1.79E-01	-4.31E-01	-4.63E-01	4.45E-01	7.67E-01
625	1.58E-05	6.79E-06	5.50E-06	-5.62E-02	-8.77E-01	4.77E-01	-8.83E-01	-1.79E-01	-4.33E-01	-4.65E-01	4.46E-01	7.65E-01
650	1.58E-05	6.88E-06	5.61E-06	-5.85E-02	-8.76E-01	4.78E-01	-8.82E-01	-1.78E-01	-4.35E-01	-4.67E-01	4.47E-01	7.63E-01
675	1.59E-05	6.98E-06	5.71E-06	-6.13E-02	-8.76E-01	4.79E-01	-8.82E-01	-1.77E-01	-4.37E-01	-4.67E-01	4.49E-01	7.62E-01
700	1.60E-05	7.09E-06	5.81E-06	-6.45E-02	-8.75E-01	4.80E-01	-8.82E-01	-1.75E-01	-4.37E-01	-4.67E-01	4.52E-01	7.60E-01
725	1.60E-05	7.20E-06	5.89E-06	-6.83E-02	-8.74E-01	4.81E-01	-8.83E-01	-1.72E-01	-4.38E-01	-4.65E-01	4.54E-01	7.60E-01
750	1.61E-05	7.32E-06	5.97E-06	-7.27E-02	-8.73E-01	4.82E-01	-8.83E-01	-1.68E-01	-4.38E-01	-4.63E-01	4.57E-01	7.59E-01
775	1.62E-05	7.44E-06	6.05E-06	-7.75E-02	-8.72E-01	4.83E-01	-8.84E-01	-1.63E-01	-4.37E-01	-4.60E-01	4.61E-01	7.59E-01
800	1.63E-05	7.57E-06	6.12E-06	-8.28E-02	-8.71E-01	4.83E-01	-8.85E-01	-1.58E-01	-4.37E-01	-4.57E-01	4.64E-01	7.59E-01
825	1.64E-05	7.70E-06	6.18E-06	-8.87E-02	-8.70E-01	4.84E-01	-8.87E-01	-1.52E-01	-4.37E-01	-4.54E-01	4.68E-01	7.58E-01
850	1.65E-05	7.84E-06	6.23E-06	-9.52E-02	-8.69E-01	4.85E-01	-8.88E-01	-1.46E-01	-4.36E-01	-4.50E-01	4.72E-01	7.58E-01
875	1.66E-05	7.98E-06	6.28E-06	-1.02E-01	-8.68E-01	4.85E-01	-8.89E-01	-1.39E-01	-4.36E-01	-4.47E-01	4.76E-01	7.58E-01
900	1.67E-05	8.13E-06	6.32E-06	-1.10E-01	-8.67E-01	4.86E-01	-8.90E-01	-1.32E-01	-4.37E-01	-4.43E-01	4.80E-01	7.57E-01
925	1.68E-05	8.28E-06	6.35E-06	-1.18E-01	-8.66E-01	4.86E-01	-8.90E-01	-1.25E-01	-4.38E-01	-4.40E-01	4.84E-01	7.56E-01
950	1.69E-05	8.43E-06	6.37E-06	-1.26E-01	-8.65E-01	4.86E-01	-8.91E-01	-1.17E-01	-4.39E-01	-4.36E-01	4.88E-01	7.56E-01
975	1.71E-05	8.59E-06	6.39E-06	-1.35E-01	-8.63E-01	4.86E-01	-8.91E-01	-1.09E-01	-4.41E-01	-4.34E-01	4.93E-01	7.55E-01

1000	1.72E-05	8.76E-06	6.40E-06	-1.45E-01	-8.62E-01	4.86E-01	-8.91E-01	-1.00E-01	-4.43E-01	-4.31E-01	4.97E-01	7.53E-01
1025	1.73E-05	8.92E-06	6.41E-06	-1.55E-01	-8.61E-01	4.85E-01	-8.90E-01	-9.12E-02	-4.46E-01	-4.28E-01	5.01E-01	7.52E-01
1050	1.75E-05	9.09E-06	6.40E-06	-1.66E-01	-8.59E-01	4.84E-01	-8.89E-01	-8.20E-02	-4.50E-01	-4.26E-01	5.05E-01	7.51E-01
1075	1.76E-05	9.26E-06	6.39E-06	-1.77E-01	-8.58E-01	4.83E-01	-8.88E-01	-7.26E-02	-4.54E-01	-4.24E-01	5.09E-01	7.49E-01
1100	1.78E-05	9.44E-06	6.37E-06	-1.88E-01	-8.56E-01	4.82E-01	-8.87E-01	-6.28E-02	-4.58E-01	-4.22E-01	5.13E-01	7.47E-01
1125	1.79E-05	9.61E-06	6.35E-06	-2.00E-01	-8.54E-01	4.80E-01	-8.85E-01	-5.27E-02	-4.63E-01	-4.21E-01	5.17E-01	7.45E-01
1150	1.81E-05	9.79E-06	6.32E-06	-2.13E-01	-8.52E-01	4.78E-01	-8.82E-01	-4.24E-02	-4.69E-01	-4.20E-01	5.21E-01	7.43E-01
1175	1.83E-05	9.97E-06	6.28E-06	-2.26E-01	-8.50E-01	4.75E-01	-8.80E-01	-3.17E-02	-4.74E-01	-4.18E-01	5.25E-01	7.41E-01
1200	1.85E-05	1.02E-05	6.23E-06	-2.39E-01	-8.48E-01	4.73E-01	-8.77E-01	-2.08E-02	-4.81E-01	-4.17E-01	5.29E-01	7.39E-01
1225	1.87E-05	1.03E-05	6.17E-06	-2.53E-01	-8.46E-01	4.70E-01	-8.73E-01	-9.64E-03	-4.87E-01	-4.17E-01	5.33E-01	7.36E-01
1250	1.89E-05	1.05E-05	6.11E-06	-2.66E-01	-8.44E-01	4.66E-01	-8.70E-01	1.76E-03	-4.94E-01	-4.16E-01	5.37E-01	7.34E-01
1275	1.91E-05	1.07E-05	6.04E-06	-2.81E-01	-8.41E-01	4.62E-01	-8.65E-01	1.34E-02	-5.01E-01	-4.15E-01	5.41E-01	7.32E-01
1300	1.93E-05	1.09E-05	5.96E-06	-2.95E-01	-8.39E-01	4.58E-01	-8.61E-01	2.52E-02	-5.08E-01	-4.15E-01	5.44E-01	7.29E-01
1325	1.95E-05	1.11E-05	5.88E-06	-3.10E-01	-8.36E-01	4.53E-01	-8.56E-01	3.71E-02	-5.16E-01	-4.14E-01	5.48E-01	7.27E-01
1350	1.98E-05	1.13E-05	5.79E-06	-3.24E-01	-8.33E-01	4.49E-01	-8.51E-01	4.92E-02	-5.24E-01	-4.14E-01	5.51E-01	7.24E-01
1375	2.00E-05	1.15E-05	5.69E-06	-3.39E-01	-8.30E-01	4.43E-01	-8.45E-01	6.14E-02	-5.31E-01	-4.14E-01	5.55E-01	7.22E-01
1400	2.03E-05	1.16E-05	5.58E-06	-3.54E-01	-8.26E-01	4.38E-01	-8.39E-01	7.36E-02	-5.39E-01	-4.13E-01	5.58E-01	7.19E-01
1425	2.06E-05	1.18E-05	5.47E-06	-3.69E-01	-8.23E-01	4.32E-01	-8.33E-01	8.58E-02	-5.47E-01	-4.13E-01	5.61E-01	7.17E-01
1450	2.09E-05	1.20E-05	5.35E-06	-3.83E-01	-8.20E-01	4.26E-01	-8.26E-01	9.79E-02	-5.55E-01	-4.13E-01	5.65E-01	7.15E-01
1475	2.12E-05	1.22E-05	5.22E-06	-3.98E-01	-8.16E-01	4.20E-01	-8.19E-01	1.10E-01	-5.63E-01	-4.13E-01	5.68E-01	7.12E-01
1500	2.15E-05	1.24E-05	5.08E-06	-4.12E-01	-8.12E-01	4.13E-01	-8.12E-01	1.22E-01	-5.71E-01	-4.13E-01	5.71E-01	7.10E-01

Appendix G.8

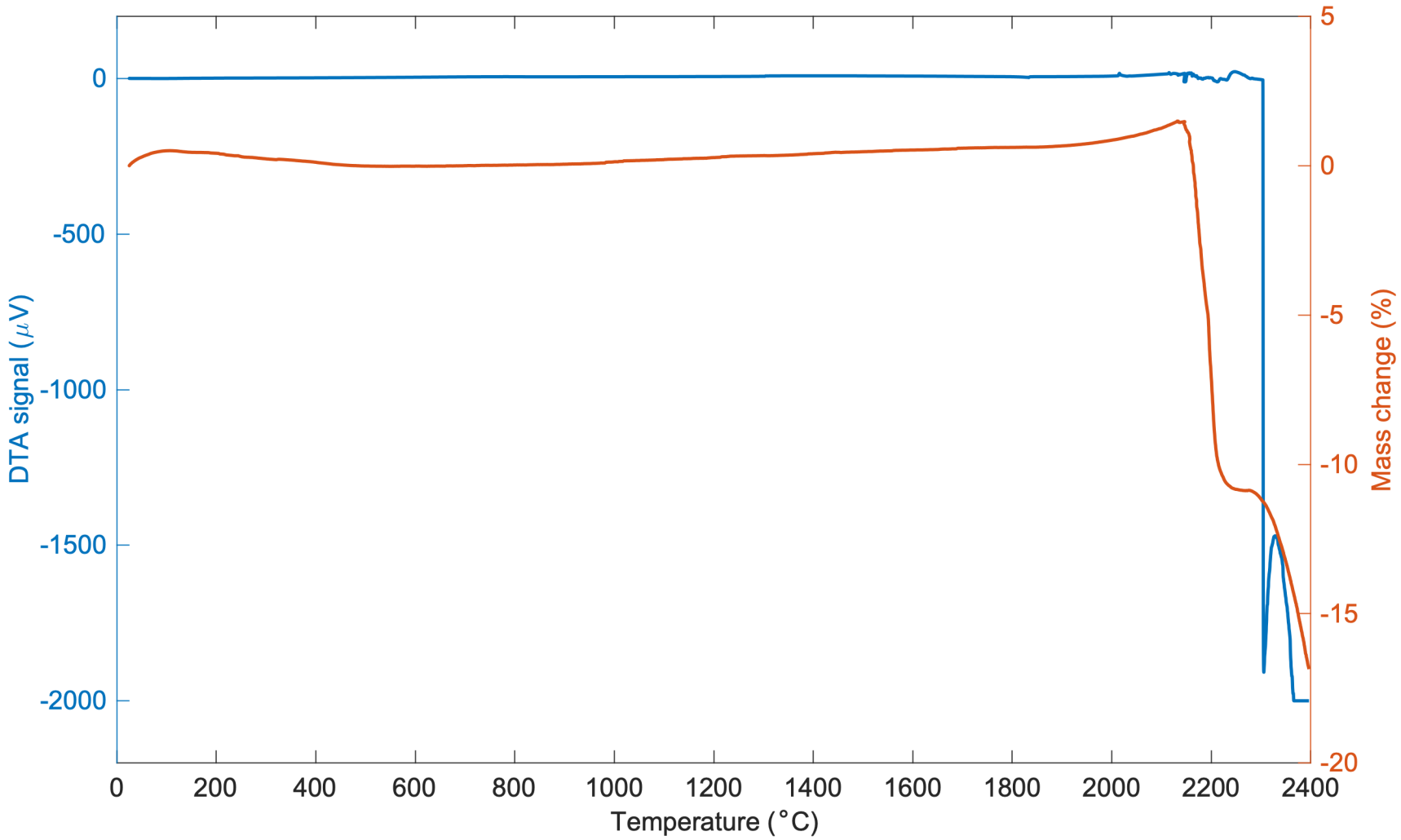

Figure G.8. Full 2400°C differential thermal analysis (blue) and thermogravimetric analysis (orange) results of doped SAS.

Appendix G.9

Annealing experiments were performed on precursor pellets for 10 hours to evaluate the amount of doped SAS that forms at temperatures lower than 1600°C. Since the doped SAS used in this work is reacted at 1600°C for 10 hours, it is expected that this thermal profile will produce a phase-pure pellet of doped SAS. However, it is unclear the extent of reaction that can occur at lower temperatures if the precursor mixture is annealed for a longer duration. XRD patterns and SEM/BSE images of the annealed pellets at a range of temperatures are presented in Figure G9.1. From the XRD data, the only crystalline phases observed are Sc_2O_3, $Sc_2Si_2O_7$, and doped SAS. Weight fractions of each observed crystalline phase, along with experimentally determined densities of annealed pellets, are presented in Table G9.1.

Based on this analysis, the doped SAS phase forms as the majority phase after the 1300°C anneal and increases in weight fraction with increasing annealing temperature, until it is the sole phase observed after the 1600°C anneal. These results indicate that the reactions observed in the high-temperature XRD experiment may be kinetically limited since additional time at each temperature allows for more doped SAS to form. It is noted that longer heat treatments (>10 hours) may result in even more SAS conversion than the results presented here at lower temperatures. Based on the results of Table G9.1, it appears that the majority of the doped SAS reaction occurs by the 1500°C anneal, which produces a pellet that is ~95 wt% doped SAS. There is a relatively limited amount of reaction that occurs between 1500°C and 1600°C. In the DTA data, the endothermic heat of reaction has an inflection point at ~1550°C, indicating that the reaction is approaching completion by 1550°C. Additionally, by comparing these data to the high-temperature XRD results (Figure 6.11), it appears that the reaction continues with additional time spent at 1500°C, but the rate of the reaction slows. The ~42 minute anneal at 1500°C in the high-temperature XRD produces a powder that is ~ 85% doped SAS. In comparison, the 10-hour anneal at 1500°C produces a pellet that is ~95% doped SAS, a relatively small increase over the high-temperature XRD results. This effect is likely due to the decreasing fraction of $Sc_2Si_2O_7$ with increasing doped SAS conversion, requiring longer times for the SiO_2 in $Sc_2Si_2O_7$ to diffuse and react with Sc_2O_3 and other dopant oxides to form the doped SAS phase.

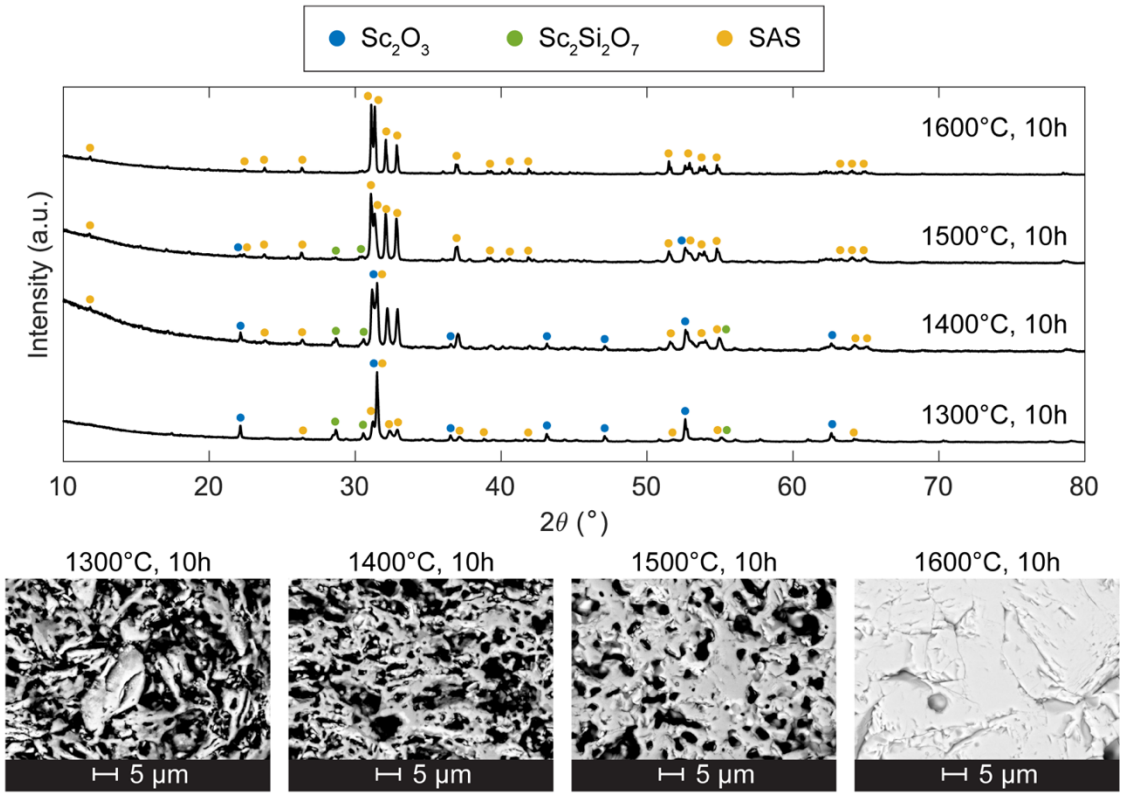

Figure G.9. XRD (Cu Kα) patterns and SEM/BSE images of precursor pellets annealed at 1300°C, 1400°C, 1500°C, and 1600°C for 10 hours.

Table G.9. Weight fraction and density of precursor pellets after 10-hour heat treatment in air.

Temperature	Weight percent			Density (g/cm^3)
	Doped SAS	Sc_2O_3	$Sc_2Si_2O_7$	
1300°C	55.2	30.6	14.2	2.005
1400°C	84.4	10.6	5.1	2.287
1500°C	95.3	2.9	1.8	2.746
1600°C	100	-	-	3.375